LATERAL RESPONSE OF STIFF COLUMN-SUPPORTED SHALLOW FOUNDATIONS

Alfonso José Rivera Rojas

Dissertation submitted to the faculty of the Virginia Polytechnic Institute and State University in partial fulfillment of the requirements for the degree of

Doctor of Philosophy
In
Civil Engineering

Celal G. Olgun, Co-Chair
Thomas L. Brandon, Co-Chair
Adrian Rodriguez-Marek
Joseph E. Dove

April 8, 2019
Blacksburg, VA

Keywords:
Stiff Columns
Lateral Response
Load Transfer
Centrifuge Tests
Numerical Modeling

LATERAL RESPONSE OF STIFF COLUMN-SUPPORTED SHALLOW FOUNDATIONS

Alfonso José Rivera Rojas

ACADEMIC ABSTRACT

The mechanisms that control the lateral response of stiff column-supported shallow foundations, resulting from the application of horizontal load on shallow foundations supported by stiff columns, are uncertain. Stiff columns constructed in soft clayey soil have been used to support retaining walls and in such cases, the lateral thrust applied behind these geotechnical structures is a source of horizontal loading. For seismic events, stiff columns constructed in soft clayey soil have been used to support shallow foundations subjected to horizontal load coming from the upper structure of buildings. Due to its practical applications, it has become important to understand the consequences of subjecting a shallow foundation supported by stiff columns to horizontal load by identifying the factors that control the lateral response of such systems.

A series of centrifuge tests were carried out to examine the lateral response of stiff column-supported shallow foundations. The experimental trends suggested that the thickness of the coarse-granular mattress placed above the soil-column composite, called the Load Transfer Platform (LTP), controlled the lateral capacity and the overall lateral response of these systems. A numerical study using the finite element method confirmed the experimental trends. A parametric analysis was conducted with the purpose of investigating the influence of different geometry-based and material-based variables in the lateral response of these systems. The results of the parametric analysis further

confirmed the importance of the thickness of the LTP in controlling the lateral response. The parametric results also emphasized the contribution of other variables to this lateral response, and these variables included the undrained shear strength of the soft clayey soil around the stiff columns, the stiff column diameter, and the spacing of the stiff columns after they are constructed in the soft clayey soil.

LATERAL RESPONSE OF STIFF COLUMN-SUPPORTED SHALLOW FOUNDATIONS

Alfonso José Rivera Rojas

GENERAL AUDIENCE ABSTRACT

Ground improvement is the process of improving the properties of weak soils. In practice, there are several ways to accomplish the ground improvement of weak soils. One way is to use stiff columns. Stiff columns are solid cylinders that are constructed in the weak soil in order to produce a stiff and strong soil-column composite capable of better supporting the square-shaped foundations of structures.

Under horizontal load, there is uncertainty on the factors that control the lateral behavior of the stiff columns when used for the support of the square-shaped foundations of structures. An experimental and numerical approach was used to determine these factors and to understand their influence in the lateral behavior of such systems. The findings showed that the controlling factors of this lateral behavior included the thickness of a sand layer placed above the stiff columns, the diameter of the stiff columns, the spacing of the stiff columns after they are constructed in the weak soil, and the strength of the soil around the stiff columns. These findings will aid in improving the design of stiff columns used for the support of square-shaped foundations of structures subjected to horizontal load.

ACKNOWLEDGMENTS

I like to thank Frederic Masse and DGI Menard USA for providing financial support to this research project. I also would like to thank my co-advisors Dr. Guney Olgun and Dr. Thomas Brandon for providing constant guidance and support throughout this research. I also would like to thank Dr. Joseph Dove and Dr. Adrian Rodriguez-Marek for their valuable feedback to help improve this research. I also would like to thank Dr. John McCartney and Dr. Min Zhang for providing support during the experimental work carried out at the University of Colorado Boulder.

I would like to thank God for giving me the energy, stamina and perseverance to complete this research. I like to thank my family, my parents Alfonso Rivera Alvarez and Reyna Odilí Rojas García de Rivera, my brothers Diego Andrés Rivera Rojas and Jacobo Gabriel Rivera Rojas, for their unconditional support, encouragement and love. I thank my little niece Alaia Anneliese Rivera for given me joy and laughter in the home stretch of this project. I also thank Martita for her unconditional support over the years. During my studies at Virginia Tech I made numerous friends but I would like to particularly thank Edgar de León Izeppi and Bonnie Sumner who were unconditionally supportive during my stay in Blacksburg. I also would like to acknowledge Karla Santacruz, Daniel Mogrovejo, Ashly Cabas, Celso Castro, Adrian Tola, Soheil Kamalzare, Mohammad Khosravi, Melis Sutman and Zhanyu “Grace” Huang. Your friendship has made me a better person and for this and much more, I thank you all.

TABLE OF CONTENTS

LIST OF FIGURES

LIST OF TABLES

CHAPTER 1: INTRODUCTION

1.1 BACKGROUND AND MOTIVATION

The use of ground improvement technologies for a wide variety of applications have demanded further understanding of the interaction of such technologies under different loading conditions. This is the case of the ground improvement technology known as stiff columns. Stiff columns are used to transfer the foundation load, from slabs, footings and embankments, to deeper strata and under such conditions, extensive studies have been carried out with the purpose of characterizing their response under vertical load (ASIRI 2012). The presence of additional horizontal load (Figure 1.1), in particular, has increased the interest of examining the lateral response of these rigid vertical elements when employed for the support of shallow foundations. Sources of horizontal loading can include lateral thrusts behind retaining walls and horizontal loads coming from the upper structure of buildings during seismic events. Presently, studies that have investigated the lateral behavior of stiff columns have been focused towards the lateral response of stiff columns supporting embankments for roadway applications. On the other hand, studies that have investigated the lateral response of stiff columns for the support of shallow foundations have been relatively scarce. As such, the overall purpose of this work was to address this problem by means of experimental and numerical studies that aimed at identifying the factors that control the lateral response of stiff columns constructed for the support of shallow foundations subjected to horizontal load.

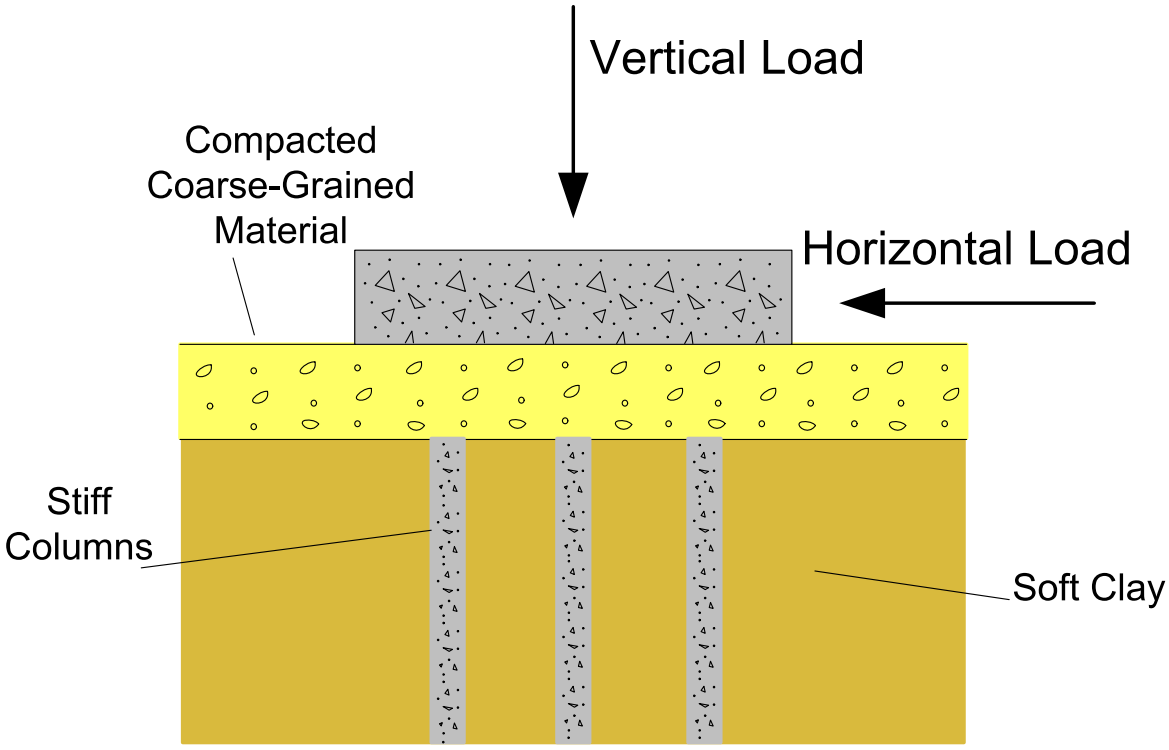

Fig. 1.1. Shallow foundation supported by stiff columns subjected to vertical and horizontal loads.

1.2 RESEARCH OBJECTIVES

This research had the following objectives:

- Review the current state of knowledge of stiff column-supported shallow foundations under vertical load.
- Review previous experimental and numerical studies that investigated the lateral behavior of stiff column-supported shallow foundations under horizontal load. References related to the lateral response of stiff columns used for the support of shallow foundations were compiled and examined.

- Experimentally determine the influence of the Load Transfer Platform (LTP) thickness in the lateral response of stiff column-supported shallow foundations. This was accomplished by using small scale physical models in centrifuge tests.
- Verify the trends observed in the experimental study using a numerical approach employing the finite element method. This was accomplished by constructing numerical models and subjecting them to the experimental conditions tested. The finite element software built for geotechnical applications PLAXIS in both its 2D and 3D versions were used.
- Numerically study the lateral response of stiff column-supported shallow foundations using a parametric analysis. Specific parametric variations of geometry-based and material-based variables were examined. The finite element software PLAXIS 3D was used in the parametric study.
- Identify the factors that controlled the lateral response of stiff column-supported shallow foundations. After the experimental and numerical studies were completed, the variables that controlled the lateral response were identified and conclusions were gathered in regards to their influence in the lateral response of the systems examined.

1.3 DOCUMENT OUTLINE

This dissertation is comprised of eight chapters. The first chapter provides the background and motivation behind this research. It includes the research objectives that were accomplished and an outline of the chapters included in the dissertation. The second chapter presents a literature review that provides background and context on the current state of knowledge of stiff columns for the support of shallow foundations under vertical and horizontal loads. The second chapter

also provides an overview of this ground improvement technology and the types of stiff columns employed in practice. Finally, the second chapter provides an overview of previous studies that have examined the lateral response of stiff column-supported shallow foundations.

The third chapter presents, in detail, the experimental stage of this research in which centrifuge testing was used to assess the lateral performance of stiff column supported-shallow foundations. The theory employed in centrifuge testing, scaling laws, testing equipment, the centrifuge model construction procedure and the experimental results are discussed in this chapter.

The fourth chapter describes the numerical background, and the procedure used to construct and run a series of models that were employed to numerically investigate and verify the experimental trends described in the third chapter. The numerical results were compared with the experimental results and a discussion of the trends is presented.

The fifth chapter expands the numerical work of the fourth chapter by describing a parametric analysis that was used to further investigate the lateral behavior of stiff column-supported shallow foundations. The variables selected for the parametric analysis along with the range of values considered for each variable are presented and justified accordingly. This chapter discusses the importance of the variables and their influence in the lateral response of these systems.

Chapter six summarizes the main conclusions gathered from earlier chapters. Chapter seven provides a list of the references employed throughout the research, and chapter eight provides a

list of appendices that provide complementary information not presented in the main core chapters of the dissertation.

CHAPTER 2: LITERATURE REVIEW

2.1 INTRODUCTION

This chapter provides a review of references that detail the operating mechanisms that control the load transfer in stiff column-supported shallow foundations, including the types of stiff columns employed in practice, typical applications of this ground improvement technology and construction considerations. A review of studies that examine the lateral response of stiff column-supported shallow foundations is also presented.

2.2 STIFF COLUMNS

2.2.1 *Definition*

Stiff columns are a type of ground improvement technology in which rigid slender vertical elements, often cylindrical in shape and mechanically continuous, are constructed in soft compressible subsurface conditions with the purpose of producing a soil-column composite with improved mechanical properties. Stiff columns are constructed in grid-patterned groups (square or triangular) and are designed based on project specific load and soil conditions. Benefits that result from improving the foundation subgrade include an increase in the bearing capacity of the soil-column composite, and an increase in the stiffness of the soil-column composite resulting in meeting serviceability requirements in terms of settlement.

Stiff columns do not rely on confinement of the soil for stability and performance because of the stronger tensile strength of the material they are made from, a critical difference compared to the design of “softer-type” columns such as stone columns or rammed aggregate piers (Buschmeier and Masse 2012).

Stiff columns can be considered as an intermediate foundation solution in addressing strength and settlement requirements. When such requirements are not met using a conventional shallow foundation design (Figure 2.1a), a deep foundation solution (Figure 2.1b) is often implemented. However, under certain loading conditions, a stiff column-supported shallow foundation (Figure 2.1c) can provide a cost-effective solution in addressing such requirements without having to implement an over-designed and costly deep foundation solution.

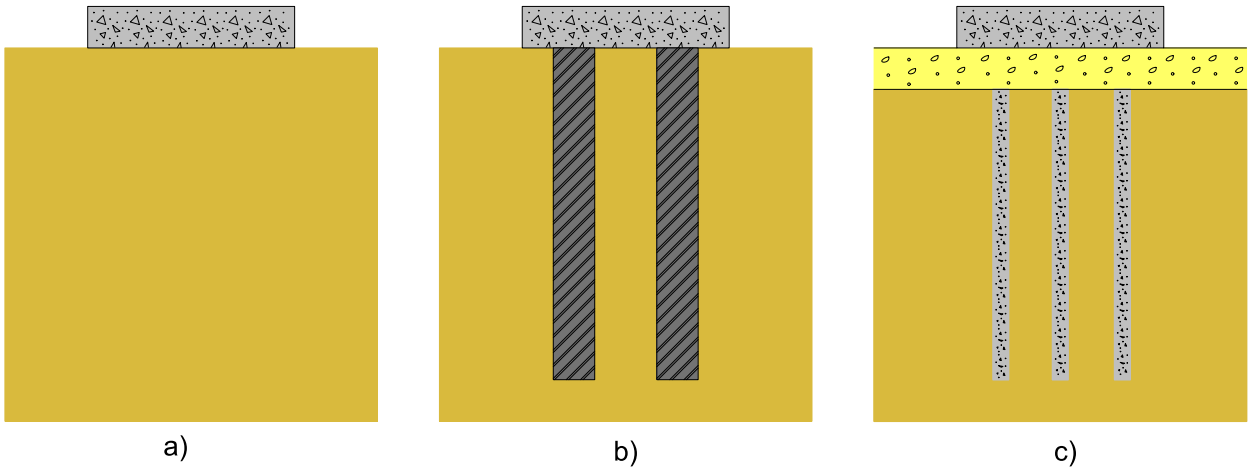

Fig. 2.1. a) Shallow foundation, b) deep foundation and c) stiff column-supported shallow foundation (after ASIRI 2012).

2.2.2 *Components of a Stiff Column-Supported Shallow Foundation*

Stiff column-supported shallow foundations and deep foundations share similarities and important differences in their design and examination as observed in Figure 2.1. While vertical elements are associated with both types of systems, in deep foundations the vertical elements are rigidly connected to a pile cap whose purpose is to share the structural load between the vertical elements. On the other hand, no mechanical connection exists between the stiff columns and the shallow foundation but rather a granular mattress made of well graded coarse material, known as the *Load Transfer Platform* (LTP), is placed between the shallow foundation and the stiff columns. The presence of this coarse-granular mattress produces changes in the load transfer mechanisms that take place in the stiff column-supported shallow foundation.

Figure 2.2 shows in more detail the components of a stiff column-supported shallow foundation. As observed in this figure, the stiff columns are constructed in the soft soil and they are usually embedded in a bearing stratum. While the thickness of the LTP is dependent on the loading conditions, a minimum thickness of 30 cm is adopted to provide minimum load transfer between the stiff columns and the soil (ASIRI 2012). The LTP may or may not include a layer of geosynthetic that can further aid in transferring the foundation load to the stiff columns (Lawson 1992, Russell and Pierpoint 1997, Kempton et al. 1998, Han and Wayne 2000, Han and Gabr 2002, Smith 2005).

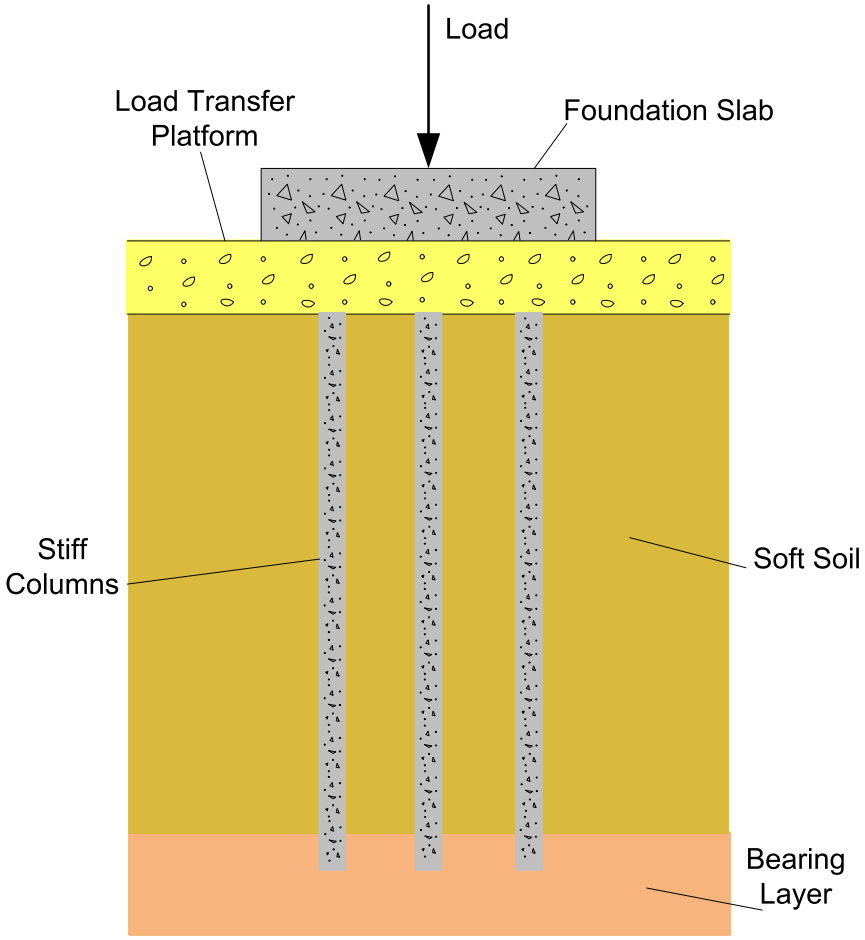

Fig. 2.2. Components of a stiff column-supported shallow foundation (after ASIRI 2012).

2.2.3 *Applications*

Stiff columns are most applicable in soft ground i.e. cohesive soil deposits with high moisture, high compressibility and low strength (Porbaha 1998a). Soft soils include fat clays, silts and peats. Moreover, stiff columns are most beneficial when used to support structures with distributed-type loading which include (ASIRI 2012):

- Slabs and footings of industrial and commercial buildings.
- Reservoir structures used for the storage of water, oil products or liquid chemicals.

- Retention structures, which include mechanically stabilized earth walls.
- Highway embankments or railway embankments.

2.2.4 *Types*

Different types of stiff columns are available to address settlement and strength issues of structures supported on soft compressible soils. The following section provide an overview of the most common types of stiff columns employed in practice, including a brief description of construction considerations for each of the types described. The reader is cautioned that the following summary is not exhaustive in presenting the technical details of each of the columnar technologies described, but rather the intention is to highlight the most relevant features of each technology. When applicable, further references will be provided to complement the information presented.

2.2.4.1 Controlled Modulus Columns

Controlled Modulus Columns (CMCs) from DGI-Menard are a type of grout-based stiff column technology. CMCs are constructed using a proprietary displacement auger. The lean cement-based grout (usually a lean sand-cement grout) is placed with enough pressure to avoid collapse of the displaced soil during auger withdrawal (Masse et al. 2012). The unconfined compressive strength of the grout is adapted to the requirements of the design and typically varies between 6.9 to 20.7 MPa. Figure 2.3 shows the typical CMC construction procedure. As observed in this figure, the auger is advanced and displaces the soil (Figure 2.3a). As a result of the displacement of the soil during insertion of the auger, spoils are not conveyed to the surface. Upon reaching the desired depth (Figure 2.3b), grout is pumped as the auger is withdrawn (Figure 2.3c). Column diameters typically range from 280 to 450 mm and are selected based on the structural

demand and the geotechnical conditions of the site. The depth of CMC construction is limited to 35 m (Masse et al. 2012). Load conditions under which this ground improvement is beneficial range from light, to medium-sized loads, which corresponds to bearing pressures under footings of 191.5 kPa to 383 kPa (Masse et al. 2012).

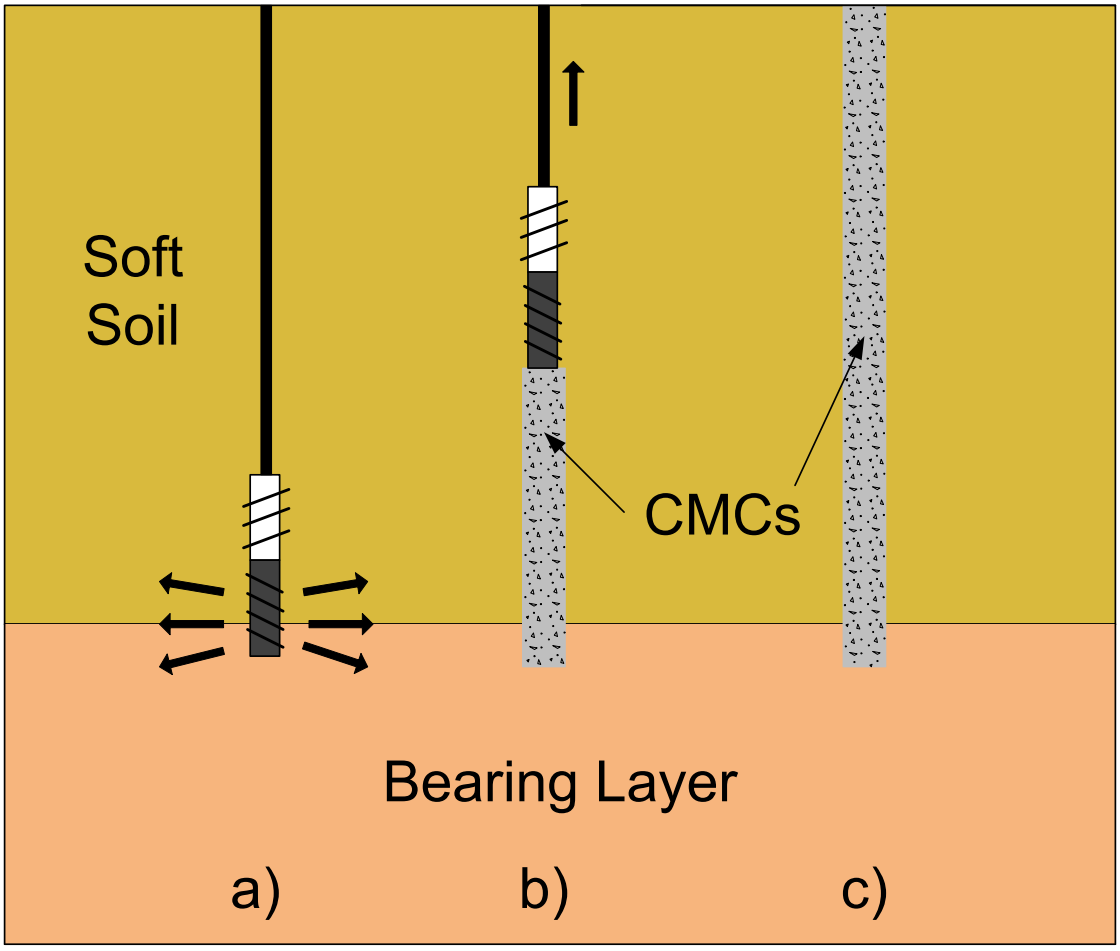

Fig. 2.3. Typical CMC construction procedure: a) the auger is advanced and it displaces the soil, b) upon reaching the desired depth, grout is pumped as the auger is withdrawn c) resulting in the construction of the CMC (after Masse et al. 2012).

For details on construction considerations of CMCs and case studies involving application of this columnar technology, the reader is referred to Plomteux et al. (2004), Masse et al. (2009), Masse

et al. (2011a), Masse et al. (2011b), Wilson-Fahmy et al. (2011), Masse et al. (2012) and Buschmeier et al. (2012).

2.2.4.2 Deep Mixed Columns

Deep Mixed Columns (DMC) refer to inclusion-type elements that are constructed using Deep Mixing Methods. In the Deep Mixing Method, cementitious (cement, lime, fly ash, etc.) or chemical reagents are combined with soil via rotary mixing tools to produce a composite with improved engineering properties resulting in higher strength and increased stiffness. From a historical standpoint, the various techniques employed in the Deep Mixing Method were originated and pioneered in the 1960s and 1970s independently in Sweden through the Swedish Geotechnical Institute, and in Japan by the Port and Harbour Research Institute (Porbaha 1998a, Kitazume and Terashi 2013). This has resulted in an extensive body of work that includes design, installation procedures and applications of the Deep Mixing Method. Smith (2005) provided a summary of the history of the Deep Mixing Method and its introduction to US practice. Stiff column included in this category include lime columns, lime-cement columns, cement columns and soil-cement columns. While a thorough description of the different Deep Mixing Method procedures is beyond the scope of this review, Navin (2005) provides a list of key references, shown in Table 2.1, that describe the construction, equipment, installation and application of the Deep Mixing Method to the construction of stiff columns. Additional useful references not listed by Navin (2005) are incorporated in this table as well.

Table 2.1. References that describe the construction of stiff columns using Deep Mixed Methods

Reference	Title
Bruce and Bruce (2003)	The practitioner's guide to deep mixing.
Bruce et al. (2013)	FHWA Design Manual: Deep mixing for embankment and foundation support.
Federal Highway Administration (1999)	Demonstration project 116 Ground improvement technical summaries, Vols. I & II.
Hansbo and Massarsch (2005)	Standardization of deep mixing methods
Holm (2002)	Nordic dry deep mixing method execution procedure.
Kitazume and Terashi (2013)	The deep mixing method
Nakanishi (2002)	Execution and equipment of cement deep mixing (CDM) method.
Porbaha (2001)	State of the art in construction aspects of deep mixing technology.
Porbaha (1998a)	State of the art in deep mixing technology; Part I. Basic concepts and overview.
Porbaha (1998b)	State of the art in deep mixing technology; Part II. Applications.
Stocker and Seidel (2005)	Twenty-seven years of soil mixing in Germany: The Bauer mixed-in-place-technique
Terashi (2002)	Development of deep mixing machine in Japan.
Yasui et al. (2005)	Recent technical trends in dry mixing (DJM) in Japan

The unconfined compressive strength of deep mixed materials is influenced by several factors. These factors include the stabilizer content, mixing efficiency, curing time, curing temperature, water content of the mixture, and the organic content of the base soil (Navin 2005). For instance, soils treated with the dry method of Deep Mixing, in which the reagents are introduced and mixed in dry powder form, the unconfined compressive strength may range from 13.8 kPa to 2.8 MPa. For soils treated with the wet method of Deep Mixing, in which the reagents are introduced in slurry form, the unconfined compressive strength may range from about 138 kPa to 28 MPa (Japanese Geotechnical Society 2000, Baker 2000, Jacobson et al. 2003). The high variability of the strength of deep mixed materials for the construction of stiff columns has resulted in the

development of mix design studies, utilizing soil obtained from a project site of interest, to properly estimate the target strength of stiff columns constructed using Deep Mixing Methods.

2.2.4.3 Vibro-Concrete Columns

Another type of stiff column often employed in practice is the *Vibro-Concrete Column* (VCC). The construction procedure of this type of stiff column is similar to the one described for Controlled Modulus Columns, however VCCs have their own distinct constructive features. A bottom feed vibrator is first inserted into the soil before concrete is introduced and a bulb of concrete is formed at the base of the column after which the vibrator is withdrawn forming the shaft of the VCC. The top of the VCC can be expanded at the ground surface in order to assist with the load transfer (Hussin 1994). Typical VCC diameters can range from 400 mm to 600 mm. Figure 2.4 provides a schematic of the construction procedure of VCCs. Due to the proprietary nature of the technology employed to construct VCCs, information on this type of stiff column is limited; however, Table 2.2 provides a list of additional references that detail further construction considerations and case studies in which VCCs have been employed.

Table 2.2. List of references that describe the construction of Vibro-Concrete Columns

Reference	**Title**
Hussin (1994)	Ground Modification with Vibro Concrete Columns
Hussin et al. (2001)	Embankment Construction in Soft Soils using Vibro Concrete Columns
Mankbadi et al. (2004)	Ground Improvement Utilizing Vibro-Concrete Columns
Welsh (1997)	Excellence in Geotechnical Engineering: Ground Modification Milestones
Zamiskie et al. (2004)	Vibro Concrete Columns Solve Problems for Victory Bridge Approach Fill

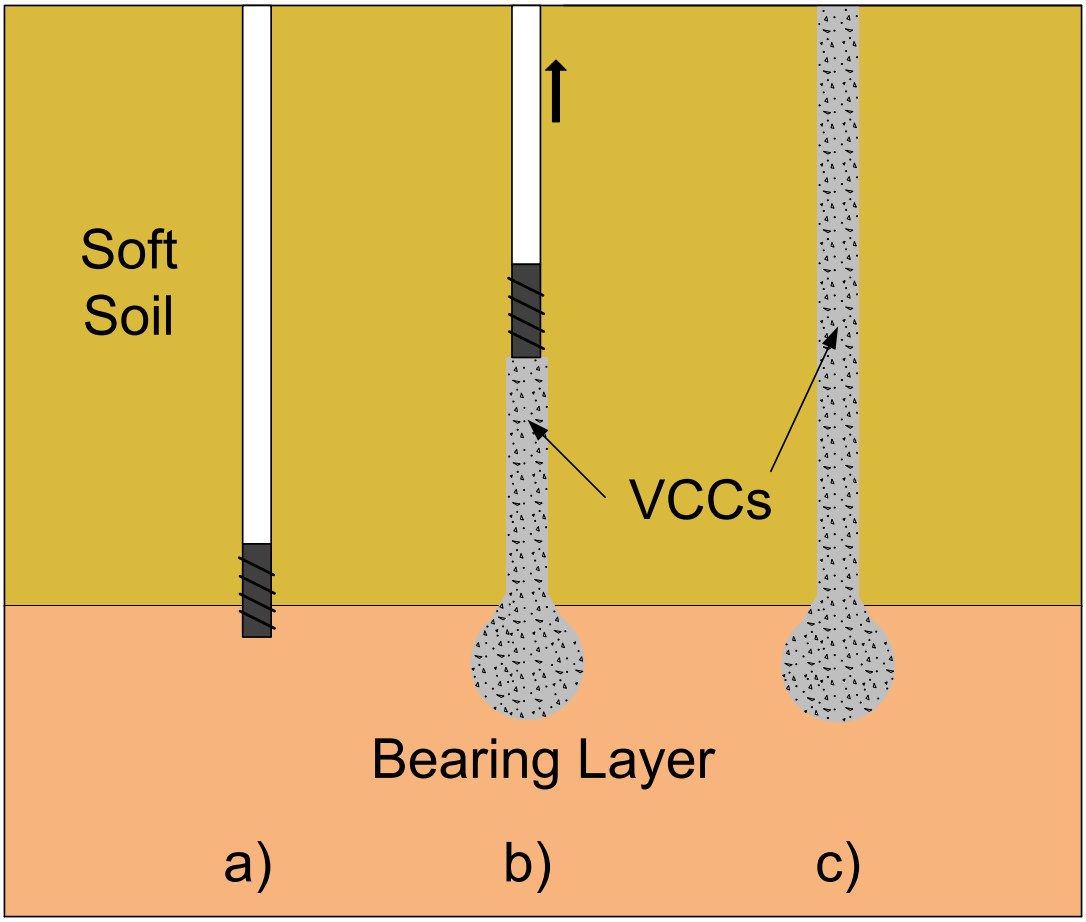

Fig. 2.4. Typical VCC construction procedure: a) bottom feed vibrator is lowered to bearing layer, b) concrete is pumped forming a bulb of concrete and the vibrator is withdrawn c) forming the shaft of the VCC (after Mankbadi et al. 2004).

2.2.4.4 Jet Grouted Columns

Jet Grouted Columns are another type of stiff column that is employed in practice. In general, the process of jet grouting consists of breaking up or eroding the soil using fluid jetting. The fluid itself is a cement-based slurry. The fluid is injected at high velocities and pressure that the "jet" essentially breaks down the soil, combining the dissolved soil with the fluid to produce a soil-cement material in the form of circular columns (Warner 2004). Figure 2.5 provides a schematic of the jet grouting column construction procedure. The construction sequence consists on drilling and lowering the rod of the rig through the soft soil (Figure 2.5a). The cement-based slurry grout

is pumped under high velocity conditions through the rotating rod and down to a series of injection nozzles that are installed at the tip of the drilling rod (Figure 2.5b). The jet disintegrates the soil while mixing with the injected slurry. This procedure is repeated while the rotating rod is slowly withdrawn to form the column (Figure 2.5c). Any excess soil-cement mix is pushed to the surface and the spoils are disposed regularly.

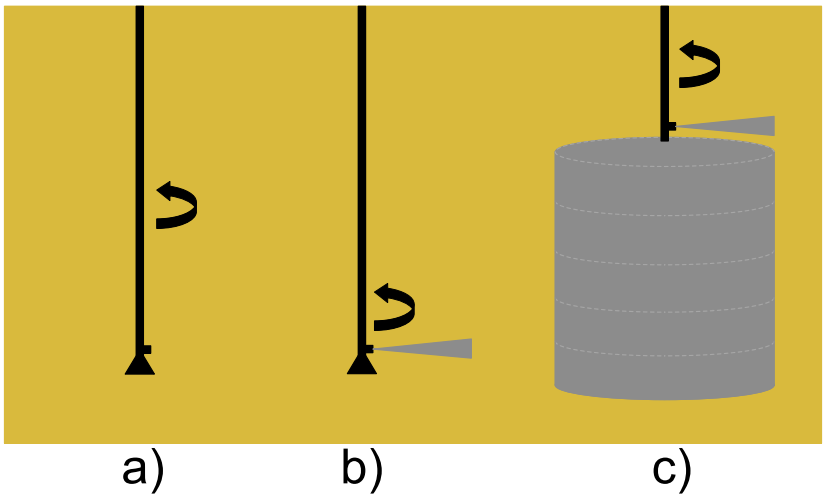

Fig. 2.5. Jet grouting construction procedure using the single-fluid system: a) drilling rod is lowered, b) binder fluid in injected at high velocity and pressure, breaking down soil and c) the procedure continues as the rod is withdrawn from the ground (after Burke 2004).

The type of jet grouting system used along with the subsurface conditions of the site will determine the geometrical (size) and mechanical conditions (compressive strength) of the stiff columns. The procedure shown in Figure 2.5 is typical of the single-fluid system which is the simplest system employed in jet grouting. In this system, the only fluid injected into the soil is the slurry and column diameters can range between 400 to 600 mm in cohesive soil, while up to 1200 mm diameter thick columns are obtainable in cohesionless soils (Warner 2004). In addition to the single-fluid jet system, further complexity can be added to the jet grouting column construction procedure with the two-fluid and three-fluid systems. In the case of the two-fluid system, the slurry or grout is encased within a shroud of compressed air, with the two fluids

coming out from a single set of nozzles resulting in improved soil-cutting efficiency. Column diameters in the order of 600 mm to 900 mm can be obtained in cohesive soils with up to 1800 mm in cohensionless soils using the two-fluid system (Warner 2004). In the case of the three-fluid system, air-encased water is used to erode the soil through a set of nozzles, while in a separate set of nozzles, the slurry is injected. The three-fluid system produces the largest columns yet, with diameters of 600 to 1500 mm in cohesive soils and up to 3600 mm in cohesionless soil. The unconfined compressive strength of the column can reach up to 13.8 MPa in cohensionless soils and up to 3.4 MPa in cohesive soils (Warner 2004). For more information on jet grouting, including specific information on equipment employed in the construction of these types of stiff columns, the reader is referred to Warner (2004).

2.3 STIFF COLUMN-SUPPORTED SHALLOW FOUNDATIONS

2.3.1 *Vertical Load*

This section will describe the governing load transfer mechanisms that take place in stiff column-supported shallow foundations. This will provide a basic framework in understanding the various interactions between the components of a stiff column-supported shallow foundation subjected to vertical load.

2.3.1.1 Interaction between the Soil-Column Composite and Load Transfer Platform

The influence of the LTP in transferring the structural load from the foundation to the improved soil-column composite has been a subjected of extensive research and study. For instance, it has been established that the geometrical and mechanical characteristics of the LTP and the type of

foundation supported will influence the amount of load transferred to the soil-column composite (ASIRI 2012). The LTP essentially spreads the structural load between the stiff columns and the soft soil, but due to the greater stiffness of the rigid vertical elements, the stiff columns attract a greater portion of the structural load (Buschmeier and Masse 2012). This produces “arching” of the load inside the LTP which increases the load at the top of the stiff columns with time due to consolidation, and hence settlement, of the soil between the rigid vertical elements (Reid and Buchanan 1984, Ooi et al. 1987, Huat et al. 1994).

Studies related to the transfer of the foundation load inside the LTP have highlighted that stresses develop inside the LTP, and these manifest in the form of stress chain networks (Chevalier et al. 2010a). Such studies have also found that the greatest development of stress chain networks occur close to or at the top of the stiff columns producing the arch-type stress field. The mechanics of this arching mechanism were demonstrated early on by Terzaghi (1943) using a trap door experiment and has become an important mechanism in understanding how the load is transferred in stiff column-supported shallow foundations under vertical load.

The development of stress-arching inside the LTP is directly related to the concept of critical height of this coarse-granular layer. The critical height of the LTP constitutes the height of this coarse-granular mattress at which the stress-arching fully develops. Studies have indicated that this critical height is closely related to the spacing between stiff columns (Jenck 2005, Baudouin 2010, McGuire 2011). These studies also show that the critical thickness determines the magnitude of differential settlements developed at the surface of the LTP. When considering the critical thickness of the LTP in relation to the support of footings, studies have shown that for a

given LTP thickness less than the critical height, the load transferred to the stiff columns in the soil-column composite decreases with increasing LTP thickness, while the bending moments that develop in the footing decrease (Dinh 2009). Moreover, numerical studies by Laurent (2002) have indicated the presence of zones of increased stress concentration inside the LTP. These regions of high concentration become the preferred zones in transferring the structural load to the soil-column composite, thus increasing the load at the top of the stiff columns.

2.3.1.2 Interaction between Surrounding Soil and Stiff Columns

While the mechanisms described in the previous section result in the load increasing at the top of the stiff columns, not all the load is actually transferred to the rigid vertical elements, but rather, part of the load is transferred to the soil between stiff columns. The interaction between the stiff columns and the surrounding soil during vertical loading is described by the development of downdrag in the stiff columns. This downdrag load, also known as negative skin friction, is a type of loading condition that has been classically observed and studied in piles (Fellenius 1999). Downdrag develops when the soil around a vertical element settles more than the element itself, producing additional load in the vertical element. This phenomenon can become critical in cases where pile groups are installed in soft soil and a fill is placed above the soft soil. The placement of the fill induces excess pore-water pressures in the soil between the piles that later dissipate with time, resulting in the relative downward motion of the surrounding soil with respect to the piles, and thus the development of downdrag load in the piles. Downdrag can cause issues in structures supported by pile groups (Coduto et al. 2015) especially in light of the mechanical linkage that exists between top of the piles and the pile cap. For this reason, different approaches have been proposed to address the problems generated by downdrag in piles (Salgado 2008).

In the context of stiff columns however, downdrag becomes an important mechanism in transferring the foundation load to deeper competent soil layers. As the soil settles more than the stiff columns (Figure 2.6), load coming from the LTP to the soft soil is transferred directly to the stiff columns by the downdrag phenomenon, producing a negative shaft resistance, f_N, at the edge of the column thus increasing the compressive load Q_T at the top of the stiff columns with depth until a maximum load $Q_T + F_N$ is reached (Figure 2.7) where settlements between the soil and the stiff columns are equal. The location of settlement equilibrium between the stiff column and the soil at depth h_c is called the neutral plane. In this case, F_N represents the total shaft load induced along the column shaft above the neutral plane. Below the neutral plane, the stiff columns settle more than the soil (Figure 2.6), load is transferred to the soil and the column experiences conventional positive shaft resistance f_P. The maximum compressive load $Q_T + F_N$ in the column gradually decreases with depth until $Q_B = Q_T + F_N - F_P$ (Figure 2.7) where F_P is the total shaft load below the neutral plane and Q_B is the load at the bottom of the column. The remainder of the load at the bottom of the column, including the load in the soil around it, is transferred to the bearing stratum. Figure 2.8 summarizes the load distribution that occurs in the columns and the surrounding soil as the foundation load is transferred from the LTP to the bearing layer.

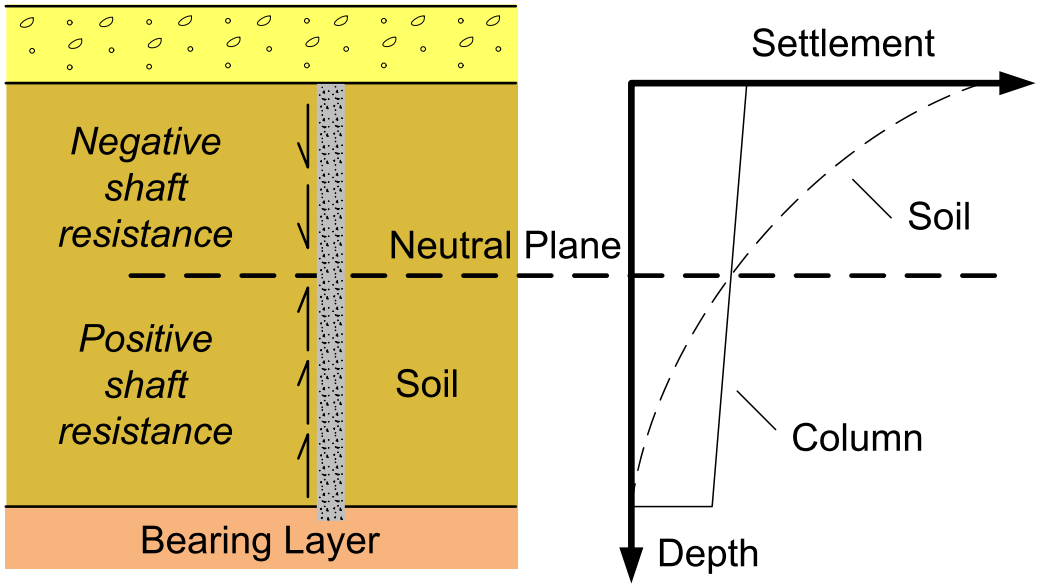

Fig. 2.6. Settlement distribution between the soil and a stiff column (after Masse et al. 2012).

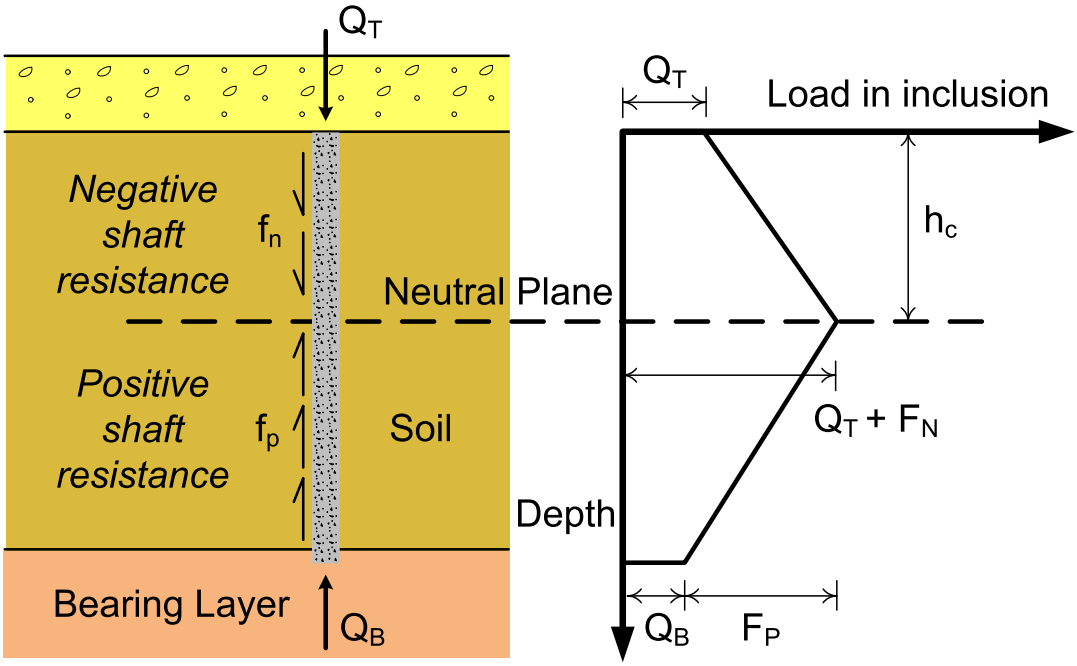

Fig. 2.7. Load distribution in a stiff column (after ASIRI 2012).

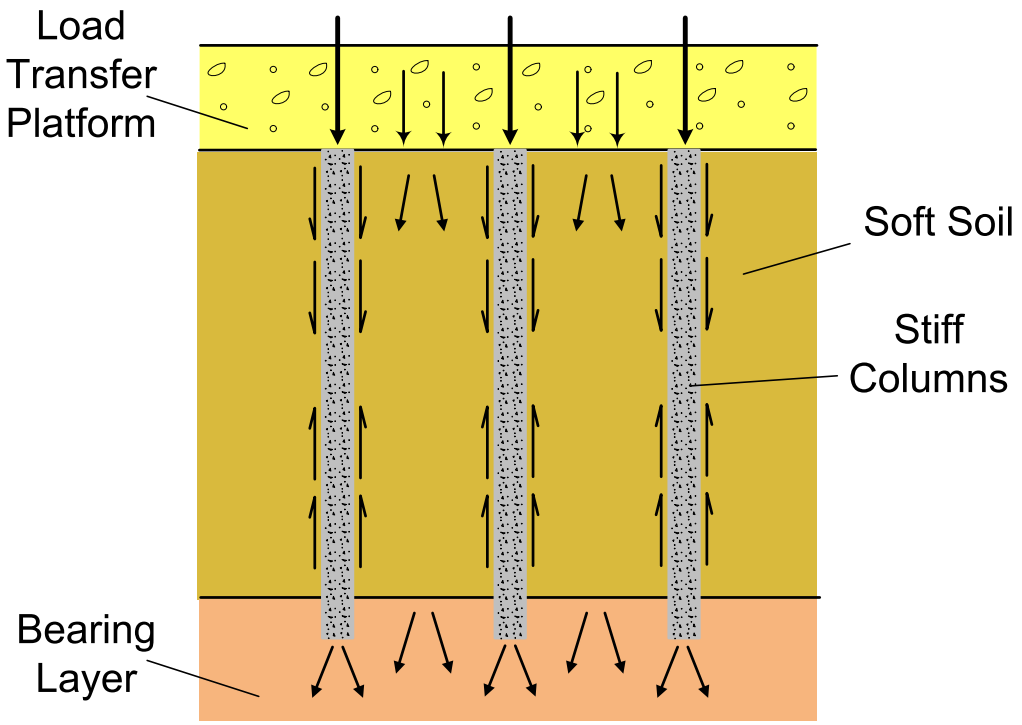

Fig. 2.8. Load distribution between the soil and a stiff column network (after Masse et al. 2012).

2.3.1.3 Additional Studies

The following table provides a list of additional studies that have increased the understanding of the vertical load transfer mechanisms in stiff column-supported shallow foundations and embankments. The purpose is to complement the information presented up to this point. Each study includes the type of foundation examined, all applicable numerical and experimental analyses performed, and remarks that clarify the overall objective of the study. The list is not limited to only shallow foundations since many of the load transfer mechanisms described previously have also been observed and investigated in embankments supported by stiff columns.

Table 2.3. Additional studies related to the vertical examination of stiff column-supported shallow foundations and embankments

Reference	Type of Foundation	Numerical Study	Experimental Study	Remarks
Alamgir et al. (1996)	NA	Finite Element Analysis	NA	Comparison of a theoretical model that predicts the deformations of a soil-column composite with finite element results
Bai et al. (2001)	NA	Finite Element Analysis	Full-scale test	Assessment of load transfer and settlement distribution in a soil-column composite
Baker (1999a)	NA	Finite Difference	NA	Examination of settlements due to consolidation of soil-column composite
Baker (1999b)	Embankment	Finite Element Analysis	NA	Examination of the stress distribution in a soil-column composite
Chevalier et al. (2010b)	Embankment	Discrete Element Method	Full-scale test	Examination of the load transfer mechanisms inside the LTP
Chevalier et al. (2011)	Emkbankment/Shallow Foundation	Finite and Discrete Element Method	NA	Examination of load transfer mechanisms inside the LTP
Fiovarante et al. (1997)	Shallow Foundation	NA	Centrifuge tests	Use of centrifuge testing to examine the factors that control settlement in a soil-column composite
Hewlett and Randolph (1988)	Embankment	NA	Full-scale and small-scale tests	Examination of the arching effect in stiff column-supported embankments
Low et al. (1994)	Embankment	NA	Small-scale tests	Examination of the arching effects in stiff column-supported embankments

2.3.2 *Horizontal Load*

This section provides a review of numerical and experimental studies that have investigated the lateral response of stiff column-supported shallow foundations. The current procedures used to examine these systems under horizontal load are also described.

2.3.2.1 Background

In general, the examination of the lateral load behavior of stiff columns has focused on the analysis of the mechanics of lateral deformation and resistance of a soil-column composite used for the support of embankments for roadway applications. Important findings that have contributed to the understanding of these mechanics have come from studies performed in Scandinavia (Kivelo 1997, Kivelo 1998, Kivelo and Broms 1999), Japan (Hasegawa et al. 1984, Amano et al. 1986, Hayashi et al. 1990, Miyake et al. 1991, Kitazume 1994, 2006, Kitazume and Maruyama 2005, 2006, 2007, Kitazume 2008) and the United States (Navin 2005, Filz 2009, Adams 2011). These studies have also been directed towards the analytical, numerical and physical examination of failure modes in stiff column-supported embankments, and improving their design methodology to better assess their external and internal stability. Kitazume (2008) summarized the failure modes observed in stiff columns constructed in soft soil for the support of embankments as following:

- Sliding failure (Figure 2.9a): A type of external failure mode in which the stiff columns move horizontally together.
- Rupture breaking failure (Figure 2.9b): A type of internal failure mode in which the slip surface passes through the embankment and the soil-column composite.
- Racking failure (Figure 2.9c): A type of internal failure mode in which the stiff columns tilt laterally.
- Shear failure (Figure 2.9d): A type of internal failure mode in which the stiff columns experience shear failure but the slip surface does not reach the embankment.
- Bending failure (Figure 2.9e): A type of internal failure mode in which the flexural resistance of the stiff columns is reached.

These failure modes have been extensively studied. On the other hand, studies that have examined the lateral load behavior of stiff columns constructed in soft soil for the support of shallow foundations such as footings and slabs are scarce. A summary of studies related to the investigation of the lateral response of stiff column-supported shallow foundations available in the literature is presented.

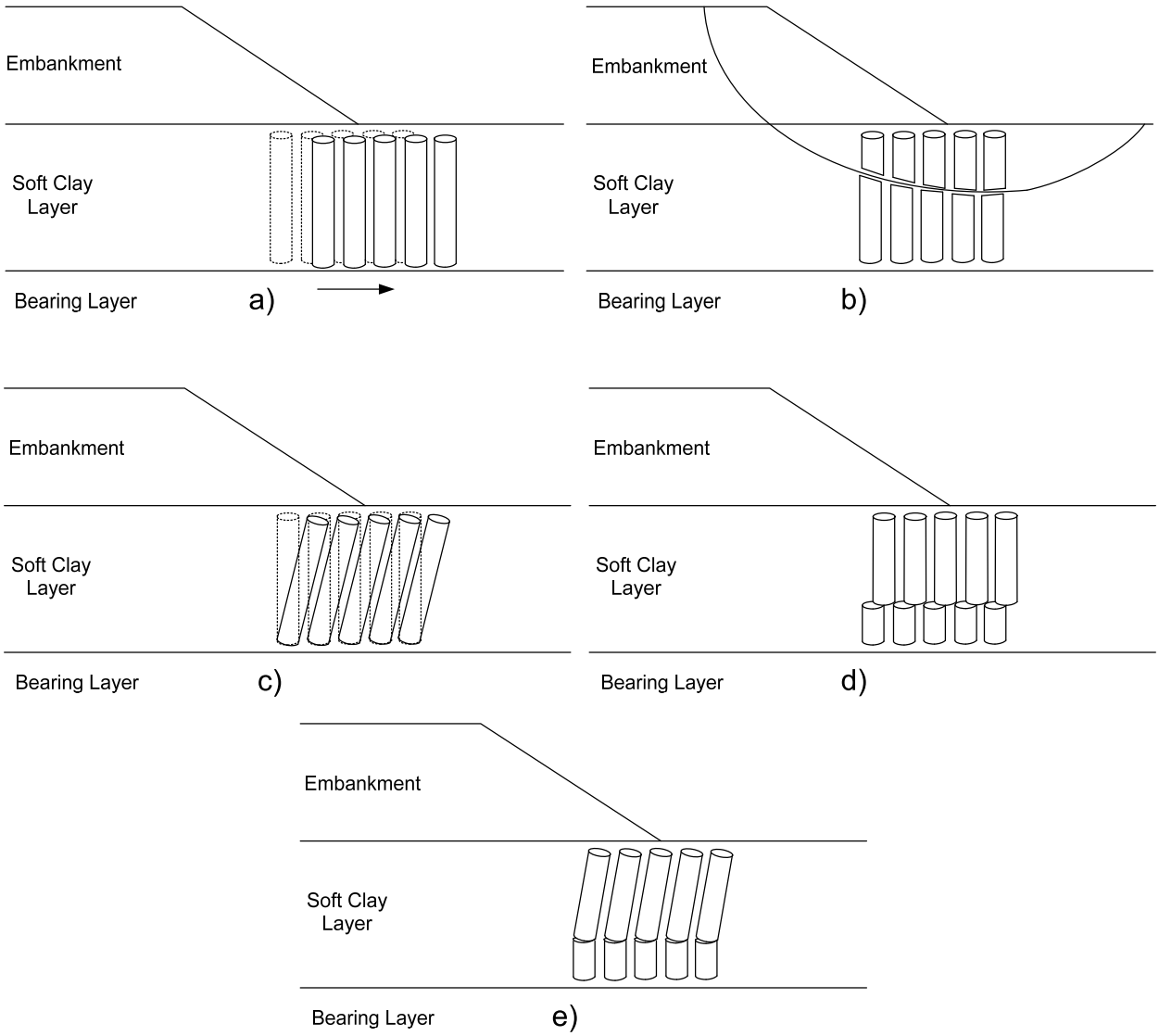

Fig. 2.9. Failure modes in stiff column-supported embankments, a) sliding failure, b) rupture breaking failure, c) racking failure, d) shear failure, e) bending failure (after Kitazume 2008).

2.3.2.2 Previous Studies

Terashi et al. (1991):

The purpose of the study was to investigate the bearing capacity, under vertical and horizontal loads, of a soil-column composite typically used in Japan for the support of breakwater systems in the coastal area of this country. Sand compaction piles were used as the stiff columns in the system examined. Other major conditions examined in the system were that an area replacement ratio of 28% was employed, a sand layer was placed above the soil-column composite, the soil around the stiff columns was normally consolidated, a shallow foundation referred as a caisson in the study, was used, and the stiff columns were embedded in a bearing layer underneath the soil-column composite. Four centrifuge tests were performed along with a full scale model test in order to investigate the response of the system under different vertical and horizontal loading conditions. Of the four centrifuge tests performed, one was subjected to vertical load only, while the remaining tests were subjected to different vertical and horizontal loading conditions. The full scale test was subjected to vertical load only. The authors presented extensive details on the construction and testing conditions employed for both the centrifuge models and the full scale model. Among the findings presented in the study, it was shown that the loads at yield from each centrifuge test compared well to an envelope plotted in a horizontal-vertical load diagram constructed using limit equilibrium stability analyses. The authors argued that the experimental results confirmed the validity of using limit equilibrium analyses for the design of such systems under combined vertical and horizontal loads.

Kitazume et al. (1996) and Karastanev et al. (1997):

A study was conducted to examine, using centrifuge testing, the bearing capacity of a shallow foundation supported by a soil-column composite under various vertical and horizontal loading conditions. The foundation tested is typical of those employed in breakwater systems in Japan. Two publications were published for this study, Kitazume et al. (1996) and Karastanev et al. (1997). Similarly to the Terashi et al. (1991) study, the centrifuge models were constructed such that a sand layer was also placed above the soil-column composite and the stiff columns were embedded in a bearing layer. Differences include the adoption of Deep Mixed Columns as the stiff columns, the unconfined compressive strength of the stiff columns was measured and reported, the area replacement ratio was of 79%, and the soft soil around the stiff columns was overconsolidated. Four centrifuge models were tested, of which one was subjected to vertical load only. The references provided additional details regarding the construction and testing conditions of the centrifuge models. Both references presented similar findings. For instance, the references reported load vs. lateral displacement/settlement curves for the centrifuge tests, and pictures were provided showing the type of failure observed in the soil-column composite along with the movement experienced by the shallow foundation during testing. In a similar fashion to the Terashi et al. (1991) study, both publications presented results of the vertical and horizontal load at failure in a horizontal-vertical load diagram, and compared the experimental data with curves obtained using limit equilibrium analyses. Each study differed by considering different shear strength values for the columns which were employed in the limit equilibrium analyses. The shear strength of the columns was taken as a percentage of their unconfined compressive strength. The authors concluded that brittle-type failure was observed in the models tested, and

that overall capacity of the system was dependent on the unconfined compressive strength of the stiff columns.

Omine et al. (1999):

This study consisted in the proposal of a homogenization method that was used to examine a soil-column composite. The soil-column composite was treated as a two-phase mixture, and the authors employed numerical and experimental analyses to verify the homogenization method. The experimental analyses consisted on running 1g tests on soft clay improved by Deep Mixed Columns under different vertical and horizontal loading conditions. Area replacement ratios of 22 and 42% were employed in the model tests. The 1g tests neither considered a bearing layer nor an upper sand layer. The vertical and horizontal loads were applied directly to the soil-column composite using a rigid plate. The experimental results were compared to numerical results obtained from finite element analyses that employed stiffness parameters and an extended von Mises yield criterion derived from the homogenization method. Results presented in the study included load vs. lateral displacement/settlement curves for both the 1g tests and the numerical simulations, and comparisons between vertical and horizontal coefficients of subgrade reaction derived from the experimental and numerical analyses. Also included were comparisons between experimental and numerical envelopes presented in horizontal-vertical load diagrams, with the purpose of assessing the influence of different area replacement ratios and unconfined compressive strength conditions for the stiff columns. The authors concluded that good agreement was obtained between the results from the 1g tests and the numerical analyses, resulting in the verification of the proposed homogenization method.

Kitazume et al. (2000):

The objective of the study was to investigate the failure patterns of stiff columns constructed in soft soil for the support of shallow foundations, when subjected to various vertical and horizontal loading conditions. Similarly to previous Japanese studies, the shallow foundation examined in the study was typical of those used to support breakwater systems in coastal areas of Japan. Centrifuge tests, numerical analyses and limit equilibrium analyses were performed in the study. Deep Mixed Columns were the type of stiff column employed. The reference provided extensive information on the construction and testing of the centrifuge models, and details on the numerical analyses performed. The major conditions employed in this study were similar to those described in Kitazume et al. (1996) and Karastanev et al. (1997), and included the preparation of an overconsolidated soil, preparation and testing of specimens to estimate the unconfined compressive strength of the stiff columns, the stiff columns were embedded in a bearing layer, a sand layer was placed above the soil-column composite and an area replacement ratio of 79% was employed. Major differences to the previous studies included the construction and testing of sixteen centrifuge models, of which four were subjected to vertical load only. The results of the study emphasized the failure modes observed in the stiff columns, and included the comparison of the experimental results with limit equilibrium analyses and finite element analyses. The results were presented in terms of load vs. lateral displacement/settlement curves, envelopes in horizontal-vertical load space and pictures showing the types of failure patterns observed in the tests. The study concluded that the failure patterns observed ranged from complete rupture of the stiff columns when the strength of the rigid vertical elements was low compared to the applied load, to racking of the stiff columns in the direction of horizontal loading when the strength of the stiff columns was relatively high.

The following table provides a summary of the studies previously discussed. In summary, the studies physically examined the application of a horizontal load to a vertically loaded shallow foundation supported by a soil-column composite. When applicable, the physical studies were complemented by numerical analyses. Different replacement area ratios were examined. In most cases, the stiff columns were supported in a bearing layer and a coarse-granular layer was placed above the soil-column composite. The majority of the studies presented concluded that the loading conditions and the strength of the stiff columns determined the type of failure mode experienced by the stiff column-supported shallow foundation. These studies provided useful information and details that were employed in the physical stage of the research described in this dissertation. The studies also provided insight into the variables that influenced the response of these systems when subjected to horizontal load.

Table 2.4. Summary of previous studies related to the lateral examination of stiff column-supported shallow foundations

Reference	**Column Type**	**LTP**	**A_s (%)**	**Vertical Tests**	**Lateral Tests**	**Physical Modeling**	**Numerical Modeling**
Terashi et al. (1991)	Sand Compaction Piles	Yes	28	Yes	Yes	Centrifuge, Full-Scale	NA
Kitazume et al. (1996), Karastanev et al. (1997), Kitazume et al. (2000)	Deep Mixed Columns	Yes	79	Yes	Yes	Centrifuge	Finite Element Analyses
Omine et al. (1999)	Deep Mixed Columns	No	22-42	Yes	Yes	1g Tests	Finite Element Analyses

2.3.2.3 Current Practice

Presently, ASIRI (2012) is the only reference that effectively provides guidance for the calculation of bending moments and shear distribution in a stiff column due to the application of horizontal load in a footing or slab foundation. The distribution of loads (bending moment and shear) are estimated using simplified procedures in which the displacement field produced by the applied horizontal load in the foundation is used in combination with subgrade reaction analyses. In two of the simplified procedures, the evaluation of the displacement field requires the knowledge of the shear stress distribution produced by the laterally loaded foundation, and each simplified procedure uses different assumptions for this distribution. For instance, one procedure considers that no shear is transmitted to the soil, while another considers the combination of the LTP and the soil-column composite as an elastic system in which elasticity theory can be applied to estimate the shear stress distribution. A third simplified procedure considers the laterally loaded stiff column-supported shallow foundation as an homogenized monolith with equivalent stiffness properties which is analyzed using an approach similar to studying a laterally loaded pile, with a horizontal load and a moment applied at its top. As opposed to the classical study of a laterally loaded pile that employs a thin beam model, shear deformations are accounted for in the monolith model due to its limited length-to-width ratio.

Beyond the description of the simplified procedures previously mentioned, ASIRI (2012) provides little to no insight into the behavioral mechanisms of a stiff column-supported shallow foundation subjected to horizontal load, acknowledging the need of further studies to better assess the lateral response of the system and its components. This suggests that the current state of knowledge of the lateral response of these systems is limited, and as a consequence, this work aimed to improve the understanding of this lateral response. As such, the use of numerical

modeling in combination with physical modeling employing centrifuge testing aided in quantifying the lateral performance and identifying the variables that controlled the lateral behavior of stiff column-supported shallow foundations. Details on each experimental and numerical study performed, along with the results gathered from each study, will be described in subsequent chapters.

2.4 CONCLUSIONS

Stiff columns are constructed in soft soil with the purpose of producing an improved soil-column composite capable of supporting foundation loads by providing sufficient bearing capacity and a composite stiff enough to allow the control of settlements in order to meet serviceability requirements. These rigid vertical elements are constructed in conjunction with a coarse-granular mattress called the Load Transfer Platform (LTP) whose function is to transfer the foundation load to the soil-column composite located underneath it. Different types of stiff columns are available in practice with each having different construction procedures being, in most cases, proprietary in nature. Under vertical load, stiff columns rely on downdrag to transfer the foundation load to deeper competent bearing strata. The lateral response of stiff columns supporting embankments has been extensively studied, but the same is not true for shallow foundations. Under horizontal load, different simplified procedures allow the calculation of the load induced in the stiff columns constructed for the support of shallow foundations however, these procedures are approximate.

CHAPTER 3: PHYSICAL MODELING OF STIFF COLUMN-SUPPORTED SHALLOW FOUNDATIONS WITH CENTRIFUGE TESTING

3.1 INTRODUCTION

This chapter presents the experimental work that was carried out to investigate the behavioral mechanisms of stiff column-supported shallow foundations subjected to horizontal load. Footings are the type of shallow foundation examined in this experimental study. A pulley-based testing setup was employed to laterally load a footing supported on a soil-column composite. Different LTP thicknesses were tested. Results in the form of load and pore-water pressure measurements are presented. Observations were made in regards to the lateral deformation experienced by the stiff columns in the soil-column composite.

3.2 GEOTECHNICAL CENTRIFUGE TESTING

3.2.1 *Definition*

Centrifuge testing is a procedure that allows the investigation of engineering problems using models that are representative of 1:1 prototype systems by means of scaling laws (Taylor 1995). In this approach, the small-sized model is subjected to a radial acceleration field using equipment that spins the model around a fixed axis inducing an increased gravitational field due to centrifugal forces. The increased gravitational field imposes a state of stresses within the small-sized model equivalent to the state of stresses of the larger-sized prototype system subjected to Earth's gravitational field (Figure 3.1). This equivalency of stresses between the small-sized

model and the larger-sized prototype system is achieved by imposing an increased gravitational field in the small-sized model that is directly proportional to Earth's gravitational field. In order examine this equivalency, centrifuge testing uses a series of scaling relationships to interpret the variables measured in a small-sized model in terms of the larger-sized prototype system of interest. This allows the extrapolation of results gathered from the small-sized model to the representative larger-sized prototype and thus consistently maintaining equivalency between model and prototype.

In the context of geotechnical engineering, because of the dependence of soil behavior in stress level and stress history, centrifuge testing becomes particularly effective in addressing and examining geotechnical problems (Taylor 1995). The following sections provide an overview of the basic scaling laws employed in geotechnical centrifuge testing.

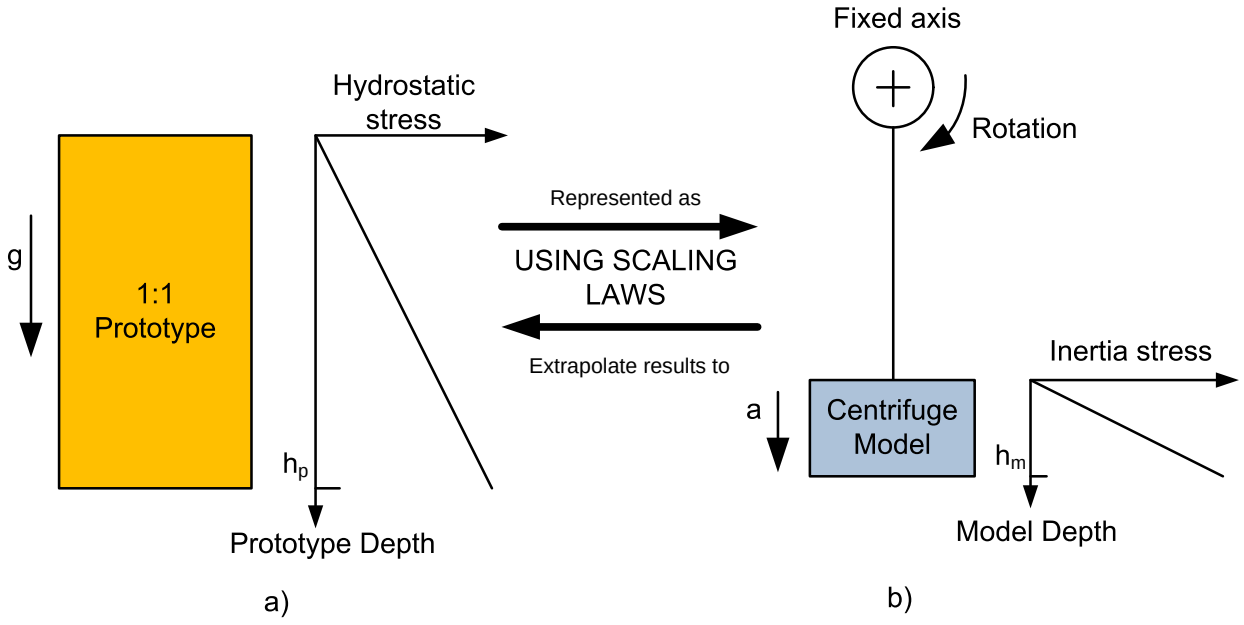

Fig. 3.1. Relationship between a) gravitational stresses in a prototype system and b) inertial stresses in a centrifuge model (after Taylor 1995).

3.2.2 *Scaling Laws*

In order to maintain consistency and equivalency between the model and prototype, the stresses between the scaled model σ_m and the prototype σ_p must be identical (Taylor 1995). This is referred to a scaling law or more specifically:

$$\sigma^* = \frac{\sigma_m}{\sigma_p} = 1 \tag{3.01}$$

Where σ^* is the scaling factor for stresses or other parameters with stress units that include pressure, shear strength and elastic moduli (Kutter 1992). As stated in the previous section, the model will be subjected to an acceleration a_m in proportion to Earth's gravity a_p or g, and in centrifuge practice this factor is called N. The acceleration or gravity experienced by the model is expressed as:

$$a_m = Na_p$$

$$a^* = \frac{a_m}{a_p} = N \tag{3.02}$$

And a^* is the scaling factor for acceleration or gravity. Because the scaled centrifuge model is a representation of a larger-sized prototype then the materials of the scaled model are meant to represent the materials of the prototype. In mathematical terms, the mass density between the model ρ_m and the prototype ρ_p is described by (Kutter 1992):

$$\rho^* = \frac{\rho_m}{\rho_p} = 1 \tag{3.03}$$

Where ρ^* represents the scaling factor for mass density. A block of material located at a depth h_m in the model subjected to an acceleration g_m in a centrifuge will have a vertical stress σ_{vm} equal to:

$$\sigma_{vm} = \rho_m g_m h_m$$

Utilizing the scaling law for acceleration:

$$\sigma_{vm} = \rho_m (Ng) h_m$$

$$\sigma_{vm} = \rho_m N g h_m$$

The vertical stress for a block of material located at a depth h_p in the prototype system σ_{vp} will be:

$$\sigma_{vp} = \rho_p g h_p$$

Utilizing the stress and mass density scaling laws presented at this point, it is possible to obtain the scaling law for linear dimensions (Taylor 1995):

$$\sigma_{vm} = \sigma_{vp}$$

$$\rho_m N g h_m = \rho_p g h_p$$

$$N h_m = h_p$$

$$\frac{h_m}{h_p} = \frac{1}{N}$$

$$L^* = h^* = \frac{h_m}{h_p} = \frac{L_m}{L_p} = \frac{1}{N} \qquad (3.04)$$

And L^* is the scaling factor for linear dimensions. From the scaling laws described as this point, it is possible to derive other scaling laws useful in geotechnical engineering. The scaling law for strains uses the scaling law for linear dimensions as following (Taylor 1995):

$$\varepsilon^* = \frac{\varepsilon_m}{\varepsilon_p}$$

$$\varepsilon^* = \frac{\frac{\Delta L_m}{L_{mo}}}{\frac{\Delta L_p}{L_{po}}} = \frac{\frac{\Delta L_p / N}{L_{po} / N}}{\frac{\Delta L_p}{L_{po}}}$$

$$\varepsilon^* = 1 \tag{3.05}$$

Where ε^* is the scaling factor for strains. The scaling laws for area and volume are derived as follows (Kutter 1992):

$$A^* = \frac{A_m}{A_p}$$

$$A^* = \frac{{L_m}^2}{{L_p}^2} = \frac{\left(\frac{L_p}{N}\right)^2}{{L_p}^2} = \frac{\frac{{L_p}^2}{N^2}}{{L_p}^2}$$

$$A^* = \frac{1}{N^2} \tag{3.06}$$

$$V^* = \frac{V_m}{V_p}$$

$$V^* = \frac{{L_m}^3}{{L_p}^3} = \frac{\left(\frac{L_p}{N}\right)^3}{{L_p}^3} = \frac{\frac{{L_p}^3}{N^3}}{{L_p}^3}$$

$$V^* = \frac{1}{N^3} \tag{3.07}$$

Where A^* and V^* are the scaling factors for area and volume respectively. The scaling law for mass employs the scaling law for mass density and volume as follows (Kutter 1992):

$$m^* = \frac{m_m}{m_p}$$

$$m^* = \frac{\rho_m V_m}{\rho_p V_p} = \frac{V_m}{V_p}$$

$$m^* = \frac{1}{N^3} \tag{3.08}$$

Where m^* is the scaling factor for mass. The scaling law for force utilizes Newton's second law of motion, the acceleration and mass scaling laws as following (Kutter 1992):

$$F^* = \frac{F_m}{F_p}$$

$$F^* = \frac{m_m a_m}{m_p a_p}$$

$$F^* = \frac{\left(\frac{m_p}{N^3}\right) N a_p}{m_p a_p}$$

$$F^* = \frac{1}{N^2} \tag{3.09}$$

Where F^* is the scaling factor for force. The scaling law for time of consolidation can be derived by considering that for a same degree of consolidation, the time factor T_v will be the same in the prototype and the model (Taylor 1995):

$$T_{vm} = T_{vp}$$

$$\frac{c_{vm}t_m}{H_m^{\,2}} = \frac{c_{vp}t_p}{H_p^{\,2}}$$

Where c_v is the coefficient of consolidation and H is the drainage path length. Using the scaling law for linear dimensions:

$$\frac{c_{vm}t_m}{\left(\frac{H_p}{N}\right)^2} = \frac{c_{vp}t_p}{H_p^{\,2}}$$

$$\frac{t_m}{t_p} = \frac{1}{N^2}\frac{c_{vp}}{c_{vm}}$$

Considering that the same soil is used in the prototype and scaled model, the scaling law can be further simplified:

$$t^* = \frac{1}{N^2} \qquad (3.10)$$

Where t^* is the scaling factor for time of consolidation. Table 3.1 summarizes the scaling laws. The scaling laws previously derived were used during the construction and testing of the centrifuge test program described in this chapter and these laws were also used to extrapolate the model results to the prototype scale.

Table 3.1. Centrifuge scaling laws (after Kutter 1992 and Taylor 1995)

Quantity	Units	Scale Factor
Length	L	$1/N$
Area	L^2	$1/N^2$
Volume	L^3	$1/N^3$
Acceleration, Gravity	L/T^2	N
Mass	m	$1/N^3$
Force	$m\ L/T^2$	$1/N^2$
Stress	m/LT^2	1
Strain	-	1
Mass Density	m/L^3	1
Time (diffusion)*	T	$1/N^2$

* If the same soil is used in the centrifuge model and prototype.

Note: L = length; T = time; m = mass.

3.3 CENTRIFUGE TESTS ON LATERALLY LOADED STIFF COLUMN-SUPPORTED SHALLOW FOUNDATIONS

3.3.1 *Facilities*

The 15 g-ton centrifuge located at the University of Colorado Boulder was used in the centrifuge test program. As described by Ko (1988), Shin (1987) and Ketcham (1989), the 15 g-ton centrifuge is a Genisco 1230-5 accelerator that has been modified for geotechnical applications and it has been in use since 1981. It has a symmetrical arm comprised of aluminum beams that carry swinging-baskets at either end, as shown in Figures 3.2, 3.3 and 3.4. Each 41.3-kg basket (Figure 3.5) can accommodate a payload with a base area up to 457 × 455 mm and a height of 584 mm. In the in-flight extended position, the radius of the basket's center of mass is 1320 mm, and the radius at the basket base is 1359 mm. The centrifuge is located inside a 3 m-diameter cylindrical steel container for safety purposes.

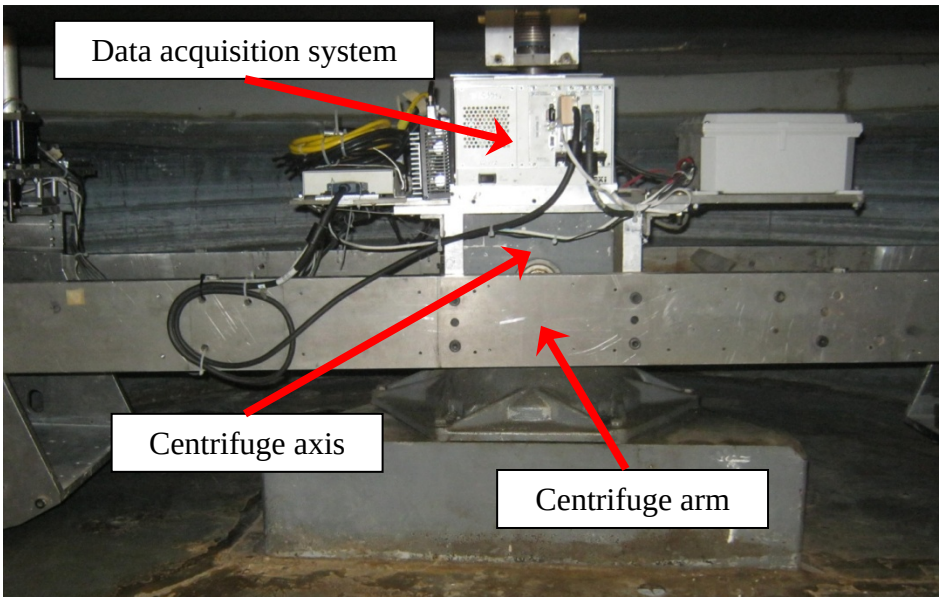

Fig. 3.2. View of the 15 g-ton centrifuge inside steel container with the data acquisition system in the centrifuge axis.

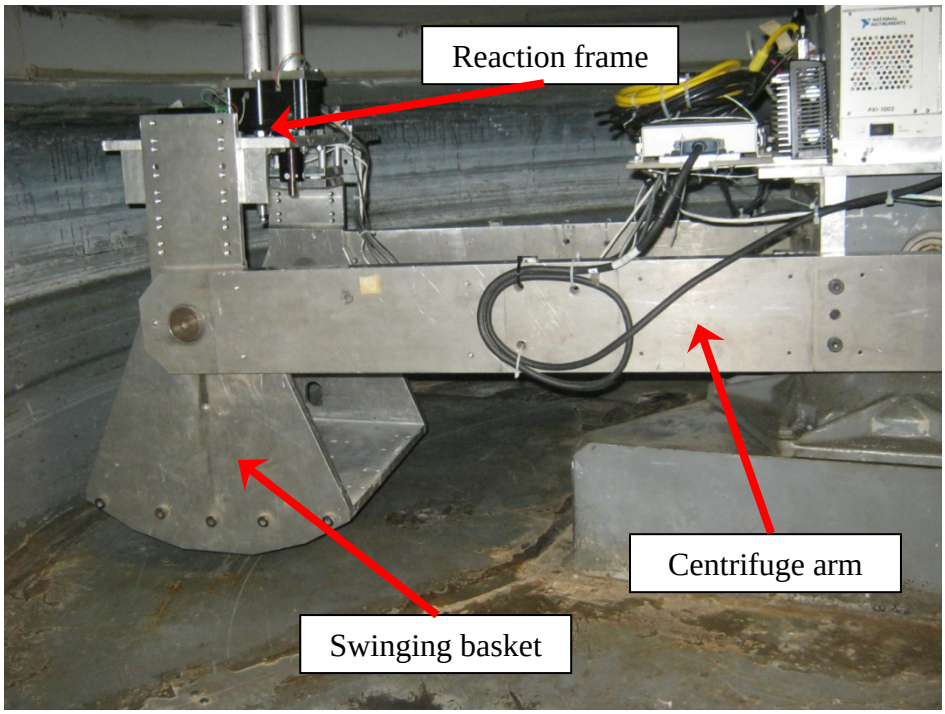

Fig. 3.3. View of the 15 g-ton centrifuge with the reaction frame used for in-flight testing above the centrifuge basket.

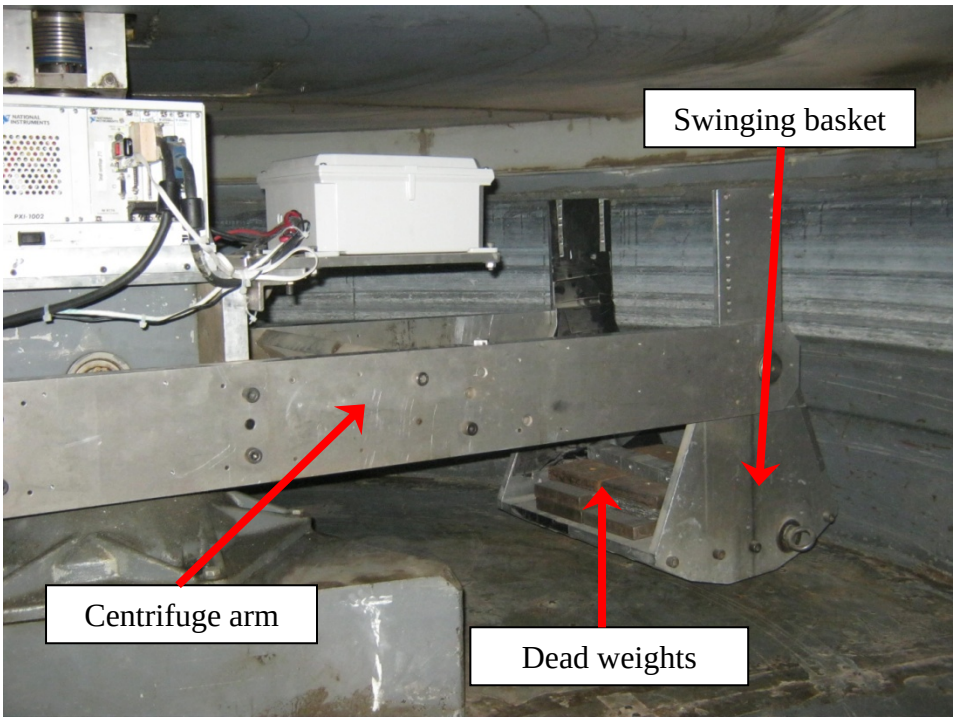

Fig. 3.4. View of the 15 g-ton centrifuge with dead weights inside the centrifuge basket to guarantee balance during testing.

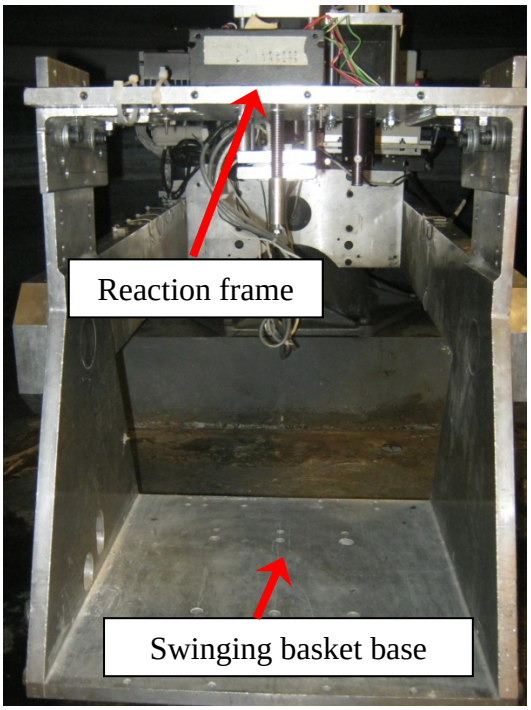

Fig. 3.5. Centrifuge basket with the reaction frame at the top.

3.3.2 *Layouts of the Experimental Setup*

A schematic layout of the prototype-scale system tested using the 15 g-ton centrifuge is shown in Figures 3.6 and 3.7. The prototype-scale model consisted of a square footing supported by a two by two grid of stiff columns extending to a depth of 8.0 m below the initial soil grade. The subsurface profile in the model was chosen to be representative of soft soil conditions underlain by a bearing layer. The stiff columns were embedded 0.5 m into the bearing stratum. The four stiff columns under the 2.40 m-wide square footing resulted in an area replacement ratio a_s of 5.5%. The area replacement ratio is defined as the ratio of the cross-sectional area of one column (A_c) to the total cross-sectional area of the improved "unit cell" attributed to each column (A). The area replacement ratio can be further defined as following (Kosho 2011):

$$a_s = \frac{A}{A_c} = k\left(\frac{r}{s}\right)^2 \tag{3.11}$$

Where r is the radius of the column, s is the center to center column spacing and k is equal to π for square layouts and $2\pi/\sqrt{3}$ for triangular layouts. Typical area replacement ratios used in practice in stiff column-supported shallow foundations range from 2 to 12% (Buschmeier and Masse 2012).

A total of five tests were performed at 50g centrifugal acceleration. In one of these tests, a vertical load was applied to the stiff column-supported footing in order to infer its ultimate vertical capacity. Four additional tests were performed where a progressively increasing horizontal load was applied laterally to the footing while a vertical load was maintained on the footing at 25% of the ultimate vertical capacity of the vertical load test. The thickness of the LTP was varied between each lateral load test (Figure 3.6).

3.3.3 *Equipment and Instrumentation*

The centrifuge models were constructed in two aluminum cylindrical containers. The containers have a 381-mm inner diameter and a 296-mm height. A porous stone was located at the base the containers to provide a free-drainage bottom boundary during the consolidation stages. A drainage line was connected to the side of the container to redirect the water drained through the porous stone to the top of the container.

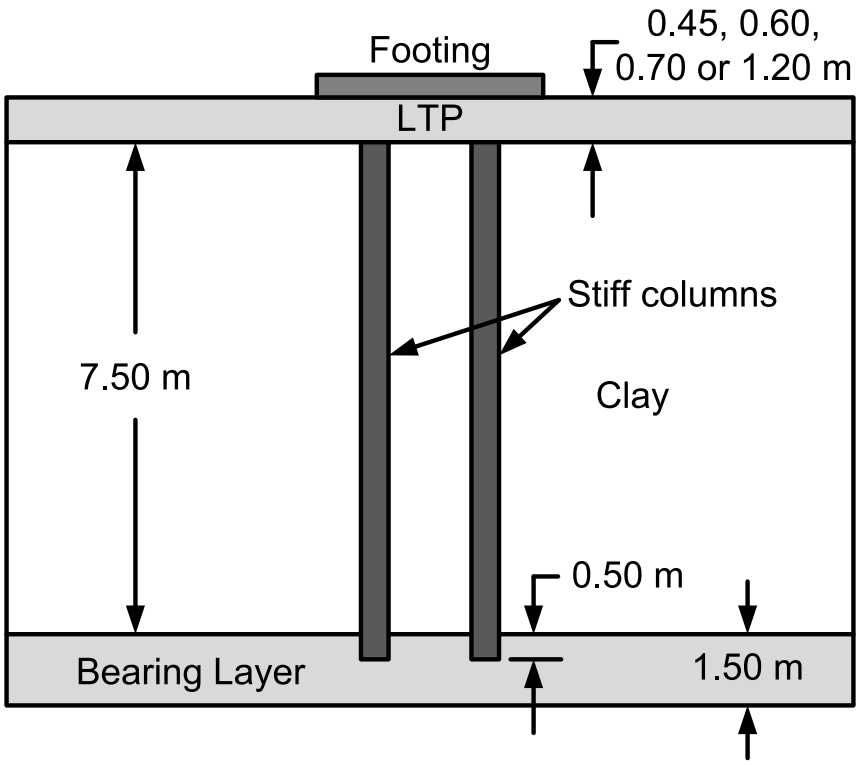

Fig. 3.6. Cross-section of the stiff column-supported footing. Prototype-scale system (not to scale).

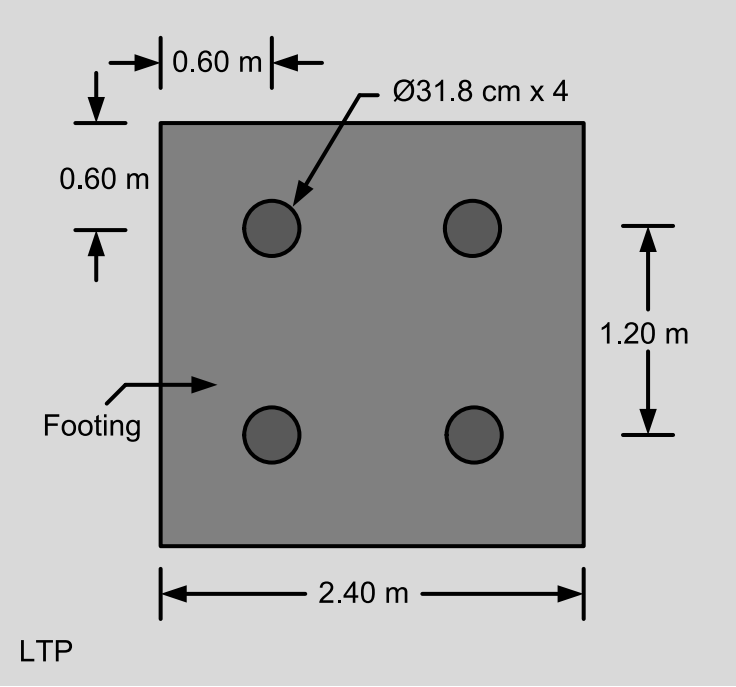

Fig. 3.7. Plan view of the stiff column-supported footing. Prototype-scale system (not to scale).

Three Druck PDCR-81 miniature pore pressure transducers (PPTs) were used to monitor the development of excess pore-water pressures during the consolidation and testing stages. A linearly variable deformation transformer (LVDT) was used to measure the lateral displacements of the model footing during testing. A load cell was used to record the lateral forces. A 76 mm-long × 11 mm-diameter T-bar penetrometer was used to infer the undrained shear strength profile of the soft soil subsequent to the completion of the initial in-flight consolidation stage at 50g. Two stepper motors attached to the reaction frame fixed to the top of the centrifuge basket were used to control two vertical actuators. One actuator was used to laterally load the stiff column-supported shallow foundation at 50g and the other was used for T-bar penetration tests. The actuators were controlled with a National Instruments data acquisition system located at the rotational axis of the centrifuge.

3.3.4 *Soil Properties*

Speswhite clay was used as the soft soil layer in this study. This soil contains predominantly kaolinite particles, and has been used in previous centrifuge studies (Macari et al. 1987, Cinicioglu 2005). The properties of speswhite clay are summarized in Table 3.2.

Nevada sand was used in the bearing layer and the LTP. Nevada sand has a relatively uniform grain size distribution with an average particle size of 0.13 mm. The properties of the Nevada sand used in the centrifuge test program are summarized in Table 3.3.

Table 3.2. Properties of speswhite clay (after Macari et al. 1987)

Index Properties	
Liquid Limit (%)	53
Plastic Limit (%)	32
Plasticity Index	21
Unified Soil Classification	MH
Specific Gravity	2.66
Percent of minerals present:	
Kaolinite	> 99
Illite	< 1

Table 3.3. Properties of Nevada sand (after Hushmand 2011, 2014)

Soil	No. 100 Nevada Sand
Classification	Uniform, fine sand; SP
Grain sizes, D_{50}, D_{10} (mm)	0.13, 0.09
Coefficient of Uniformity, C_u	1.55
Coefficient of Curvature, C_c	0.96
Maximum Void Ratio, e_{max}	0.843
Minimum Void Ratio, e_{min}	0.555
Specific Gravity, G_s	2.65

3.3.5 *Model Construction*

The first stage of the construction of the centrifuge models consisted on the pluviation of the bearing layer. Dry Nevada sand was rained from a hopper from a constant drop height of 1.85 m over the cylindrical container in multiple passes. The top of the bearing layer was then leveled to achieve a prototype thickness of 1.5 m. A relative density of 75% was achieved with dry pluviation resulting in a dense bearing layer. The bearing layer was saturated by gravity flow of water prior to the placement of the speswhite clay slurry. The slurry was thoroughly mixed at a water content equal to twice the liquid limit of the clay. The clay was consolidated in three lifts in three of the tests, and one lift in the remaining test. Each lift was consolidated at 1g under a dead-weight surcharge of 5 kPa for 24 hours.

Once the consolidation of all three clay lifts at 1g was completed, the container was placed inside the centrifuge basket for in-flight self-weight consolidation at 50g. Because of changes in stress history imposed in the model by the 5 kPa surcharge at 1g in combination with the linear distribution of stress imposed in the model due to the self-weight of the soil at 50g, a normally consolidated clay layer with an overconsolidated portion near the surface was produced. During in-flight self-weight consolidation, excess pore-water pressures at different depths were monitored using the three PPTs. The clay was consolidated until 90% consolidation was achieved. The value of t_{90} (time for 90% consolidation) was estimated using Taylor's square of root time method. The time to achieve 90% consolidation varied slightly with each model, but was approximately 25 hours.

After the end of consolidation, the T-bar was lowered at a model scale rate of 1 mm/sec to infer the undrained shear strength profile of the clay layer. Using a bar factor of 10.5 and the nominal diameter of the T-bar, the force measurements from a load cell in line with the T-bar were expressed in terms of undrained shear strength using the approach of Stewart and Randolph (1994). Due to equipment limitations, the T-bar reached a prototype depth of about 5.0-6.5 m below grade and did not penetrate the entire thickness of the clay layer. Nevertheless, the results were still sufficient to observe an increase in undrained shear strength with depth typical of a normally consolidated clay profile, as presented in Figure 3.8. With the exception of the test with a LTP thickness of 0.70 m (which corresponded to the test in which a single clay lift was used), the undrained shear strength profiles obtained for the rest of tests fall within a narrow and consistent range with an average undrained shear strength ratio s_u/σ_v' of 0.285 in the normally consolidated portion and 0.33 in the overconsolidated portion near the top of the soil profile.

Next, the container was removed from the centrifuge and the model stiff columns were installed in the soft soil. The stiff columns were constructed using a neat mix of water and cement at a water to cement ratio of 50% by weight. Portland cement type I/II was used in the mix. The mix was injected into straws that functioned as forms having an inside diameter in the prototype scale of 0.318 m. The cement-filled straws were later placed in a vibrating table in order to remove bubbles. The columns were permitted to cure in a high humidity environment. After 48 hours of curing, the stiff columns were removed from the straws and they were trimmed to a prototype length of 8 m. The stiff columns were then inserted in the soft soil at 1g. This involved placing a light wood template above the soil which served as a “lead” to help keep a consistent spacing

and maintain the verticality of the stiff columns during insertion. The stiff columns were not instrumented. After the stiff columns were installed, Nevada sand was pluviated from a height of 1.85 m under dry conditions above the soil-column composite to produce a LTP with a relative density of 75%. Then the container was placed inside the centrifuge in order to consolidate the soil profile in-flight under the weight of the LTP at 50g. Placement and consolidation under the LTP changed the stress history of the soft soil profile, and subsequent changes to the undrained shear strength of the soft soil were not measured. After consolidation, the container was removed from the centrifuge in order to make the necessary preparations for vertical and lateral testing.

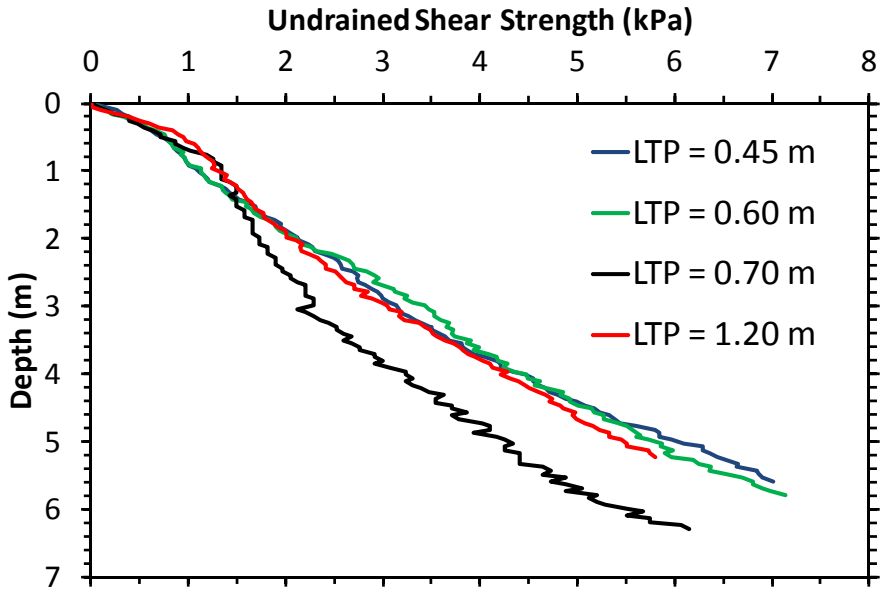

Fig. 3.8. Undrained shear strength profiles after self-weight centrifugation at 50g. Prototype scale.

3.3.6 *Vertical Testing Setup and Procedure*

Figure 3.9 shows the testing setup used in the vertical load test. The thickness of the LTP employed in the vertical test was 1.20 m. A load cell was attached to the top of the footing, and

both in turn were secured to a vertical actuator using a metallic rod. At 50g centrifugal acceleration, the footing was lowered at a model scale rate of 0.1 mm/sec once excess pore-water pressures reached equilibrium in the soil-column composite.

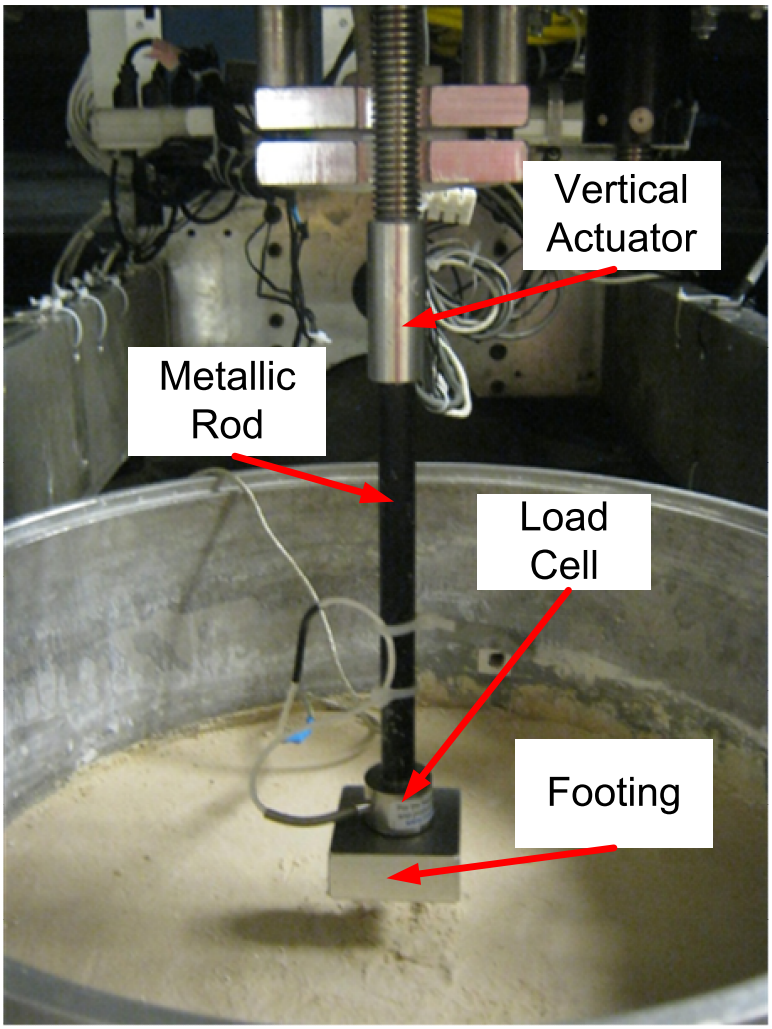

Fig. 3.9. Testing setup used in the vertical load test.

Figure 3.10 shows the vertical load-settlement response of the footing as it settled in the LTP. The response observed was characterized by an initial nearly linear increase in vertical load with settlement that later transitioned to a subsequent linear increment in vertical load, at a lower rate,

before the vertical load dramatically decreased with further settlement. Yield or failure was defined as the load at the end of the initial linear response, just before the transition to the subsequent linear response commenced. Based on this criterion, the ultimate vertical capacity of the system was estimated at approximately 2500 kN. In order to avoid balance issues of the footing during lateral testing and to maintain sufficient headroom above the foundation, a vertical load of 620 kN was applied to the footing of the lateral load tests. The vertical load applied corresponded to nearly 25% of the ultimate vertical capacity of the stiff column-supported footing.

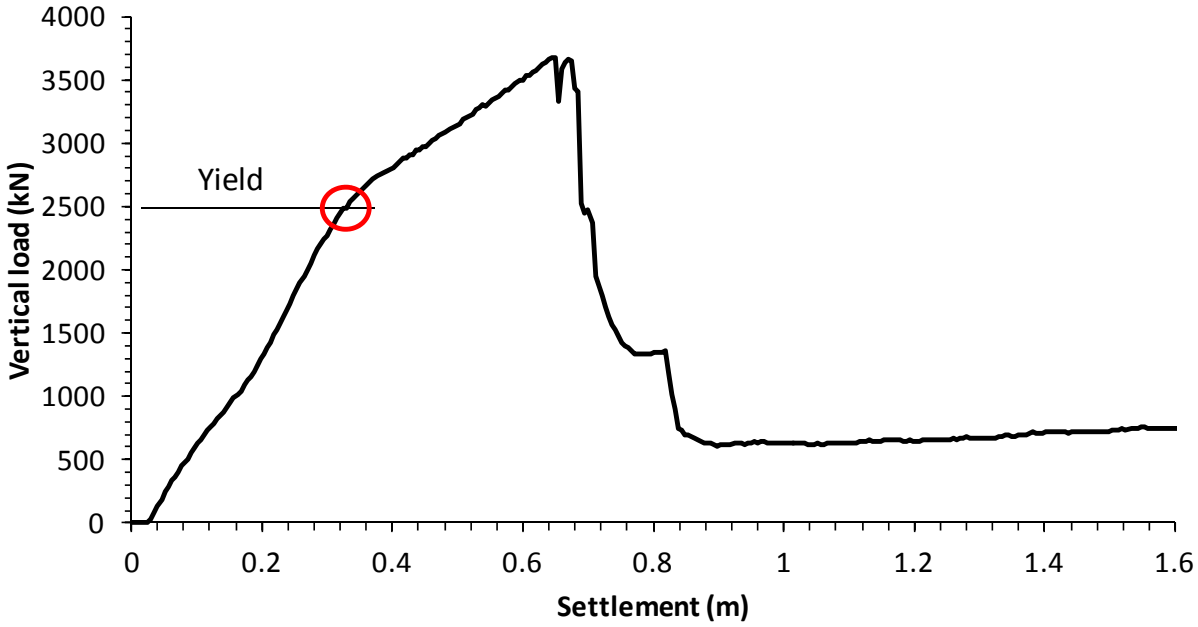

Fig. 3.10. Vertical load-settlement behavior of the vertical load test.

3.3.7 *Lateral Testing Setup and Procedure*

An overview of the lateral load testing setup inside the container is shown in Figure 3.11. The model footing was placed above the surface of the LTP and it was not embedded. Dead weights

were placed above the model footing to provide a constant vertical load and a load cell was attached to the side of the footing in order to record the lateral load applied to the footing during testing. The combination of the dead weights, the self-weight of the footing and the load cell produced an applied vertical load on the footing of 620 kN at the prototype scale. The dead weights were eccentrically placed to counter the moment produced by the laterally attached load cell with respect to the center of mass of the footing. A steel cable was secured to the load cell and was then routed through the pulleys so that its other end could be connected to the vertical actuator at the center of the reaction frame. The LVDT was attached to the rear of the footing using a rod. The centrifuge was then activated and the model was spun to 50g centrifugal acceleration. Once the excess pore-water pressures stabilized, the horizontal load was applied to the footing by lowering the vertical actuator at the center of the setup at a model scale rate of 0.1 mm/sec (Figure 3.12), thus laterally loading the stiff column-supported shallow foundation.

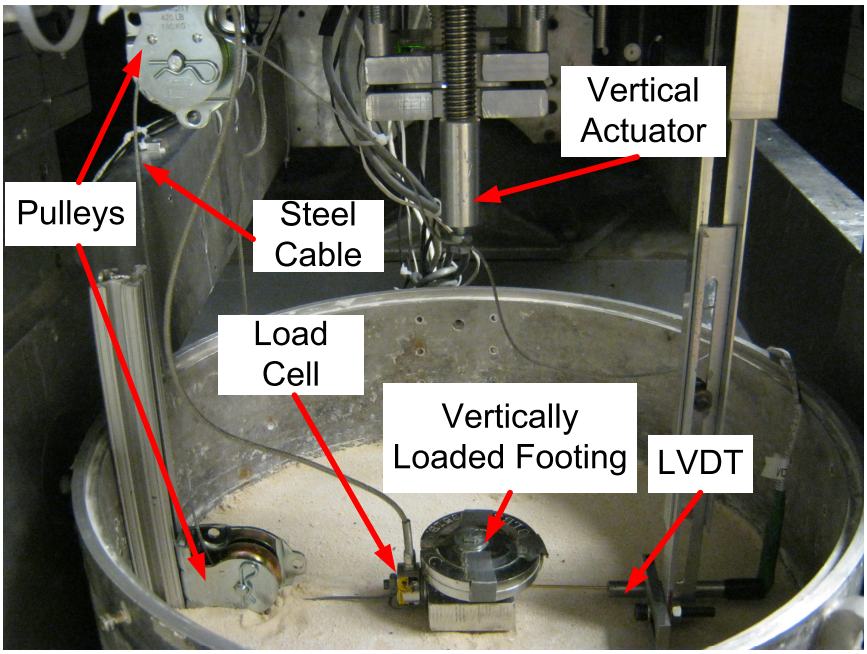

Fig. 3.11. Testing setup used in the lateral load tests.

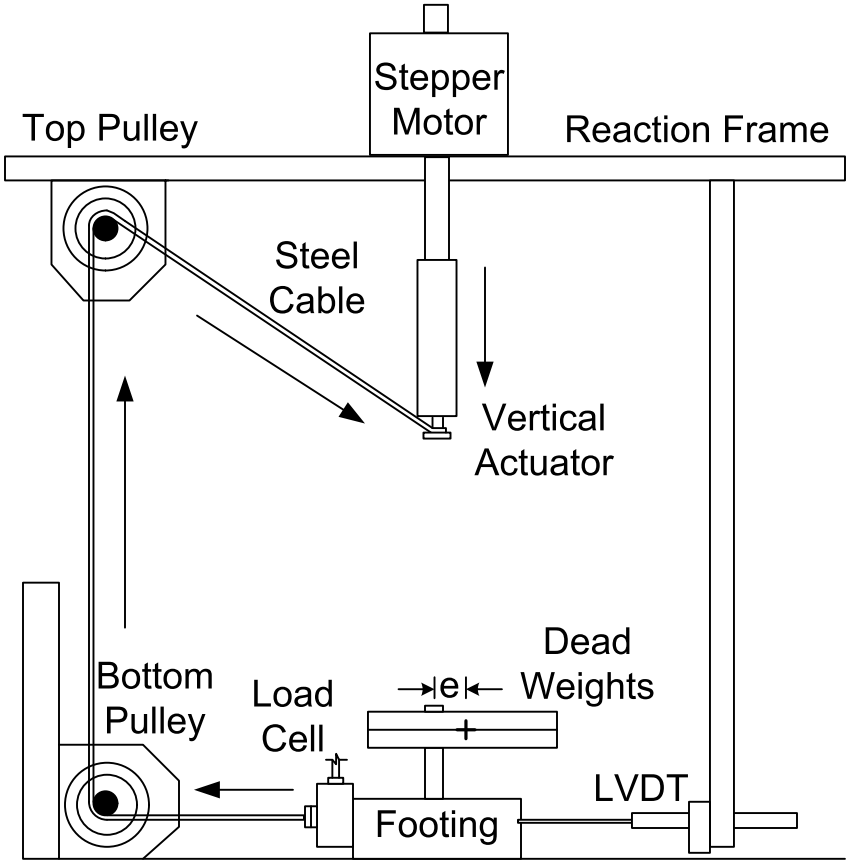

Fig. 3.12. Application of horizontal load to footing during in-flight centrifugation at 50g.

3.4 LATERAL LOAD TEST RESULTS

3.4.1 *Lateral Load-Displacement Behavior*

The lateral load-displacement responses of the four laterals tests are shown in Figure 3.13. The points of yield or failure for each of the curves shown in Figure 3.13 were defined using a work criterion in which the accumulated area beneath the load-displacement curve (i.e. the work done) was plotted against the lateral load measured. Two lines were fitted to the accumulated work vs. lateral load data and their intersection corresponded to the yield load for each test. The details of identifying the yield load using the work principles are presented in the Appendix at the end of

the dissertation. The yield loads from the four lateral tests were plotted against the LTP thickness in Figure 3.14, and a linear fit was added to the experimental data.

The experimental results shown in Figure 3.13 suggest that the lateral capacity of the stiff column-supported shallow foundation, as indicated by the yield load in each lateral load test, increased with increasing LTP thickness. From Figure 3.14, the lateral capacity increased nearly 2.6 times from a stiff column-supported footing having a LTP thickness of 0.45 m, the thinnest LTP tested, to a system with a LTP thickness of 1.20 m which was the thickest LTP tested. This suggested a linear increase of around 1.7 kN per centimeter of LTP thickness in the lateral capacity. Additionally, the lateral capacity of the system with a LTP thickness of 0.45 m was approximately 13.0% of the vertical load applied to the footing. With a LTP thickness of 1.20 m, this percentage increased to around 34%.

To examine the dependence between the pre-yield lateral load-displacement response and the LTP thickness in Figure 3.13, a stiffness secant value at 100% strength k_{100} was used. This secant stiffness k_{100} was defined as the slope of a line that extends from the origin and intersects the yield point of each lateral load-displacement curve in Figure 3.13. The results of k_{100} are shown in Table 3.4. The results of this table show that the pre-yield lateral load-displacement stiffness in terms of k_{100}, increased with increasing LTP thickness.

The post-yield lateral load-displacement responses in Figure 3.13 were characterized by reduced softening with increasing LTP thickness. As evidenced in the tests with LTP thicknesses of 0.45 and 0.60 m, softening occurred immediately after the lateral capacity was reached and was

considered to be likely associated with the brittle-like failure of the stiff columns. For LTPs thicker or equal to 0.70 m, post-yield softening response became less significant and a hardening response controlled. This trend seemed to suggest that the lateral load behavior of the stiff column-supported footing was likely controlled by the stiff columns rather than by the actual LTP, when the LTP thickness was 0.45 and 0.60 m. With LTP thicknesses of 0.70 m and 1.20 m, the lateral load behavior was also likely influenced by the coarse-granular soil of the LTP, which seemed to provide greater lateral capacity to the system and influenced its post-yield lateral load response. While the contributions of the LTP and the stiff columns were not quantified individually in any of the lateral load tests of the centrifuge test program, the results seemed to suggest a greater contribution from the dense coarse-granular material when the LTP was sufficiently thick.

It is important to further discuss the positive effect of the LTP thickness in increasing the lateral capacity of the stiff column-supported shallow foundation. Global lateral responses were obtained using the load cell measurements, and due to the lack of instrumentation inside the LTP, soft soil and stiff columns, no measurements were made of the load induced in any of these. As a result, the individual contributions of each of these components to the lateral capacities were not quantified. However, to better understand the influence of the thickness of the LTP in the lateral response of the stiff column-supported shallow foundations tested, it is still possible to make educated observations based on the mechanics of loading and shearing that took place in the lateral load tests. As the results showed, the lateral capacity increased with increasing LTP thickness. An increase in the lateral capacity was accompanied by an increase in the magnitude of the resultant load obtained from the vertical load and the lateral load at yield

that acted on the foundation. In addition, the direction of the resultant load changed because the lateral load at yield increased while the vertical load remained constant in the centrifuge models tested. In more specific terms, the angle between the vertical load and the resultant load increased with thicker LTPs. Because of the increase of the angle of the resultant load with respect to the vertical load as the LTP thickness increased, the direction of the resultant load shifted towards a location of the LTP not underlain by stiff columns. This is confirmed by the fact that only two of the four columns in the lateral test with a LTP thickness of 1.20 m, the thickest of the LTPs tested, laterally deformed and failed.

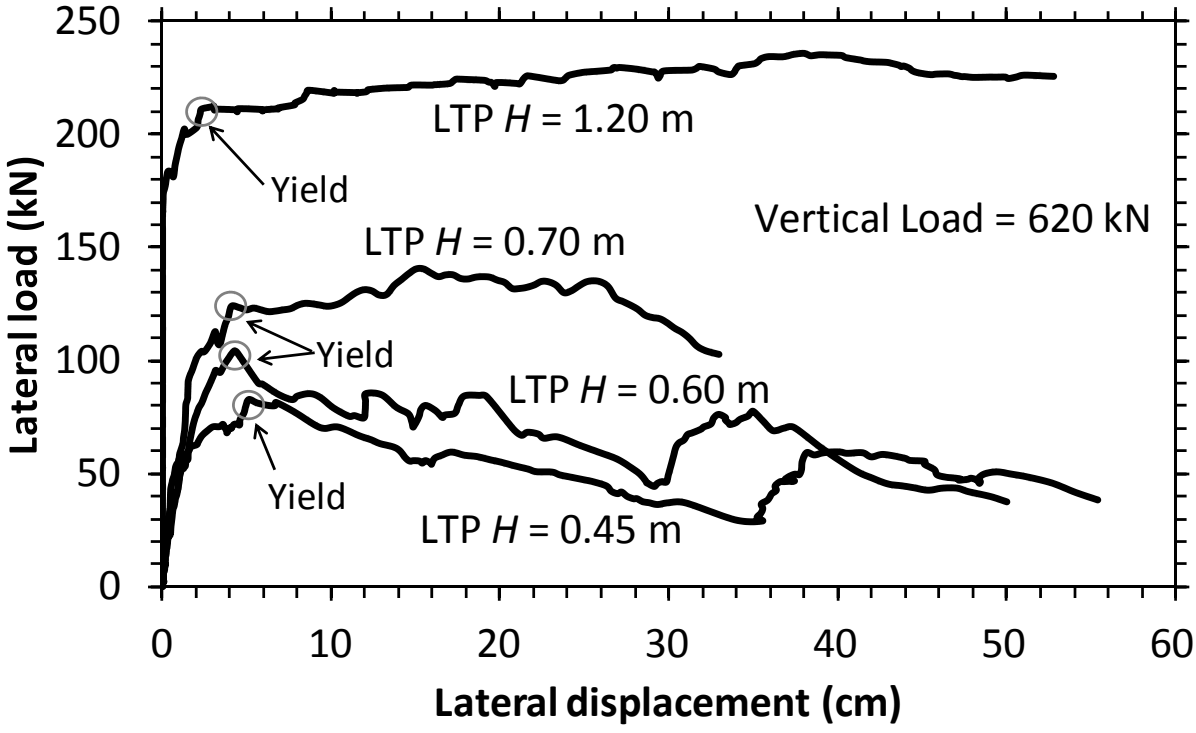

Fig. 3.13. Lateral load-displacement behavior of the lateral load tests with different LTP thicknesses *H* - All units in prototype scale.

The shift in direction of the resultant load allowed for a larger LTP-soft soil volume free of stiff columns to be further strained and sheared. The increase of the thickness of the LTP resulted in an increase of the shear strength of the clayey soil around the stiff columns due to consolidation under a thicker LTP. Furthermore, the increase of the LTP thickness resulted in a larger volume of confined dense coarse-granular soil of the LTP that, when sheared by means of application of the horizontal load in the shallow foundation and in combination with the stronger clayey soil, likely resulted in larger lateral capacities than those that would result from the shearing resistance of the soil-column composite with a thin LTP. The previous trends likely resulted in the very stiff pre-yield response and the post-yield hardening response recorded in the lateral load-displacement results when the thickness of the LTP was 1.20 m.

On the other hand, when the direction of the resultant load was closer to the vertical load for thicknesses of the LTP closer to 0.45 m, the stiff columns were more heavily loaded, and the brittle-like response of the soil-column composite controlled producing the less stiff pre-yield lateral load-displacement response and post-yield softening behavior observed. In addition, the clayey soil around the stiff columns also gained strength due to consolidation under the thin LTP (but not likely of the same magnitude as with a thicker LTP), and considering that all four columns laterally deformed and failed, this suggests that the resistance provided by all of the stiff columns, the slightly stronger clayey soil, and the thin LTP was not enough to produce a significant increase in lateral capacity compared to the use of a thicker LTP. These educated observations, while not conclusive, provide a better understanding of the positive effect of the thickness of the LTP in increasing the lateral capacity of the stiff column-supported shallow foundations tested.

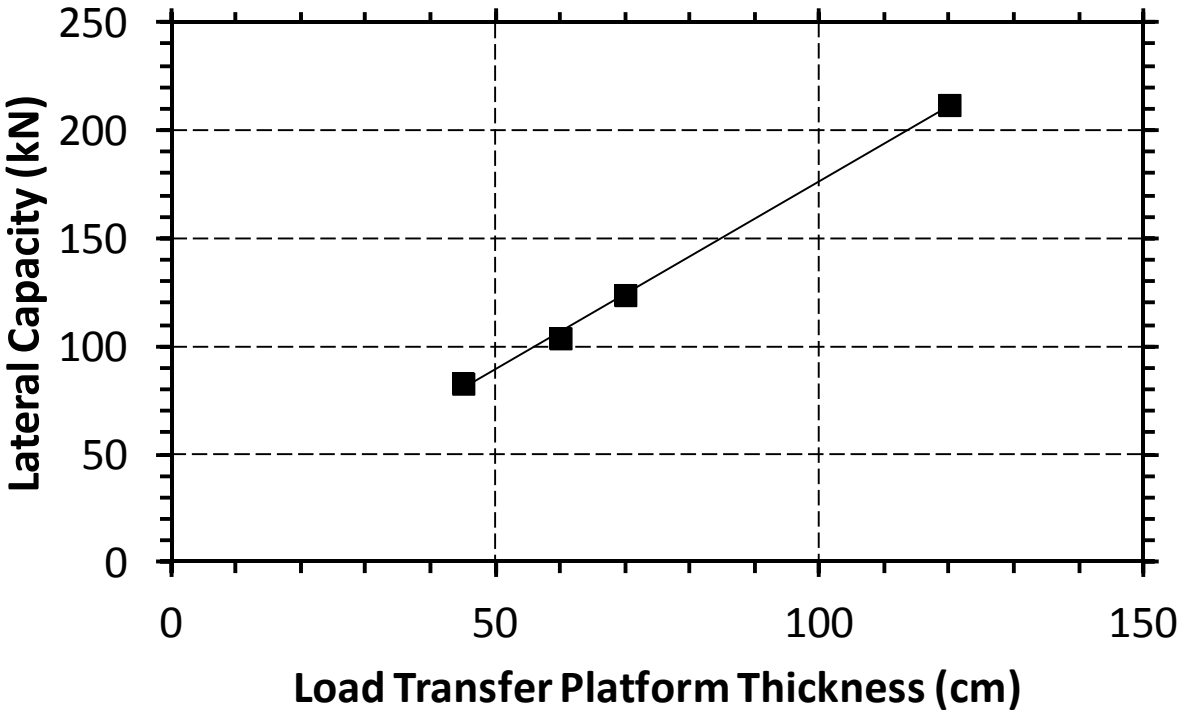

Fig. 3.14. Influence of the LTP thickness in the lateral capacity of the stiff column-supported shallow foundation - All units in prototype scale.

Table 3.4. Secant stiffness at 100% strength

LTP H (m)	k_{100} (kN/m)
0.45	1624
0.60	2436
0.70	3032
1.20	7681

3.4.2 *Excess Pore-Water Pressures during Lateral Testing*

Pore pressure transducers were used to record excess pore-water pressure measurements during lateral testing. A schematic of the location of the PPTs inside the soft soil with respect to the location of the shallow foundation is shown in Figure 3.15. Information on the dimensions is summarized in Table 3.5. The changes in positive excess pore-water pressure by means of the pore-water pressure ratio r_{uxs} (a quantity that normalizes the excess pore-water pressure measurements with respect to the total overburden stress) with lateral displacement for each of the lateral load tests are presented in Figure 3.16. A summary of the influence of the LTP thickness on the values of r_{uxs} at yield is shown in Figure 3.17 for each PPT.

In the case of the excess pore-water pressure measurements recorded in the tests with LTP thicknesses between 0.45 to 0.70 m (Figures 3.16a, 3.16b and 3.16c), in all pore pressure transducers there was a steady increase of excess pore-water pressure with lateral displacement before yielding was reached. However, because PPT3 was located closest to the shallow foundation, measurements at this location were significantly higher compared to the rest. In the case of the post-yield behavior in these tests, measurements at PPT3 showed a drop in excess pore-water pressure followed by a steady and slow increase in pore-water pressure which, in the case of the tests with LTP thicknesses of 0.45 and 0.60 m, was followed by a significant increase in pore-water pressure. On the other hand, post-yield pore-water pressure measurements at PPT1 and PPT2 remained somewhat constant or increased slightly with increasing LTP thickness.

The excess pore-water pressure measurements recorded in the test with a LTP thickness of 1.20 m (Figure 3.16d) showed a similar yet distinct trend compared to those recorded in the rest of

tests. In all PPTs, there was a pre-yield increase in excess pore-water pressure measurements. Post-yield excess pore-water pressure measurements were characterized by an ongoing and continuous increase that was later followed by a smooth decrease. This trend was clearly noticeable in the measurements recorded at PPT3, while the trend was also observed at PPT2, albeit with a lower degree of definition compared to PPT3. The post-yield excess pore-water pressure measurements at PPT1 remained essentially constant during lateral testing.

The above observations highlight the importance of the location of the PPTs with respect to the footing, in the excess pore-water pressure measurements recorded during lateral testing. Measurements at PPT3, located closest to the footing, were consistently and significantly greater than those at PPT1 and PPT2 in each test. When comparing excess pore-water pressure measurements at yield for each of the tests, not only was the previous trend confirmed, but it was also possible to examine the influence of the LTP thickness in the magnitude of the excess pore-water pressure measurements (Figure 3.17). Although there is scatter in the data, the development of excess pore-water pressure generally increased with increasing LTP thickness. As the thickness of the LTP increased, the resultant load applied in the soil-column composite increased, and an increase in positive excess pore-water pressure development was captured by the PPT measurements when the system was essentially sheared with the lateral displacement of the shallow foundation above the surface of the LTP.

Table 3.5. Location of the PPTs

PPT	Q (m)	U (m)	V (m)
1	4.200	--	5.000
2	4.900	2.375	--
3	1.200	2.375	--

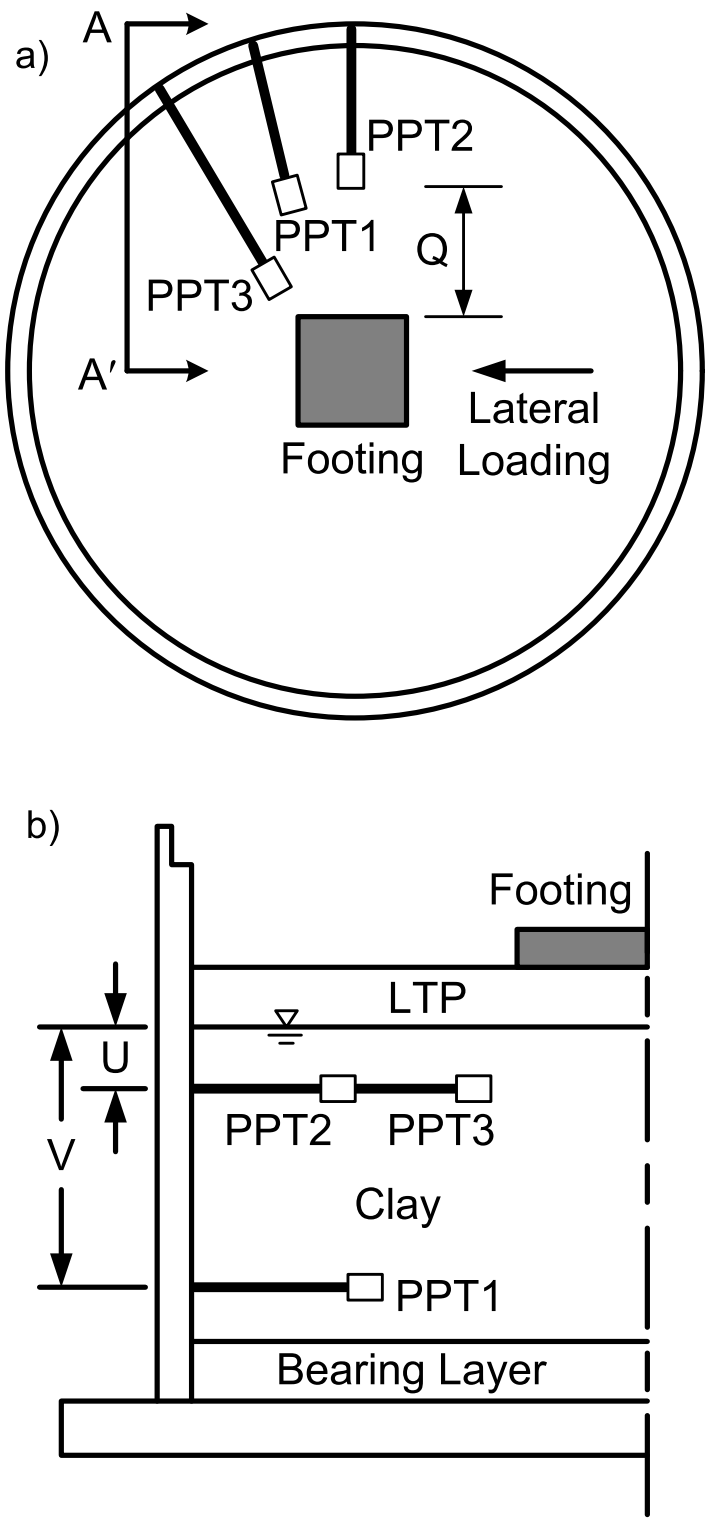

Fig. 3.15. Location of the PPTs, a) Plan view, and b) Cross-section through AA′. See Table 3.5 for details.

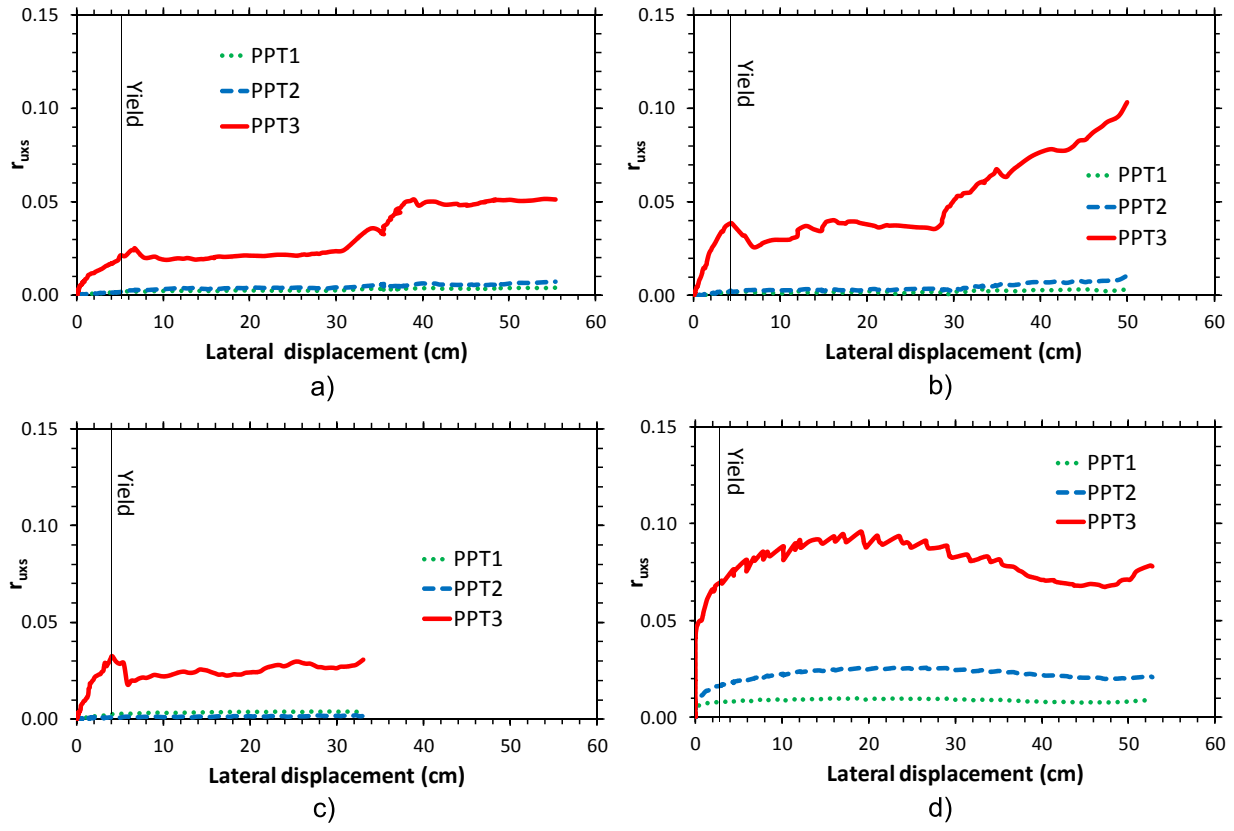

Fig. 3.16. Variation of the excess pore-water pressure ratio r_{uxs} during lateral load tests with LTP thicknesses of a) 0.45 m, b) 0.60 m, c) 0.70 m and d) 1.20 m.

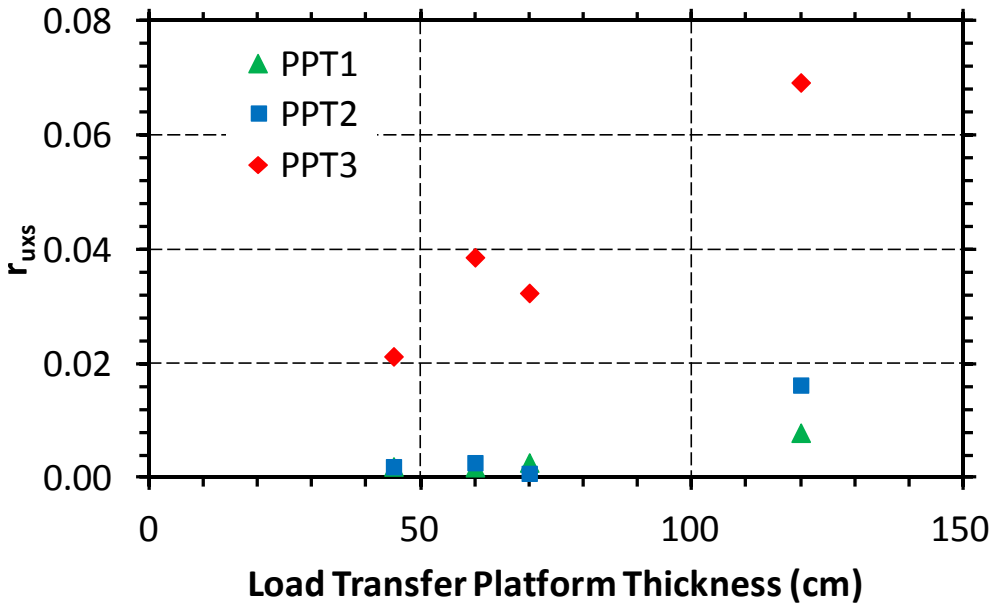

Fig. 3.17. Influence of the LTP thickness in excess pore-water pressure ratio at failure during lateral testing.

3.4.3 *Stiff Column Deformation after Lateral Testing*

Post-test photographs taken during the excavation of the stiff columns of two of the four models tested are shown in Figure 3.18. The stiff columns laterally tilted along the direction of the horizontal load, and with the exception of two columns in the test with a LTP thickness of 1.20 m, all stiff columns experienced failure, which was likely associated with the development of flexural-type deformations in the rigid vertical elements. During excavation of the models, the point of failure was identified in each stiff column and the distance from the top of the column to the location of failure surface was recorded. These distances are summarized in Table 3.6.

The results in Table 3.6 suggest that failure was observed at an average distance equal to 1/3 of the stiff column length in the soft soil, measured from the top of the rigid vertical element. The failure pattern observed in each stiff column is shown in the photograph in Figure 3.19. Compressive stress failure features, typical of flexural deformations, were observed around the failure plane. In addition, the linear feature in the failure patterns observed suggests that the stiff columns experienced tensional stresses at their backside.

When examining the influence of the LTP thickness on the failure mode of the stiff columns, the results show that when the LTP was 1.20 m thick, the vertical and horizontal loads applied produced deformation and failure to only two of the four columns (LL and UL columns in legend of Table 3.6). On the other hand, when the LTP thickness was 0.70 m or less, failure was observed in all four columns. These results suggest that the LTP thickness controlled the lateral deformations experienced by the stiff columns. This further emphasizes the importance of the

LTP thickness in controlling the lateral load behavior of stiff column-supported shallow foundations.

Table 3.6. Examination of the stiff columns after lateral testing (prototype scale)

Test	Column ID	Length in Clay W (m)	Failed Length X (m)	X/W (%)
LTP = 1.20 m	LR	7.50	NA	NA
	LL	7.50	2.25	30.00
	UR	7.50	NA	NA
	UL	7.50	2.25	30.00
			Average:	30.00
LTP = 0.70 m	LR	7.50	2.55	34.00
	LL	7.50	2.50	33.33
	UR	7.50	2.20	29.33
	UL	7.50	2.50	33.33
			Average:	32.50
LTP = 0.60 m	LR	7.50	2.30	30.67
	LL	7.50	2.45	32.67
	UR	7.50	2.75	36.67
	UL	7.50	2.30	30.67
			Average:	32.67
LTP = 0.45 m	LR	7.50	2.80	37.33
	LL	7.50	2.80	37.33
	UR	7.50	2.65	35.33
	UL	7.50	2.30	30.67
			Average:	35.17
			Overall Average:	32.95

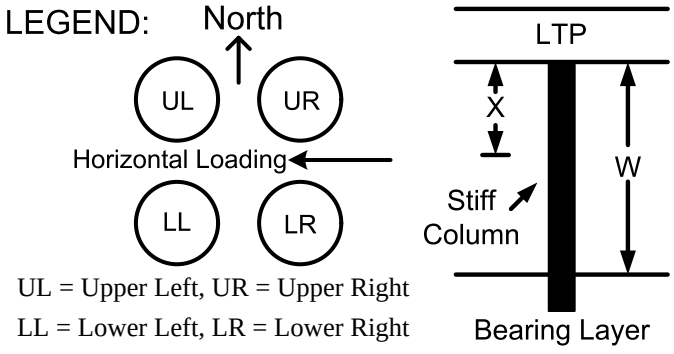

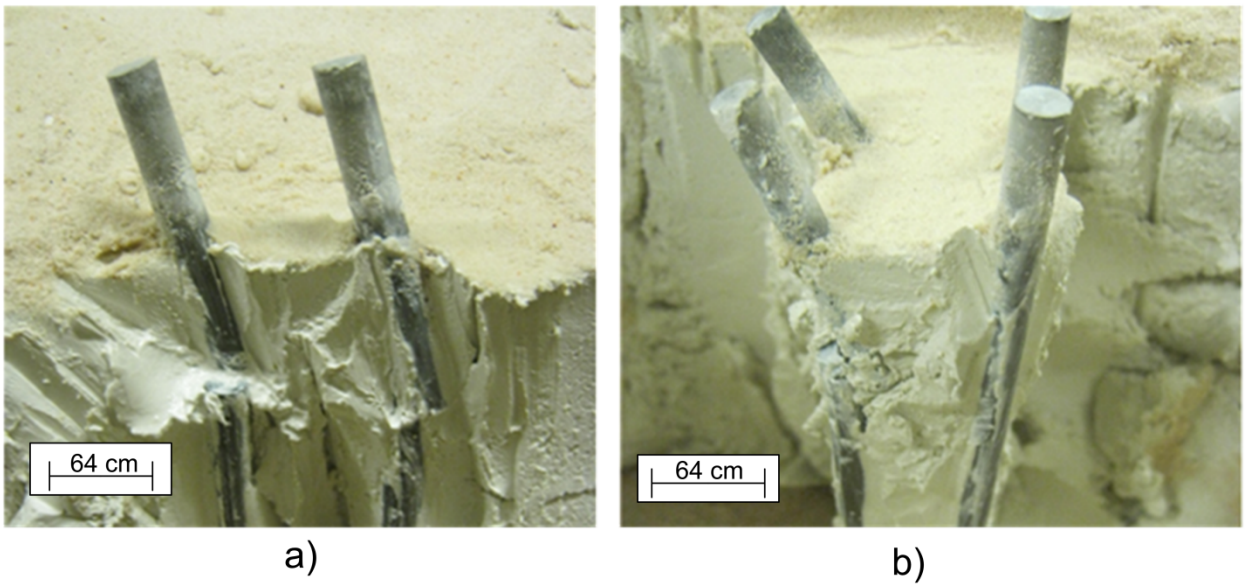

Fig. 3.18. Deformation of the stiff columns after lateral testing at 50g centrifugal acceleration on test with a LTP thickness of a) 0.70 m and b) 1.20 m. Prototype scale.

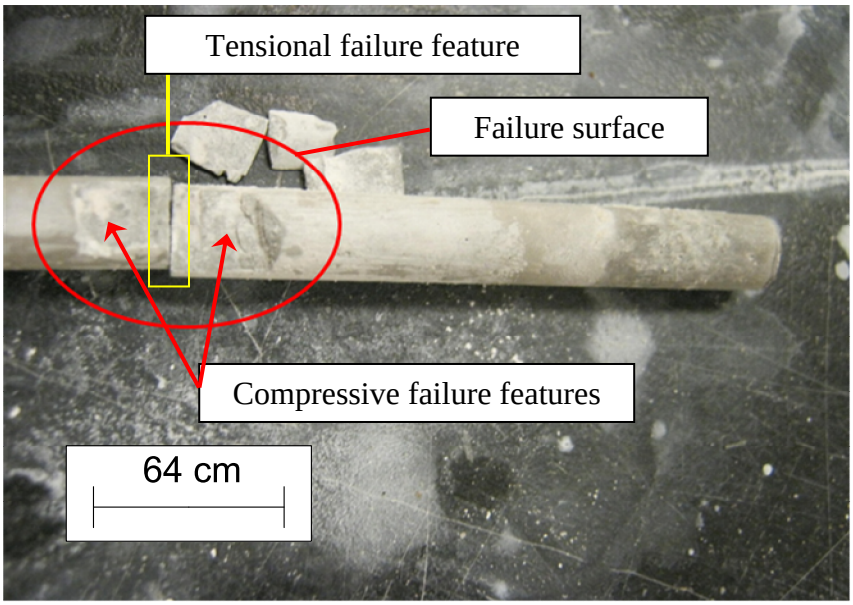

Fig. 3.19. Typical failure patterns observed in the stiff columns. Prototype scale.

3.5 CONCLUSIONS

Results presented in this chapter showed that the thickness of the LTP influenced the lateral capacity of the stiff column-supported shallow foundations tested in the centrifuge. An increase in lateral capacity with increasing LTP thickness was measured. It was hypothesized that for the thinner LTPs tested, the lateral capacity of the system was controlled by the shearing resistance of the soil-column composite rather than by the LTP. As the LTP thickness increased, the contribution of the shearing resistance of the LTP to the lateral capacity of the system increased. Due to lack of instrumentation, it was not possible to quantify the relative contributions of the shearing resistance of the soil-column composite and LTP to the lateral capacity of each of the stiff column-supported shallow foundations tested.

The thickness of the LTP controlled the pre-yield and post-yield behavior of the laterally loaded stiff column-supported shallow foundations tested in the centrifuge. The pre-yield lateral load-displacement response became stiffer with increasing thickness of the LTP. For sufficiently thick LTPs on the order of 0.70 m or greater, post-yield behavior was characterized by nearly constant lateral capacity with lateral displacement. On the other hand, for LTP thicknesses less than 0.60 m, the post-yield behavior was characterized by a drop in lateral capacity with lateral displacement. Such responses were also likely the result of the influence of the LTP thickness in the shearing resistance of the system.

Excess pore-water pressure measurements during lateral testing of the stiff column-supported shallow foundations were also influenced by the thickness of the LTP. In general, an increase in the LTP thickness led to an increase in the excess pore-water pressure measurements in the soil-

column composite. Increasing the thickness of the LTP produced an increase in the resultant of the vertical and lateral load applied to the soil-column composite. This increase in the resultant load produced greater excess pore-water pressure measurements in the soft soil when the shallow foundation was laterally loaded during testing.

Loading of the stiff column-supported shallow foundation during lateral testing resulted in the development of failure in the top one-third of the stiff columns. In addition, failure was not observed in some stiff columns, further underscoring the importance of the LTP thickness in controlling the lateral deformations of the rigid vertical elements in the stiff column-supported shallow foundations tested.

CHAPTER 4: NUMERICAL MODELING OF STIFF COLUMN-SUPPORTED SHALLOW FOUNDATIONS WITH THE FINITE ELEMENT METHOD

4.1 INTRODUCTION

This chapter presents the results of the numerical analyses that were carried out to examine the lateral response of the stiff column-supported shallow foundations tested in the centrifuge test program. Three-dimensional finite element analyses were carried out to examine this lateral response. A brief review of the finite element formulation and constitutive models employed in the numerical analyses is presented. Two-dimensional numerical analyses were carried out, and their relevance to the three-dimensional numerical analyses is explained. The procedure used to numerically implement the three-dimensional geometry of the centrifuge models is described. The properties adopted for the various components of the stiff column-supported shallow foundations tested in the centrifuge test program are justified. The numerical results are examined, and they are compared to the experimental results.

4.2 FINITE ELEMENT FORMULATION

The numerical analyses were carried out using PLAXIS 2D Version 8.6 and PLAXIS 3D Version 2013, software developed for geotechnical applications. These programs accommodate two- and three-dimensional finite element analyses, respectively, and are capable of fully coupling changes in effective stress and shear strength in soils with changes in excess pore-water

pressure. While a detailed description of the deformation theory and finite element discretization employed by the software is beyond the scope of this work, emphasis will be given to summarizing the numerical formulation of the different types of elements employed in the numerical analyses. For further details on the numerical formulation of the elements and the numerical procedures employed by the finite element software to solve geotechnical-related boundary value problems, the reader is referred to Brinkgreve et al. (2006, 2013).

4.2.1 *Tetrahedral Elements*

For the numerical analyses, 10-noded tetrahedral elements were employed in the construction of the three-dimensional numerical models (Figure 4.1) in PLAXIS 3D. This type of element considers second-order interpolation for displacements (Brinkgreve et al. 2013).

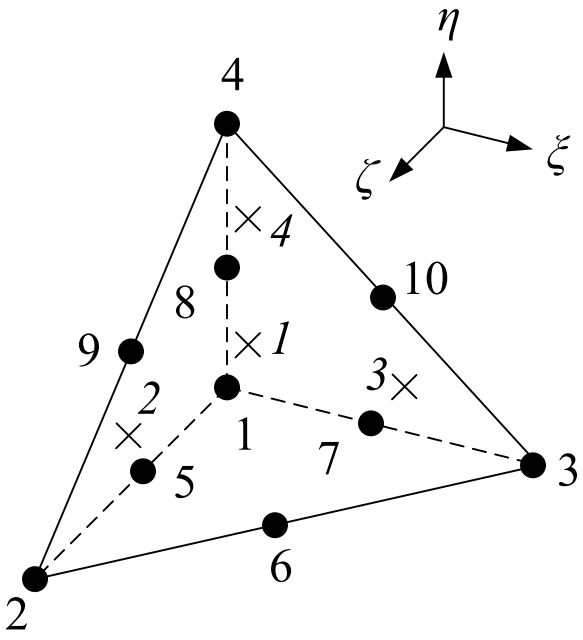

Fig. 4.1. 10-noded tetrahedral finite element with position of nodes (•) and integration points (x) (after Brinkgreve et al. 2013).

Considering a local coordinate system and three axes (ξ, η and ζ) in the definition of a tetrahedral element, the shape functions N_i for these elements in the local coordinate system are:

$$N_1 = (1-\xi-\eta-\zeta)(1-2\xi-2\eta-2\zeta) \tag{4.01}$$

$$N_2 = \zeta(2\zeta-1)$$

$$N_3 = \xi(2\xi-1)$$

$$N_4 = \eta(2\eta-1)$$

$$N_5 = 4\zeta(1-\xi-\eta-\zeta)$$

$$N_6 = 4\xi\zeta$$

$$N_7 = 4\xi(1-\xi-\eta-\zeta)$$

$$N_8 = 4\eta(1-\xi-\eta-\zeta)$$

$$N_9 = 4\eta\zeta$$

$$N_{10} = 4\xi\eta$$

In addition, the tetrahedral elements have three translational degrees of freedom per node (u_x, u_y and u_z). The shape function matrix $\underline{\underline{N}}_i$ can be defined as:

$$\underline{\underline{N}}_i = \begin{bmatrix} N_i & 0 & 0 \\ 0 & N_i & 0 \\ 0 & 0 & N_i \end{bmatrix} \tag{4.02}$$

The Cartesian strain components can be estimated as:

$$\begin{bmatrix} \varepsilon_{xx} \\ \varepsilon_{yy} \\ \varepsilon_{zz} \\ \gamma_{xy} \\ \gamma_{yz} \\ \gamma_{xz} \end{bmatrix} = \sum_i \underline{\underline{B}}_i \begin{bmatrix} v_{ix} \\ v_{iy} \\ v_{iz} \end{bmatrix} \tag{4.03}$$

Where $\underline{v} = [v_{ix}\ v_{iy}\ v_{iz}]^T$ is the nodal displacement vector and $\underline{\underline{B}}$ is the strain interpolation matrix that contains the spatial derivatives of the interpolation functions and is defined as

$$\underline{\underline{B}}_i = \begin{bmatrix} \frac{\partial N_i}{\partial x} & 0 & 0 \\ 0 & \frac{\partial N_i}{\partial y} & 0 \\ 0 & 0 & \frac{\partial N_i}{\partial z} \\ \frac{\partial N_i}{\partial y} & \frac{\partial N_i}{\partial x} & 0 \\ 0 & \frac{\partial N_i}{\partial z} & \frac{\partial N_i}{\partial y} \\ \frac{\partial N_i}{\partial z} & 0 & \frac{\partial N_i}{\partial x} \end{bmatrix} \tag{4.04}$$

In the finite elements, derivatives are calculated with respect to the local coordinate system (ξ, η, ζ). The Jacobian J is used to relate the local and global derivatives:

$$\begin{bmatrix} \frac{\partial N_i}{\partial \xi} \\ \frac{\partial N_i}{\partial \eta} \\ \frac{\partial N_i}{\partial \zeta} \end{bmatrix} = \begin{bmatrix} \frac{\partial x}{\partial \xi} & \frac{\partial y}{\partial \xi} & \frac{\partial z}{\partial \xi} \\ \frac{\partial x}{\partial \eta} & \frac{\partial y}{\partial \eta} & \frac{\partial z}{\partial \eta} \\ \frac{\partial x}{\partial \zeta} & \frac{\partial y}{\partial \zeta} & \frac{\partial z}{\partial \zeta} \end{bmatrix} \begin{bmatrix} \frac{\partial N_i}{\partial x} \\ \frac{\partial N_i}{\partial y} \\ \frac{\partial N_i}{\partial z} \end{bmatrix} = J \begin{bmatrix} \frac{\partial N_i}{\partial x} \\ \frac{\partial N_i}{\partial y} \\ \frac{\partial N_i}{\partial z} \end{bmatrix} \tag{4.05}$$

Or inversely:

$$\begin{bmatrix} \frac{\partial N_i}{\partial x} \\ \frac{\partial N_i}{\partial y} \\ \frac{\partial N_i}{\partial z} \end{bmatrix} == J^{-1} \begin{bmatrix} \frac{\partial N_i}{\partial \xi} \\ \frac{\partial N_i}{\partial \eta} \\ \frac{\partial N_i}{\partial \zeta} \end{bmatrix} \tag{4.06}$$

Numerical integration over a 10-noded tetrahedral element can be formulated as:

$$\iiint F(\xi,\eta,\zeta) d\xi \; d\eta \; d\zeta \approx \sum_{i=1}^{k} F(\xi_i,\eta_i,\zeta_i) w_i \tag{4.07}$$

Where $F(\xi_i, \eta_i, \zeta_i)$ is the value of the function F at position ξ_i, η_i, ζ_i and w_i is the weight factor for point i, and k is the number of sample points used. A typical tetrahedral element contains 4-sample points over which Gaussian integration is performed. Table 4.1 shows the position and weight factors of the integration points.

The element stiffness matrix $\underline{\underline{K}}^e$ is calculated by the integral:

$$\underline{\underline{K}}^e = \int \underline{\underline{B}}^T \underline{\underline{D}}^e \underline{\underline{B}} \; dV \tag{4.08}$$

Where $\underline{\underline{D}}^e$ represents the elastic material matrix. Using the change of variables theorem, the previous integral can be expressed in terms of the local coordinate system:

$$\underline{\underline{K}}^e = \int \underline{\underline{B}}^T \underline{\underline{D}}^e \underline{\underline{B}} \; |J| dV * \tag{4.09}$$

Where $|J|$ is the determinant of the Jacobian. The integral is estimated by numerical integration as previously described and considering that $\underline{\underline{K}}^e$ is composed of submatrices $\underline{\underline{K}}_{ij}^e$ where i and j represent local nodes, the process of calculating the element stiffness matrix can be rewritten as:

$$\underline{\underline{K}}_{ij}^e = \sum_k \underline{\underline{B}}_i^T \underline{\underline{D}}^e \underline{\underline{B}}_j |J| w_k \tag{4.10}$$

Table 4.1. 4-point Gaussian integration for 10-noded tetrahedral elements

Point	ξ_i	η_i	ζ_i	w_i
1	1/4 - 1/20√5	1/4 - 1/20√5	1/4 - 1/20√5	1/24
2	1/4 - 1/20√5	1/4 - 1/20√5	1/4 + 3/20√5	1/24
3	1/4 + 3/20√5	1/4 - 1/20√5	1/4 - 1/20√5	1/24
4	1/4 - 1/20√5	1/4 + 3/20√5	1/4 - 1/20√5	1/24

4.2.2 *Interface Elements*

The tetrahedral finite elements are compatible with other types of finite elements integrated in PLAXIS 3D. For instance, the numerical analyses also employed interface elements to characterize the soil-structure interaction between the bottom of the shallow foundation and the top of the LTP. The interface elements are formulated as area-type finite elements (Figure 4.2) that employ two sets of 6-noded triangular elements, one overlying the other. Such formulation results in interface elements with pairs of nodes rather than single nodes, with each node having three translational degrees of freedom (u_x, u_y, u_z) producing the development of differential slipping and gapping displacement between the node pairs. Considering two local coordinates (ξ and η) in combination with an auxiliary coordinate $\zeta = 1 - \xi - \eta$, the shape functions for these triangular finite elements are:

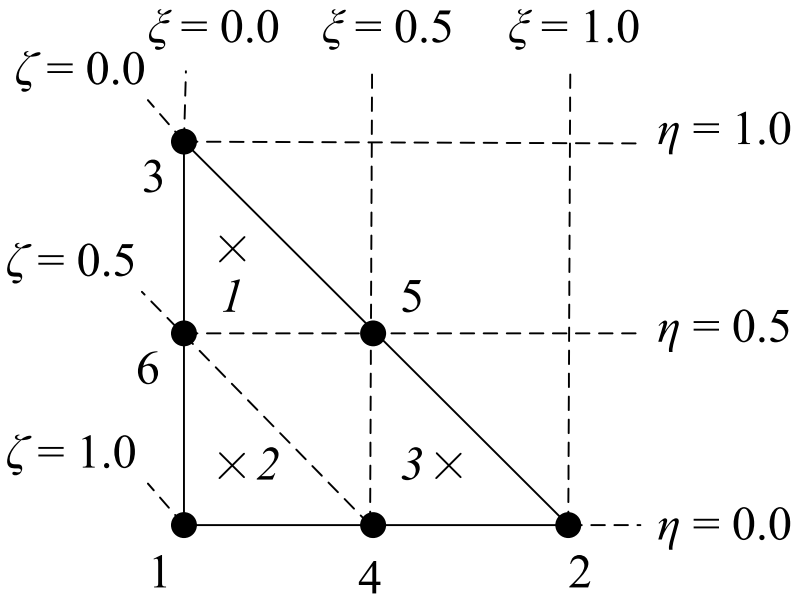

Fig. 4.2. 6-noded triangular finite element with position of nodes (•) and integration points (x) (after Brinkgreve et al. 2013).

$$N_1 = \zeta(2\zeta - 1) \tag{4.11}$$

$$N_2 = \xi(2\xi - 1)$$

$$N_3 = \eta(2\eta - 1)$$

$$N_4 = 4\xi\zeta$$

$$N_5 = 4\xi\eta$$

$$N_6 = 4\eta\zeta$$

In a similar fashion to the tetrahedral elements, the numerical integration over the triangular elements can be formulated as following:

$$\iint F(\xi,\eta)d\xi\ d\eta \ \approx \sum_{i=1}^{k} F(\xi_i,\eta_i)w_i \tag{4.12}$$

And finally, 6-noded triangular elements employed as interfaces utilize 3-point Gaussian integration (Table 4.2).

Table 4.2. 3-point Gaussian integration for 6-noded triangular elements

Point	ξ_i	η_i	w_i
1	1/6	2/3	1/3
2	1/6	1/6	1/3
3	2/3	1/6	1/3

4.2.3 *Triangular Elements*

In the two-dimensional finite element analyses carried out in PLAXIS 2D, 15-noded triangular elements were employed in the construction of the models. Figure 4.3 shows a schematic of a typical 15-noded triangular element. These elements use fourth order interpolation functions for the calculation of displacements and excess pore-water pressures in the finite elements. Considering two coordinates (ξ and η) in the definition of 15-noded triangular elements, in addition to the auxiliary coordinate $\zeta = 1 - \xi - \eta$, the shape functions for these elements are:

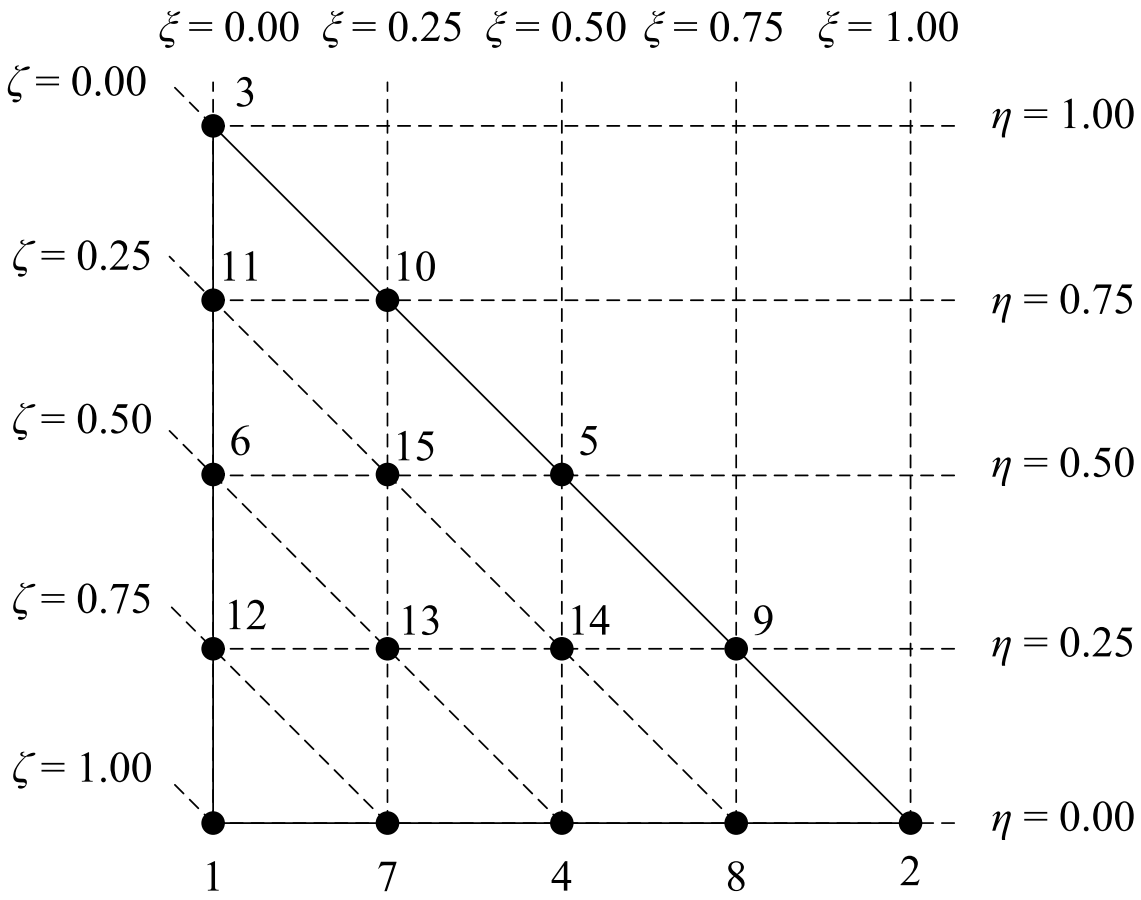

Fig. 4.3. 15-noded triangular finite element (after Brinkgreve et al. 2006).

$$N_1 = \zeta(4\zeta - 1)(4\zeta - 2)(4\zeta - 3)/6 \quad (4.13)$$

$$N_2 = \xi(4\xi - 1)(4\xi - 2)(4\xi - 3)/6$$

$$N_3 = \eta(4\eta - 1)(4\eta - 2)(4\eta - 3)/6$$

$$N_4 = 4\zeta\xi(4\zeta - 1)(4\xi - 1)$$

$$N_5 = 4\xi\eta(4\xi - 1)(4\eta - 1)$$

$$N_6 = 4\eta\zeta(4\eta - 1)(4\zeta - 1)$$

$$N_7 = \xi\zeta(4\zeta - 1)(4\zeta - 2) * 8/3$$

$$N_8 = \zeta\xi(4\xi - 1)(4\xi - 2) * 8/3$$

$$N_9 = \eta\xi(4\xi - 1)(4\xi - 2) * 8/3$$

$$N_{10} = \xi\eta(4\eta - 1)(4\eta - 2) * 8/3$$

$$N_{11} = \zeta\eta(4\eta - 1)(4\eta - 2) * 8/3$$

$$N_{12} = \eta\zeta(4\zeta - 1)(4\zeta - 2) * 8/3$$

$$N_{13} = 32\eta\xi\zeta(4\zeta - 1)$$

$$N_{14} = 32\eta\xi\zeta(4\xi - 1)$$

$$N_{15} = 32\eta\xi\zeta(4\eta - 1)$$

Numerical integration in 15-noded triangular elements uses twelve Gauss or stress points. The position and weight factors are shown in Table 4.3

Table 4.3. 12-point Gaussian integration for 15-noded triangular elements

Point	ξ_i	η_i	ζ_i	w_i
1, 2 & 3	0.063089	0.063089	0.873821	0.050845
4 to 6	0.249286	0.249286	0.501426	0.116786
7 to 12	0.310352	0.053145	0.636502	0.082851

4.2.4 *Beam Elements*

Beam elements are 3-noded linear elements (Figure 4.4) that were used to model the flexural rigidity of the stiff columns and to quantify the load induced them. Beam elements adopt Mindlin's theory (Mindlin 1951) in their numerical formulation. The beam elements used in PLAXIS 3D have six degrees of freedom per node, which include three translational degrees (u_x, u_y, u_z) and three rotational degrees (r_x, r_y, r_z) in the global coordinate system. In the rotated coordinate system, the beam elements have five degrees of freedom which include, one axial displacement u_x*, two transverse displacements u_y* and u_z*, and two rotations r_y* and r_z*. Beam elements employ only one local coordinate ξ in the direction parallel to its axis. Since the beam element is defined as a 3-noded finite element, it allows quadratic interpolation of axial displacements and the shape functions are defined as:

$$N_1 = -\tfrac{1}{2}(1-\xi)\xi \tag{4.14}$$

$$N_2 = (1+\xi)(1-\xi)$$

$$N_3 = \tfrac{1}{2}(1+\xi)\xi$$

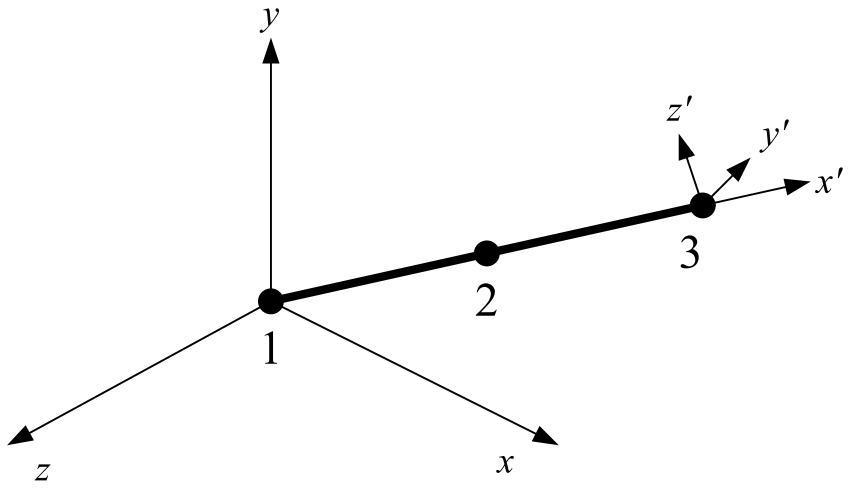

Fig. 4.4. 3-noded beam element.

Numerical integration over linear finite elements is obtained using the following expression:

$$\int_{\xi=-1}^{1} F(\xi)d\xi \approx \sum_{i=1}^{k} F(\xi_i)w_i \tag{4.15}$$

Beam elements are integrated over their length using 2-point Gaussian integration (Table 4.4). The beam elements were used in combination with tetrahedral finite elements to model the cylindrical stiff columns using the “volume pile” approach from Dao (2011). In this approach, the beam elements with decreased proportional stiffness are placed at the center of cylindrical regions composed of tetrahedral finite elements. The combination of these cylindrical regions and the beam elements produced three-dimensional objects that essentially modeled the three-dimensional space the stiff columns would occupy inside the soft soil, thus producing a more realistic representation of the stiff columns in the numerical models. For additional information regarding the numerical formulation of beam elements, the reader is referred to Brinkgreve et al. (2013).

Table 4.4. 2-point Gaussian integration for 3-noded linear elements

Point	ξ_i	w_i
1	$-1/\sqrt{3}$	1
2	$+1/\sqrt{3}$	1

4.3 CONSTITUTIVE MODELS

An overview is provided of the constitutive models used to characterize the stress-strain relationship of the various components of the stiff column-supported shallow foundations tested in the centrifuge test program. Information presented in this section is summarized from Brinkgreve et al. (2013).

4.3.1 *Mohr-Coulomb Model*

Strains $\underline{\varepsilon}$ and strain rates $\underline{\dot{\varepsilon}}$ can be decomposed in elastic and plastic components as follows:

$$\underline{\varepsilon} = \underline{\varepsilon}^{e} + \underline{\varepsilon}^{p} \qquad \underline{\dot{\varepsilon}} = \underline{\dot{\varepsilon}}^{e} + \underline{\dot{\varepsilon}}^{p} \tag{4.16}$$

Where $\underline{\varepsilon}^{e}$ and $\underline{\varepsilon}^{p}$ are the elastic and plastic strains respectively, $\underline{\dot{\varepsilon}}^{e}$ and $\underline{\dot{\varepsilon}}^{p}$ are the elastic and plastic strain rates, respectively. A constitutive model describes the relationship between effective stresses and effective strains and in the more general sense, it relates effective stress rates with strain rates:

$$\dot{\underline{\sigma}}' = \underline{\underline{M}}\,\dot{\underline{\varepsilon}} \tag{4.17}$$

Where $\dot{\underline{\sigma}}'$ is the effective stress rate, and $\underline{\underline{M}}$ is the material stiffness matrix which acquires different forms depending on the constitutive model employed.

The Mohr-Coulomb model is a linear elastic-perfectly plastic stress-strain relationship in which the elastic part follows Hooke's law, and the constitutive relationship in this case is:

$$\begin{bmatrix} \dot{\sigma}'_{xx} \\ \dot{\sigma}'_{yy} \\ \dot{\sigma}'_{zz} \\ \dot{\sigma}'_{xy} \\ \dot{\sigma}'_{yz} \\ \dot{\sigma}'_{xz} \end{bmatrix} = \frac{E'}{(1-2\nu')(1+\nu')} \begin{bmatrix} 1-\nu' & \nu' & \nu' & 0 & 0 & 0 \\ \nu' & 1-\nu' & \nu' & 0 & 0 & 0 \\ \nu' & \nu' & 1-\nu' & 0 & 0 & 0 \\ 0 & 0 & 0 & \frac{1}{2}-\nu' & 0 & 0 \\ 0 & 0 & 0 & 0 & \frac{1}{2}-\nu' & 0 \\ 0 & 0 & 0 & 0 & 0 & \frac{1}{2}-\nu' \end{bmatrix} \begin{bmatrix} \dot{\varepsilon}_{xx} \\ \dot{\varepsilon}_{yy} \\ \dot{\varepsilon}_{zz} \\ \dot{\gamma}_{xy} \\ \dot{\gamma}_{yz} \\ \dot{\gamma}_{xz} \end{bmatrix} \tag{4.18}$$

In which the stiffness matrix is $\underline{\underline{D}}^{e}$ and the above expression can be rewritten as

$$\dot{\underline{\sigma}}' = \underline{\underline{D}}^{e}\,\dot{\underline{\varepsilon}} \tag{4.19}$$

And using Eq. 4.16:

$$\dot{\underline{\sigma}}' = \underline{\underline{D}}^e \left(\dot{\underline{\varepsilon}} - \dot{\underline{\varepsilon}}^p \right) \tag{4.20}$$

The plastic strain rate is proportional to the derivative of the yield function with respect to the stresses according to the classical plasticity theory (Hill 1950):

$$\dot{\underline{\varepsilon}}^p = \lambda \frac{\partial f}{\partial \underline{\sigma}'} \tag{4.21}$$

Where f is the yield function and λ is the plastic multiplier. However, under this classical principle, called *associated plasticity*, dilatancy is overestimated in the Mohr-Coloumb model. To correct for this, a plastic potential function g is introduced such that $g \neq f$. This is called *non-associated plasticity* and the plastic strain rate is expressed as:

$$\dot{\underline{\varepsilon}}^p = \lambda \frac{\partial g}{\partial \underline{\sigma}'} \tag{4.22}$$

For elastic behavior, λ is zero, while λ is positive for plastic behavior. Smith and Griffith (1988) and Vermeer and Borst (1984) combined the previous expressions to obtain a unified equation that relates the effective stress rates with the strain rates:

$$\dot{\underline{\sigma}}' = \left(\underline{\underline{D}}^e - \frac{\alpha}{d} \underline{\underline{D}}^e \frac{\partial g}{\partial \underline{\sigma}'} \frac{\partial f}{\partial \underline{\sigma}'}^T \underline{\underline{D}}^e \right) \dot{\underline{\varepsilon}} \tag{4.23}$$

Where

$$d = \frac{\partial f}{\partial \underline{\sigma}'}^{T} \underline{\underline{D}}^{e} \frac{\partial g}{\partial \underline{\sigma}'} \tag{4.24}$$

In this expression, α is a variable than can either be zero for elastic behavior or equal to one for plastic behavior. Plastic behavior occurs when f = 0 and in the case of the Mohr-Coulomb constitutive model, yield is described by the following set of yield functions:

$$f_{1a} = \frac{1}{2}(\sigma'_2 - \sigma'_3) + \frac{1}{2}(\sigma'_2 + \sigma'_3)\sin\phi' - c'\cos\phi' \le 0 \tag{4.25}$$

$$f_{1b} = \frac{1}{2}(\sigma'_3 - \sigma'_2) + \frac{1}{2}(\sigma'_3 + \sigma'_2)\sin\phi' - c'\cos\phi' \le 0$$

$$f_{2a} = \frac{1}{2}(\sigma'_3 - \sigma'_1) + \frac{1}{2}(\sigma'_3 + \sigma'_1)\sin\phi' - c'\cos\phi' \le 0$$

$$f_{2b} = \frac{1}{2}(\sigma'_1 - \sigma'_3) + \frac{1}{2}(\sigma'_1 + \sigma'_3)\sin\phi' - c'\cos\phi' \le 0$$

$$f_{3a} = \frac{1}{2}(\sigma'_1 - \sigma'_2) + \frac{1}{2}(\sigma'_1 + \sigma'_2)\sin\phi' - c'\cos\phi' \le 0$$

$$f_{3b} = \frac{1}{2}(\sigma'_2 - \sigma'_1) + \frac{1}{2}(\sigma'_2 + \sigma'_1)\sin\phi' - c'\cos\phi' \le 0$$

In the above expressions, σ'_1, σ'_2 and σ'_3 are the effective major, intermediate and minor compressive principal stresses, respectively. It is worth noting that the finite element software

used in the numerical analyses adopts negative normal stresses as compressive stresses and positive normal stresses as tensile stresses. In addition, ϕ' and c' are the effective angle of internal friction and cohesion, respectively. The condition $f_i = 0$ for all yield functions (where f_i is used to denote each individual yield function) represents a fixed hexagonal cone in principal stress space where each yield function represents a yield surface (Figure 4.5). Stress states inside the hexagonal cone ($f_i < 0$) represent elastic states that obey Hooke's law while stress states in yield surfaces represent plastic states. The Mohr-Coulomb constitutive model also considers six plastic potential functions:

$$g_{1a} = \frac{1}{2}(\sigma'_2 - \sigma'_3) + \frac{1}{2}(\sigma'_2 + \sigma'_3)\sin\psi \tag{4.26}$$

$$g_{1b} = \frac{1}{2}(\sigma'_3 - \sigma'_2) + \frac{1}{2}(\sigma'_3 + \sigma'_2)\sin\psi$$

$$g_{2a} = \frac{1}{2}(\sigma'_3 - \sigma'_1) + \frac{1}{2}(\sigma'_3 + \sigma'_1)\sin\psi$$

$$g_{2b} = \frac{1}{2}(\sigma'_1 - \sigma'_3) + \frac{1}{2}(\sigma'_1 + \sigma'_3)\sin\psi$$

$$g_{3a} = \frac{1}{2}(\sigma'_1 - \sigma'_2) + \frac{1}{2}(\sigma'_1 + \sigma'_2)\sin\psi$$

$$g_{3b} = \frac{1}{2}(\sigma'_2 - \sigma'_1) + \frac{1}{2}(\sigma'_2 + \sigma'_1)\sin\psi$$

In the plastic potential functions, ψ is the dilatancy angle which is used to model positive plastic volumetric strain increment. The introduction of non-associated plasticity in terms of potential functions allows the control of dilatancy in the Mohr-Coulomb model.

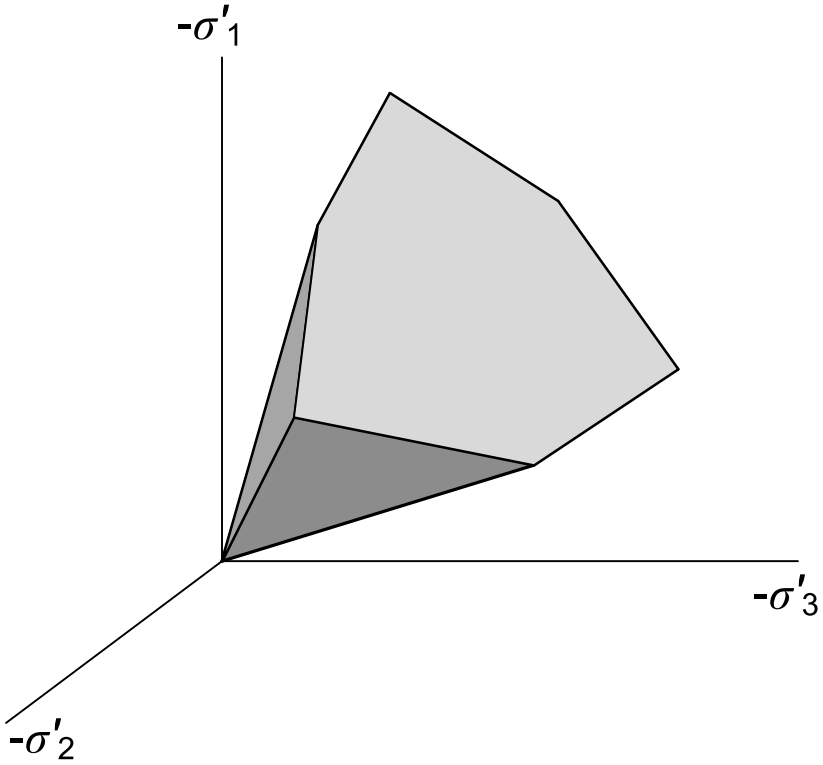

Fig. 4.5. The Mohr-Coulomb yield surface in principal stress space ($c' = 0$) (after Brinkgreve et al. 2013).

When the cohesion c' is greater than zero, the standard Mohr-Coulomb criterion allows tension. A tension cut-off is introduced to eliminate any tensile strength, considering that soils can sustain little to no tension. The tension cut-off introduces three additional yield functions which adopt an associated flow rule:

$$f_4 = \sigma'_1 - \sigma_t \leq 0 \tag{4.27}$$

$$f_5 = \sigma'_2 - \sigma_t \leq 0$$

$$f_6 = \sigma'_3 - \sigma_t \leq 0$$

Where σ_t is the allowable tensile stress. In addition to the shear strength parameters c', ϕ' and ψ, input is required of the elastic Young's modulus E and Poisson's ratio ν.

4.3.2 *Soft Soil Model*

The Soft Soil model is a non-linear Cam-Clay type constitutive model that considers stress-dependent stiffness, provides distinction between primary loading and unloading/reloading, and failure is determined by the Mohr-Coulomb criterion (Brinkgreve et al. 2013).

During primary or virgin isotropic loading, this constitutive model considers a logarithmic relation between volumetric strain ε_v and the mean effective stress p' expressed as (Brinkgreve et al. 2013):

$$\varepsilon_v - \varepsilon_v^0 = -\lambda^* \ln\left(\frac{p'}{p^0}\right) \tag{4.28}$$

In which λ^* is the modified compression index which specifies the compressibility of the material during primary or virgin loading at stress levels below the preconsolidation stress p_p. The modified compression index is a function of volumetric strain as opposed to the classical compression index λ, which is a function of void ratio or specific volume (Wood 1990). The variables ε_v^0 and p^0 are the initial volumetric strain during virgin compression and initial mean effective stress, respectively. During isotropic unloading and reloading, the previous formulation acquires the following form:

$$\varepsilon_v^e - \varepsilon_v^{e0} = -\kappa^* \ln\left(\frac{p'}{p^0}\right) \tag{4.29}$$

In the previous expression, κ^* is the modified swelling index which specifies the compressibility of the material during unloading and reloading. In a similar fashion to the modified compression index, κ^* is a function of volumetric strain. In this case, $\varepsilon_v^{\,0}$ is the initial volumetric strain during unloading/reloading. The response of the soil during unloading and reloading up to the preconsolidation stress is assumed elastic and obeys Hooke's law. Figure 4.6 summarizes the logarithmic relationships described in the previous equations. In this figure, an infinite number of unloading/reloading lines can exist, each one corresponding to a specific value of the isotropic preconsolidation stress. During unloading/reloading, the preconsolidation stress remains constant, but during primary loading, it increases with stress causing irreversible plastic volumetric strains. Equation 4.29 implies linear stress dependency of the bulk modulus K_{ur} during unloading/reloading conditions:

$$K_{ur} = \frac{E_{ur}}{3\left(1-2\nu_{ur}\right)} = \frac{p'}{\kappa^*} \tag{4.30}$$

Where E_{ur} and ν_{ur} refer to Young's modulus and Poisson's ratio in unloading/reloading conditions, respectively. In the previous expression, ν_{ur} and κ^* are used as constants in the part of the model that computes the elastic strains.

To further understand the response of the Soft Soil constitutive model during yielding, biaxial loading conditions ($\sigma'_2 = \sigma'_3$) will be considered. For such a state of stress, the yield function of this model is defined as (Brinkgreve et al. 2013):

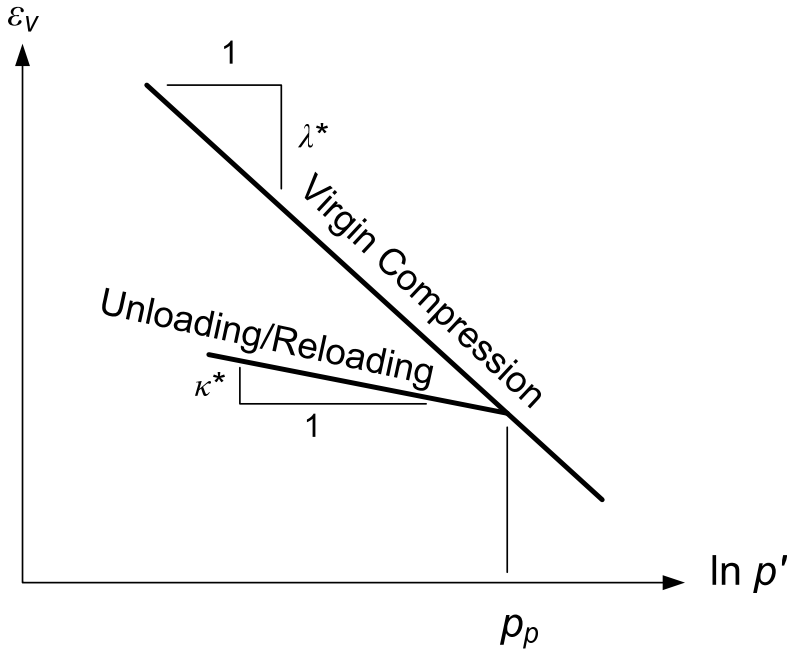

Fig. 4.6. Relationship between the volumetric strain and the mean stress in the Soft Soil model (after Brinkgreve et al. 2013).

$$f = f' - p_p \tag{4.31}$$

Where f' is a function of the stress state p' (mean effective stress) and q (deviatoric stress), while the preconsolidation stress p_p is a function of the plastic volumetric strain ε_v^p such that:

$$f' = \frac{q^2}{M^2\left(p' + c'\cot\phi'\right)} + p' \tag{4.32}$$

$$p_p = {p_p}^0 \exp\left(\frac{-\varepsilon_v^p}{\lambda^* - \kappa^*}\right) \tag{4.33}$$

Where ${p_p}^0$ is the initial isotropic preconsolidation stress in the hardening relation shown in Eq. 4.33. The yield function f describes an ellipse in the $p' - q$ plane as shown in Figure 4.7. In the Soft Soil model, the parameter M determines the height of the ellipse. In the context of traditional critical state soil mechanics, the M-line in Figure 4.7 is referred to as the critical state line and represents post peak failure. In the Soft Soil model, however, failure is modeled using

the Mohr-Coulomb criterion and it is observed as a straight line in the figure with a slope smaller to the *M*-line. The yield function produces irreversible volumetric strains in primary compression and forms the cap of the yield contour. The total yield contour, as shown by the bold lines in Figure 4.7, is the boundary of the elastic stress area. The failure line is fixed, but the cap may increase in primary compression. The isotropic preconsolidation stress p_p determines the extent of the ellipse along the p'-axis. In total, the Soft Soil model requires the input of four parameters: λ^*, κ^*, c' and ϕ'.

For any general state of stress, the plastic behavior of the Soft Soil model is defined by a total of six yield functions; three compression yield functions and three Mohr-Coulomb yield functions (Brinkgreve et al. 2013). The total yield contour in principal stress space resulting from the six yield functions is indicated in Figure 4.8.

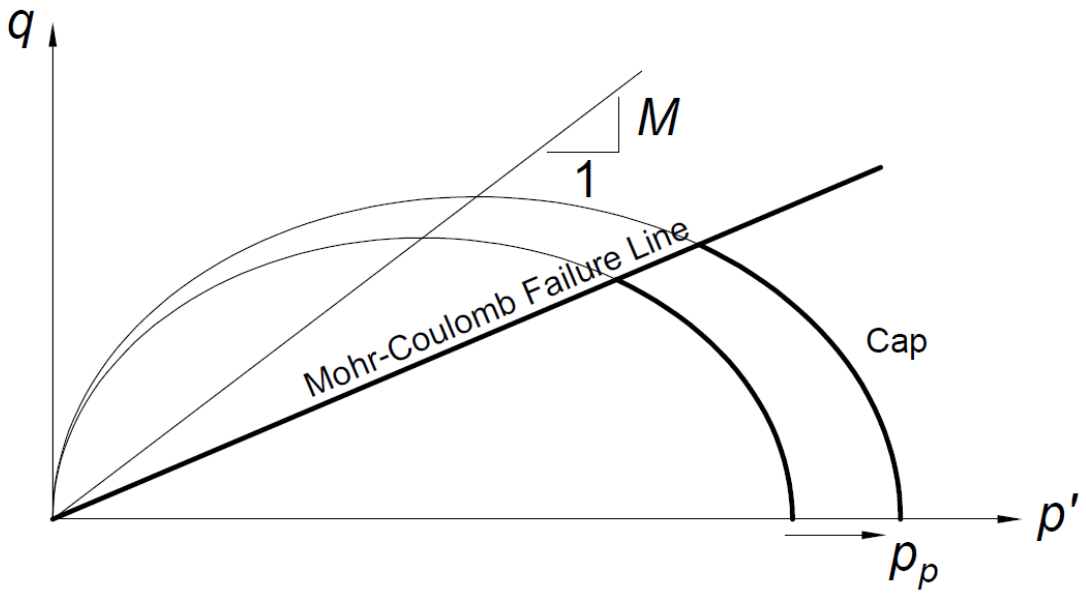

Fig. 4.7. Yield surface of the Soft Soil model in p'-q space (after Brinkgreve et al. 2013).

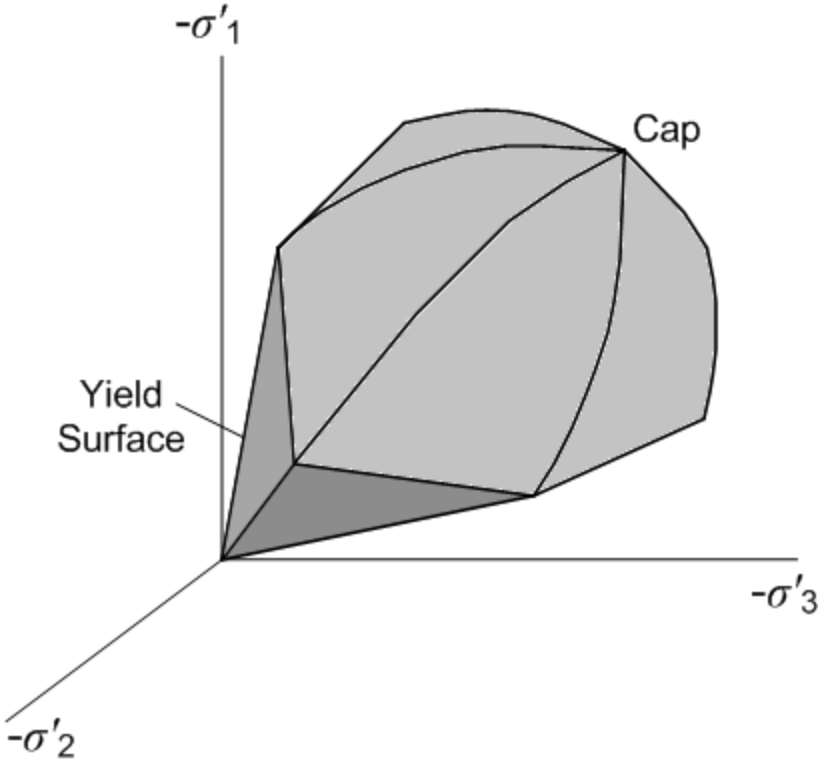

Fig. 4.8. Total yield contour of the Soft Soil model in principal stress space (after Brinkgreve et al. 2013).

4.3.3 *Elastic-Plastic Model for Interfaces*

An elastic-plastic model is used in the finite element software to describe the behavior of the interfaces (Brinkgreve et al. 2013) in order to model the interaction between the shallow foundation and the LTP. The Mohr-Coulomb criterion is used to distinguish between elastic and plastic behavior. For the interface to remain elastic, the shear stress τ is given by:

$$|\tau| < -\sigma'_n \tan\phi_i + c_i \tag{4.34}$$

Where σ'_n is the effective normal stress. For plastic behavior τ is given by:

$$|\tau| = -\sigma'_n \tan\phi_i + c_i \tag{4.35}$$

Where ϕ_i and c_i are, respectively, the friction angle and cohesion of the interface. The shear strength properties of the interface are related to the shear strength properties of the soil, or materials located at the immediate vicinity of the interface using a strength reduction factor R_{inter} such that:

$$c_i = R_{\text{inter}} c_{soil} \tag{4.36}$$

$$\tan\phi_i = R_{\text{inter}} \tan\phi_{soil} \leq \tan\phi_{soil} \tag{4.37}$$

$$\psi_i = 0 \text{ for } R_{\text{inter}} < 1, \text{otherwise } \psi_i = \psi_{soil} \tag{4.38}$$

Where ψ_i is the dilation angle of the interface. When the interface is elastic, both slipping (or shear) displacements Δ_S and gapping (or normal) displacements Δ_N can occur. The magnitudes of the interface displacements are:

$$\Delta_N = \frac{\sigma_n}{K_n} = \frac{\sigma_n t_i}{E_{oed,i}} \tag{4.39}$$

$$\Delta_S = \frac{\tau}{K_s} = \frac{\tau\, t_i}{G_i} \tag{4.40}$$

Where G_i is the shear modulus of the interface, $E_{oed,i}$ is the one-dimensional compression modulus of the interface, t_i is the virtual thickness of the interface generated during the creation of the interfaces in the geometry model, K_n is the elastic interface normal spring stiffness and K_s is the elastic interface shear spring stiffness. The shear and compression moduli of the interface are related as following:

$$E_{oed,i} = 2G_i \frac{1-\nu_i}{1-2\nu_i} \tag{4.41}$$

$$G_i = R_{\text{inter}}^2 G_{soil} \leq G_{soil} \tag{4.42}$$

Where ν_i is Poisson's ratio of the interface and has a non-editable constant value of 0.45 in the finite element software. The previous expressions show that the strength reduction factor R_{inter} will not only control the strength conditions of the interface, but it will also control the stiffness of the interface using the stiffness of the soil or materials at the vicinity of the interface.

4.4 DRAINED/UNDRAINED EFFECTIVE STRESS ANALYSES AND CONSOLIDATION

An undrained effective stress analysis with effective stiffness and effective strength parameters (Brinkgreve et al. 2013) was used to model the undrained behavior of the clayey soil in the three-dimensional numerical models employed in this study. In an undrained effective stress analysis, numerical undrained behavior is modeled by the PLAXIS finite element software by considering an undrained bulk modulus K_u for the soil defined as:

$$K_u = K' + \frac{K_w}{n} \tag{4.43}$$

Where K' is the bulk modulus of the soil skeleton, K_w is the bulk modulus of water and n is the porosity. Based on this definition, it is possible for the finite element software to differentiate between total stresses, effective stresses and excess pore-water pressures:

$$\Delta\sigma = K_u \Delta\varepsilon_v \tag{4.44}$$

$$\Delta\sigma' = K' \Delta\varepsilon_v \tag{4.45}$$

$$\Delta u = \frac{K_w}{n} \Delta \varepsilon_v \tag{4.46}$$

Where $\Delta\varepsilon_v$ is the volume change experienced by the soil mass. The finite element software calculates the undrained bulk modulus and the bulk modulus of the soil skeleton using elasticity:

$$K_u = \frac{2G(1+\nu_u)}{3(1-2\nu_u)} \tag{4.47}$$

$$K' = \frac{E'}{3(1-2\nu')} \tag{4.48}$$

$$G = \frac{E'}{2(1+\nu')} \tag{4.49}$$

Where E' and ν' are Young's modulus and Poisson's ratio of the soil skeleton respectively, G is the shear modulus of the soil mass and ν_u is the undrained Young's modulus. The bulk modulus of the water is estimated by solving Eq. 4.43 for K_w/n in combination with the previous elasticity expressions resulting in:

$$\frac{K_w}{n} = \frac{3(\nu_u - \nu')}{(1-2\nu_u)(1+\nu')} K' \tag{4.50}$$

To avoid numerical problems from exceedingly high values of the bulk modulus, fully incompressible behavior is modeled by considering ν_u = 0.495 in the previous expression, rather than ν_u = 0.50 which represents no volume change corresponding to true undrained behavior. The finite element software later adds the bulk stiffness of the water to the stiffness matrix in the numerical computations. In the case of drained behavior, the bulk modulus of water is ignored and no excess pore-water pressures are generated, and all numerical calculations are related to

the soil skeleton. Coarse-granular soil layers were modeled as drained materials in the three-dimensional numerical analyses. In addition, the shallow foundation and the stiff columns were modeled as non-porous materials thus no initial static pore-water pressure distributions were assumed in them. For additional information on the definition of drained, undrained and non-porous behavior in the PLAXIS finite element software, the reader is referred to Brinkgreve et al. (2013).

In regards to the consolidation theory employed in PLAXIS, the major aspects of its formulation in the finite element software will be subsequently described. The following information was summarized from Brinkgreve et al. (2013). The consolidation theory implemented in PLAXIS follows Biot's theory (Biot 1956). Assumptions adopted in its basic formulation include Darcy's law (Darcy 1856) and the elastic deformation of the soil skeleton. The finite element software PLAXIS adopts Terzaghi's effective stress principle (Terzaghi 1925) in the following form:

$$\underline{\sigma} = \underline{\sigma}' + \underline{m}\left(p_{steady} + p_{excess}\right) \tag{4.51}$$

Where $\underline{\sigma} = [\sigma_{xx}\ \sigma_{yy}\ \sigma_{zz}\ \sigma_{xy}\ \sigma_{yz}\ \sigma_{xz}]^T$ is the vector with total stresses, $\underline{\sigma}'$ is the effective stresses, p_{excess} is the excess pore-water pressure, p_{steady} is the pore-water pressure under steady state or static conditions established during the initial conditions of the numerical model, and $\underline{m} = [1\ 1\ 1\ 0\ 0\ 0]^T$. The finite element approximation for consolidation-type stages requires the following expressions:

$$\underline{u} = \underline{\underline{N}}\,\underline{v} \tag{4.52}$$

$$\underline{p} = \underline{\underline{N}}\,\underline{p_n} \tag{4.53}$$

$$\underline{\varepsilon} = \underline{\underline{B}}\,\underline{v} \tag{4.54}$$

Where $\underline{v}$ is the nodal displacement vector, $\underline{u}$ is the displacement vector within a finite element, $\underline{p}$ is the pore-water pressure, $\underline{p_n}$ is the excess pore-water pressure vector, $\underline{\underline{N}}$ is the shape function matrix and $\underline{\underline{B}}$ is the strain interpolation matrix. In PLAXIS, the interpolation functions for displacements and pore-water pressures are the same. The above finite element approximation can be used with the incremental form of the equilibrium equation to obtain the following:

$$\int \underline{\underline{B}}^T d\underline{\sigma} dV = \int \underline{\underline{N}}^T d\underline{b}\, dV + \int \underline{\underline{N}}^T d\underline{t}\, dS + \underline{r_0} \tag{4.55}$$

Where is $\underline{b}$ the body force due to self-weight, $\underline{t}$ is the surface tractions, $\underline{r_0}$ is the residual force vector, and dV and dS represent integration over volume and surface area, respectively. Using Terzaghi's effective stress principle along with the constitutive relationship in Eq. 4.17, the following expression denotes the nodal equilibrium:

$$\underline{\underline{K}}\, d\underline{v} + \underline{\underline{L}}\, d\,\underline{p_n} = d\,\underline{f_n} \tag{4.56}$$

$$\underline{\underline{K}} = \int \underline{\underline{B}}^T \underline{\underline{M}}\,\underline{\underline{B}}\, dV \tag{4.57}$$

$$\underline{\underline{L}} = \int \underline{\underline{B}}^T \underline{m}\,\underline{\underline{N}}\, dV \tag{4.58}$$

$$d\,\underline{f_n} = \int \underline{\underline{N}}^T d\underline{b}\, dV + \int \underline{\underline{N}}^T d\underline{t}\, dS \tag{4.59}$$

Where $\underline{\underline{K}}$ is the stiffness matrix, $\underline{\underline{L}}$ is the coupling matrix and $d\underline{f_n}$ is the incremental load vector. In regards to flow, the continuity equation takes the following form:

$$\nabla^T \underline{\underline{R}} \nabla\left(\gamma_w y - p_{steady} - p\right)/\gamma_w - \underline{m}^T \frac{\partial \underline{\varepsilon}}{\partial t} + \frac{n}{K_w}\frac{\partial p}{\partial t} = 0 \tag{4.60}$$

$$\underline{\underline{R}} = \begin{bmatrix} k_x & 0 & 0 \\ 0 & k_y & 0 \\ 0 & 0 & k_z \end{bmatrix} \tag{4.61}$$

Where $\underline{\underline{R}}$ is the permeability matrix and γ_w is the unit weight of water. Of note is that the previous continuity expression adopts the sign convention of positive p_{steady} and p. The continuity equation adopts the following form when considering a steady state solution:

$$\nabla^T \underline{\underline{R}} \nabla p / \gamma_w + \underline{m}^T \frac{\partial \underline{\varepsilon}}{\partial t} - \frac{n}{K_w} \frac{\partial p}{\partial t} = 0 \tag{4.62}$$

Applying Galerkin's method along with prescribed boundary conditions in the finite element discretization, the following continuity equation can be obtained:

$$-\underline{\underline{H}}\,\underline{p_n} + \underline{\underline{L}}^T \frac{d\underline{v}}{dt} - \underline{\underline{S}} \frac{d\,\underline{p_n}}{dt} = \underline{q_n} \tag{4.63}$$

$$\underline{\underline{H}} = \int \left(\nabla \underline{\underline{N}}\right)^T \underline{\underline{R}} \nabla \underline{\underline{N}} / \gamma_w \, dV \tag{4.64}$$

$$\underline{\underline{S}} = \int \frac{n}{K_w} \underline{\underline{N}}^T \underline{\underline{N}} \, dV \tag{4.65}$$

Where $\underline{q_n}$ is the vector of prescribed outflow at the boundary. The equilibrium equation in Eq. 4.56 and the continuity equation in Eq. 4.63 can be solved using an integration procedure that is described in detail in Brinkgreve et al. (2013). In addition, an iterative procedure is required when a non-linear constitutive model is used, which entails adopting a sub-incremental form of Eq. 4.56. For additional information related to the implementation and handling of consolidation in PLAXIS, the reader is referred to Brinkgreve et al. (2013).

4.5 TWO-DIMENSIONAL FINITE ELEMENT ANALYSES OF STIFF COLUMN INSTALLATION

Cavity expansion theory along with two-dimensional finite element analyses were conducted to evaluate the values of the earth pressure coefficient representative of the post-installation stress changes around the stiff columns of the centrifuge models. These earth pressure coefficient values, termed K_{RD} values, were defined as the ratio of the post-installation horizontal effective stress to the vertical effective stress around a stiff column. The calculation of the distribution of the K_{RD} values required the knowledge of the changes in horizontal effective stress at the vicinity of the stiff columns following their installation in the soft soil, which was simulated as an undrained process and subsequent reconsolidation around the rigid vertical elements. To estimate these changes in horizontal stress, a model described by Carter et al. (1979) that combined cylindrical cavity expansion with the finite element method was used.

4.5.1 *Cylindrical Cavity Expansion in a Tresca Soil*

The length-to-diameter ratio of a stiff column allows for strains perpendicular to a horizontal cross-section through the column (i.e. parallel to column axis) to be approximated to zero and the problem of modeling the stiff column installation is essentially reduced to a plane strain problem. With this simplification, the increase in horizontal stress around a stiff column can be estimated by approximating the installation of a stiff column as the expansion of a cylindrical cavity in the soft soil from zero-initial radius to a radius equal to the final stiff column radius. This plane strain cylindrical cavity approach has been previously used to analyze pile driving effects in clayey soil (Carter et al. 1979, Randolph and Wroth 1979, Randolph et al. 1979). This cylindrical

cavity approach was used to quantify the changes in stress and pore-water pressure in the soft soil around the stiff columns that were installed in the centrifuge models.

A linear elastic-perfectly plastic soil model with yielding described by the Tresca criterion (Tresca 1864) was adopted. The Tresca criterion for an expanding cylindrical cavity in soils is defined as (Yu 2000):

$$\sigma_r - \sigma_\theta = 2s_u \tag{4.66}$$

Where σ_r = total horizontal stress in the radial direction r; σ_θ = total horizontal stress in the circumferential direction θ and s_u = undrained shear strength. The previous expression adopts the traditional geotechnical sign convention of positive compression. Two zones are defined during cylindrical cavity expansion in a linear elastic-perfectly plastic Tresca soil from zero-initial radius: an inner plastic zone, where yielding is defined by the Tresca criterion, and an outer elastic zone where Hooke's law applies (Figure 4.9).

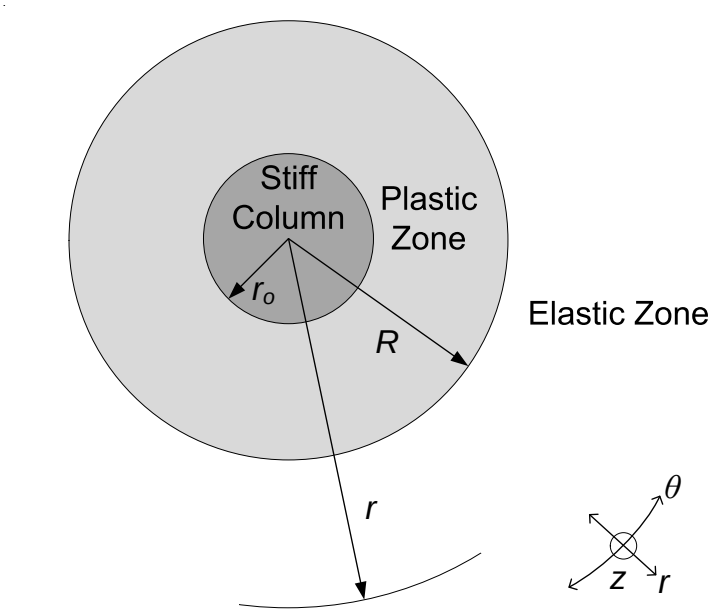

Fig. 4.9. Horizontal cross-section with plastic and elastic zones around an installed stiff column.

Closed-form solutions that describe the variation of the horizontal radial and circumferential stresses with radial distance in the elastic and plastic zones for a cylindrical cavity expanded from zero-initial radius in an infinite-extending linear elastic-perfectly plastic Tresca soil have been summarized by Yu (2000) and are presented here:

Elastic zone:

$$\sigma_r = \frac{s_u R^2}{r^2} + \sigma_h \tag{4.67}$$

$$\sigma_\theta = -\frac{s_u R^2}{r^2} + \sigma_h$$

Plastic zone:

$$\sigma_r = 2s_u \ln\left(\frac{R}{r}\right) + s_u + \sigma_h \tag{4.68}$$

$$\sigma_\theta = 2s_u \ln\left(\frac{R}{r}\right) - s_u + \sigma_h$$

Where $R/r_o = (G/s_u)^{1/2}$ provides the radial extent of the plastic zone after expansion and σ_h = total horizontal stress, R = radius of the plastic region; r_o = current cavity radius or final stiff column radius; r = radial distance from the cavity center and G = shear modulus of the soil. The aforementioned closed-form solutions provide the increase in total stress since cavity expansion occurred under short-term undrained conditions; however, strength in soils is controlled by the effective stresses that result from direct particle-to-particle contact in the soil skeleton. As a result, the calculation of the horizontal effective stress distribution around an installed stiff

column required information on the excess pore-water pressures that developed immediately following the installation of these rigid vertical elements in the centrifuge models.

Based on the consideration that the effective stress remains unchanged during undrained cylindrical cavity expansion in a linear elastic-perfectly plastic soil, Randolph and Wroth (1979) derived an analytical expression that calculated the initial excess pore-water pressure distribution immediately following expansion from zero-initial radius or before any reconsolidation took place:

$$u_o = 2s_u \ln\left(\frac{R}{r}\right) \quad r_o \le r \le R \tag{4.69}$$

$$u_o = 0 \qquad r \ge R$$

Where $R/r_o = (G/S_u)^{1/2}$ and u_o = initial excess pore-water pressure above the hydrostatic pressure immediately following cylindrical expansion resulting from stiff column installation. The previous expression indicates that excess pore-water pressures developed in the plastic zone after cylindrical cavity expansion from zero-initial radius. No excess pore-water pressures were expected in the elastic zone.

4.5.2 *Carter et al. (1979) Model*

Expansion of a cavity from zero-initial radius is essentially an infinite-strain problem (Baguelin et al. 1978), producing difficulties in its numerical implementation. To model the expansion from zero-initial radius in a finite element model, Carter et al. (1979) successfully approximated such behavior by considering that expanding a cylindrical cavity from $r = 0$ to $r = r_o$ can be

reasonably approximated by expanding a preexisting cavity with radius a_o from a radial distance $r = a_o$ to $r = 2a_o$ under the condition that, if both types of radial expansion ($r = 0$ to $r = r_o$ and $r = a_o$ to $r = 2a_o$) occur under constant volume conditions, then

$$r_o = a_o\sqrt{3} \tag{4.70}$$

The proposed approximation method for the creation of a cylindrical cavity allows for stresses and pore-water pressures to be estimated for distances greater than $r = 2a_o = 1.15r_o$. Values of interest in the range from $r = r_o$ to $r = 1.15r_o$ (Figure 4.10) must be calculated by means of extrapolation of the finite element results for $r \geq 1.15r_o$. This approach proved to be useful in approximating the expansion of a cylindrical cavity from zero-initial radius and as a result, it was used to simulate the installation of the stiff columns.

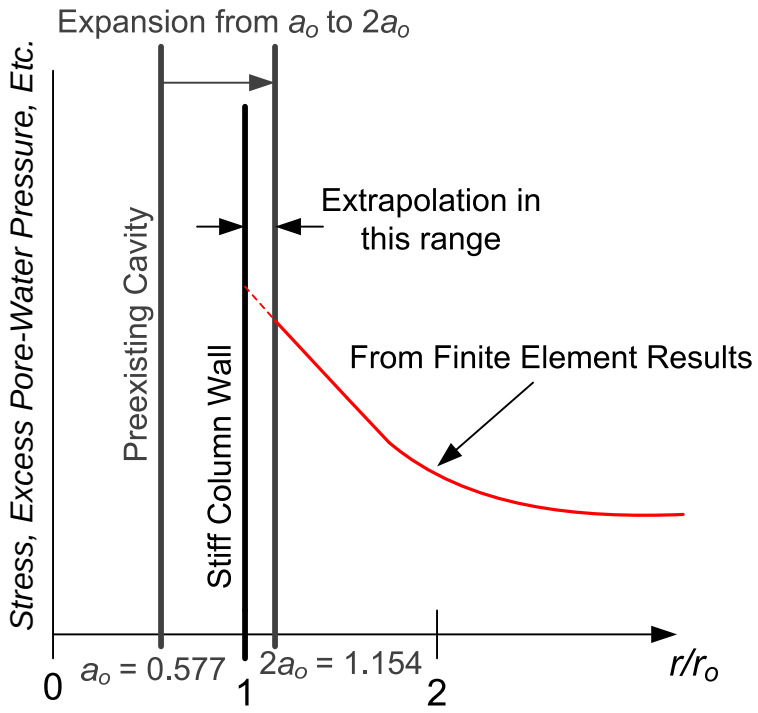

Fig. 4.10. Carter et al. (1979) model approach.

4.5.3 *Implementation of Carter et al. (1979) Model in PLAXIS 2D*

The Carter et al. (1979) model that allowed the evaluation of the installation-induced horizontal stresses around the stiff columns of the centrifuge models was implemented in PLAXIS 2D. Figure 4.11 shows a schematic of the typical finite element model used for the two-dimensional numerical analyses. The schematic shown is this figure represents an axisymmetric radial cross-section representative of plane strain conditions in the stiff column. No particular criterion was used to specify the radial distance U of the domain of the model, but rather U was adjusted continuously until the changes in total horizontal stress in the free field following doubling of the cavity were sufficiently close to zero, occurring approximately at a ratio of U/a_o of 1000. Similarly, the height V of the model was adjusted continuously until a ratio of U/V of 5 provided stable numerical results. An "Undrained" material type with $\phi = 0$ was adopted for the linear elastic-perfectly plastic Mohr-Coulomb soil around the stiff columns. Undrained effective stress analyses with undrained strength parameters were considered for all the models. These types of analyses used effective stiffness parameters with direct input of the undrained shear strength $\phi = \phi_u = 0$ and $c = s_u$ as indicated in Brinkgreve et al. (2006). Under these conditions, the Mohr-Coulomb soil around the stiff columns reduced to a Tresca soil. Cylindrical cavity expansion from zero-initial radius was modeled in PLAXIS 2D by applying a prescribed displacement a_o at the wall of a preexisting cavity with a radius of a_o such that the resulting final cavity radius was $2a_o$ as per Carter et al. (1979). Roller-type boundary conditions were prescribed at the upper and lower boundaries in such a way that allowed the soil to freely move in the direction of the prescribed displacement while remaining fixed in the perpendicular direction. Roller-type boundary conditions were also applied at the remaining lateral boundary. Additionally, closed-flow boundaries were prescribed in both the upper and lower boundaries as well as in the

preexisting cavity wall such that flow during reconsolidation was essentially one-dimensional, with the flow of water following a radial direction away from the stiff column. Even though no flow was expected at the vertical boundary away from the stiff column due to its distance to the prescribed displacement zone, this boundary was still assigned open-flow conditions. The finite element mesh of the models used 15-noded triangular elements and was refined at close proximity to the location of the prescribed displacement, and the mesh gradually became coarser with radial distance away from this boundary (Figure 4.12). Finally, to account for large deformations during application of the prescribed displacement a_o, the models were run with an *Updated Mesh* option enabled and calculations based on this option utilized an Updated Lagrangian Formulation (Bathe 1982) integrated in the finite element software.

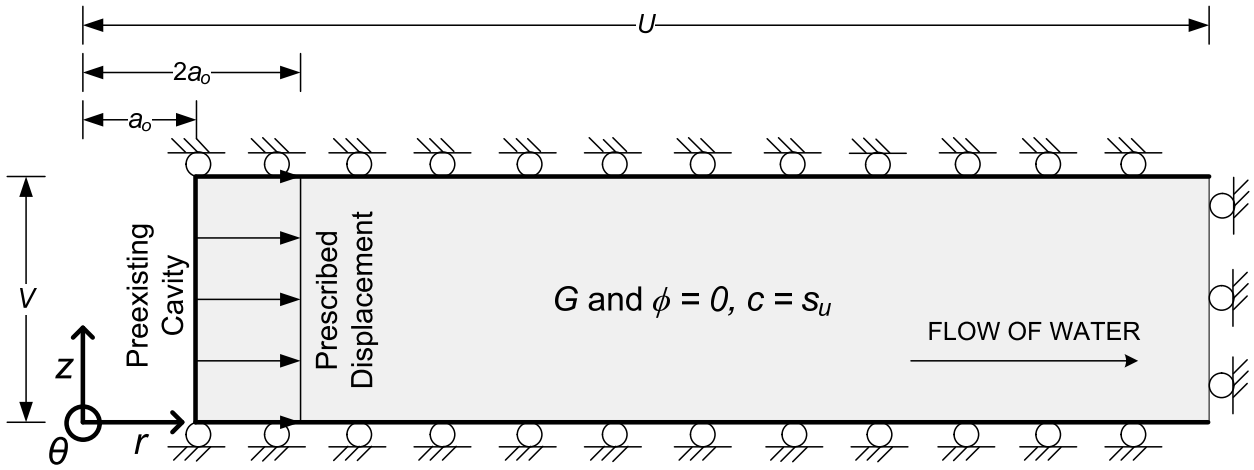

Fig. 4.11. Finite element model implemented in PLAXIS 2D.

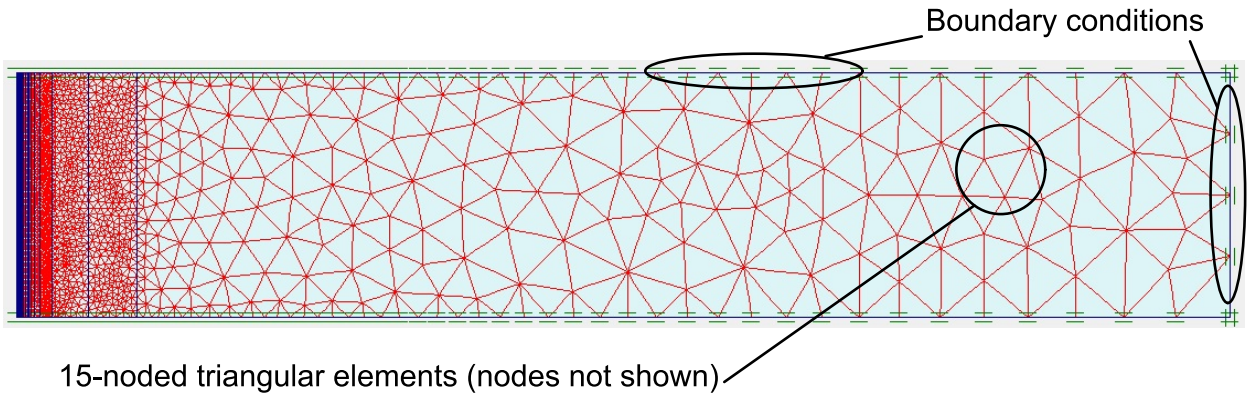

Fig. 4.12. Finite element mesh in PLAXIS 2D.

4.5.4 *Carter et al. (1979) Model Validation*

The Carter et al. (1979) model was first validated in PLAXIS 2D before it was used in subsequent numerical calculations. Figure 4.13 shows the excess pore-water pressure distributions for different times following the implementation of the Carter et al. (1979) model in PLAXIS 2D that simulated the installation of a stiff column. In the figure, T is the time factor used in one-dimensional consolidation theory and defined by Randolph and Wroth (1979) on the basis of elastic deformation of the soil during reconsolidation as following:

$$T = \frac{k}{\gamma_w m_v}\frac{t}{r_o^2} = \frac{k}{\gamma_w}\frac{2G(1-\nu')}{(1-2\nu')}\frac{t}{r_o^2} \tag{4.71}$$

Where G = shear modulus of soil, ν' = effective Poisson's ratio of soil, m_v = compressibility, γ_w = unit weight of water, k = permeability, r_o = stiff column radius and t = time of interest. In the previous expression, the compressibility of the soil m_v is expressed in terms of shear modulus G and effective Poisson's ratio ν' as per the elasticity condition prescribed. Elastic soil deformation during the run of consolidation-type stages is integrated internally in the finite element software.

In Figure 4.13, the finite element results obtained by implementing the Carter et al. (1979) model in PLAXIS 2D were compared to the finite element results presented in Carter et al. (1979) for an elastic-plastic soil with $G/s_u = 50$, $s_u/\sigma_v' = 0.33$ and an effective Poisson's ratio $\nu' = 0.30$. The excess pore-water pressure Δu distributions were normalized by the undrained shear strength s_u and the radial distance was normalized by the stiff column radius r_o. It can be seen that the initial radial distribution of excess pore-water pressures predicted by Eq. 4.69 agreed well with the PLAXIS 2D finite element results and with the Carter et al. (1979) finite element results for $T = 0$. For the remainder of normalized distributions shown, there was a very good agreement between the PLAXIS 2D finite element results and the Carter et al. (1979) finite element results.

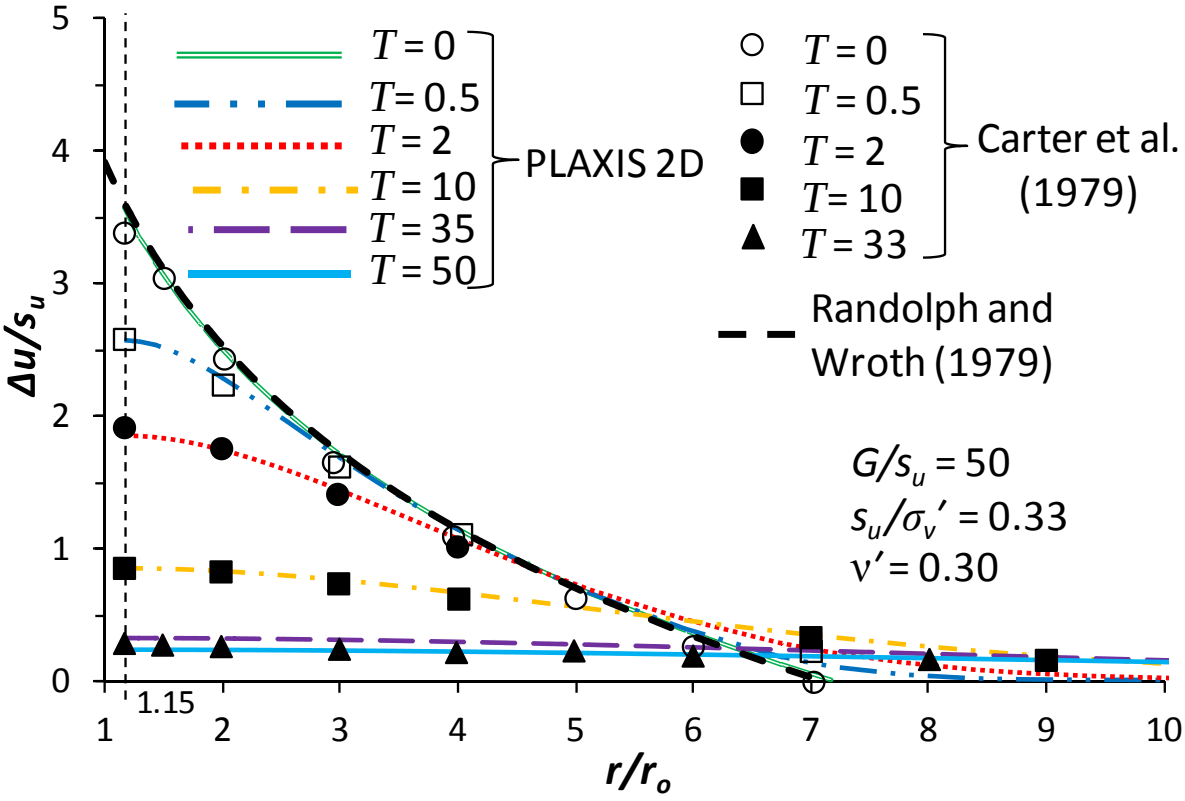

Fig. 4.13. Normalized excess pore-water pressure distribution with radial distance.

Figure 4.14 shows the dissipation of excess pore-water pressures at the stiff column wall (i.e. r/r_o = 1 obtained with extrapolation) with T immediately following installation of the stiff column. In this figure, the PLAXIS 2D finite element results were compared with results of Carter et al. (1979) in which the latter used a numerical-analytical solution proposed by Randolph and Wroth (1979). As observed, both sets of results agreed well for T greater than approximately 0.5, however, there was a small deviation in the results for T close to zero.

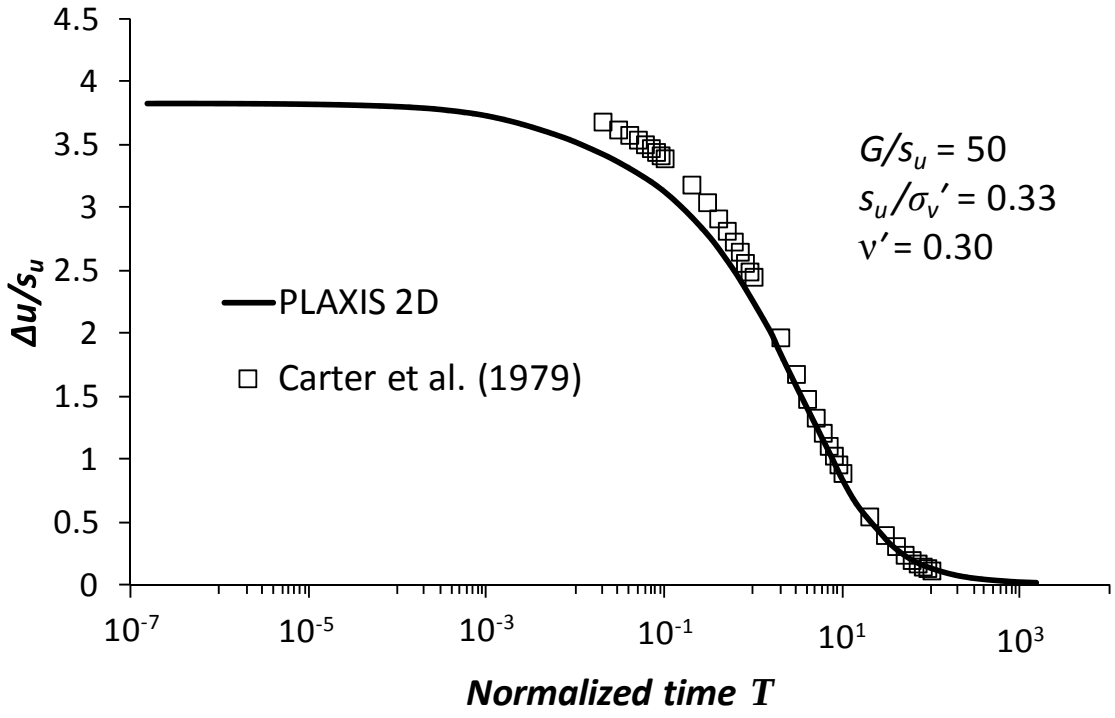

Fig. 4.14. Dissipation of normalized excess pore-water pressure at the stiff column wall.

It is expected for the effective stresses to increase with dissipation of excess pore-water pressures following the installation of the stiff column. This trend was confirmed by Carter et al. (1979) and by the PLAXIS 2D finite element results as observed in Figures 4.15 and 4.16. Figure 4.15 shows the horizontal effective stress distribution in the radial direction obtained from the

PLAXIS 2D finite element results expressed in terms of $K_{RD} = \sigma_r'/\sigma_v'$ for different times during reconsolidation. From Figure 4.15, immediately following the installation of the stiff column (T = 0), two zones were distinguished: a plastic zone in which K_{RD} remained nearly constant at a value of K_{RD} = 0.83 up to a normalized radial distance of r/r_o = 7 and an elastic zone in which K_{RD} decreased to $K_{RD} = K_o$ = 0.50 in the free field. The numerical distribution at T = 0 was compared with the theoretical distribution obtained by subtracting both the static pore-water pressure and the initial excess pore-water pressure distribution calculated with the Randolph and Wroth (1979) closed-form solution in Eq. 4.69, from the total horizontal stress distribution estimated from Eq. 4.68. As reconsolidation progressed and the plastic zone started to decrease in size, the K_{RD} values at the immediate vicinity of the stiff column wall increased while there was a slight decrease of K_{RD} close to the elastic-plastic boundary due to the outward radial progression of the excess pore-water pressure front during reconsolidation. In the final distribution when nearly full-reconsolidation was achieved (T = 155), K_{RD} gradually decreased with radial distance from a value of about twice the initial in-situ vertical effective stress to K_o conditions in the free field.

Assessment of the change in horizontal stress next to the installed stiff column was further examined when the variation of K_{RD} during reconsolidation was followed at the stiff column wall (r/r_o = 1). This can be seen in Figure 4.16. In this figure, the PLAXIS 2D results were compared to results from Carter et al. (1979). The increase of K_{RD} with time at the stiff column wall is evident. Similarly to Figure 4.14, the results agreed well for T greater than approximately 0.5, however there was a deviation of the results for K_{RD} values for T close to zero.

The results from the two-dimensional PLAXIS 2D analyses confirmed and validated the trends reported by Carter et al. (1979) in which the horizontal effective stress at the vicinity of a stiff column increased with time during reconsolidation. Such changes in effective stress are significant and, as a result, it became important to numerically capture these stress changes in the soft soil surrounding the stiff columns that were installed in the centrifuge models. In this sense, the increase in horizontal effective stress around an installed stiff column was expressed in terms of a K_{RD}-value radial distribution in the three-dimensional numerical analyses. Information on the K_{RD}-value radial distribution that was used in the three-dimensional numerical analyses will be presented later.

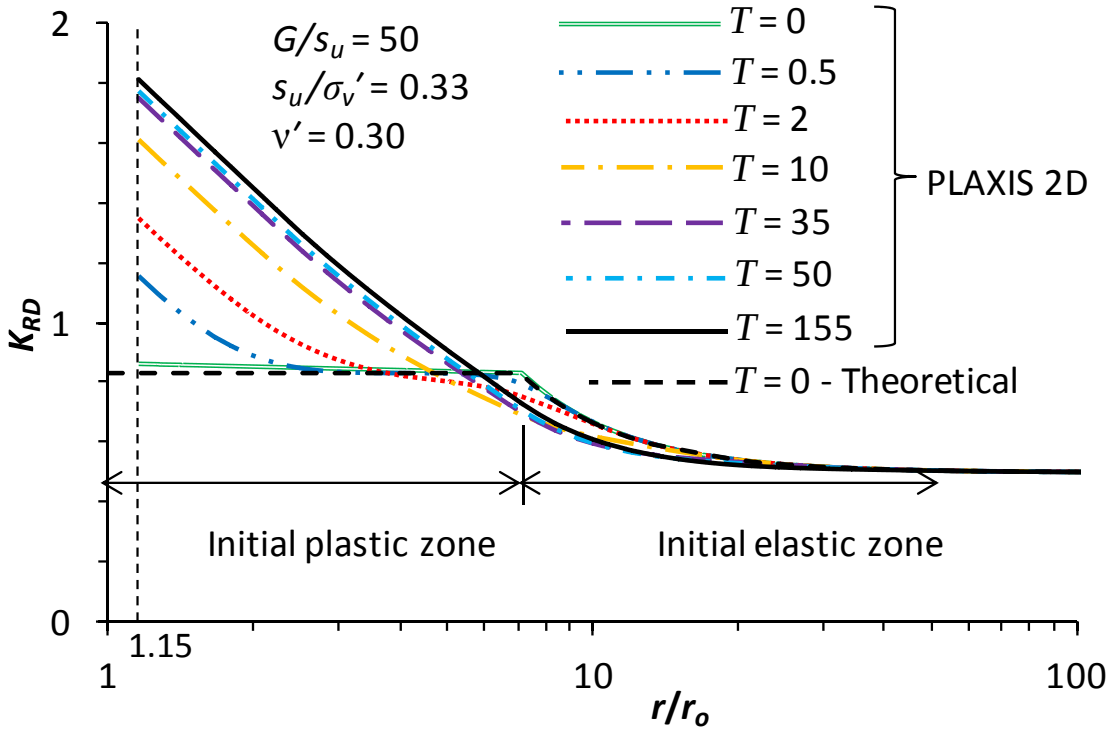

Fig. 4.15. Variation of K_{RD}-value radial distribution with time.

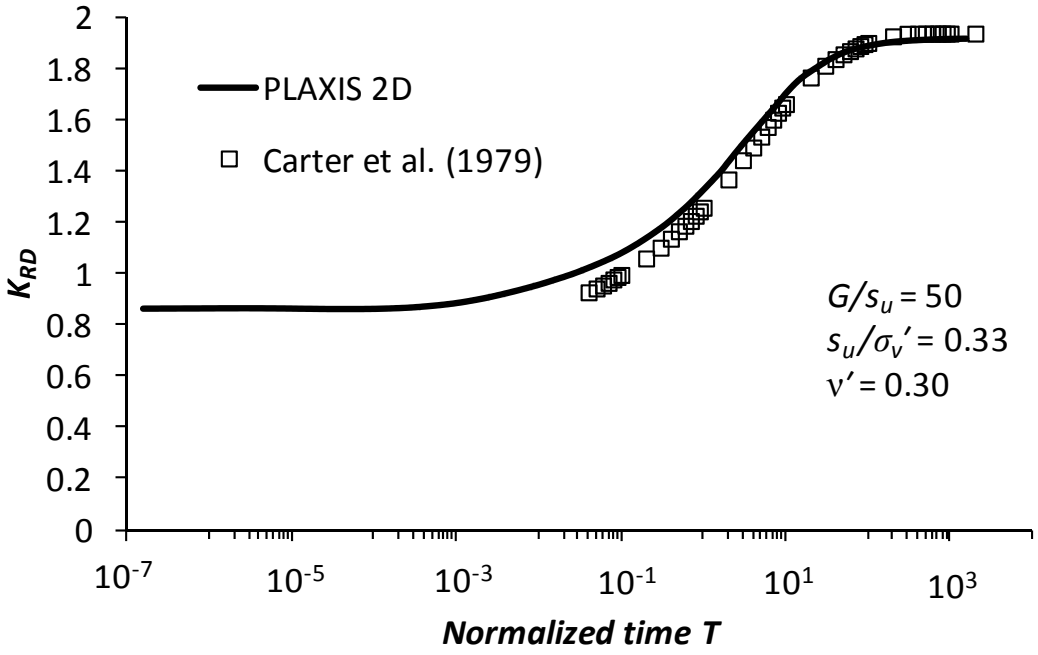

Fig. 4.16. Variation of K_{RD} value with time at the stiff column wall.

4.6 THREE-DIMENSIONAL FINITE ELEMENT ANALYSES

Three-dimensional finite element analyses were used to examine the results and trends observed in the centrifuge tests. The procedure used to construct and run the three-dimensional numerical models is presented. PLAXIS 3D was employed in the numerical calculations.

4.6.1 *Geometry*

Figure 4.17 shows a plan view and typical cross-section of the geometry of the numerical models constructed in PLAXIS 3D. The same geometry employed in the centrifuge tests was used in the numerical models. Four stiff columns in a two by two square layout were used with a center-to-center spacing of 1.20 m. The diameter of the columns was 0.32 m and the width of the square

footing was 2.40 m resulting in an area replacement ratio of 5.5%. The length of the stiff columns inside the clayey compressible soil was 7.50 m and an additional 0.50 m was used for embedment of the columns in the bearing layer thus producing a total column length of 8.00 m. Four numerical models were constructed and lateral load analyses were performed in PLAXIS 3D with LTP thicknesses of 0.45, 0.60, 0.70 and 1.20 m. To reduce computational time and to take advantage of the symmetry of the problem, only half of the full three-dimensional geometry was constructed in the software. The half-geometry implemented consisted of the upper left (UL) and upper right (UR) columns of the four-column layout. The modeled domain had a footprint of 20 m x 10 m, and this size was selected to reduce the influence of the boundaries of the model in the numerical results. Following the construction of the half-geometry, the mesh was generated. Figure 4.18 shows the final mesh used in the numerical calculations. The generated mesh had approximately 16000 elements and the mesh was refined locally near the footprint of the footing.

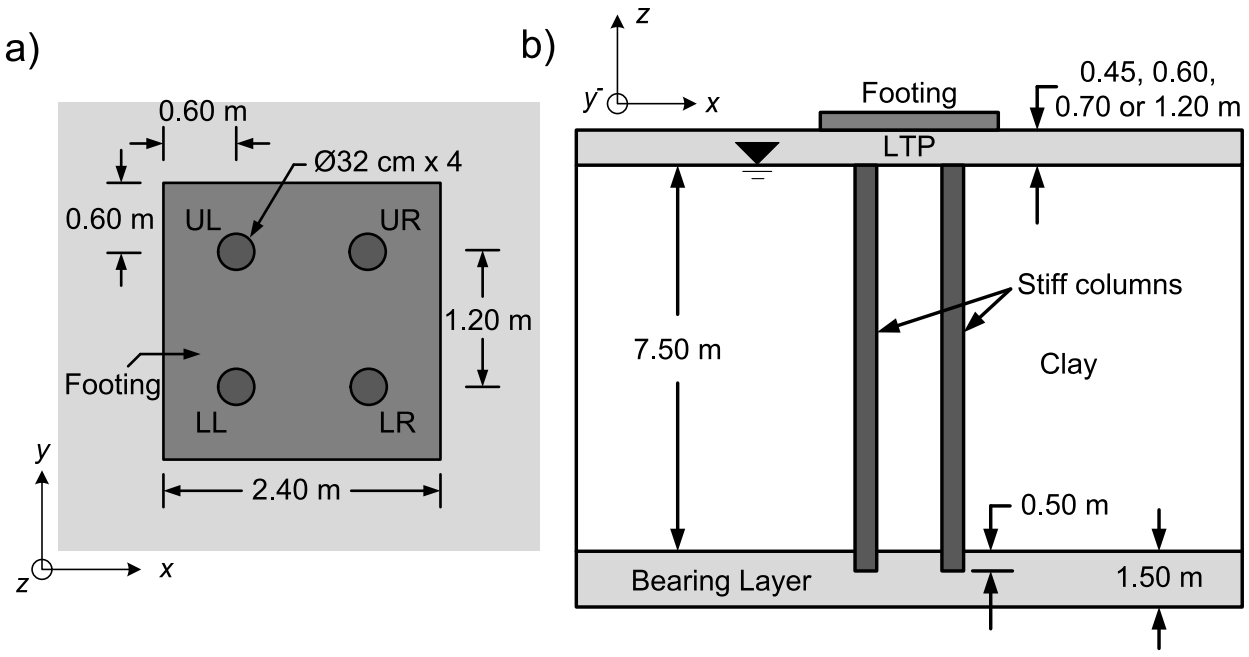

Fig. 4.17. Geometry examined in the numerical study, a) plan view above shallow foundation and b) cross-section. Not to scale.

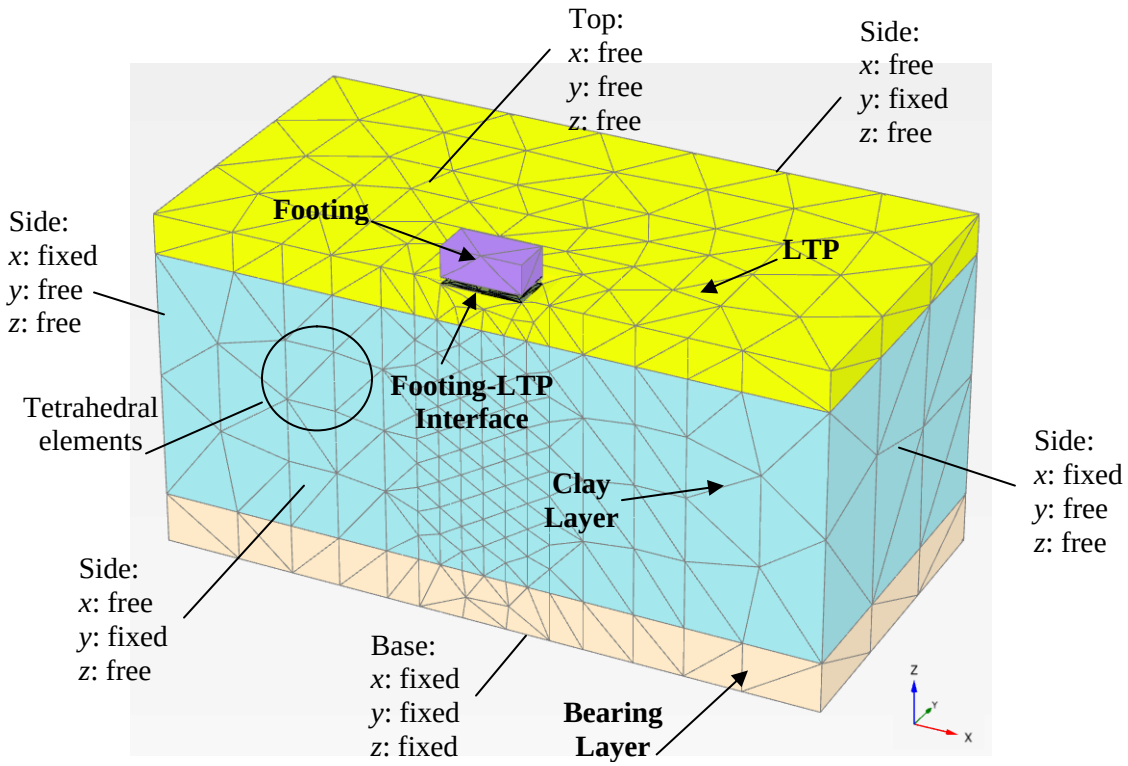

Fig. 4.18. Schematic of the finite element mesh with boundary conditions of the half-geometry used in the three-dimensional numerical analyses.

4.6.2 *Boundary Conditions*

Boundary conditions prescribed in the model included the fixities shown in Figure 4.18. Free translational movement was prescribed to the nodes of the tetrahedral elements located at the surface of the LTP, and roller fixities were prescribed at the sides of the shallow foundation in order to allow vertical movement of the foundation in the *z*-direction and avoid numerical instabilities. In regards to flow of water during consolidation, closed-flow boundary conditions were prescribed in both sets of *x*-*z* and *y*-*z* planes while open-flow boundary conditions were prescribed in the top and bottom *x*-*y* planes. This resulted in vertical flow of water during the various consolidation stages and improved numerical stability during calculations. In all cases, the water table was located at the top of the surface of the clay layer as shown in Figure 4.17b.

4.6.3 *Properties and Initial Conditions*

Table 4.5 summarizes the properties of the soil layers and structures of the stiff column-supported shallow foundations modeled in PLAXIS 3D. The properties shown are consistent with the materials used in the centrifuge tests. As mentioned earlier, drained behavior was specified for all the coarse-granular material in the system consisting of the LTP and the bearing layer. The linear elastic-perfectly plastic Mohr-Coulomb constitutive model was employed for all coarse-granular layers. The stiffness and strength properties of the coarse-granular layers were taken from previous numerical analyses performed by Popescu and Prevost (1993) with Nevada sand, the coarse-granular material used in the centrifuge test program. Undrained behavior was modeled using effective stress analyses. For this reason, effective shear strength parameters were specified for the low-permeability clayey soil in the system. The properties of the clayey material were estimated from a series of isotropically consolidated undrained triaxial compression tests (ICU-TC) and isotropic consolidation tests reported by Macari et al. (1987). Due to the applicability of the Soft Soil constitutive model being best suited for nearly normally consolidated soft soils, it was adopted to model the soft clayey material of the centrifuge models.

Table 4.5. Properties in PLAXIS 3D of the stiff column-supported shallow foundations tested in the centrifuge

Component	Constitutive Model	Drainage	Unit Weight (kN/m³)	E' (MPa)	ν'	G (MPa)	c' (kPa)	ϕ' (°)	ψ (°)	Tension cut-off (kPa)	R_{inter}	k (cm/s)	κ^*	λ^*
Clay Layer	SS	UN	14	-	-	-	2	20.2	0	0	-	10^{-7}	0.021	0.087
Bearing Layer	MC	DR	16	91	0.30	35	2	37	0	0	-	10^{-5}	-	-
LTP	MC	DR	16	91	0.30	35	2	33	0	0	-	10^{-5}	-	-
Columns	MC	NP	22.6	8100	0.20	3375	1500	0	0	600	-	-	-	-
Footing	LE	NP	27	69000	0.32	26136	-	-	-	-	-	-	-	-
Interface	MC	-	-	34.65	0.45	3.15	0.6	11	0	0	0.3	-	-	-

Note: SS = Soft Soil; MC = Mohr-Coulomb; LE = Linear Elastic; UN = Undrained; DR = Drained; NP = Non-Porous; E' = effective Young's modulus; ν' = effective Poisson's ratio; G = shear modulus; c' = effective cohesion; ϕ' = effective angle of internal friction; ψ = dilatancy angle; R_{inter} = strength reduction factor; k = permeability; κ^* = modified swelling index; λ^* = modified compression index.

The elastic properties of the shallow foundation used in the centrifuge tests were those of aluminum (Beer et al. 2006) which is the material the footing was made of. The strength of the stiff columns was estimated from the results of the centrifuge test in which only a vertical load was applied in a stiff column-supported shallow foundation. The stiffness of the columns was estimated using the modulus of elasticity E_c relationship (ACI 2011) that considers the stiffness of normal weight concrete as a function of the unconfined compressive strength f'_c in MPa:

$$E_c = 4700\sqrt{f'_c} \tag{4.72}$$

In the case of the interface and as described in previous sections, a strength reduction factor R_{inter} was specified to model the soil-structure interaction between the base of the footing and the surface of the LTP. A strength reduction factor of 0.30 was specified resulting in an interface friction angle of 11 degrees between the fine sand of the LTP, and the polished base of the footing. The LTP-footing interface friction angle is consistent with published values between fine sand and polished metal-type surfaces (U.S. Department of Navy 1982).

4.6.4 *K_{RD}-Value Radial Distribution*

Following the definition of all relevant model properties, the stiff column installation-induced stresses were specified around the stiff columns in each of the three-dimensional numerical models. As mentioned previously, the stiff column installation-induced stresses were expressed in terms of a K_{RD}-value radial distribution. The K_{RD}-value radial distribution was calculated using separate two-dimensional finite element analyses in PLAXIS 2D that implemented the Carter et al. (1979) procedure described in previous sections. After the K_{RD}-value radial distribution was estimated, it was later used as input in each of the three-dimensional numerical models. To

calculate the K_{RD}-value radial distribution, it was first necessary to estimate the G/s_u ratio and the undrained shear strength ratio s_u/σ_v' of the clayey soil of the centrifuge models. Using the plasticity index of the clayey soil used in the centrifuge tests (PI = 21%) and an overconsolidation ratio of 1, a ratio E_u/s_u = 750 or G/s_u = 250 was estimated using the relationship proposed by Duncan and Buchignani (1976). An average initial undrained shear strength ratio of approximately 0.285 was estimated from the undrained shear strength T-bar measurements of the centrifuge tests (Figure 4.19), without consideration of the lateral load test with a LTP thickness of 0.70 m. Figure 4.20 shows the K_{RD}-value radial distribution that was calculated in PLAXIS 2D, and employed in the three-dimensional numerical analyses in PLAXIS 3D.

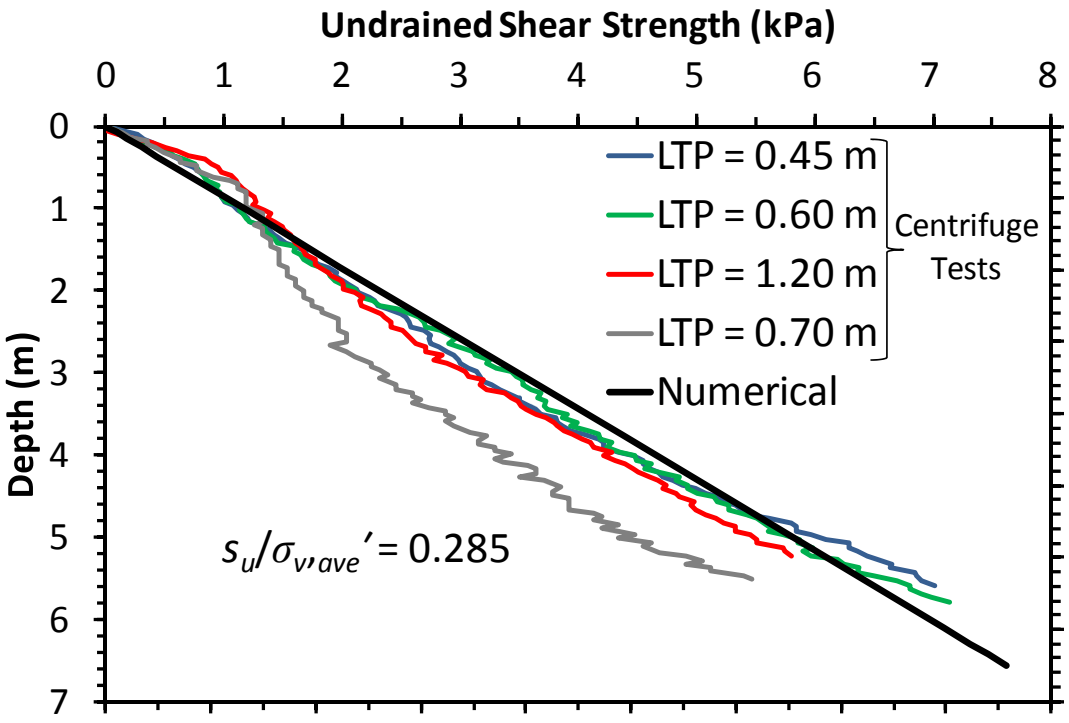

Fig. 4.19. Initial undrained shear strength profile – Comparison of experimental measurements with the numerical approximation.

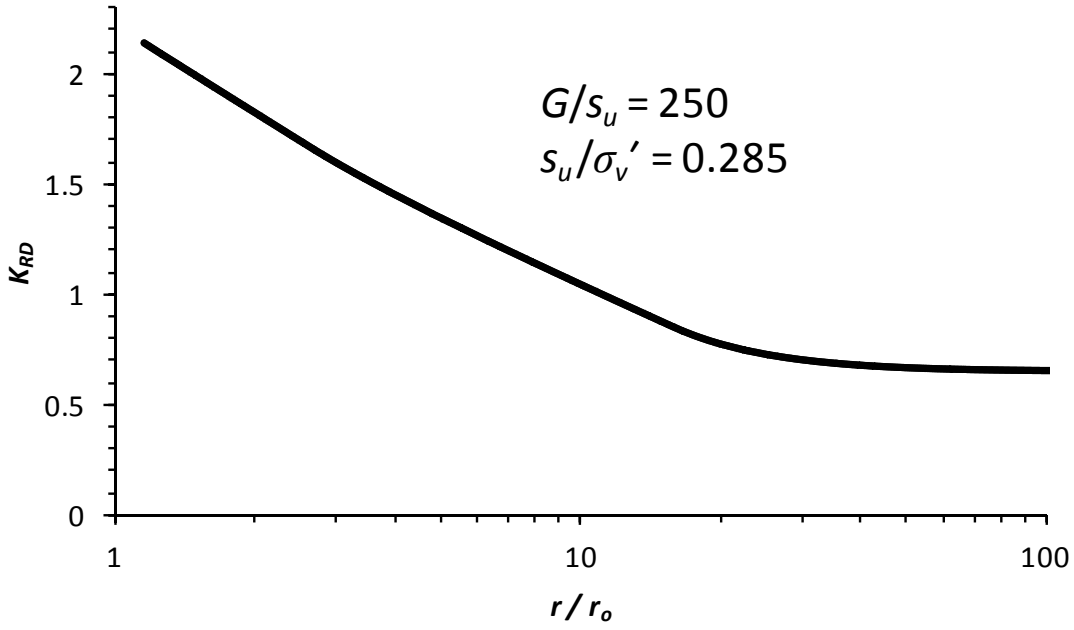

Fig. 4.20. K_{RD}-value radial distribution employed in the PLAXIS 3D models.

4.6.5 *Modeling Stage Construction*

Numerical calculations were performed through a series of sequential stages that simulated the construction procedure of the stiff column-supported shallow foundations in the centrifuge test program. All numerical stages were run with the Updated Mesh option enabled in order to allow for large deformations in the system. The first stage consisted in defining the initial conditions in the model, which included establishing the initial geostatic stress distribution in the system, initial undrained shear strength profile, static pore-water pressure distribution, and the aforementioned changes in horizontal effective stress in the soft soil due to the installation of the stiff columns. An assumption was made in the first stage that the stiff columns were already installed in the soft soil. The next stage was the undrained placement of the LTP and footing, followed by a consolidation stage in which the excess pore-water pressures were left to dissipate

under the combined LTP and footing surcharge. In the next stage, a point load was applied to the footing to produce a total vertical load (including self-weight of the footing) of 310 kN in the half-model and 620 kN in the full-model, resulting in a bearing pressure of 108 kPa. The total vertical load applied to the footing of the numerical models corresponded to the vertical load applied to the footing of the centrifuge tests. Further dissipation of excess pore-water pressures was allowed under the additional vertical load. The final stage consisted of applying the horizontal load to the footing under undrained conditions. This was achieved by applying a surface prescribed displacement at the side of the footing in order to model the lateral displacement the footing experienced in the centrifuge tests and to capture the lateral load response of the system. The lateral displacement of the footing was directed towards the negative *x*-axis (Figures 4.17 or 4.18). Boundary conditions around the footing were accordingly modified in order to allow full horizontal displacement of the footing during this time.

4.7 RESULTS

4.7.1 *Lateral Load-Displacement Behavior*

Figure 4.21 shows the lateral load-displacement responses of the four lateral load tests that were implemented and run in the finite element software PLAXIS 3D. The numerical lateral load-displacement responses, presented as colored curves in the figure, are compared to their corresponding experimental counterparts, presented as black curves in the figure. To remain consistent, yield or failure for each numerical lateral load-displacement response was defined using a work criterion in which the accumulated area beneath the curve (i.e. the work done) was plotted against the lateral load measured, in a similar fashion to the centrifuge test results. This resulted in a curve with two distinct sections, in which two lines were fitted and their intersection corresponded to the yield load of each curve. The details of identifying the yield load in the numerical lateral load-displacement curves using the work principles are also presented in the Appendix at the end of the dissertation. Based on this procedure, the yield load for each numerical model was identified. The yield load for each numerical model was plotted against its corresponding LTP thickness in Figure 4.22 and a linear fit was added to the numerical data. For comparison purposes, the linear fit of the experimental data was also included. The numerical results presented in the figures confirm several of the experimental trends previously observed and reported: 1) The pre-yield lateral load-displacement response became stiffer with increasing LTP thickness, 2) Less softening was observed in the post-yield lateral load-displacement response with increasing LTP thickness and 3) The lateral capacity of the system increased with increasing LTP thickness. Although there was scatter in the numerical data in Figure 4.22, the results nonetheless confirmed the increasing trend in lateral capacity with increasing LTP

thickness. The numerical results underscore the importance of the LTP thickness in controlling the lateral response and the lateral capacity of stiff column-supported shallow foundations.

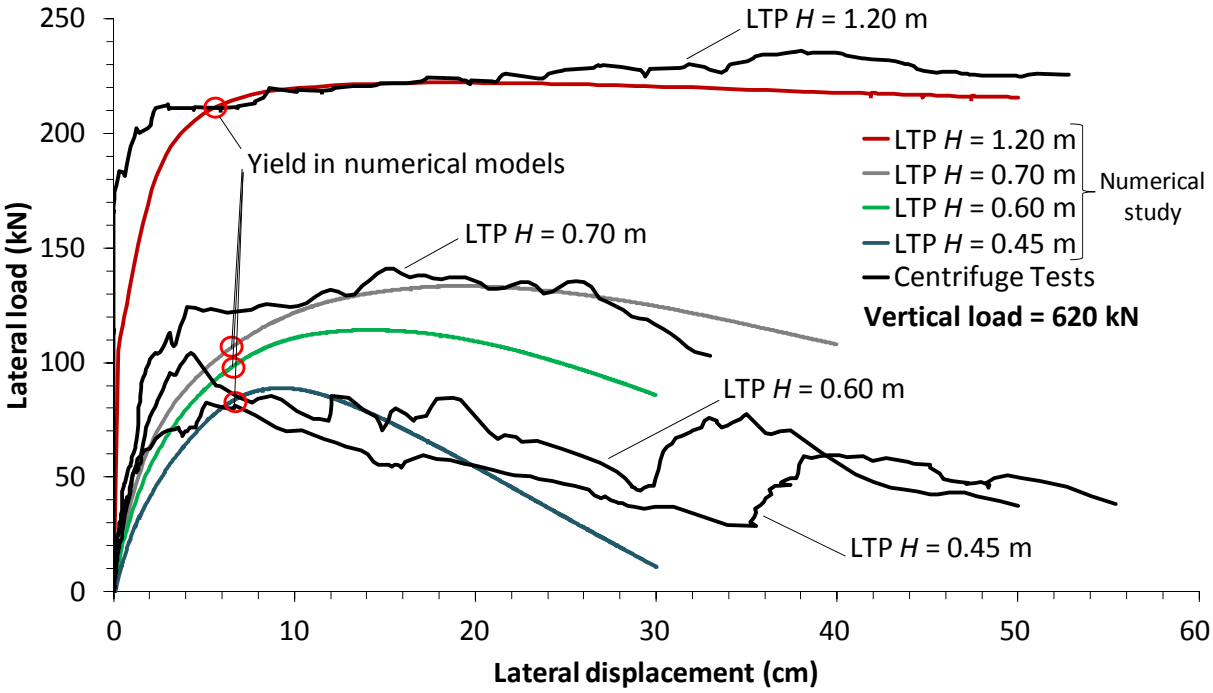

Fig. 4.21. Lateral load-displacement behavior of the lateral load tests with different LTP thicknesses H – Comparison of numerical and experimental results.

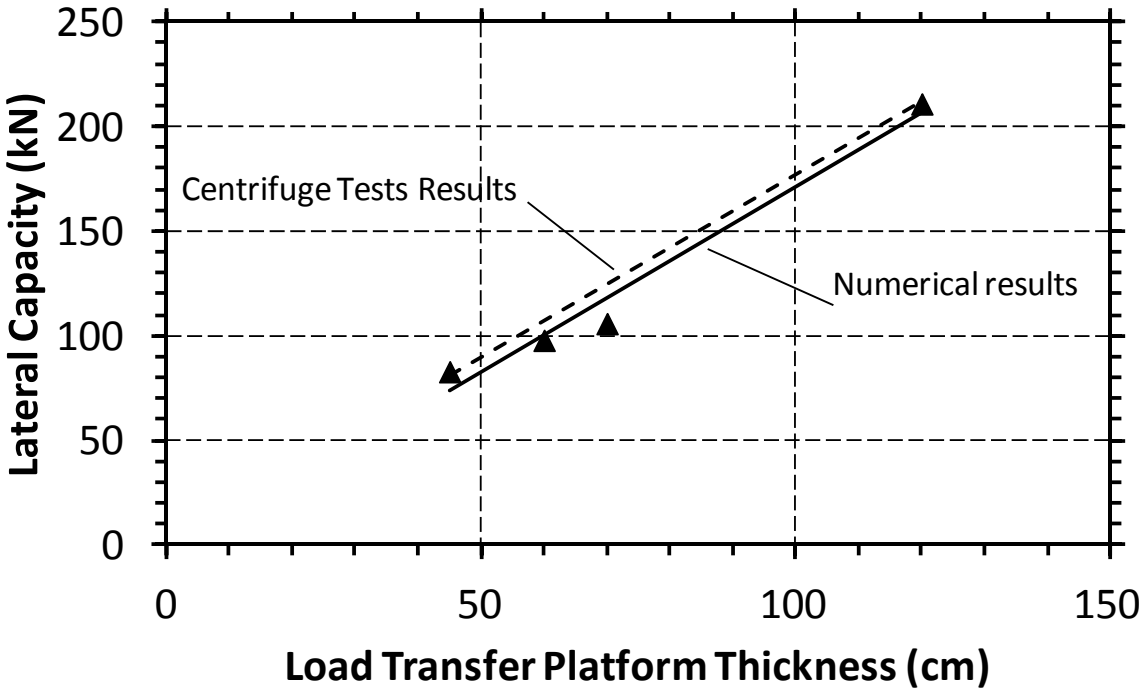

Fig. 4.22. Influence of the LTP thickness in the lateral capacity of the stiff column-supported shallow foundation – Comparison of numerical and experimental results.

4.7.2 *Lateral Deformation of the Stiff Columns*

Figure 4.23 shows the lateral displacement distributions of the upper left stiff column at yield, after the shallow foundation was laterally loaded in the numerical models. The direction of the distributions is parallel to the direction of the laterally loaded footing, or the *x*-axis as shown in the included legend. By symmetry, the lateral displacement distributions in the figure also applied to the lower left column. Figure 4.24 shows the lateral displacement distributions of the upper left stiff column, but in direction perpendicular to the direction of the laterally loaded footing, or the *y*-axis. In a similar fashion, Figures 4.25 and 4.26 show the lateral displacement distributions of the upper right column in the *x*- and *y*-directions, respectively.

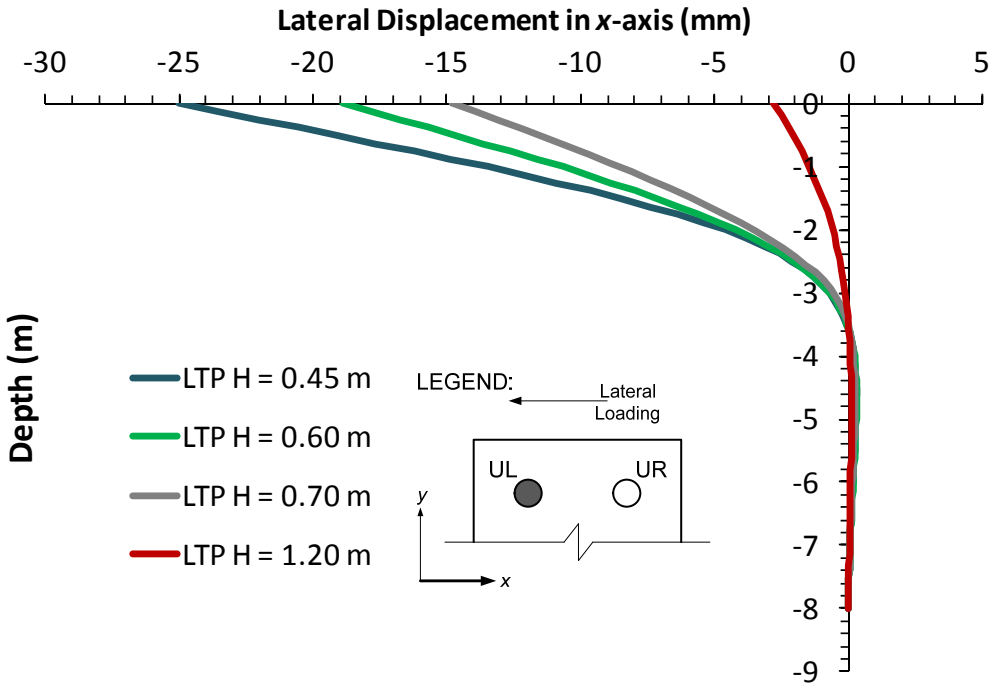

Fig. 4.23. Distribution of the lateral displacements in the *x*-direction of the upper left column.

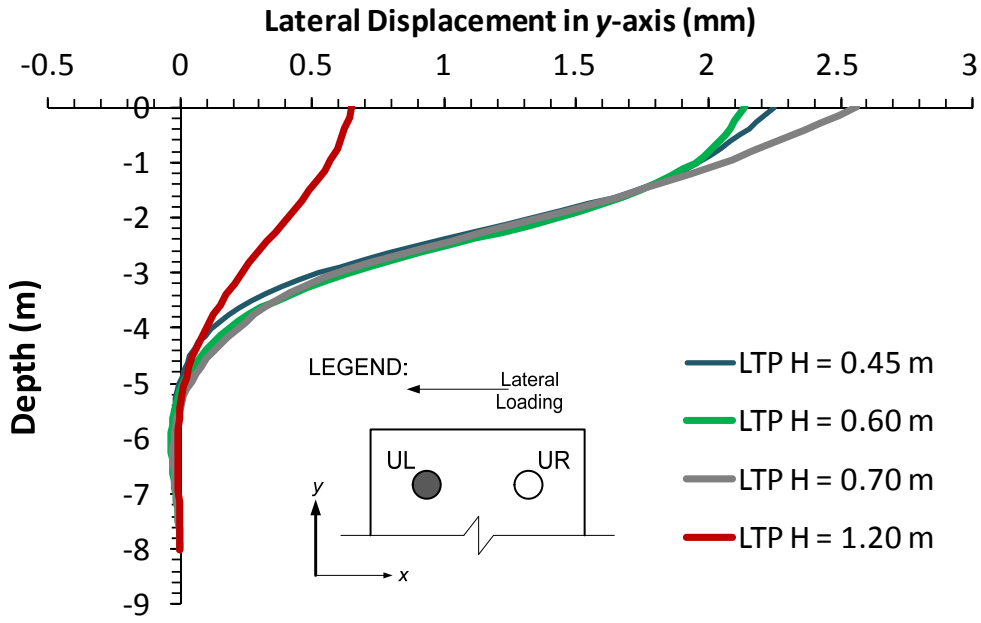

Fig. 4.24. Distribution of the lateral displacements in the *y*-direction of the upper left column.

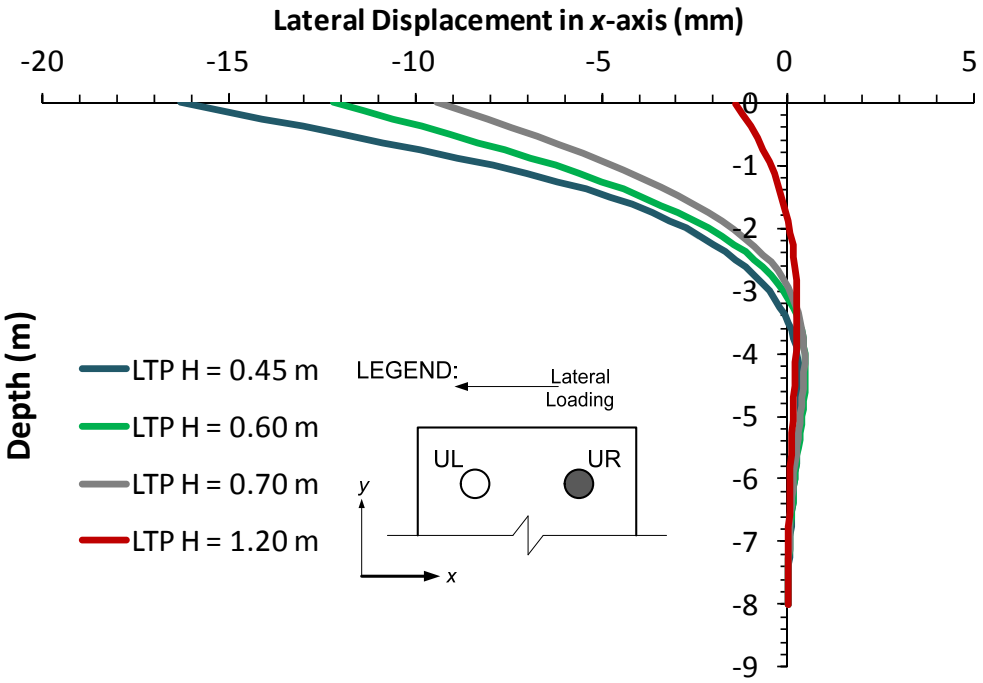

Fig. 4.25. Distribution of the lateral displacements in the *x*-direction of the upper right column.

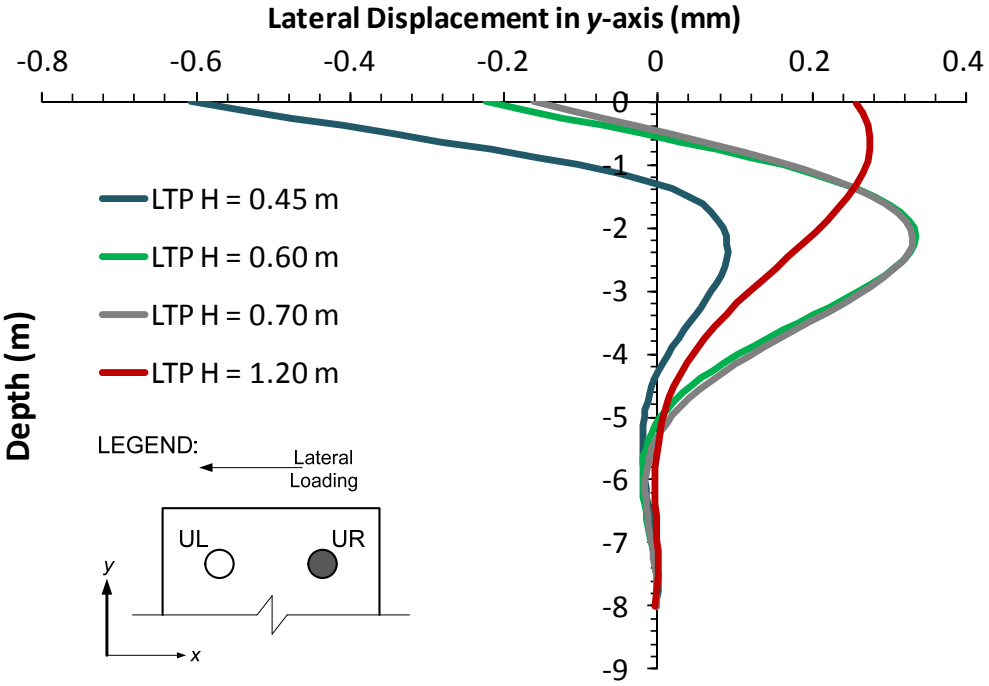

Fig. 4.26. Distribution of the lateral displacements in the *y*-direction of the upper right column.

Several trends were gathered from the previous results. Larger lateral deformations were calculated in the *x*-direction than in the *y*-direction, suggesting a heavier concentration of lateral deformations in the former direction compared to the latter as expected. The lateral deformations experienced at the top of each stiff column in the *x*-direction, decreased with increasing LTP thickness. On the other hand, the magnitudes of lateral deformation at the top of the stiff columns in the *y*-direction were considerably lower to those of the *x*-direction. Lateral deformations at the top of the left column in the *y*-direction ranged from approximately 8.5% of those of the *x*-direction, in the case of a LTP with a thickness of 0.45 m, up to 20% for a LTP with a thickness of 1.20 m. In the right column, this range varied from approximately 4% in a LTP with a thickness of 0.45 m, up to 20% in a LTP with a thickness of 1.20 m. These trends highlight the importance of the thickness of the LTP in controlling the lateral deformation response of the stiff columns under horizontal load.

4.7.3 *Load Distribution in the Stiff Columns*

The shear, bending moment, and axial load distributions of the stiff columns were tabulated from the numerical results. Figures 4.27 and 4.28 show, respectively, the parallel (*x*-direction) and perpendicular (*y*-direction) distributions of shear in the upper left column, at yield, for each of the lateral load tests examined in the numerical study. Figures 4.29 and 4.30 show the distributions of bending moment in the upper left column for both directions examined. Figure 4.31 shows the axial load distribution in this column. Figures 4.32 through 4.35 show the shear and bending moment distributions in the upper right column, in both directions considered. Figure 4.36 shows the axial load distribution in the upper right column. Similar to the trends observed in the lateral deformations, the distributions of shear and bending moment in the stiff

columns were heavily concentrated in the *x*-direction. It was also observed that the maximum bending moment and maximum shear that developed in the stiff columns in the *x*-direction, increased as the thickness of the LTP decreased. A similar trend was observed when examining the axial load distribution in the left column, where the maximum axial load increased with decreasing LTP thickness although the axial load distribution in the right column did not follow this trend. These trends further reinforce the importance of the LTP thickness in controlling the load transferred to the soil-column composite and ultimately influencing the distribution of shear, bending moments, and axial load in the stiff columns.

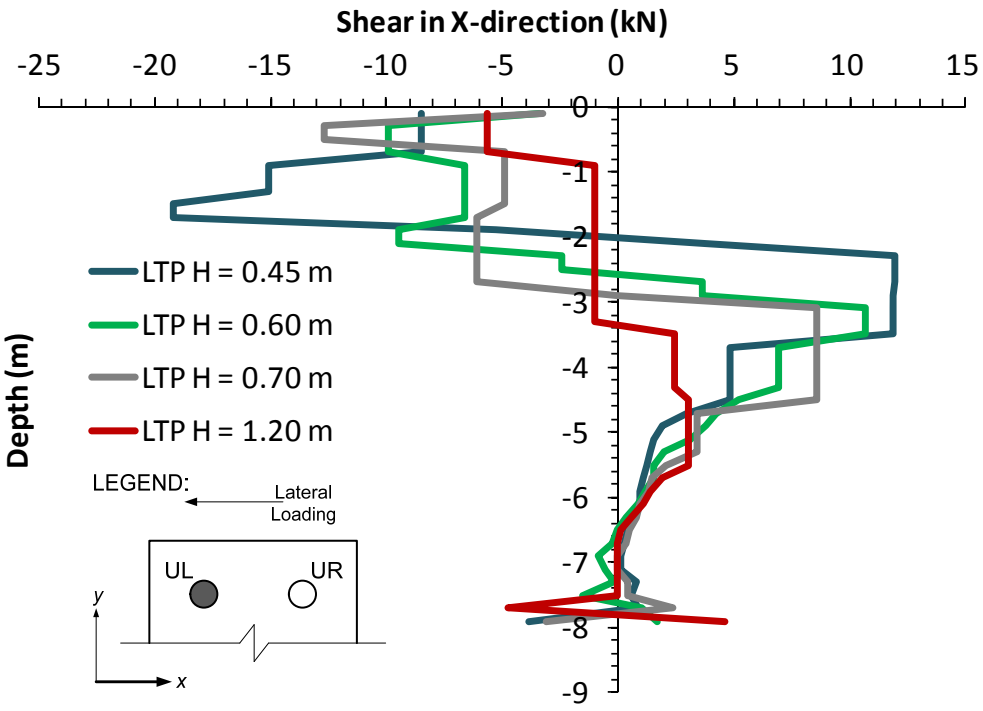

Fig. 4.27. Distribution of the shear in the *x*-direction of the upper left column.

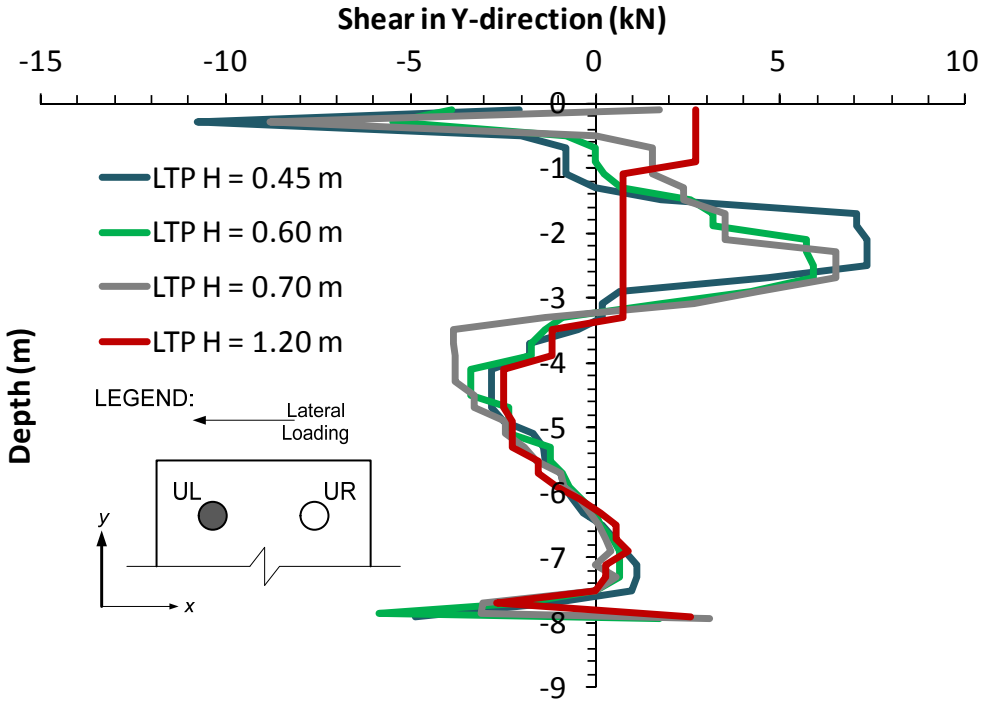

Fig. 4.28. Distribution of the shear in the *y*-direction of the upper left column.

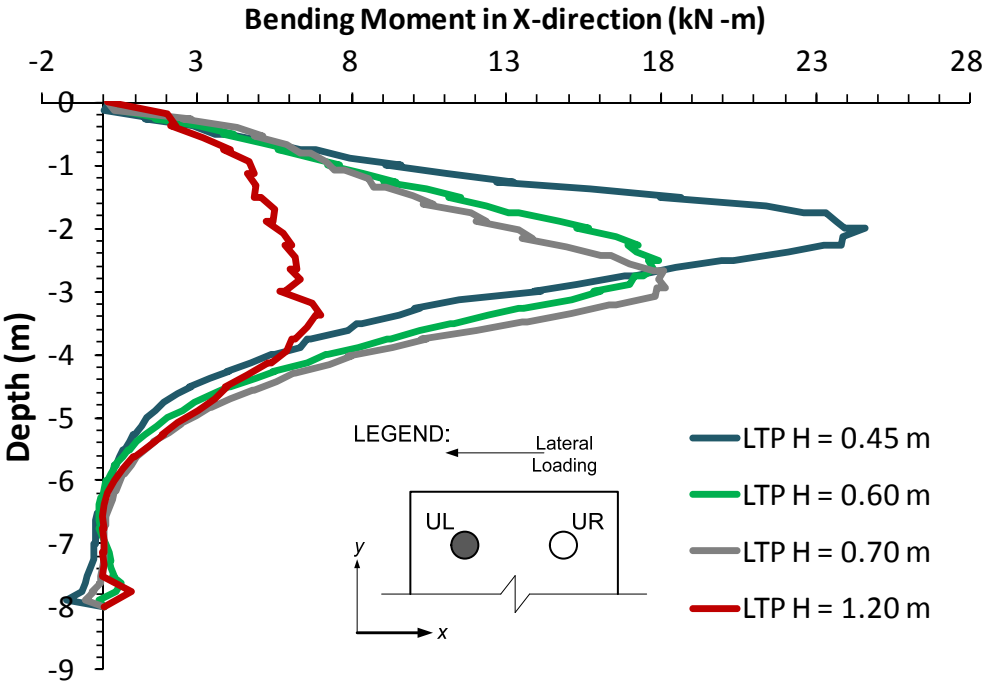

Fig. 4.29. Distribution of the bending moment in the *x*-direction of the upper left column.

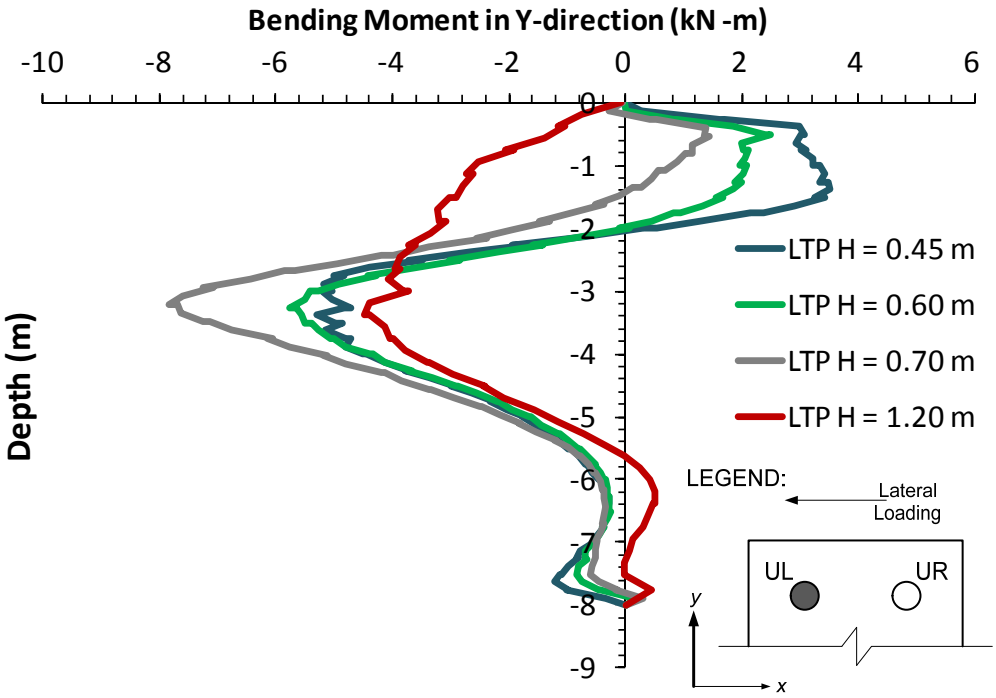

Fig. 4.30. Distribution of the bending moment in the *y*-direction of the upper left column.

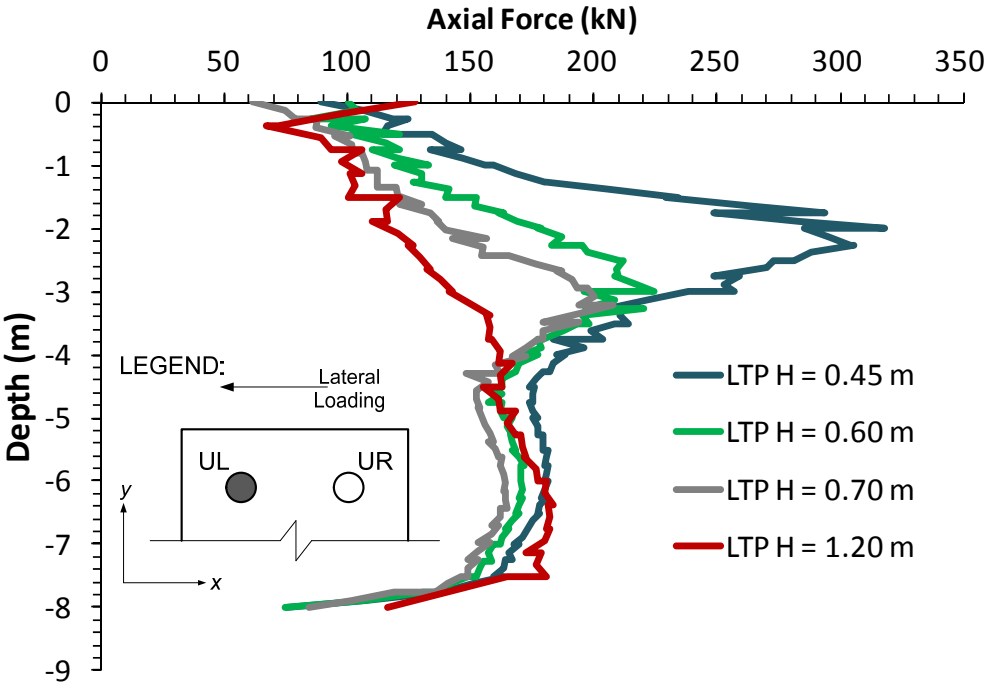

Fig. 4.31. Distribution of the axial load of the upper left column.

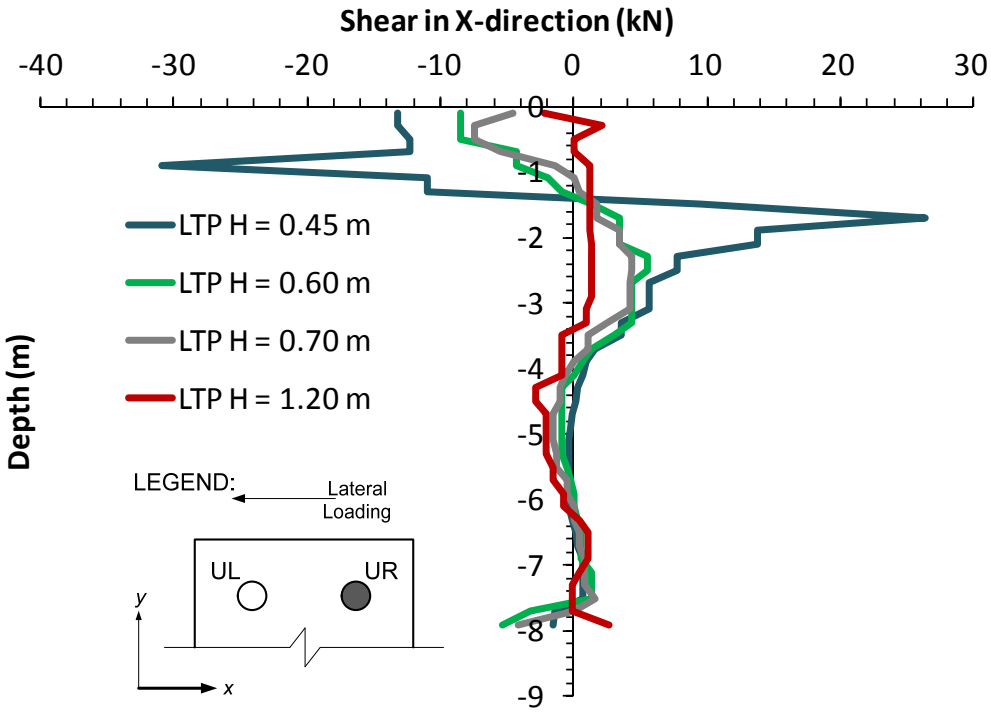

Fig. 4.32. Distribution of the shear in the *x*-direction of the upper right column.

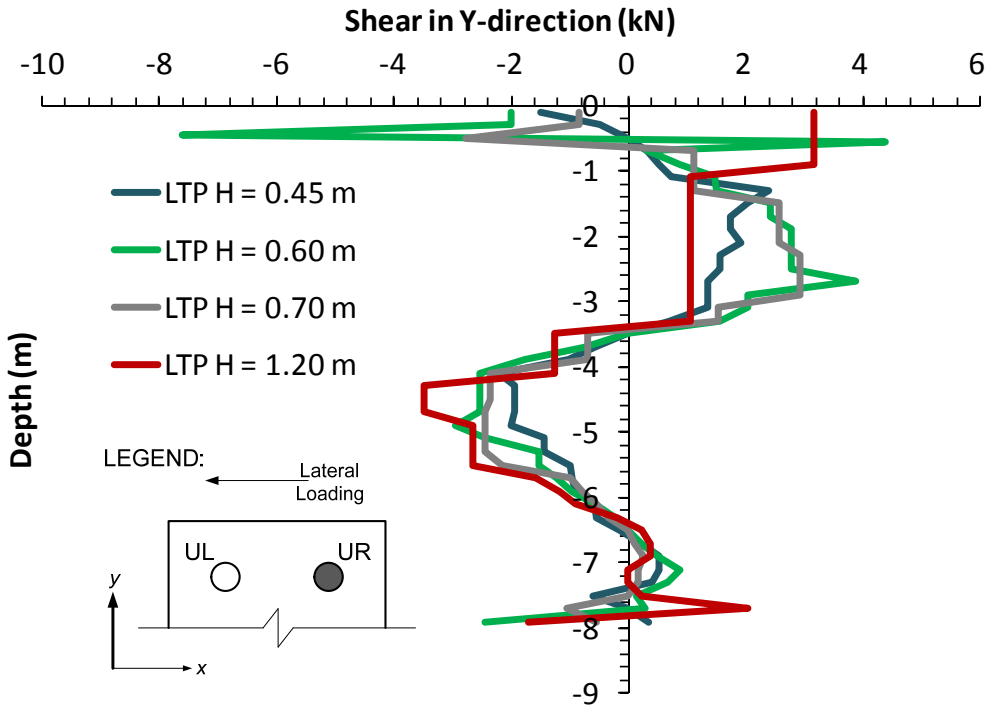

Fig. 4.33. Distribution of the shear in the *y*-direction of the upper right column.

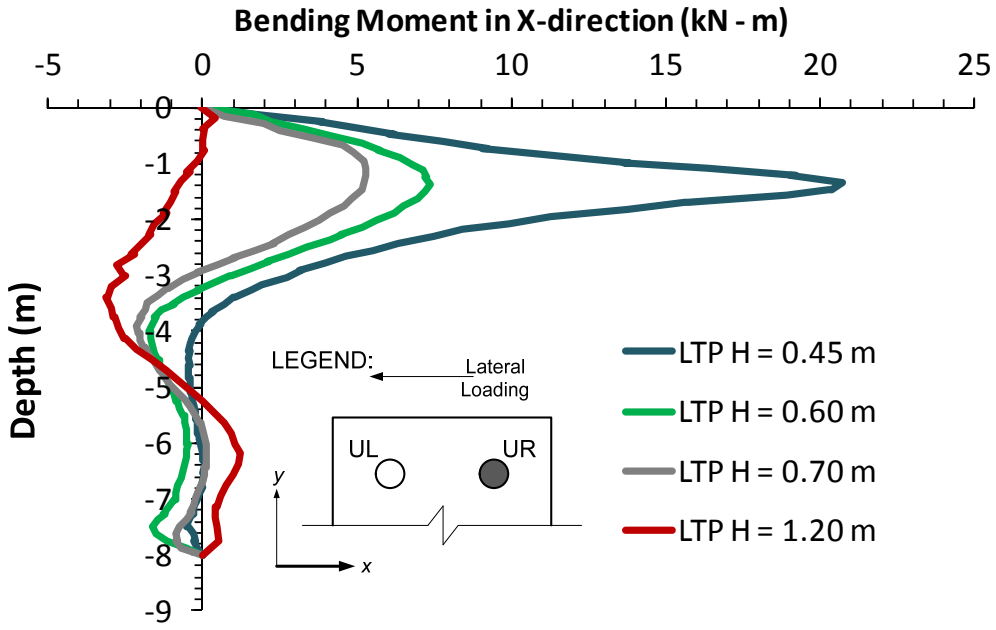

Fig. 4.34. Distribution of the bending moment in the *x*-direction of the upper right column.

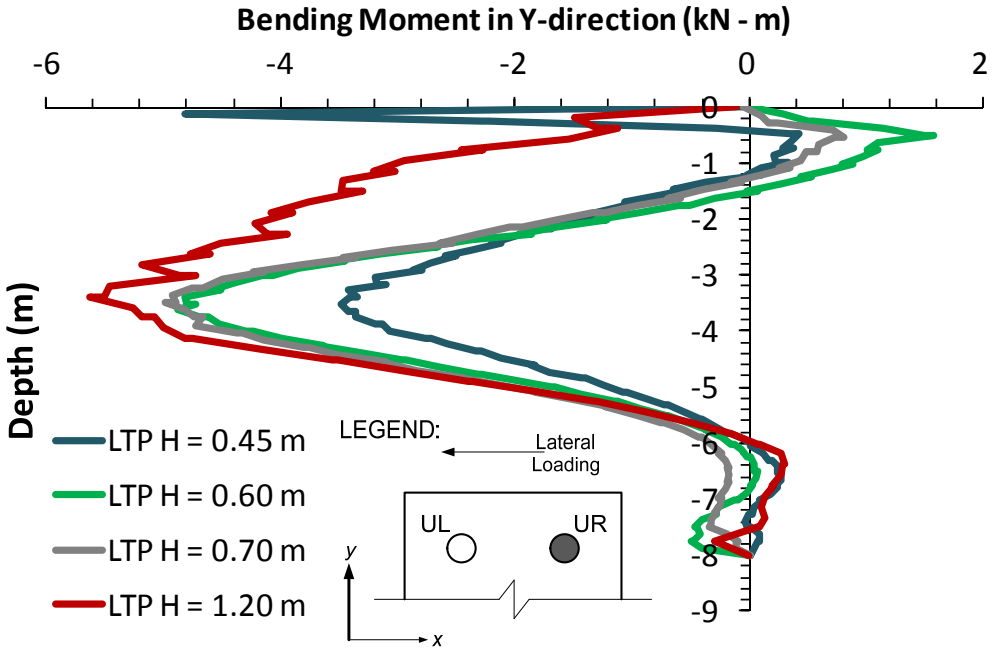

Fig. 4.35. Distribution of the bending moment in the *y*-direction of the upper right column.

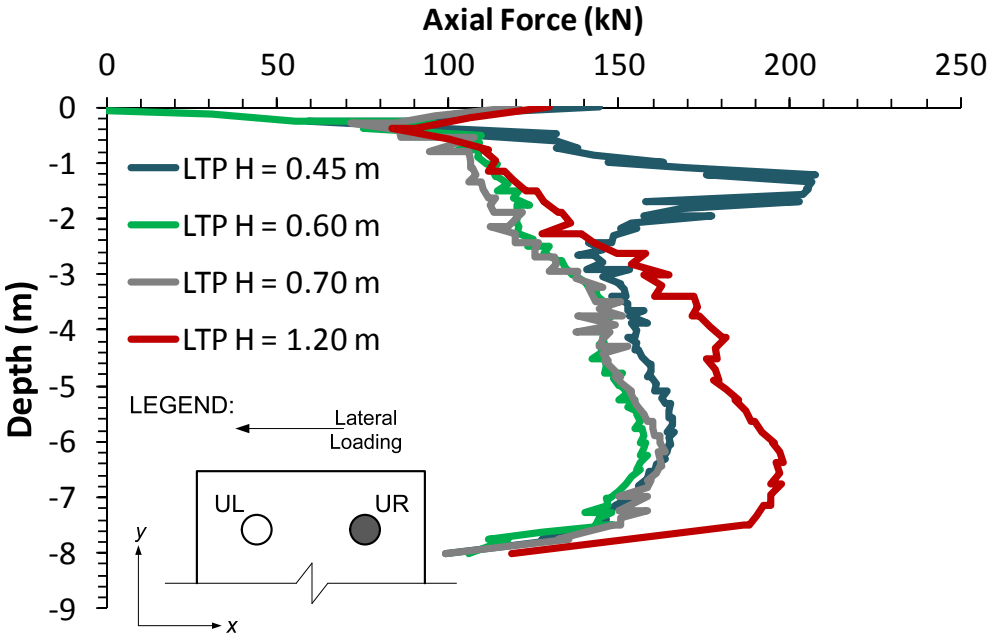

Fig. 4.36. Distribution of the axial load of the upper right column.

The results further showed that the maximum bending moment and axial load of the left column developed, with the exception of the model with a LTP thickness of 1.20 m, at depths between 2.2 m to 2.6 m, with an average depth of 2.40 m. The average calculated depth was close in magnitude to the failed length of 1/3 of the stiff column length in the soft clay, a trend reported in the results from the centrifuge tests. In the case of the distribution of bending moments in the right column, and with the exception of the model with a LTP thickness of 1.20 m, the maximum bending moment developed at an average depth of 1.5 m which, as opposed to the trends observed in the centrifuge tests, corresponded to a failed length of around 20% of the stiff column length in the soft clay. In the case of the numerical model with a LTP thickness of 1.20 m, the maximum bending moment in the left column was observed at a depth of approximately

3.50 m or 47% of the stiff column length in the soft clay, and the axial load in this same column gradually increased with depth until a maximum axial load was observed at a depth of around 6.50 m or 87% of the stiff column length in the soft clay. The right column in the model with a LTP thickness of 1.20 m also experienced an increase of axial load with depth and, in a similar fashion to its left counterpart, the maximum axial load was observed at a depth of approximately 6.50 m. On the other hand, the maximum bending moment of the right column in the test with a LTP thickness of 1.20 m was observed at a depth of around 3.20 m (or 43% of the stiff column length in the soft clay) and as opposed to the maximum bending moment observed in the left column, the maximum bending moment that developed in the right column was negative rather than positive. It is worth clarifying that a maximum positive bending moment was observed at a depth of approximately 6.20 m in the right column of the test with a LTP thickness of 1.20 m (or 83% of the stiff column length in the soft clay), but its magnitude was lower compared to the magnitude of the maximum negative bending moment calculated in this same column. In general, the discrepancies between the numerical and experimental results previously highlighted underscore the complicated nature of the failure modes experienced by the stiff columns when used for the support of shallow foundations subjected to horizontal load.

Finally, to show the evolution of the load in the stiff columns when the footing was laterally loaded, Figures 4.37 and 4.38 show the change in maximum bending moment as a function of the mobilized lateral load and LTP thickness for both the left and right columns, respectively, in the *x*-direction. From these results, a LTP thickness of 0.45 m produced the greatest changes in maximum bending moment (approximately 21 kN-m in the left column and 20 kN-m in the right column) with mobilized lateral load, while a LTP thickness of 1.20 m produced the smallest

changes in maximum bending moment (approximately 1 kN-m in both stiff columns). These trends further highlight the importance of the LTP thickness in controlling the load induced in the stiff columns.

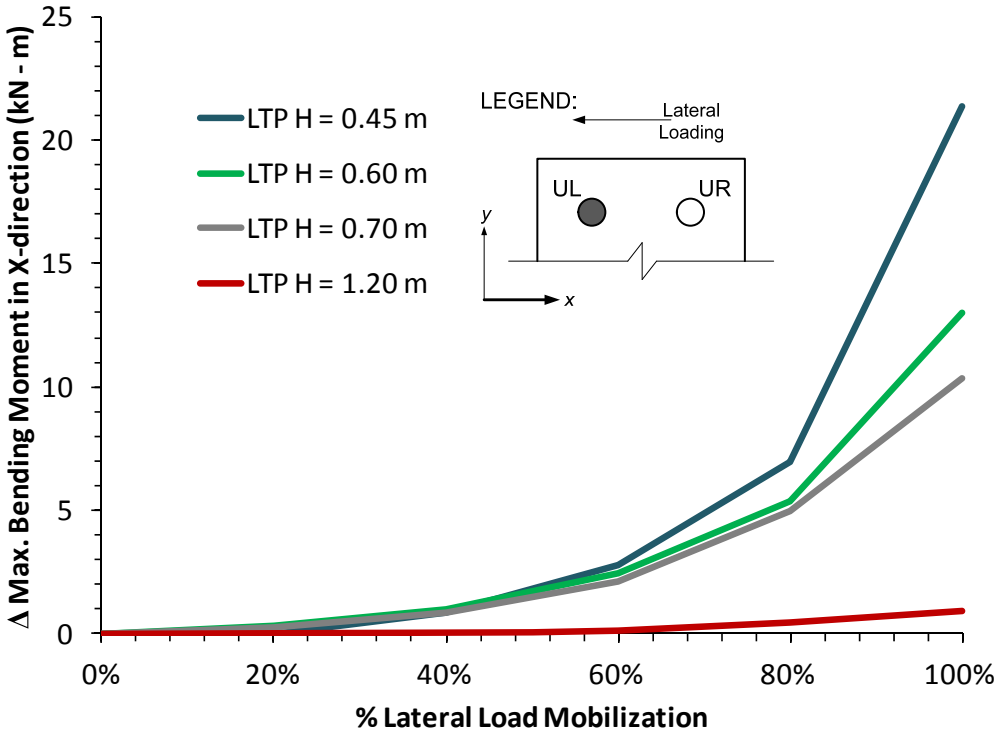

Fig. 4.37. Change in the maximum bending moment in the *x*-direction with lateral load mobilization of the upper left column.

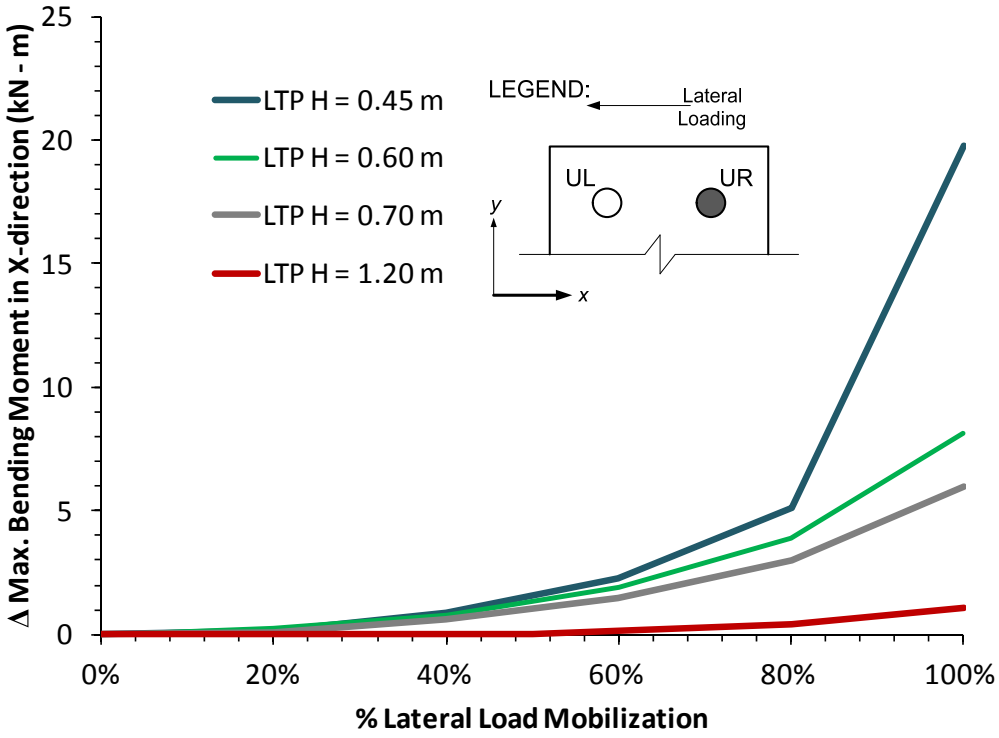

Fig. 4.38. Change in the maximum bending moment in the *x*-direction with lateral load mobilization of the upper right column.

4.8 CONCLUSIONS

In this chapter, numerical results were compared to the experimental results from the centrifuge test program. The numerical results indicated that the thickness of the LTP controlled the lateral capacity of the stiff column-supported shallow foundation. An increase in the lateral capacity of the stiff column-supported shallow foundation was observed with an increase in the thickness of the LTP. The thickness of the LTP also controlled the pre-yield and post-yield lateral load-displacement responses. The pre-yield response became stiffer with increasing LTP thickness and the post-yield response transitioned from a soft response to a hardening response with

increasing LTP thickness. The numerical results confirmed the experimental trends gathered from the centrifuge test program.

The numerical results showed that the load induced in the stiff columns, and the lateral deformations experienced by these rigid vertical elements were also controlled by the thickness of the LTP. While the loading in the stiff columns, and their lateral deformations, were observed in directions parallel and perpendicular to the direction of the laterally loaded shallow foundation, the magnitudes of load and lateral deformations were larger in the former direction compared to the latter direction. The numerical results also showed that overall and with few exceptions, the load and the lateral deformations experienced by stiff columns tended to decrease with increasing LTP thickness. The combination of maximum bending moment and axial load calculated in the left column resulted in a range of depths that similarly matched the location of the failure surface observed in the stiff columns of the centrifuge test program. However, the range of depths calculated in the right column resulted in depths that differed from the findings observed in the centrifuge test program. Moreover, in the model with a LTP thickness of 1.20 m, the range of depths that corresponded to the location of the maximum loading conditions induced in the stiff columns also differed from the experimental findings, underscoring the complicated nature of the failure mechanisms experienced by the rigid vertical elements after the stiff column-supported shallow foundation was laterally loaded.

CHAPTER 5: PARAMETRIC ANALYSIS

5.1 INTRODUCTION

This chapter presents the results of a parametric numerical study that investigated the effects of different variables in the lateral response of a stiff column-supported shallow foundation. Different geometry-based and material-based variables were investigated. The procedure used to estimate the parametric variation of the geometry-based and material-based variables is presented. Additional information related to the numerical aspects of the parametric study is also presented. Results of the parametric study are presented to highlight the effect of the variables in relation to the behavior of a stiff column-supported shallow foundation subjected to horizontal load.

5.2 ESTIMATING STANDARD DEVIATIONS

All of the variables employed in the parametric analysis were assumed to follow a normal distribution. Because of this, the parametric analysis required the mean values of each variable examined, and the calculation of their standard deviations to properly quantify the range of parametric variation of the variables. In geotechnical-related studies, data are not always sufficient to allow a direct calculation of a standard deviation (Duncan et al. 2014). When a direct calculation of the standard deviation is not possible, it is convenient to use correlations available in the literature. Different procedures are available to estimate standard deviations in geotechnical engineering practice using experience (Duncan et al. 2014):

5.2.1 *Published Values*

A wide range of values of coefficient of variation have been compiled by numerous researchers. Values of coefficient of variation tabulated in the literature are based on a large number of tests that have been carried out under specific sampling and testing conditions. Duncan et al. (2014) assembled a list of values of coefficient of variation, with their corresponding source, for different properties and in-situ tests. Once a coefficient of variation has been selected, it is possible to estimate the standard deviation using the mathematical definition of the coefficient of variation as following:

$$SD = (COV)(\bar{x}) \tag{5.01}$$

Where *SD* is the standard deviation, *COV* is the coefficient of variation and $\bar{x}$ is the mean. In this parametric analysis, specific variables required the use of values of coefficient of variation obtained from the literature in order to estimate their corresponding standard deviation.

5.2.2 *The Three-Sigma Rule*

The Three-Sigma rule consists of estimating the lowest and highest conceivable values for a variable and using the following expression to estimate the standard deviation (Duncan et al. 2014):

$$SD = \frac{HCV - LCV}{6} \tag{5.02}$$

Where *HCV* is the highest conceivable value and *LCV* is the lowest conceivable value for the variable. The number 6 comes from the fact that 99.7% of the data in a normal distribution is

covered between -3*SD* to +3*SD* from the mean (Ang and Tang 2007), thus the range limited by the highest and lowest conceivable values encompasses a total of 3 + 3 = 6 standard deviations. The validity and usefulness of this procedure is dependent on the accuracy in estimating the highest and lowest conceivable values that effectively cover nearly one hundred percent of the data of a particular variable. This method was employed to estimate the standard deviations of certain variables in the parametric analysis.

5.2.3 *The N-Sigma Rule*

In a similar fashion to the Three-Sigma rule, the N-Sigma rule employs a procedure similar to the one employed in the Three-Sigma rule:

$$SD = \frac{HCV - LCV}{N_{SD}} \tag{5.03}$$

In this case, N_{SD} is a number, lower than 6, that reflects the fact that the highest and lowest conceivable values do not always encompass 99.70% of the data (Duncan et al. 2014). In most cases, N_{SD} = 4 such that the highest and lowest conceivable values estimated encompass 95.4% of the data in a normal distribution ranging from -2*SD* to +2*SD* (Ang and Tang 2007) or 2 + 2 = 4 standard deviations. Because this method is limited by the information available for a particular variable, the validity of the procedure is dependent on using the most suitable value of N_{SD} for the highest and lowest conceivable values estimated for the variable. This method was also employed in estimating the standard deviations of specific variables in the parametric analysis.

5.3 MODIFIED CAM-CLAY CONSTITUTIVE MODEL

The Modified Cam-Clay model was used to model the constitutive behavior of the soft soil layer in the parametric analysis. The remaining layers (LTP and bearing layer) and structures (stiff columns and footing) employed the same constitutive models described in the previous chapter. The Modified Cam-Clay constitutive model assumes a logarithmic relation between void ratio e and the mean effective stress p' in isotropic virgin compression (Roscoe and Burland 1968):

$$e - e^0 = -\lambda \ln\left(\frac{p'}{p^0}\right) \tag{5.04}$$

Where λ is the Cam-Clay compression index for primary or virgin loading, and p^0 is the initial mean effective stress for an initial void ratio e^0. Similar to the Soft Soil constitutive model, the above expression results in a straight line in e-ln p' space. In the case of unloading and reloading:

$$e - e^0 = -\kappa \ln\left(\frac{p'}{p^0}\right) \tag{5.05}$$

Where κ is the Cam-Clay swelling index. The above expression also results in a straight line, albeit with a smaller slope, in e-ln p' space. From a compressibility standpoint, the Modified Cam-Clay model and the Soft Soil model are very similar in their formulation.

The yield function f of the Modified Cam-Clay model is (Roscoe and Burland 1968):

$$f = \frac{q^2}{M^2} + p'\left(p' - p_c\right) \tag{5.06}$$

Where q is the deviatoric stress, p_c is the preconsolidation stress and M is the slope of the critical state line (CSL). When $f = 0$, the yield surface is an ellipse in the p'-q space as observed in Figure

5.1. In this figure the critical state line, which determines yield or failure, is defined by the following expression:

$$q = Mp' \tag{5.07}$$

The slope or constant M determines the height of the ellipse, and it is important in the calculation of the coefficient of lateral earth pressure for normal consolidation conditions K_o^{NC}. The preconsolidation stress p_c determines the horizontal length of the ellipse. The left side of the ellipse is known as the "dry side" where yielding is associated with softening, characteristic of overconsolidated soils. The right side of the ellipse is known as the "wet side", where plastic yielding is associated with hardening, characteristic of normally consolidated soils.

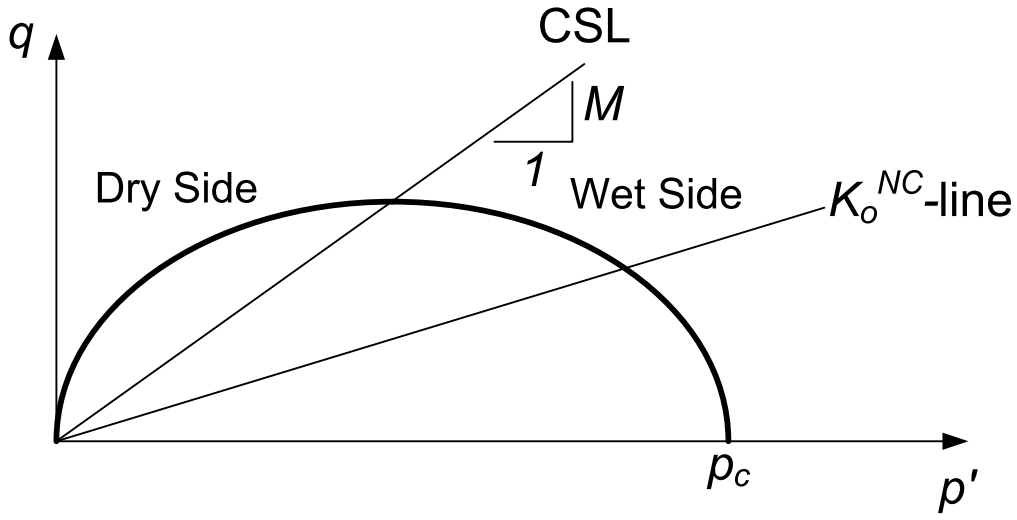

Fig. 5.1. Yield surface of the Modified Cam-Clay model in p'-q space (after Brinkgreve et al. 2013).

5.4 GEOMETRY-BASED VARIABLES

This section describes the procedure used to derive the range of parametric values of the geometry-based variables used in the parametric analysis. In general, the range of parametric values examined encompassed -2*SD* to +2*SD* with 1*SD* of increment, and this range was deemed sufficient for purposes of running the parametric analysis. The geometry-based variables examined included the LTP thickness, the stiff column diameter, the stiff column length and the stiff column spacing. A description of the derivation of the standard deviation of each variable is presented, including a summary of the range of parametric values employed.

5.4.1 *LTP Thickness H*

The lowest conceivable value of the thickness of the LTP was specified at 0.30 m (ASIRI 2012) and the highest conceivable value was specified at 1.20 m (Masse et al. 2012) based on stiff column project information. The mean value of the thickness of this layer was specified at 0.75 m. Using the Three-Sigma rule, the standard deviation of the LTP was estimated at SD_H = (1.20 – 0.30) / 6 = 0.15 m.

5.4.2 *Stiff Column Diameter D*

Based on stiff column design data by Masse et al. (2012), the lowest conceivable value of the diameter of the stiff columns was specified 0.28 m (11 inches) and the highest conceivable value at 0.45 m (18 inches) with a mean diameter of 0.36 m. Using the Three-Sigma rule, the standard deviation of the diameter was estimated at SD_D = (0.45 – 0.28) / 6 = 0.03 m.

5.4.3 *Stiff Column Length L*

In a similar fashion to the diameter, Masse et al. (2012) provide information on different stiff column lengths employed in various projects. Based on this reference, the lowest conceivable value was specified at 3 m and the highest conceivable value was specified at 35 m, with a mean length of 19 m. Using the Three-Sigma rule, the standard deviation for the length is SD_L = (35 - 3) / 6 = 5 m.

5.4.4 *Stiff Column Spacing S*

The calculation of the standard deviation of the column spacing is based on the concept of area replacement ratio (a_s). As mentioned in the earlier chapters, typical area replacement ratios used in practice in the construction of stiff columns range from 2-12% (Buschmeier and Masse 2012). The closer the spacing between columns, the higher the area replacement ratio. Considering an average diameter of 0.36 m or 0.18 m radius, the area replacement ratio of stiff columns constructed in 2 x 2 square layouts can be defined as:

$$a_s = \pi\left(\frac{r}{s}\right)^2 = \pi\left(\frac{0.18}{s}\right)^2 \tag{5.08}$$

Solving the above expression for a_s = 2% and a_s = 12%, results in spacing ranging from 0.92 m to 2.26 m. Considering these as the lowest and highest conceivable values and using the Three-Sigma rule, the standard deviation for the spacing of the columns can be calculated as SD_S = (2.26 – 0.92) / 6 = 0.20 m. An average spacing of 1.60 m was specified in the parametric analysis.

5.4.5 *Summary of the Parametric Values of the Geometry-Based Variables*

The following table summarizes the range of parametric values of the geometry-based variables that were examined in the parametric analysis.

Table 5.1. Range of values of the geometry-based variables examined in the parametric analysis

Range Examined	LTP *H* (m)	Column *D* (m)	Column *L* (m)	Column *S* (m)
-2 *SD*	0.45	0.30	9	1.20
-1 *SD*	0.60	0.33	14	1.40
Mean	0.75	0.36	19	1.60
+1 *SD*	0.90	0.39	24	1.80
+2 *SD*	1.05	0.42	29	2.00

5.5 MATERIAL-BASED VARIABLES

This section describes the procedure used to derive the range of parametric values of each of the material-based variables employed in the parametric analysis. In a similar fashion to the previous section, the range of parametric values of the material-based variables examined covered -2*SD* to +2*SD* with 1*SD* of increment. No parametric variation was considered for the bearing layer, but information on the properties selected for the bearing layer is still presented.

5.5.1 *Load Transfer Platform*

The following procedure was used to estimate the parametric values of the properties of the LTP:

1. The relative density (D_r) was adopted as the main parametric variable of the LTP.
2. The lowest conceivable value of relative density adopted for this layer was 60%.
3. The highest conceivable value of relative density adopted for this layer was 90%.
4. Using N_{SD} = 4 and employing the N-Sigma rule, a standard deviation SD_{Dr} = (90-60) / 4 = 7.5% for the relative density was estimated. A mean relative density of 75% was adopted for the LTP.
5. Table 5.2 summarizes the range of relative density values examined.
6. The Duncan et al. (2014) correlation was used with the range of relative densities examined to estimate the effective friction angle ϕ' of the cohesionless LTP layer. This expression required the calculation of the effective normal stress σ_N'. The following equation shows the Duncan et al. (2014) relationship that was used to estimate the effective friction angle:

$$\phi' = A + B(D_r) - [C + D(D_r)]\log_{10}\left(\frac{\sigma_N'}{P_a}\right) \tag{5.09}$$

Table 5.2. Range of values of the LTP D_r adopted for the parametric analysis

Range Examined	LTP D_r (%)
-2 *SD*	60.0
-1 *SD*	67.5
Mean	75.0
+1 *SD*	82.5
+2 *SD*	90.0

7. A coefficient of uniformity greater than 6 (well-graded soil) was adopted for the LTP resulting in A = 39, B = 10, C = 3 and D = 2 in the previous equation. The effective normal stress was calculated for each relative density examined by considering the forces acting in a representative wedge (Figure 5.2) underneath a square footing with a width B = 3.20 m that extends to the bottom of the LTP. The wedge has a height H equal to 0.75 m, and a point load Q is applied at the surface of the wedge that results from a 191.50 kPa bearing pressure applied at the base of the foundation. A unit weight of 20.4 kN/m³ was adopted for the LTP. Figure 5.2 shows the remaining forces considered in the wedge. The system was iteratively solved by estimating an initial ϕ' to estimate σ_N' at the base of the wedge using limiting equilibrium. The effective friction angle ϕ' was later updated using the Duncan et al. (2014) correlation with the estimated σ_N'. This entire procedure was repeated successively until a stable ϕ' was obtained for each value of D_r examined. Table 5.3 summarizes the estimated effective normal stresses and effective friction angles.

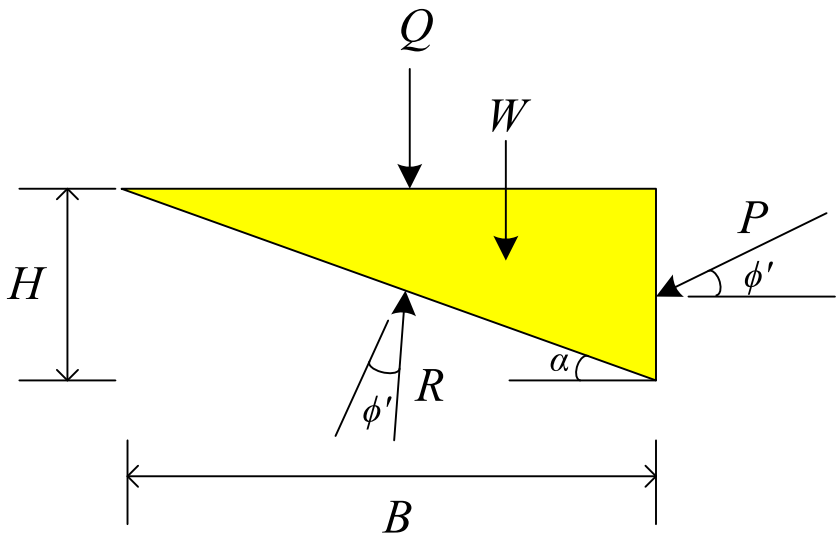

Fig. 5.2. Wedge in the LTP used to estimate σ_N'.

$$N = R\cos\phi' \tag{5.10}$$

$$\sigma_N' = \frac{N}{\sqrt{H^2 + B^2}} \tag{5.11}$$

Table 5.3. Values of ϕ' and effective normal stress σ_N' at the middle of the LTP

Range Examined	LTP D_r (%)	σ_N' (kPa)	LTP ϕ' (°)
-2 *SD*	60.0	99.5	45.0
-1 *SD*	67.5	96.7	45.8
Mean	75.0	93.9	46.6
+1 *SD*	82.5	91.2	47.4
+2 *SD*	90.0	88.1	48.3

8. The following correlation applicable to quartz sands (Brinkgreve 2005) was used to estimate the dilation angle ψ of the LTP and Table 5.4 summarizes the results:

$$\psi \approx \phi' - 30° \tag{5.12}$$

Table 5.4. Correlation of the LTP ϕ' with its ψ

Range Examined	LTP D_r (%)	LTP ϕ' (°)	LTP ψ (°)
-2 *SD*	60.0	45.0	15.0
-1 *SD*	67.5	45.8	15.8
Mean	75.0	46.6	16.6
+1 *SD*	82.5	47.4	17.4
+2 *SD*	90.0	48.3	18.3

9. The relative density was used to estimate the reference Young's modulus at 50% strength E_{50}^{ref} of the LTP based on the following correlation described in Brinkgreve (2005) for cohesionless soils. The results are shown in Table 5.5:

$$E_{50}^{ref} \approx D_r \cdot 60MPa \tag{5.13}$$

Table 5.5. Correlation of the LTP D_r with the LTP E_{50}^{ref}

Range Examined	LTP D_r (%)	E_{50}^{ref} (MPa)
-2 *SD*	60.0	36.0
-1 *SD*	67.5	40.5
Mean	75.0	45.0
+1 *SD*	82.5	49.5
+2 *SD*	90.0	54.0

10. The reference Young's modulus was corrected for confinement σ_h' using the expression shown below, also presented in Brinkgreve (2005). Considering the vertical effective stress due to hydrostatic conditions and a 2:1 spread surcharge of 153.5 kPa at the middle of this 0.75 m-thick layer (recall a 191.5 kPa surcharge at base of footing), results in a value of σ_v' = 161.1 kPa. The horizontal effective stress σ_h' was estimated on the consideration that the compaction-induced horizontal effective stresses in the LTP are greater than those under K_o conditions. The approach described in Duncan et al. (1991) and Duncan et al. (1993) was used to estimate a K_{CI} = 1.85. It was considered that the LTP was compacted using 0.15 m-thick lifts using vibratory rollers that exerted surface pressures in the order of 70 kN/m. The compaction-induced horizontal effective stress was estimated at σ_h' = 298 kPa. The results of E_{50} corrected for confinement are shown in Table 5.6:

$$E_{50} = E_{50}^{ref} \sqrt{\frac{\sigma_h'}{100\ kPa}} \tag{5.14}$$

Table 5.6. Correlation of the LTP D_r with the LTP E_{50}

Range Examined	LTP D_r (%)	E_{50}^{ref} (MPa)	E_{50} (MPa)
-2 *SD*	60.0	36.0	62.2
-1 *SD*	67.5	40.5	69.9
Mean	75.0	45.0	77.7
+1 *SD*	82.5	49.5	85.5
+2 *SD*	90.0	54.0	93.2

11. Poisson's ratio for the LTP was estimated as a function of the friction angle of this layer using the expression below from Duncan et al. (1991). These Poisson's ratio values were

used to calculate the shear modulus at 50% strength G_{50} using conventional elasticity theory. The results are summarized in Table 5.7:

$$\nu' = \frac{4 - 3\sin\phi'}{8 - 4\sin\phi'} \tag{5.15}$$

$$G_{50} = \frac{E_{50}}{2(1+\nu')} \tag{5.16}$$

Table 5.7. Correlation of the LTP D_r with the LTP G_{50}

Range Examined	LTP D_r (%)	E_{50} (MPa)	ν'	G_{50} (MPa)
-2 *SD*	60.0	62.2	0.363	22.8
-1 *SD*	67.5	69.9	0.360	25.7
Mean	75.0	77.7	0.357	28.6
+1 *SD*	82.5	85.5	0.354	31.6
+2 *SD*	90.0	93.2	0.351	34.5

12. The strength and stiffness conditions of the interface between the base of the concrete footing and the top of the LTP layer were also considered in the parametric analysis. In terms of strength, the LTP-footing interface friction ϕ_i angle was set equal to 2/3 of the friction angle of the LTP ϕ'. This relationship is typical of interfaces made of sandy soil against formed concrete. Table 5.8 shows the values of the strength reduction factors R_{inter} that guaranteed that the interface friction angle was equal to 2/3 of the friction angle of the LTP ϕ' for each parametric value examined.

Table 5.8. Values of the shear strength properties of the LTP-footing interface

Range Examined	LTP D_r (%)	LTP ϕ' (°)	ϕ_i (°)	R_{inter}
-2 *SD*	60.0	45.0	30.0	0.577
-1 *SD*	67.5	45.8	30.5	0.573
Mean	75.0	46.6	31.1	0.570
+1 *SD*	82.5	47.4	31.6	0.566
+2 *SD*	90.0	48.3	32.2	0.561

13. The strength reduction factor also determined the stiffness conditions of the LTP-footing interface. The combination of this strength reduction factor with the stiffness of the LTP in terms of its shear modulus produced a particular shear ($G_{50,i}$) and normal stiffness ($E_{50\text{-}oed,i}$) for the interface. Table 5.9 shows the calculated interface shear and normal stiffness for each parametric variation.

Table 5.9. Values of the stiffness properties of the LTP-footing interface

Range Examined	LTP D_r (%)	R_{inter}	G_{50} (MPa)	$G_{50,i}$ (MPa)	ν_i	$E_{50\text{-}oed,i}$ (MPa)
-2 *SD*	60.0	0.577	22.8	7.6	0.45	83.5
-1 *SD*	67.5	0.573	25.7	8.4	0.45	92.8
Mean	75.0	0.570	28.6	9.3	0.45	102.2
+1 *SD*	82.5	0.566	31.6	10.1	0.45	111.4
+2 *SD*	90.0	0.561	34.5	10.9	0.45	119.4

14. Following shown are the PLAXIS 3D strain-strain curves for an element of soil that was anisotropically consolidated under a state of stresses to which it would be subjected if it was located at the middle of the LTP under the foundation surcharge of 191.50 kPa, and was

subsequently sheared under drained conditions. The anisotropic state of stresses consisted of σ_v' = 161.1 kPa and σ_h' = 298 kPa. Each curve represents the parametric variation of the relative density of the LTP with its respective strength and stiffness properties that were aforementioned estimated. The curves were constructed by considering the LTP as a linear elastic-perfectly plastic material with failure following the Mohr-Coulomb criterion. A mean value of permeability k of 10^{-5} cm/s was adopted for the LTP and no parametric variation was considered for this quantity.

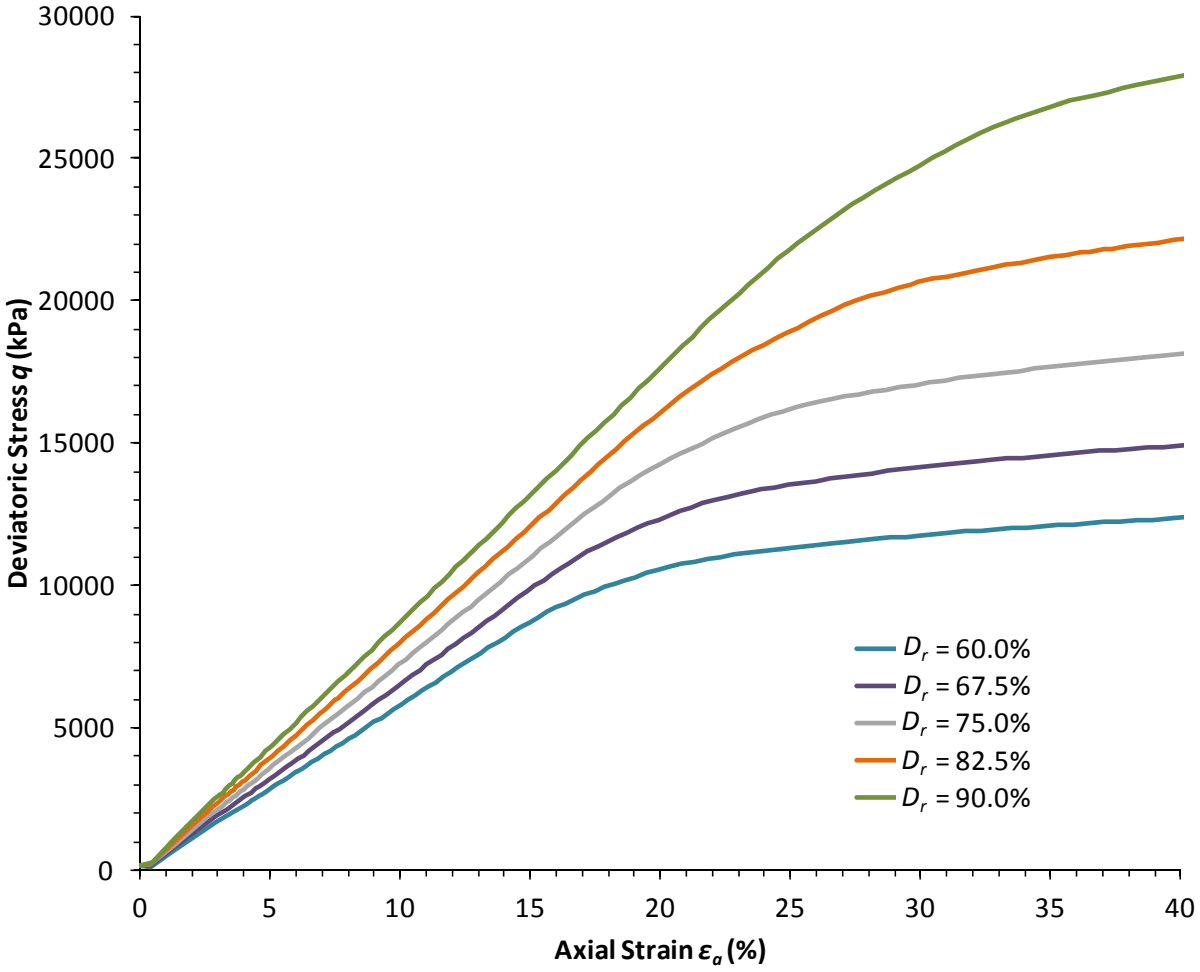

Fig. 5.3. Stress-strain curves for the different parametric variations of the relative density of the LTP.

5.5.2 *Bearing Layer*

The ASIRI (2012) reference does not provide minimum strength requirements for the bearing layer. As a result, a reference blowcount of N_{60} = 50 was used to define the strength and stiffness properties of the bearing layer and no parametric variation was made of any of the properties of this layer. The following procedure provides an overview of the correlations that were used to obtain the effective friction angle and shear modulus of the bearing layer for the aforementioned blowcount:

- Considering an effective overburden σ_v' = 190 kPa at the middle of the bearing layer normalized to 1 atm (or 100 kPa), a value of ϕ' equal to 44.8° was estimated for the bearing layer using the following correlation from Kulhawy and Mayne (1990) based on data from Schmertmann (1975):

$$\phi' = \tan^{-1}\left[\frac{N}{12.2 + 20.3\left(\frac{\sigma_v'}{P_a}\right)}\right]^{0.34} \tag{5.17}$$

- A value of ψ equal to 14.8° was estimated for this layer.
- The blowcount was also used to estimate a Young's modulus E equal to 75 MPa for this layer. This was achieved using the following correlation also presented in Kulhawy and Mayne (1990) for clean overconsolidated sands:

$$\frac{E}{P_a} = 15N_{60} \tag{5.18}$$

- A Poisson's ratio of 0.364 was estimated for the bearing layer using Equation 5.15 resulting in a shear modulus G equal to 27.5 MPa for this layer.

- The following figure shows the stress-strain curve for a soil element located at the middle of a 1.5 m-thick bearing layer underneath a 18.5 m-thick clay layer. The previous estimated properties along with a saturated unit weight of 21.2 kN/m³ were adopted for the bearing layer. It was considered that the state of stresses in the bearing layer was under K_o-conditions with K_o = 0.295 using Jacky's (1944) expression $K_o = 1 - \sin \phi'$. This soil element was consolidated to a vertical effective stress σ_v' = 190.1 kPa and horizontal effective stress σ_h' = 56.1 kPa and it was later sheared under drained conditions. The bearing layer was modeled as a linear elastic-perfectly plastic material with failure following the Mohr-Coulomb criterion. In a similar fashion to the LTP, a permeability k of 10^{-5} cm/s was adopted for the bearing layer.

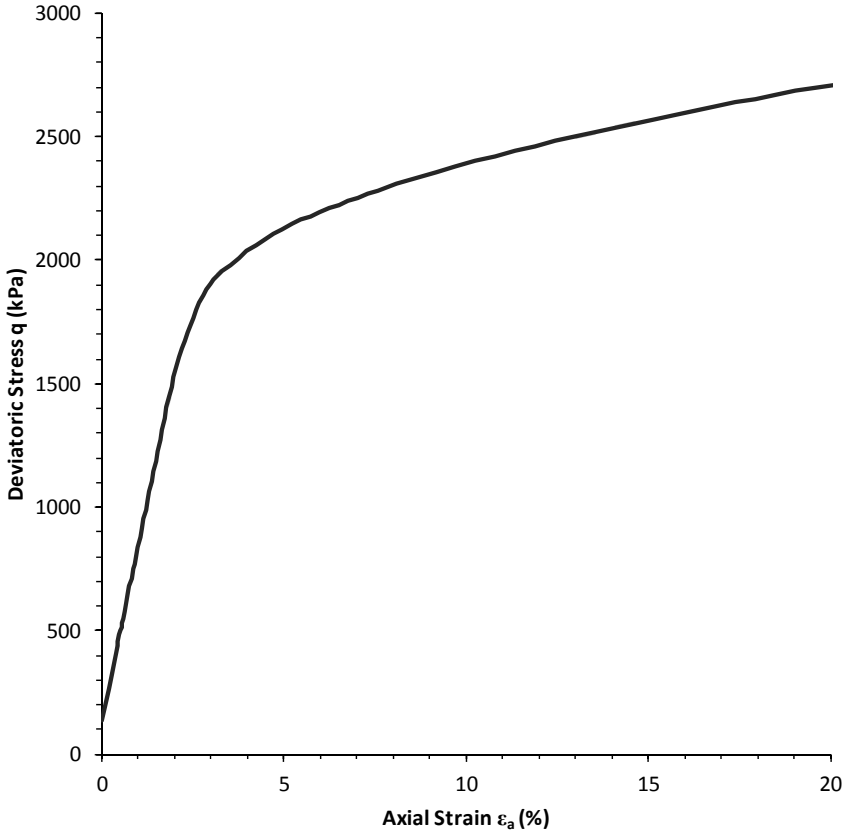

Fig. 5.4. Stress-strain curve for a soil element located at the middle of the bearing layer.

5.5.3 *Clay Layer*

The parametric variation of the undrained shear strength ratio (s_u/σ_v') of the clay layer was obtained using the liquidity index (I_L) as an indicator or index of the overconsolidation ratio (*OCR*) of the clay layer. The lowest and highest conceivable values for I_L were specified at 0.5 and 1. An upper limit of I_L of 1 was adopted to avoid the examination of highly sensitive soils (I_L > 1) while a lower limit of I_L of 0.5 was adopted to avoid the examination of highly overconsolidated clays. Using the N-Sigma rule with N_{SD} = 4, the standard deviation of the liquidity index is SD_{IL} = 0.125. Table 5.10 shows the range of values of I_L that were employed in the parametric analysis.

Table 5.10. Range of values of I_L

Range Examined	I_L
-2 *SD*	0.500
-1 *SD*	0.625
Mean	0.750
+1 *SD*	0.875
+2 *SD*	1.000

The following procedure was used to estimate the variation of s_u/σ_v' of the clay layer:

1. Figure 5.5 shows the vertical effective stress σ_{vo}' and preconsolidation pressure σ_p distributions for each I_L considered. A plastic limit (*PL*) of 20, a liquid limit (*LL*) of 40 and a plasticity index (*PI*) of 20 was adopted for all the parametric cases evaluated. The vertical effective stress distribution was constructed using an average saturated unit weight of 18.8 kN/m³. The preconsolidation pressure distributions were constructed by estimating *OCR* for

each I_L using the following useful Modified Cam-Clay correlation from Wood (1983) for uncemented, low sensitive soils:

$$OCR = 10^{[1-2.5I_L-1.25\log(\sigma_{vo}'/P_a)]} \tag{5.19}$$

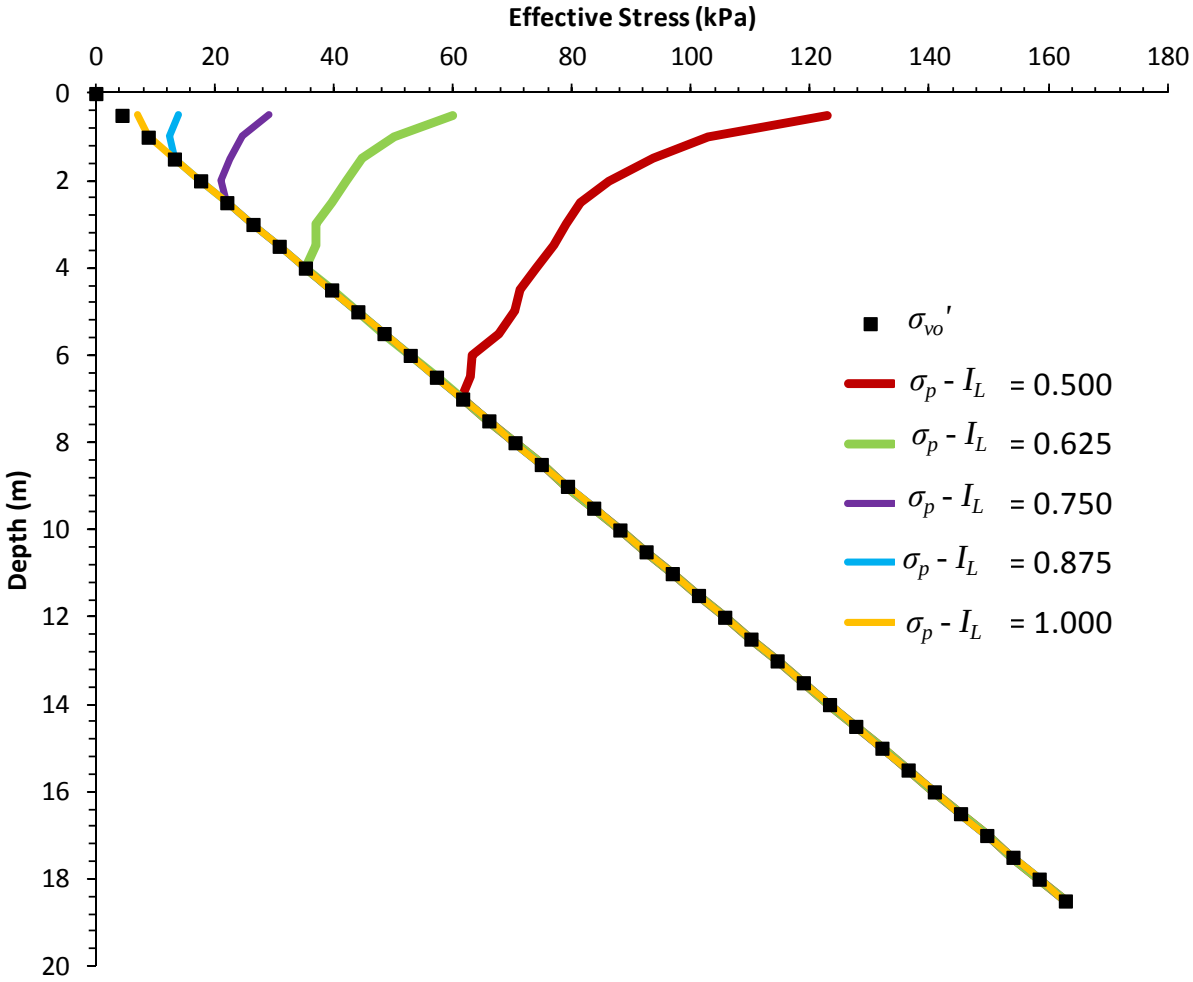

Fig. 5.5. Vertical effective stress and preconsolidation pressure distributions.

2. An average *OCR* was calculated for each distribution and the results are shown in Table 5.11:

Table 5.11. Range of values of *OCR*

Range Examined	I_L	*OCR*
-2 *SD*	0.500	2.5
-1 *SD*	0.625	1.6
Mean	0.750	1.2
+1 *SD*	0.875	1.1
+2 *SD*	1.000	1.0

3. The compression index C_c of the clay layer was estimated by adopting a relationship of the following form applicable between water contents w_n of 30 and 40% based on compression index data reported by Terzaghi et al. (1996):

$$C_c = 0.01 w_n \tag{5.20}$$

4. Terzaghi et al. (1996) indicate that the magnitude of the recompression index C_s can vary between 0.2 to 0.02 of the compression index, with the lower bound associated with structured clays and the upper bound with stiff fissured clays. Considering an average value of (0.2 + 0.02) / 2 = 0.011 the following expression was used to calculate C_s:

$$C_s = 0.011 C_c \tag{5.21}$$

5. The values of C_s and C_s were converted to the respective Modified Cam-Clay parameters λ and κ using the expressions below. The results are summarized in Table 5.12. The values of void ratio reported in Table 5.12 were calculated using a G_s = 2.70.

$$\lambda = \frac{C_c}{\ln 10} \tag{5.22}$$

$$\kappa \approx \frac{2C_s}{\ln 10} \tag{5.23}$$

Table 5.12. Range of values of λ and κ

Range Examined	I_L	w_n (%)	e	C_c	C_s	λ	κ
-2 *SD*	0.500	30.0	0.8100	0.300	0.0330	0.130	0.0287
-1 *SD*	0.625	32.5	0.8775	0.325	0.0358	0.141	0.0311
Mean	0.750	35.0	0.9450	0.350	0.0385	0.152	0.0334
+1 *SD*	0.875	37.5	1.0125	0.375	0.0413	0.163	0.0359
+2 *SD*	1.000	40.0	1.0800	0.400	0.0440	0.174	0.0382

6. The slope of the critical state line M was estimated using ϕ' with the following expression that adopts plane strain conditions with zero dilatancy (Brinkgreve 2005):

$$M = \sqrt{3}\sin\phi' \tag{5.24}$$

7. Then M was used in combination with λ and κ to estimate K_o under normal consolidation conditions K_o^{NC} (Brinkgreve 1994):

$$M = 3\sqrt{\frac{\left(1-K_o^{NC}\right)^2}{\left(1+2K_o^{NC}\right)^2} + \frac{\left(1-K_o^{NC}\right)\left(1-2\nu_{ur}\right)\left(\lambda/\kappa - 1\right)}{\left(1+2K_o^{NC}\right)\left(1-2\nu_{ur}\right)\lambda/\kappa - \left(1-K_o^{NC}\right)\left(1+\nu_{ur}\right)}} \tag{5.25}$$

Where ν_{ur} is Poisson's ratio for unloading/reloading that varies depending on the *OCR* examined. Table 5.13 shows the values of ν_{ur} considered for each parametric variation.

Table 5.13. Range of values of unloading/reloading Poisson's ratio

Range Examined	*OCR*	ν_{ur}
-2 *SD*	2.5	0.35
-1 *SD*	1.6	0.40
Mean	1.2	0.45
+1 *SD*	1.1	0.45
+2 *SD*	1.0	0.45

8. The *OCR* along with ν_{ur} and K_o^{NC} were used to estimate K_o using:

$$K_o = \frac{\sigma_{ho}'}{\sigma_{vo}'} = K_o^{NC} OCR - \frac{\nu_{ur}}{1-\nu_{ur}}(OCR - 1) \tag{5.26}$$

9. Table 5.14 summarizes the range of undrained shear strength ratios s_u/σ_v' of the clayey soil that was examined in the parametric analysis. These values of s_u/σ_v' were calculated as a function of *OCR* using the Jamiliokowski et al. (1985) approximation typical of direct simple shear conditions:

$$\frac{s_u}{\sigma_v'} = 0.23 OCR^{0.80} \tag{5.27}$$

Table 5.14. Range of values of s_u/σ_v'

Range Examined	*OCR*	s_u/σ_v'
-2 *SD*	2.5	0.479
-1 *SD*	1.6	0.335
Mean	1.2	0.266
+1 *SD*	1.1	0.248
+2 *SD*	1.0	0.230

10. The range of values of undrained shear strength ratio s_u/σ_v' examined was implemented in the initial conditions stage of the PLAXIS 3D model in order to define the shear strength of the clayey soil. The undrained shear strength ratios in the parametric models were specified as a function of ϕ', c' and K_o as following: To establish the shear strength available for a soil element under a K_o stress state, the software expands the K_o-Mohr's circle while keeping its center constant until it touches the Mohr-Coulomb failure envelope defined by c' and ϕ' (Figure 5.6). In order to implement the undrained shear strength ratio values in the numerical models, it was considered that the undrained shear strength s_u is equal to the shear stress τ_{xy} corresponding to σ_{vo}'. The undrained shear strength ratio was defined as $s_u/\sigma_v' = \tau_{xy}/\sigma_{vo}'$. It is known that s_u/σ_v' is dependent on several factors that include anisotropy and strain rate, and due to limitations of the numerical software employed, the influence of these was not incorporated in the parametric study.

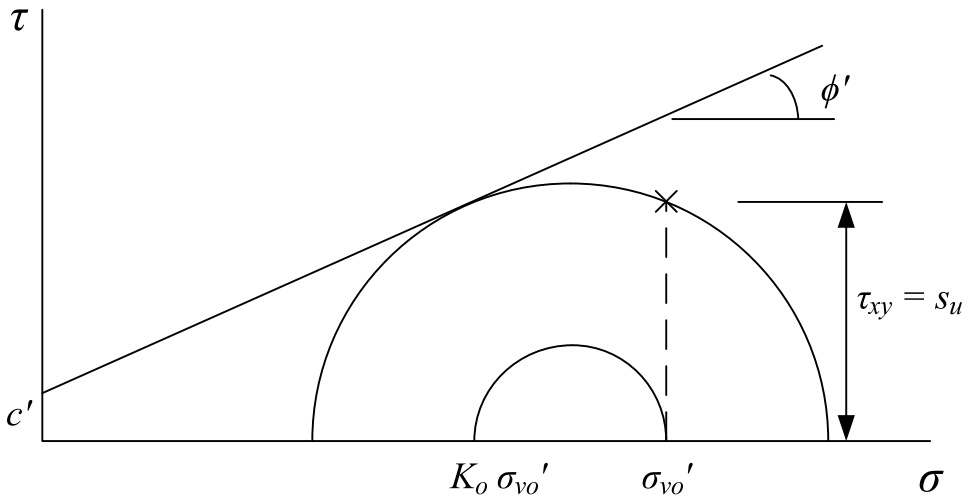

Fig. 5.6. Definition of the undrained shear strength ratio in the parametric models.

11. Considering a cohesion c' equal to zero, Table 5.15 shows the estimated values of ϕ' and K_o that were used to implement the range of undrained shear strength ratios previously defined. The table also shows the values of M estimated and used in the numerical calculations.

Table 5.15. Range of values of ϕ', M and K_o

Range Examined	s_u/σ_v'	ϕ' (°)	M	K_o
-2 *SD*	0.479	26.3	0.767	1.222
-1 *SD*	0.335	19.5	0.578	1.013
Mean	0.266	16.0	0.477	0.939
+1 *SD*	0.248	15.0	0.448	0.938
+2 *SD*	0.230	13.9	0.416	0.936

12. Figure 5.7 shows the strain-strain curves for each parametric variation of overconsolidation ratio considered, and Figure 5.8 shows the corresponding Cambridge effective stress paths. The curves were constructed by anisotropically consolidating an element of the clayey soil located at a depth of 10 m from the surface of the clay layer to the hydrostatic vertical effective stress σ_{vo}' and horizontal effective stress σ_{ho}' that it would be subjected at that depth without consideration of the LTP and foundation surcharge. The soil element was later sheared undrained accounting for the different strength and stiffness conditions investigated. In all the parametric cases examined, σ_{vo}' = 88 kPa and σ_{ho}' varied according to the K_o previously estimated. Table 5.16 summarizes the estimated σ_{ho}' values. The curves were constructed by considering the soil as a Modified Cam-Clay material. A mean value of permeability k of 10^{-7} cm/s was adopted for the clay layer and no parametric variation was considered for this quantity.

Table 5.16. Hydrostatic horizontal effective stresses at a depth of 10 m

Range Examined	*OCR*	σ_{ho}' (kPa)
-2 SD	2.5	107.6
-1 SD	1.6	89.1
Average	1.2	82.7
+1 SD	1.1	82.5
+2 SD	1.0	82.4

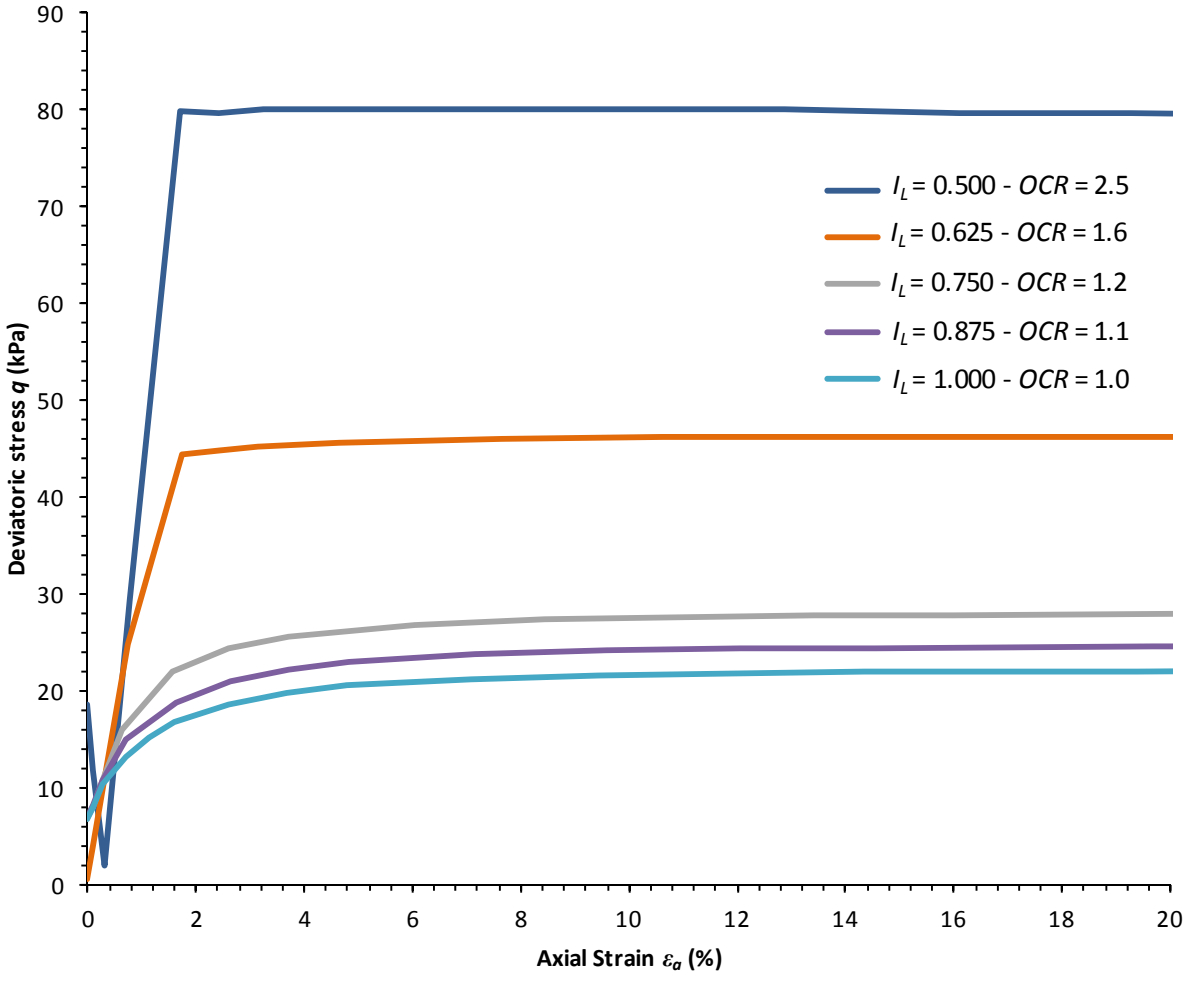

Fig. 5.7. Stress-strain curves for the different parametric variations of the overconsolidation ratio of a soil element at a depth of 10 m in the clay layer.

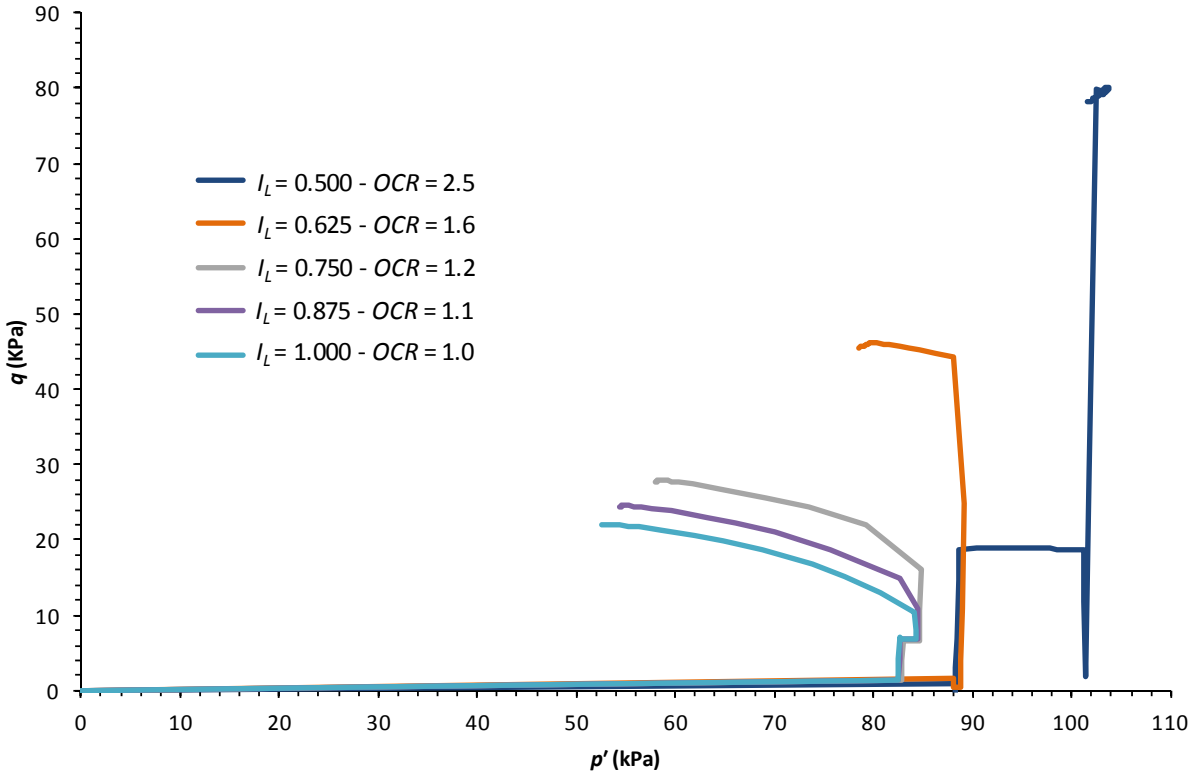

Fig. 5.8. Cambridge effective stress paths for the different parametric variations of the overconsolidation ratio of a soil element at a depth of 10 m in the clay layer.

The parametric variations made for the clay layer showed that a decreasing value of liquidity index of the soft clay was associated with an increase in its overconsolidation ratio, thus increasing the undrained shear strength and the stiffness of the clayey soil.

5.5.4 *Stiff Columns*

The following procedure was employed to estimate the range of parametric values considered for the stiff columns:

1. The unconfined compressive strength of the stiff columns, q_u, was adopted as the main parametric variable of the rigid vertical elements. A mean value of 13.8 MPa (or 2000 psi)

was adopted for the unconfined compressive strength of the stiff columns based on minimum and maximum values of 6.9 and 20.7 MPa, respectively, used in practice (Masse et al. 2012). Skjong et al. (1996) reported a coefficient of variation of 18% for the unconfined compressive strength of concrete and this *COV* was adopted for the grout-based material of the stiff columns. A standard deviation of 0.18 (13.8) = 2.5 MPa was calculated for the unconfined compressive strength of the stiff columns. Table 5.17 shows the range of values of q_u employed in the parametric analysis:

Table 5.17. Range of values of the stiff column q_u

Range Examined	q_u (MPa)
-2 *SD*	8.8
-1 *SD*	11.3
Mean	13.8
+1 *SD*	16.3
+2 *SD*	18.8

2. Values of Young's modulus of the stiff columns were estimated using the following ACI expression used to calculate Young's modulus of concrete (ACI 2011):

$$E_c = 0.043 w_c^{1.5} \sqrt{f'_c} \tag{5.28}$$

Where E_c is Young's modulus of concrete in MPa and f'_c is the unconfined compressive strength of concrete in MPa, and w_c is the density of concrete in kg/m³. Based on design specifications from Menard (Masse 2013), the Young's modulus of the stiff columns E_{RI} was

obtained by dividing E_c by 3 in order to consider long term creep of the grout. The above expression is rewritten as following:

$$E_{RI} = \frac{0.043 w_c^{1.5} \sqrt{q_u}}{3} \tag{5.29}$$

3. Table 5.18 summarizes the values of Young's modulus and shear modulus G_{RI} for each corresponding q_u considered. A density of w_c = 2300 kg/m³ was adopted for the material of the stiff columns. A Poisson's ratio of 0.20 typical of concrete (Ardiaca 2009) was considered for the range of parametric values examined.

Table 5.18. Correlation of the stiff column q_u with the Young's modulus E_{RI}

Range Examined	q_u (MPa)	E_{RI} (MPa)	Poisson's Ratio	G_{RI} (MPa)
-2 *SD*	8.8	4690.0	0.20	1954.2
-1 *SD*	11.3	5315.0	0.20	2214.6
Mean	13.8	5873.0	0.20	2447.1
+1 *SD*	16.3	6383.0	0.20	2659.6
+2 *SD*	18.8	6855.0	0.20	2856.3

4. The following figure shows the strain-strain curves for each parametric variation of strength of the stiff columns along with their corresponding variation of stiffness. The curves were constructed by conducting numerical unconfined compressive tests on an element of the stiff column with the different strength and stiffness conditions shown in Table 5.18. The material

of the stiff columns was modeled as linear elastic-perfectly plastic following the Mohr-Coulomb failure criterion with $c = s_u = q_u/2$ and $\phi = 0$:

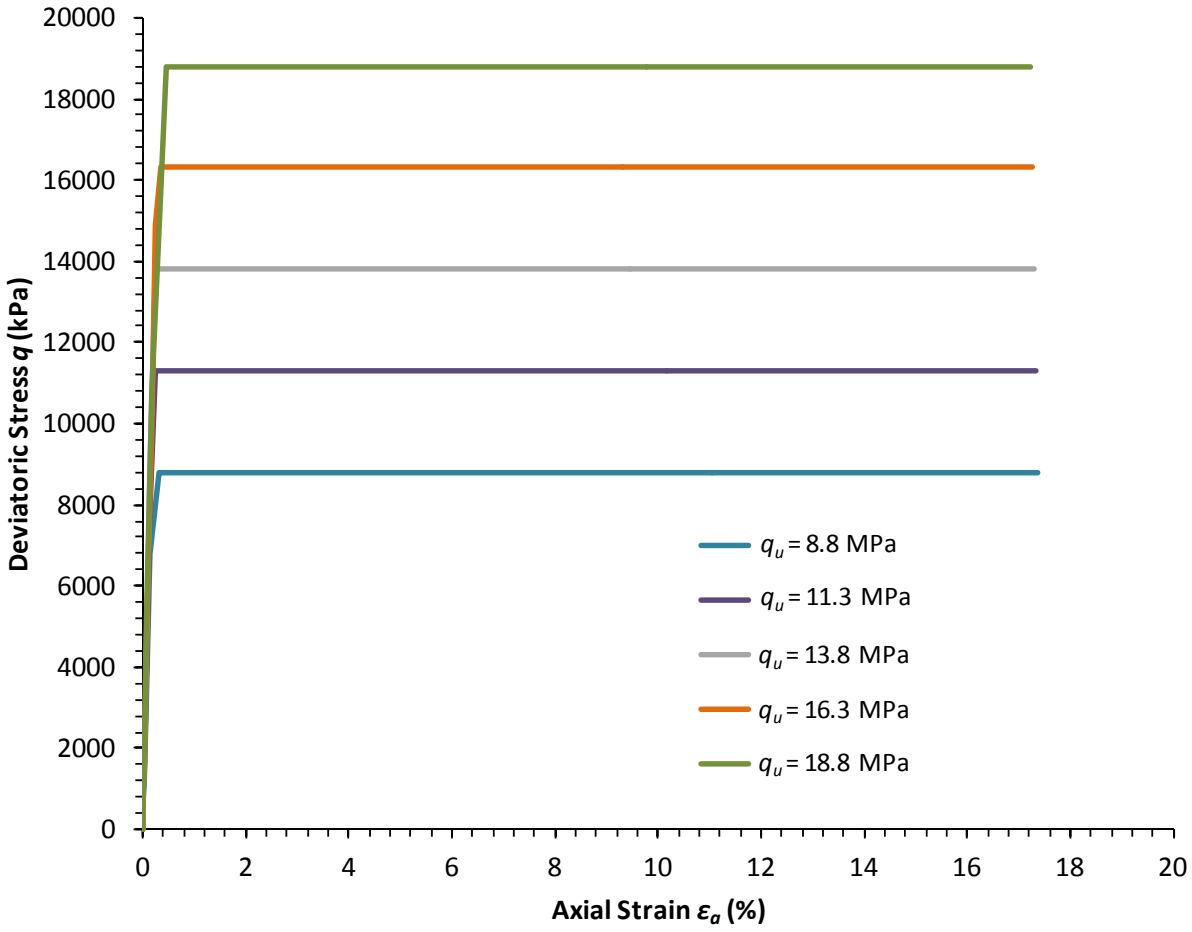

Fig. 5.9. Stress-strain curves for the different parametric variations of the unconfined compressive strength of the stiff columns.

5.5.5 *Summary of the Parametric Values of the Material-Based Variables*

The following table summarizes the range of parametric values of the material-based variables that were examined in the parametric analysis.

Table 5.19. Range of values of the material-based variables examined in the parametric analysis

Component	Variable	Unit	-2 *SD*	-1 *SD*	Mean	+1 *SD*	+2 *SD*
LTP	D_r	%	60.0	67.5	75.0	82.5	90.0
	ϕ'	°	45.0	45.8	46.6	47.4	48.3
	ψ	°	15.0	15.8	16.6	17.4	18.3
	G_{50}	MPa	22.8	25.7	28.6	31.6	34.5
	ϕ_i	°	30.0	30.5	31.1	31.6	32.2
	$G_{50,i}$	MPa	7.6	8.4	9.3	10.1	10.9
	$E_{50\text{-}oed,i}$	MPa	83.5	92.8	102.2	111.4	119.4
Clay Layer	I_L	-	0.500	0.625	0.750	0.875	1.000
	OCR	-	2.5	1.6	1.2	1.1	1.0
	s_u/σ_v'	-	0.479	0.335	0.266	0.248	0.230
	λ	-	0.130	0.141	0.152	0.163	0.174
	κ	-	0.0287	0.0311	0.0334	0.0359	0.0382
Stiff Columns	q_u	MPa	8.8	11.3	13.8	16.3	18.8
	E_{RI}	MPa	4690.0	5315.0	5873.0	6383.0	6855.0

5.6 NUMERICAL IMPLEMENTATION

The parametric analysis was implemented in the finite element software PLAXIS 3D using a similar approach to the one employed to numerically verify the experimental trends observed in the centrifuge test program. Figure 5.10 shows the full geometry of the base model that was examined in the parametric analysis. When applicable, the base geometry was modified to investigate the influence of each geometry-based variable. In order to take advantage of the symmetry of the system, the upper half-geometry of the stiff column-supported shallow foundation was constructed in the software. Figure 5.11 shows the half-geometry mesh along with its respective boundary conditions. This allowed an expedited construction of the

parametric models, and a reduction of the calculation time of each parametric run. The mesh of the parametric models contained, on average, 14000 tetrahedral elements. Each parametric model was built in a series of numerical stages with the objective of modeling the construction procedure observed in stiff column-supported shallow foundations, and modeling the horizontal loading procedure applied to these systems. These stages were:

1. Definition of the initial geostatic stress distribution in the soil-column composite:

In this stage both the vertical and horizontal effective stress distributions, including the static pore-water pressure distribution, were specified in the soil-column composite. The stiff columns were assumed to be already constructed in the soft soil clayey soil as shown in Figure 5.12. This figure identifies the stiff columns that were implemented in the finite element model.

2. Undrained placement of the LTP and footing:

After the initial conditions of the finite element model were defined, the LTP and footing were placed above the soil-column composite and no consolidation was allowed during this stage (Figure 5.13). Boundary conditions were prescribed at each side of the footing in order to guarantee only vertical movement of the foundation in the *z*-direction. This stage also implemented the LTP-footing interface with its assigned strength and stiffness conditions.

3. Consolidation of the soil-column composite under the LTP and footing self-weight surcharge:

Excess pore-water pressures were allowed to dissipate under the self-weight of the LTP and the footing. Closed-flow boundary conditions were prescribed in both sets of *x*-*z* and *y*-*z* planes while open-flow boundary conditions were prescribed in the top and bottom *x*-*y* planes of the

finite element model to allow dissipation of excess pore-water pressures in the vertical direction only (*z*-axis) and avoid numerical instabilities.

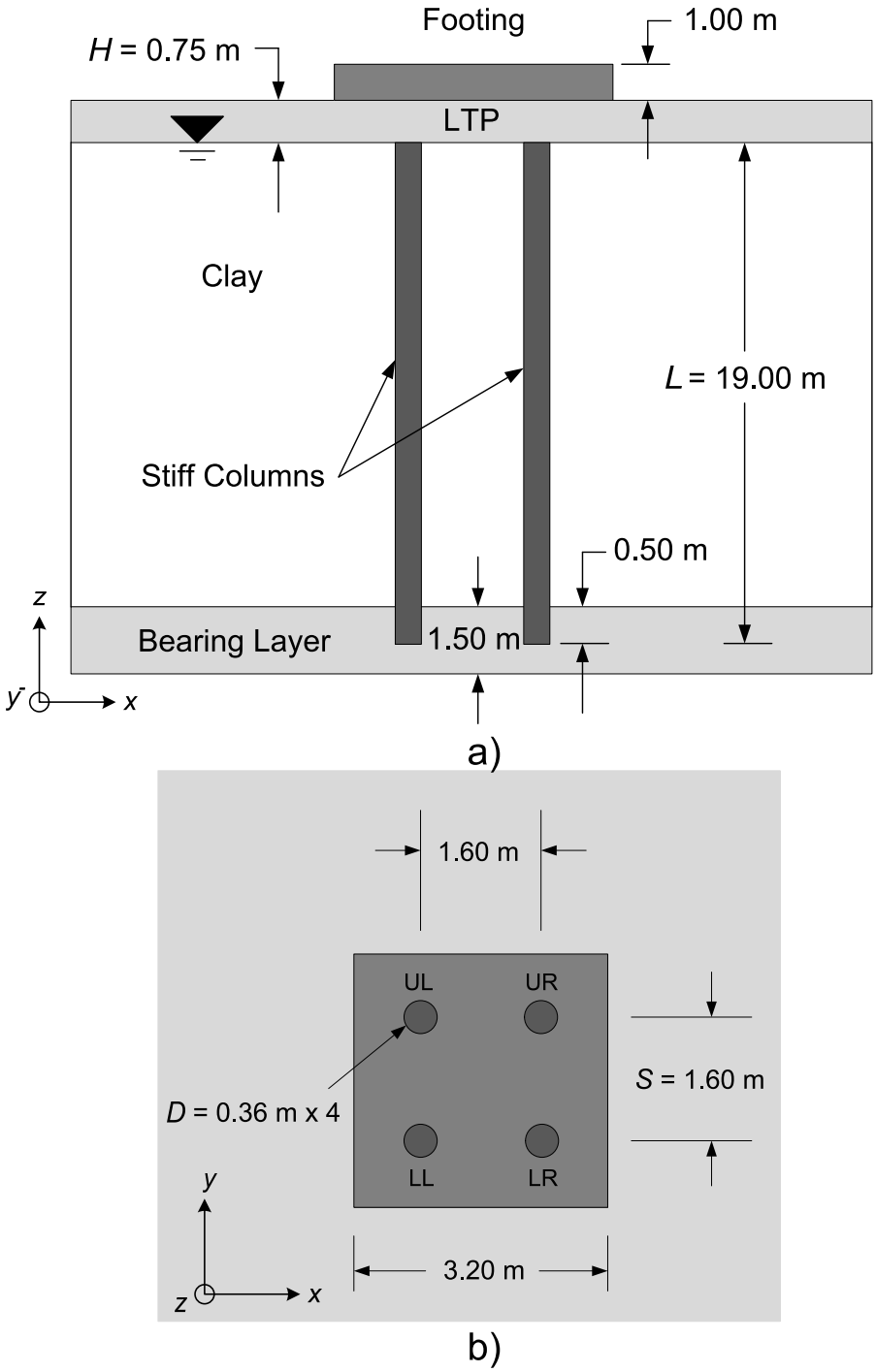

Fig. 5.10. Geometry of the base model, a) cross-section, and b) plan view (UL: Upper Left, UR: Upper Right, LL: Lower Left, LR: Lower Right). Not to scale.

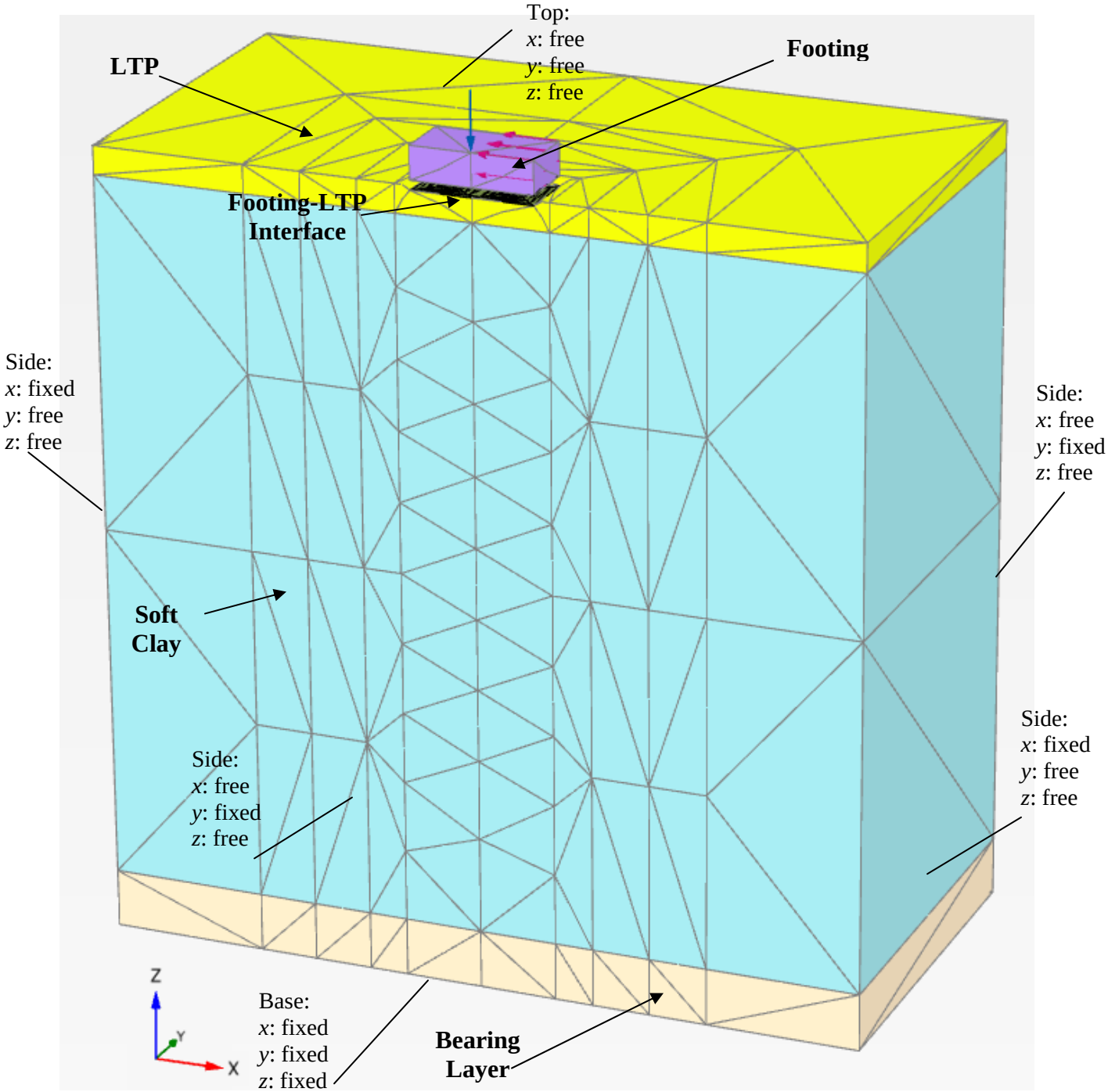

Fig. 5.11. Isometric overview of the finite element mesh with boundary conditions used in the parametric analysis implementing the upper half geometry of the stiff column-supported shallow foundation.

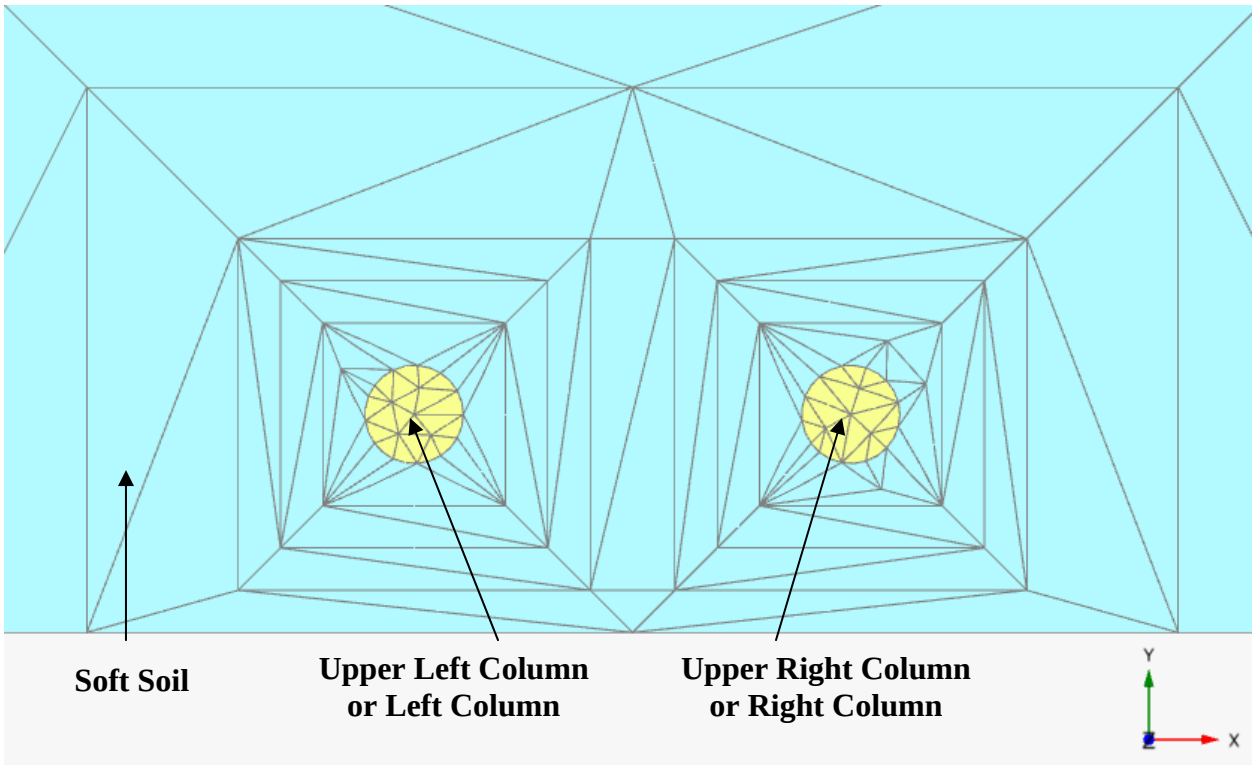

Fig. 5.12. Top view of the upper half geometry in the finite element mesh without the LTP – Initial stage.

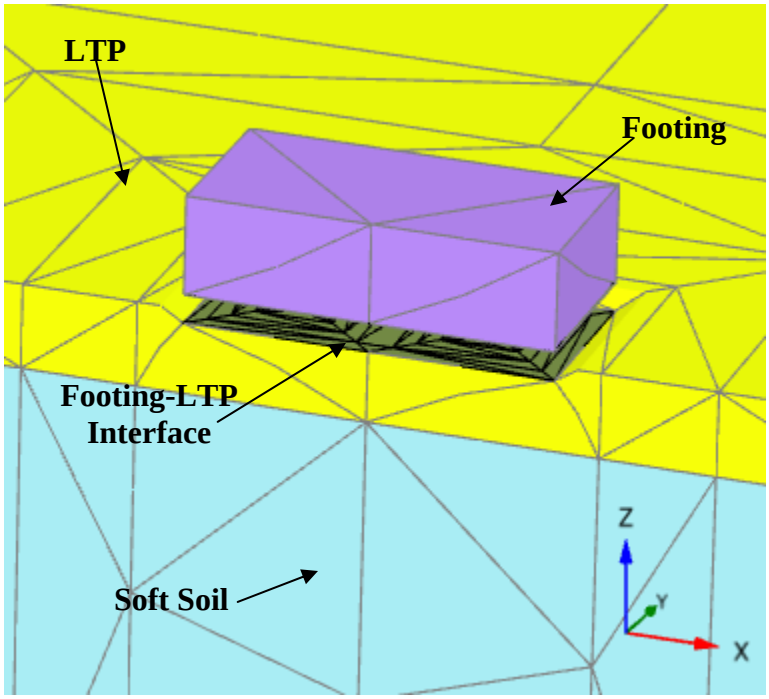

Fig. 5.13. Isometric close up of the upper half geometry of the finite element mesh – Placement of the LTP and footing.

4. Undrained vertical loading of the footing:

The footing was vertically loaded in order to produce a bearing pressure of 191.5 kPa at the base of the footing and no consolidation was allowed (Figure 5.14).

5. Consolidation of the soil-column composite under the applied vertical load of the footing:

Excess pore-water pressures were allowed to dissipate in the soil-column composite under the vertical load applied to the footing.

6. Undrained horizontal loading of the footing:

Following consolidation, the vertically loaded footing was laterally loaded using a uniform prescribed displacement. Application of the prescribed displacement occurred under undrained conditions. Figure 5.15 presents a schematic of the finite element mesh that includes the direction of the prescribed displacement applied to the shallow foundation in the numerical model. Boundary conditions around the footing were accordingly modified to allow the footing to freely move horizontally in the direction shown.

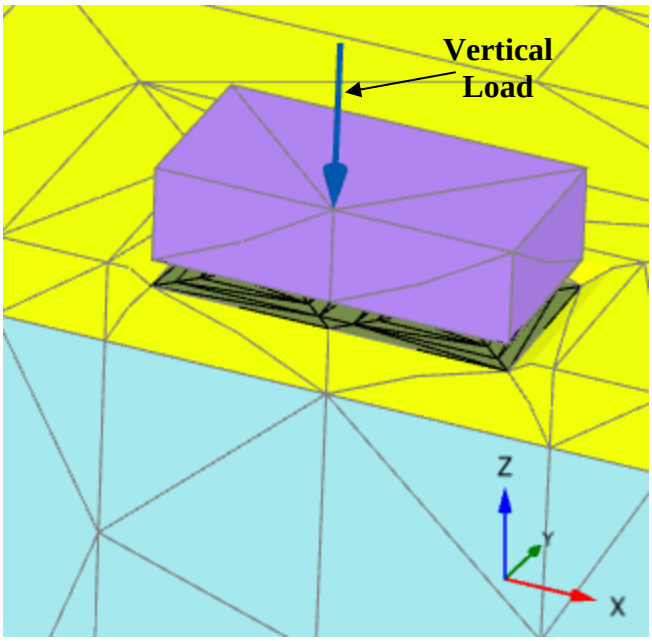

Fig. 5.14. Isometric close up of the upper half geometry of the finite element mesh – Vertical loading of footing.

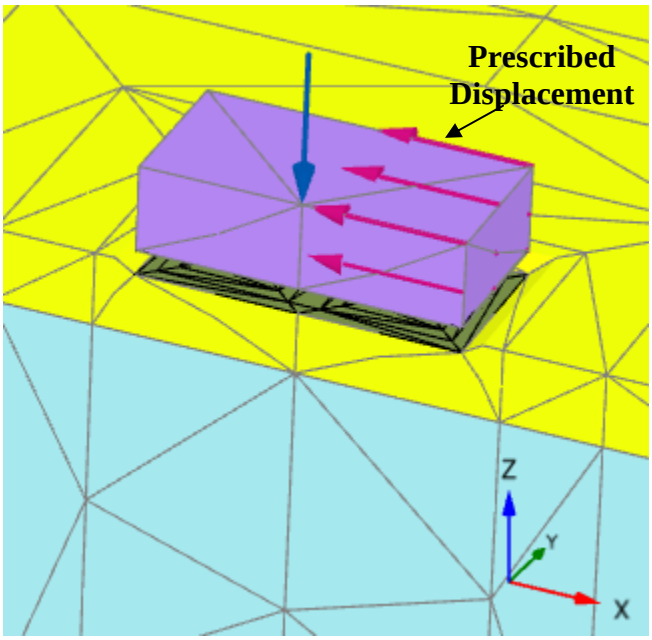

Fig. 5.15. Isometric close up of the upper half geometry of the finite element mesh – Horizontal loading of footing.

5.7 RESULTS

This section summarizes the results gathered from the parametric study. The influence of each variable in the lateral load-displacement response of the stiff column-supported shallow foundation are investigated, including the influence of the variables in the bending moment, shear, and axial load induced in the stiff columns.

5.7.1 *Lateral Load-Displacement Response*

5.7.1.1 Influence of the Load Transfer Platform Relative Density (LTP D_r)

The following figure shows the lateral load-displacement response of each parametric model that examined the influence of the relative density of the LTP:

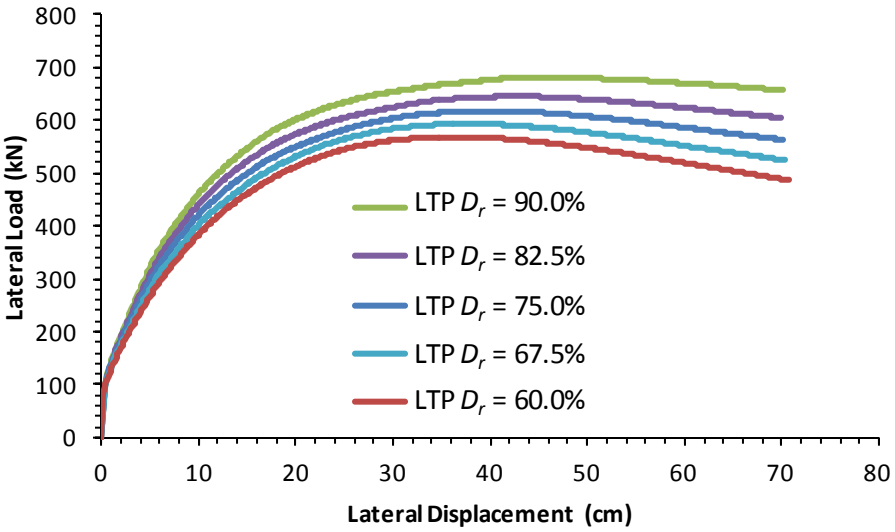

Fig. 5.16. Influence of the relative density of the LTP in the lateral load-displacement response.

The above figure shows that increasing the relative density of the LTP increased the stiffness of the lateral response and increased the lateral capacity of the system. In the parametric analysis,

the lateral capacity or the lateral load at yield (*LL*) of the stiff column-supported shallow foundation was defined as the maximum lateral load of the lateral load-displacement curve. With this consideration, it was possible to quantify the increase/decrease of the lateral capacity with changes in the LTP D_r, and the following table summarizes these results:

Table 5.20. Influence of the LTP D_r in the lateral load at yield

LTP D_r (%)	*SD*	*LL* yield (kN)	Δ% *LL* Yield (%)
60.0	-2	568.08	-7.98
67.5	-1	593.16	-3.91
75.0	0	617.32	0
82.5	1	644.62	4.42
90.0	2	680.36	10.21
$\|\bar{x}\| = \Sigma \|\Delta\%\| / 4$		=	6.63
ρ	=	0.997	

Information on the linear correlation between the variable examined and the lateral capacity is presented in terms of the coefficient of correlation ρ at the end of the table. A value $|\bar{x}|$ is shown indicating the average of the absolute value of the percent changes different to zero, that will aid in later comparing the level of influence of each variable with respect to the rest of variables examined.

5.7.1.2 Influence of the Undrained Shear Strength Ratio of the Soft Clay (s_u/σ_v') as Reflected in Values of the Overconsolidation Ratio (*OCR*) with the Liquidity Index (I_L)

The following figure shows the lateral load-displacement response of each parametric model that examined the influence of the undrained shear strength ratio of the soft clay using the liquidity index as an indicator of the overconsolidation ratio:

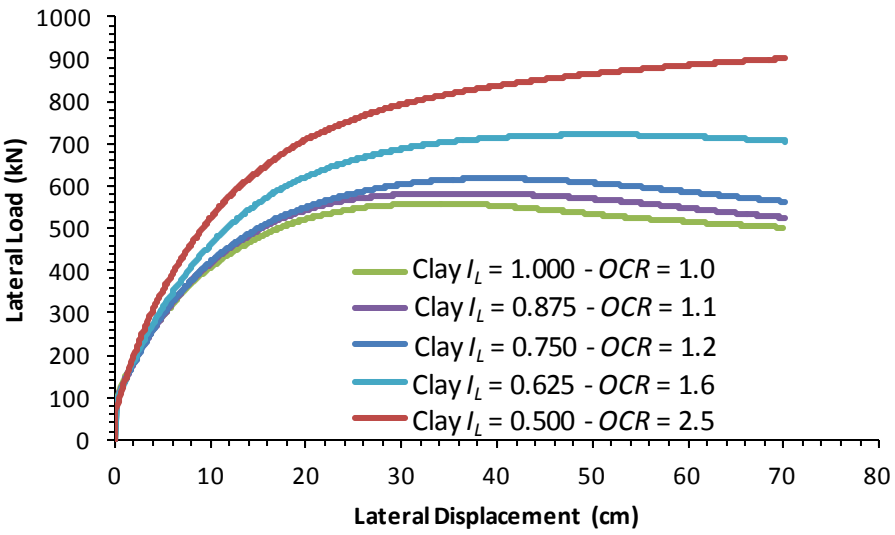

Fig. 5.17. Influence of the overconsolidation ratio, reflected by the liquidity index, of the clay layer in the lateral load-displacement response.

The following table shows the percent changes in the lateral capacity with variation in the undrained shear strength ratio of the clay layer, as reflected by changes in its overconsolidation ratio with the liquidity index. The trend shows that the lateral capacity increased with increasing undrained shear strength ratio, and hence overconsolidation ratio, shown in the table as a decrease in the liquidity index. The overall stiffness of the lateral response increased with increasing undrained shear strength ratio.

Table 5.21. Influence of the soft clay s_u/σ_v', reflected by *OCR* with I_L, in the lateral load at yield

Clay I_L	*SD*	*LL* yield (kN)	Δ% *LL* Yield (%)
0.500	-2	901.09	45.97
0.625	-1	721.07	16.81
0.750	0	617.32	0
0.875	1	581.85	-5.75
1.000	2	557.90	-9.63
$\|\bar{x}\| = \Sigma \|\Delta\%\| / 4$		=	19.54
ρ	=	-0.929	

5.7.1.3 Influence of the Unconfined Compressive Strength of the Stiff Columns (q_u)

The following figure shows the lateral load-displacement response of each parametric model that examined the influence of the unconfined compressive strength of the stiff columns:

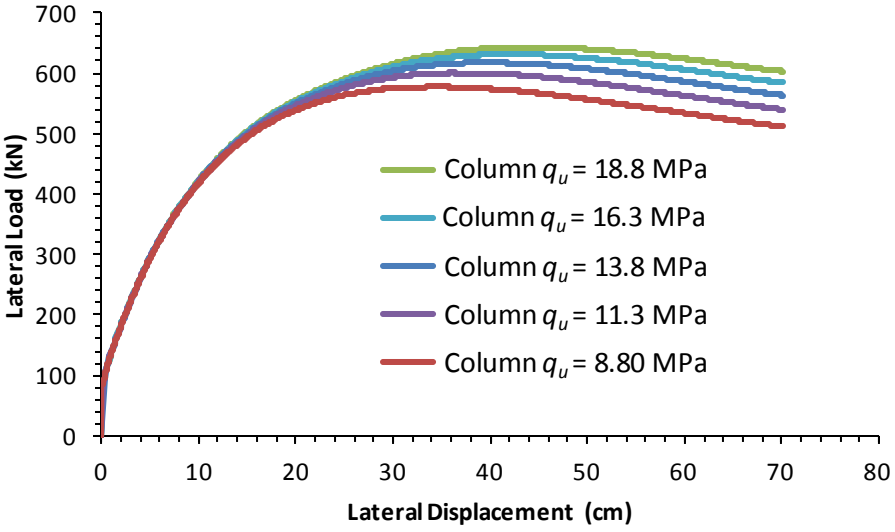

Fig. 5.18. Influence of the unconfined compressive strength of the stiff columns in the lateral load-displacement response.

The following table provides the percent change in the lateral capacity of the system with changes in the variable examined. The results show that the pre-yield stiffness remained essentially the same, regardless of changes in the unconfined compressive strength, although the calculations showed that the lateral capacity tended to increase with increasing unconfined compressive strength.

Table 5.22. Influence of the stiff column q_u in the lateral load at yield

Column q_u (MPa)	*SD*	*LL* yield (kN)	Δ% *LL* Yield (%)
8.8	-2	577.24	-6.49
11.3	-1	600.11	-2.79
13.8	0	617.32	0
16.3	1	631.18	2.25
18.8	2	643.01	4.16
$\|\bar{x}\| = \Sigma \|\Delta\%\| / 4$		=	3.92
ρ	=	0.991	

5.7.1.4 Influence of the Load Transfer Platform Thickness (LTP *H*)

The figure below shows the influence of the LTP thickness in the lateral response of the stiff column-supported shallow foundation:

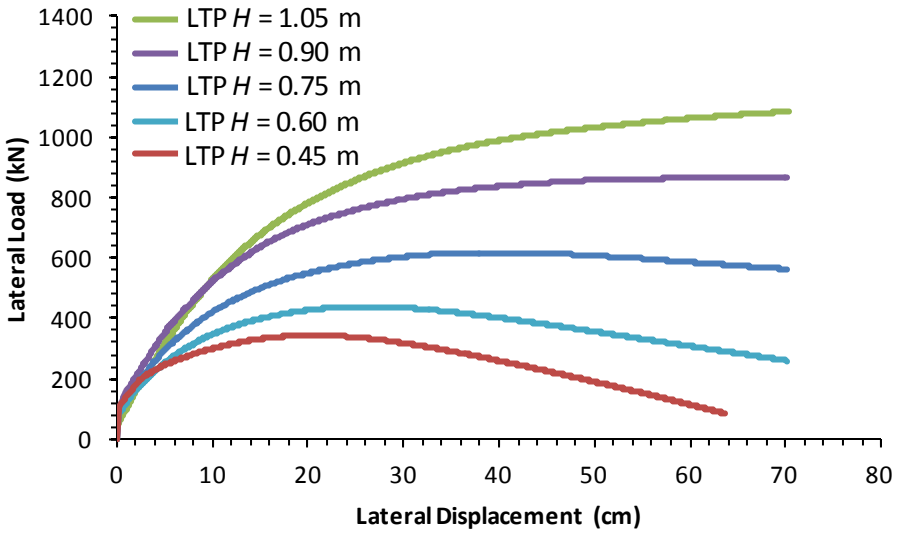

Fig. 5.19. Influence of the LTP thickness in the lateral load-displacement response.

The table below shows the percent changes of the lateral capacity of the parametric models that examined the influence of the thickness of the LTP. Similar to the experimental and numerical results presented in previous chapters, increasing the thickness of the LTP increased the lateral capacity of the stiff column-supported shallow foundation, increased the pre-yield stiffness response and decreased the post-yield softening response.

Table 5.23. Influence of the LTP *H* in the lateral load at yield

LTP *H* (m)	*SD*	*LL* yield (kN)	Δ% *LL* Yield (%)
0.45	-2	343.37	-44.38
0.60	-1	438.86	-28.91
0.75	0	617.32	0
0.90	1	864.73	40.08
1.05	2	1084.27	75.64
$\lvert\bar{x}\rvert = \Sigma \lvert\Delta\%\rvert / 4$		=	47.25
ρ	=	0.989	

5.7.1.5 Influence of the Stiff Column Diameter (Column *D*)

The figure below shows the influence of the stiff column diameter in the lateral response of the stiff column-supported shallow foundation:

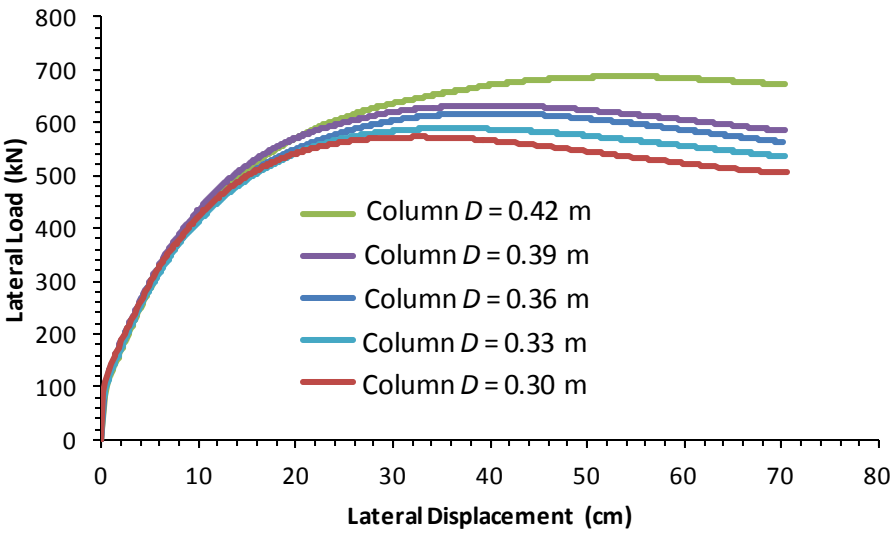

Fig. 5.20. Influence of the stiff column diameter in the lateral load-displacement response.

The table below shows the percent changes of the lateral load at yield, for each parametric variation of the stiff column diameter examined:

Table 5.24. Influence of the stiff column *D* in the lateral load at yield

Column *D* (m)	*SD*	*LL* yield (kN)	Δ% *LL* Yield (%)
0.30	-2	572.54	-7.25
0.33	-1	588.79	-4.62
0.36	0	617.32	0
0.39	1	631.89	2.36
0.42	2	686.34	11.18
$\|\bar{x}\| = \Sigma \|\Delta\%\| / 4$		=	6.35
ρ	=	0.971	

The previous results show that an increase in the diameter of the stiff column was accompanied by an increase in the lateral capacity of the system. Overall, the pre-yield stiffness response remained the same regardless of the stiff column diameter.

5.7.1.6 Influence of the Stiff Column Length (Column *L*)

The figure below shows the influence of the stiff column length in the lateral response of the stiff column-supported shallow foundation:

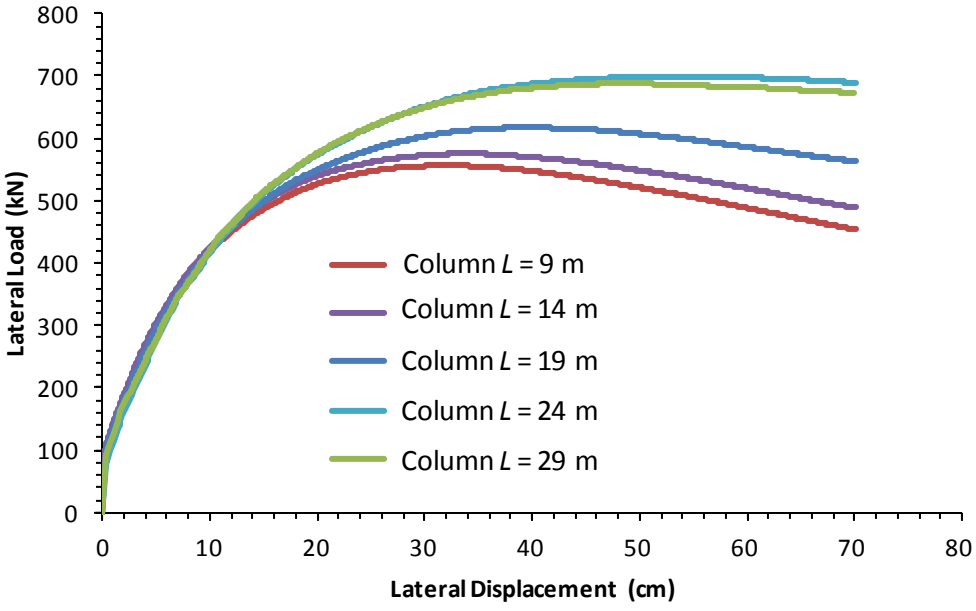

Fig. 5.21. Influence of the stiff column length in the lateral load-displacement response.

The following table shows the percent changes of the lateral load at yield, for each parametric variation of the stiff column length examined:

Table 5.25. Influence of the stiff column *L* in the lateral load at yield

Column *L* (m)	*SD*	*LL* yield (kN)	Δ% *LL* Yield (%)
9	-2	556.52	-9.85
14	-1	575.78	-6.73
19	0	617.32	0
24	1	699.00	13.23
29	2	687.73	11.41
$\|\bar{x}\| = \Sigma \|\Delta\%\| / 4$		=	10.31
ρ	=	0.948	

The trend observed for this variable indicates that the lateral capacity increased with increasing column length, although if the stiff column was sufficiently long, it was not expected for the lateral capacity to keep increasing anymore beyond this column length.

5.7.1.7 Influence of the Stiff Column Spacing (Column *S*)

The figure below shows the influence of the stiff column spacing in the lateral response of the stiff column-supported shallow foundation:

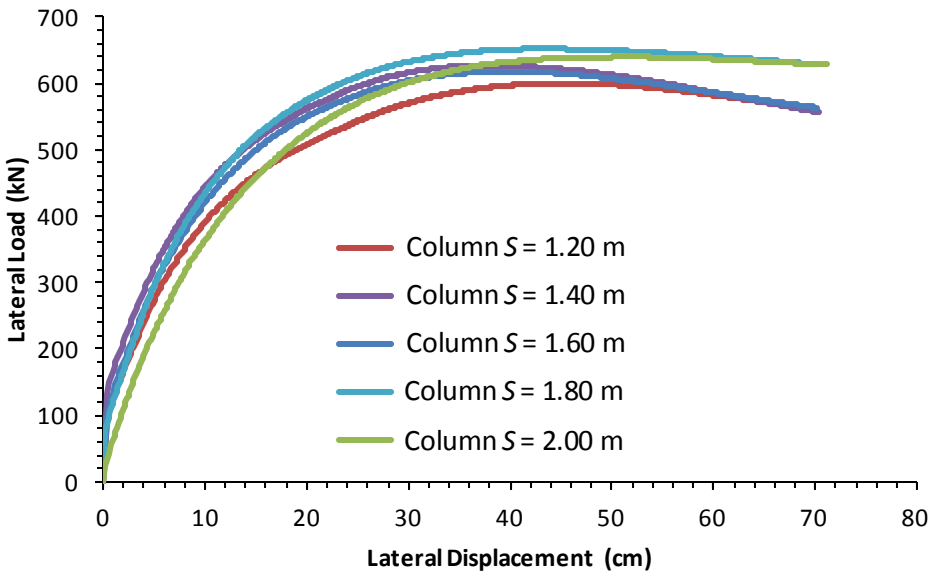

Fig. 5.22. Influence of the stiff column spacing in the lateral load-displacement response.

The following table provides a summary of the percent changes of the lateral load at yield, for each parametric variation of stiff column spacing examined:

Table 5.26. Influence of the stiff column *S* in the lateral load at yield

Column *S* (m)	*SD*	*LL* yield (kN)	Δ% *LL* Yield (%)
1.2	-2	599.83	-2.83
1.4	-1	626.35	1.46
1.6	0	617.32	0
1.8	1	651.59	5.55
2.0	2	639.62	3.61
$\lvert\bar{x}\rvert = \Sigma \lvert\Delta\%\rvert / 4$		=	3.36
ρ	=	0.830	

The results indicate an increase in the lateral capacity with stiff column spacing, although the influence of this variable in the lateral capacity exhibited the lowest linear correlation of all the variables examined.

5.7.1.8 Summary of the Effect of the Variables in the Lateral Capacity

The influences of the various material-based and geometry-based variables on the lateral capacity of the stiff column-supported shallow foundation were investigated in relation to the average of the absolute values of the percent changes $|\bar{x}|$. The results of the parametric study showed that the undrained shear strength ratio of the clay layer, using the overconsolidation ratio with the liquidity index as its indicator, was the material-based variable that most significantly influenced the overall lateral capacity of the system. The LTP thickness was the geometry-based variable that most significantly influenced the lateral capacity. The material-based variable with the least influence was the unconfined compressive strength of the stiff columns, and the geometry-based variable with the least influence was the stiff column spacing.

Based on the coefficient of correlation data presented, all variables exhibited positive linear correlation with the lateral capacity, with the exception of the liquidity index of the clay layer which exhibited a negative linear correlation as expected. However, because the liquidity index is used as an index of the overconsolidation ratio, a positive linear correlation is expected between the undrained shear strength ratio and the lateral capacity, reflected by the trend of associating an increase in the undrained shear strength ratio with an increase in the overconsolidation ratio, and the latter with a decrease in the liquidity index. The relative density

of the LTP exhibited the greatest positive correlation, and the stiff column spacing exhibited the lowest degree of linear positive correlation of all the variables examined.

5.7.2 *Bending Moment and Shear in the x-direction*

This section examines the parametric results that indicate the changes in the bending moment and shear distributions in the *x*-direction of the stiff column layout implemented in the parametric models. The load distributions of the stiff columns of the base model are presented as a baseline to highlight particular loading conditions of interest. The effect of each of the variables on the selected loading conditions was examined via additional tables. The examination of the loading in the stiff columns was carried out by considering that failure or yield of the stiff column-supported shallow foundation occurred at the maximum lateral load recorded from the lateral load-displacement curves previously shown.

5.7.2.1 Base Model Loading Conditions

The figures below show the distributions of bending moment and shear in the *x*-direction of the left and right columns of the base model:

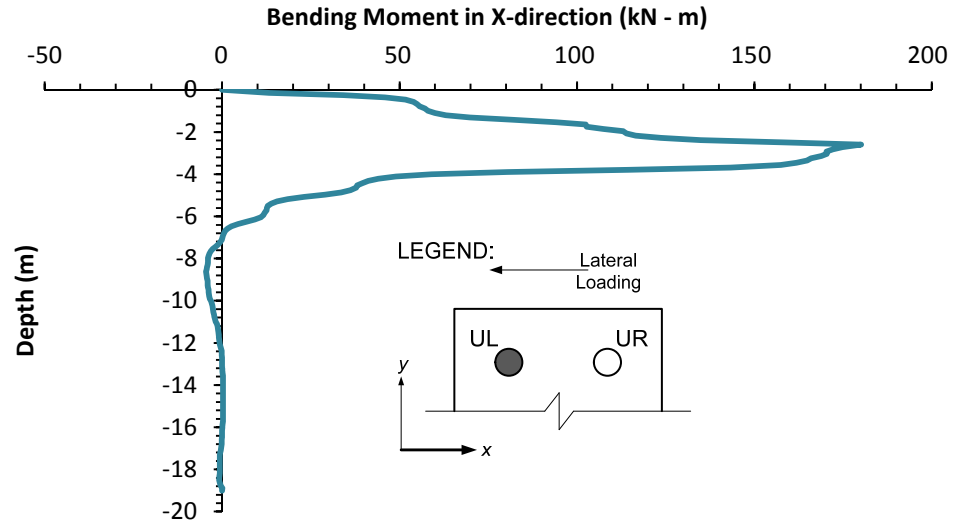

Fig. 5.23. Distribution of the bending moment in the *x*-direction of the left column – Base model.

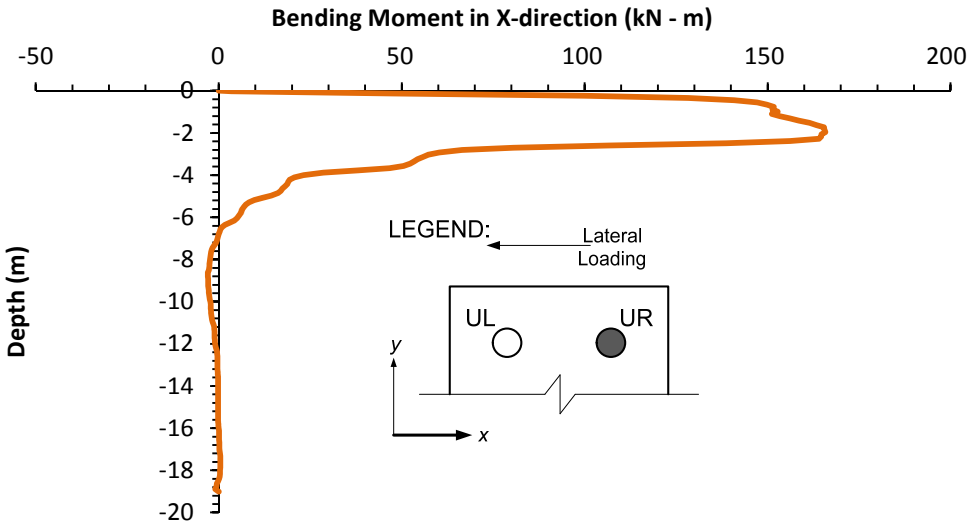

Fig. 5.24. Distribution of the bending moment in the *x*-direction of the right column – Base model.

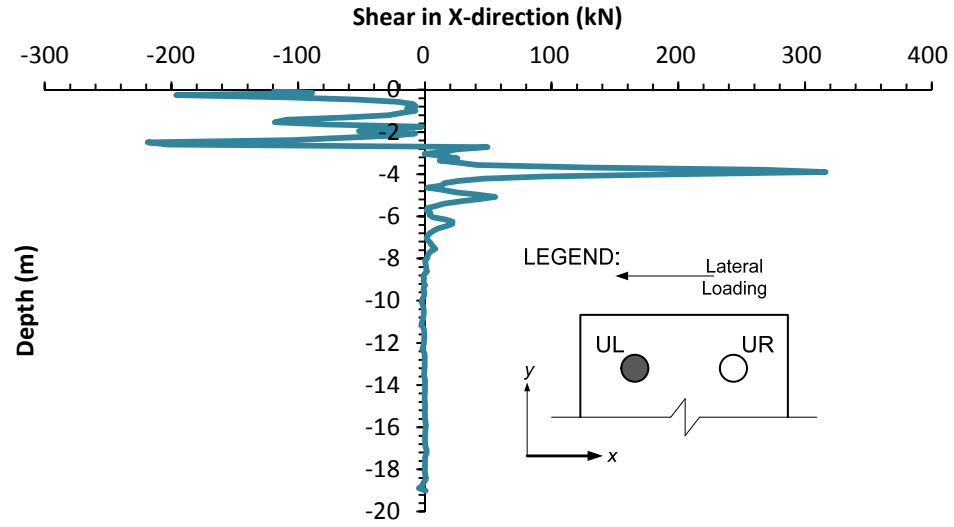

Fig. 5.25. Distribution of the shear in the *x*-direction of the left column – Base model.

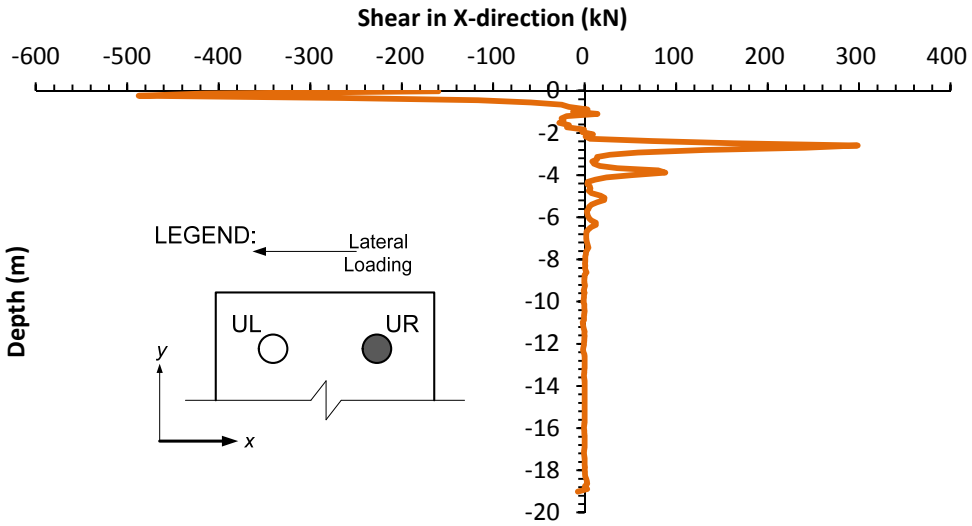

Fig. 5.26. Distribution of the shear in the *x*-direction of the right column – Base model.

Particular loading conditions of interest that were further examined include the maximum positive bending moment, and the maximum positive and negative shear experienced by the stiff

columns. Subsequent sections expand on the influence of the variables in the response of these particular loading conditions.

5.7.2.2 Influence of the Load Transfer Platform Relative Density (LTP D_r)

The following tables show the influence of the relative density of the LTP in the loading conditions selected. Similar to previous results, the average of the absolute values of the percent changes different to zero $|\bar{x}|$ was used to examine the level of influence of the parametric variable in the loading condition selected. Values of the coefficient of correlation ρ between the variable and the loading conditions examined were included at the end of each table.

Table 5.27. Influence of the LTP D_r in the maximum bending moment in the *x*-direction

		Max. Positive Bending Moment			
LTP D_r (%)	*SD*	Left (kN-m)	Δ% Left (%)	Right (kN-m)	Δ% Right (%)
60.0	-2	148.43	-17.6	147.18	-11.20
67.5	-1	157.78	-12.41	148.68	-10.30
75.0	0	180.13	0	165.75	0
82.5	1	202.86	12.62	181.80	9.68
90.0	2	241.22	33.91	243.04	46.63
$\|\bar{x}\| = \Sigma \|\Delta\%\| / 4$		=	19.14		19.45
ρ	=	0.977		0.903	

Table 5.28. Influence of the LTP D_r in the maximum positive and negative shear in the *x*-direction

		Max. Positive Shear				Max. Negative Shear			
LTP D_r (%)	*SD*	Left (kN)	Δ% Left (%)	Right (kN)	Δ% Right (%)	Left (kN)	Δ% Left (%)	Right (kN)	Δ% Right (%)
60.0	-2	260.31	-17.69	257.45	-13.76	-189.91	-13.14	-427.48	-12.27
67.5	-1	276.34	-12.62	257.14	-13.86	-193.90	-11.32	-433.32	-11.07
75.0	0	316.26	0	298.53	0	-218.64	0	-487.28	0
82.5	1	352.41	11.43	335.25	12.30	-239.81	9.68	-538.34	10.48
90.0	2	419.94	32.78	509.20	70.57	-288.79	32.08	-715.30	46.79
$\|\bar{x}\| = \Sigma \|\Delta\%\| / 4$		=	18.63		27.62		16.56		20.15
ρ	=	0.976		0.880		-0.954		-0.913	

For the loading conditions examined, the results show that an increase in the relative density of the LTP produced a positive increase in the maximum positive bending moment in both the left and right columns. In the case of the shear of both stiff columns, the maximum positive shear became increasingly positive, while the maximum negative shear became more negative with increasing relative density, resulting in the calculation of negative linear correlations between the relative density and the maximum negative shear.

5.7.2.3 Influence of the Undrained Shear Strength Ratio of the Soft Clay (s_u/σ_v') as Reflected in Values of the Overconsolidation Ratio (OCR) with the Liquidity Index (I_L)

The following tables show the influence of the undrained shear strength ratio of the soft clay, reflected by its overconsolidation ratio using the liquidity index, in the loading conditions examined:

Table 5.29. Influence of the soft clay s_u/σ_v', reflected by *OCR* with I_L, in the maximum bending moment in the *x*-direction

		Max. Positive Bending Moment			
Clay I_L	*SD*	Left (kN-m)	Δ% Left (%)	Right (kN-m)	Δ% Right (%)
0.500	-2	480.62	166.82	309.14	86.51
0.625	-1	265.85	47.59	218.01	31.53
0.750	0	180.13	0	165.75	0
0.875	1	173.18	-3.86	173.24	4.52
1.000	2	124.10	-31.11	123.16	-25.70
$\|\bar{x}\| = \Sigma \|\Delta\%\| / 4$		=	62.35		37.07
ρ		=	-0.901	-0.932	

Table 5.30. Influence of the soft clay s_u/σ_v', reflected by *OCR* with I_L, in the maximum positive and negative shear in the *x*-direction

		Max. Positive Shear				Max. Negative Shear			
Clay I_L	*SD*	Left (kN)	Δ% Left (%)	Right (kN)	Δ% Right (%)	Left (kN)	Δ% Left (%)	Right (kN)	Δ% Right (%)
0.500	-2	1439.28	355.09	740.96	148.20	-713.89	226.51	-985.47	102.24
0.625	-1	497.53	57.32	493.05	65.16	-334.76	53.11	-671.69	37.84
0.750	0	316.26	0	298.53	0	-218.64	0	-487.28	0
0.875	1	305.59	-3.37	312.26	4.60	-212.46	-2.83	-499.19	2.44
1.000	2	204.59	-35.31	165.30	-44.63	-171.83	-21.41	-335.30	-31.19
$\|\bar{x}\| = \Sigma \|\Delta\%\| / 4$		=	112.77		65.65		75.97		43.43
ρ		=	-0.830	-0.947		0.856		0.938	

A decrease in the undrained shear strength ratio, or presented in the table as an increase in the liquidity index resulting in a decrease in the overconsolidation ratio, was accompanied by a decrease in the maximum positive bending moment in the left column, and in the case of the shear experienced by this same column, the maximum positive shear became less positive, while the maximum negative shear became less negative. A similar pattern was observed in the right column. The trends resulted in the calculation of only positive linear correlations between the liquidity index and the maximum negative shear in both stiff columns.

5.7.2.4 Influence of the Unconfined Compressive Strength of the Stiff Columns (q_u)

The following tables show the influence of the unconfined compressive strength of the stiff columns in the loading conditions examined:

Table 5.31. Influence of the stiff column q_u in the maximum bending moment in the *x*-direction

		Max. Positive Bending Moment			
Column q_u (MPa)	*SD*	Left (kN-m)	Δ% Left (%)	Right (kN-m)	Δ% Right (%)
8.8	-2	150.28	-16.57	149.88	-9.57
11.3	-1	153.17	-14.97	141.96	-14.35
13.8	0	180.13	0	165.75	0
16.3	1	186.90	3.76	163.90	-1.12
18.8	2	221.29	22.85	185.88	12.14
$\|\bar{x}\| = \Sigma \|\Delta\%\| / 4$		=	14.54		9.30
ρ	=	0.961		0.882	

Table 5.32. Influence of the stiff column q_u in the maximum positive and negative shear in the *x*-direction

		Max. Positive Shear				Max. Negative Shear			
Column q_u (MPa)	*SD*	Left (kN)	Δ% Left (%)	Right (kN)	Δ% Right (%)	Left (kN)	Δ% Left (%)	Right (kN)	Δ% Right (%)
8.8	-2	194.29	-38.57	341.09	14.26	-171.90	-21.38	-433.81	-10.97
11.3	-1	241.22	-23.73	278.56	-6.69	-176.70	-19.18	-414.34	-14.97
13.8	0	316.26	0	298.53	0	-218.64	0	-487.28	0
16.3	1	346.65	9.61	248.09	-16.90	-264.60	21.02	-477.30	-2.05
18.8	2	427.25	35.09	257.63	-13.70	-349.65	59.92	-539.06	10.63
$\|\bar{x}\| = \Sigma \|\Delta\%\| / 4$		=	26.75		12.89		30.38		9.66
ρ	=	0.993		-0.843		-0.953		-0.886	

The results show that, in the case of the left column, an increase in its unconfined compressive strength increased the maximum positive bending moment it experienced. A similar trend was observed for the shear, in which the maximum positive shear became increasingly positive, while the maximum negative shear became increasingly negative with increasing stiff column strength, resulting in the calculation of a negative linear correlation for the latter. In the case of the right column, in general, the maximum positive bending moment tended to increase with increasing stiff column strength, albeit with a lower degree of linear correlation compared to its left counterpart. In the case of the shear of the right column, the maximum positive shear tended to becomes less positive with increasing stiff column strength, and the maximum negative shear tended to become more negative, resulting in the calculation of negative linear correlations for both of these loading cases.

5.7.2.5 Influence of the Load Transfer Platform Thickness (LTP *H*)

The following tables show the influence of the thickness of the LTP in the loading conditions examined:

Table 5.33. Influence of the LTP *H* in the maximum bending moment in the *x*-direction

		Max. Positive Bending Moment			
LTP *H* (m)	*SD*	Left (kN-m)	Δ% Left (%)	Right (kN-m)	Δ% Right (%)
0.45	-2	70.78	-60.71	76.24	-54.00
0.60	-1	97.76	-45.73	95.17	-42.58
0.75	0	180.13	0	165.75	0
0.90	1	275.40	52.89	277.99	67.72
1.05	2	287.64	59.68	287.40	73.39
$\|\bar{x}\| = \Sigma \|\Delta\%\| / 4$		=	54.75		59.42
ρ	=	0.975		0.965	

Table 5.34. Influence of the LTP *H* in the maximum positive and negative shear in the *x*-direction

		Max. Positive Shear				Max. Negative Shear			
LTP *H* (m)	*SD*	Left (kN)	Δ% Left (%)	Right (kN)	Δ% Right (%)	Left (kN)	Δ% Left (%)	Right (kN)	Δ% Right (%)
0.45	-2	62.69	-80.18	89.68	-69.96	-108.04	-50.59	-166.87	-65.75
0.60	-1	104.95	-66.82	120.78	-59.54	-115.09	-47.36	-214.39	-56.00
0.75	0	316.26	0	298.53	0	-218.64	0	-487.28	0
0.90	1	460.88	45.73	525.00	75.86	-402.65	84.16	-695.38	42.71
1.05	2	249.89	-20.99	386.77	29.56	-421.58	92.82	-965.46	98.13
$\|\bar{x}\| = \Sigma \|\Delta\%\| / 4$		=	54.43		58.73		68.73		65.65
ρ	=	0.715		0.865		-0.953		-0.983	

The results show that the maximum positive bending moment tended to increase with increasing LTP thickness, and this was true for both the left and right columns. When examining the shear, both the left and right columns experienced an increase in the maximum positive shear, while the maximum negative shear became increasingly negative with increasing LTP thickness, resulting in negative linear correlations for the latter loading case. Although negative, higher degrees of linear correlation were calculated between the maximum negative shear and the LTP thickness than those calculated between the maximum positive shear and the LTP thickness.

5.7.2.6 Influence of the Stiff Column Diameter (Column *D*)

The following tables show the influence of the stiff column diameter in the loading conditions examined:

Table 5.35. Influence of the stiff column *D* in the maximum bending moment in the *x*-direction

		Max. Positive Bending Moment			
Column *D* (m)	*SD*	Left (kN-m)	Δ% Left (%)	Right (kN-m)	Δ% Right (%)
0.30	-2	82.65	-54.12	81.31	-50.94
0.33	-1	118.97	-33.95	145.27	-12.36
0.36	0	180.13	0	165.75	0
0.39	1	218.74	21.43	233.15	40.66
0.42	2	413.88	129.77	302.58	82.55
$\|\bar{x}\| = \Sigma \|\Delta\%\| / 4$		=	59.82		46.63
ρ	=	0.933		0.988	

Table 5.36. Influence of the stiff column *D* in the maximum positive and negative shear in the *x*-direction

		Max. Positive Shear				Max. Negative Shear			
Column *D* (m)	*SD*	Left (kN)	Δ% Left (%)	Right (kN)	Δ% Right (%)	Left (kN)	Δ% Left (%)	Right (kN)	Δ% Right (%)
0.30	-2	106.87	-66.21	167.68	-43.83	-131.85	-39.70	-370.28	-24.01
0.33	-1	225.89	-28.57	334.07	11.91	-171.64	-21.50	-440.78	-9.54
0.36	0	316.26	0	298.53	0	-218.64	0	-487.28	0
0.39	1	315.98	-0.09	434.50	45.55	-371.72	70.01	-337.41	-30.76
0.42	2	485.47	53.50	473.85	58.73	-598.08	173.55	-516.66	6.03
$\|\bar{x}\| = \Sigma \|\Delta\%\| / 4$		=	37.09		40.00		76.19		17.59
ρ	=	0.964		0.934		-0.939		-0.394	

The results show that the maximum positive bending moment increased with increasing stiff column diameter in both the left and right columns. A similar trend was observed in both stiff columns when examining the maximum positive shear, in which this quantity became more positive with increasing stiff column diameter. In the case of the maximum negative shear in the left column, this quantity became increasingly negative with increasing column diameter, and while a similar pattern was observed in the right column, the linear correlation in the right column was significantly weaker compared to its left counterpart.

5.7.2.7 Influence of the Stiff Column Length (Column *L*)

The following tables show the influence of the stiff column length in the loading conditions examined:

Table 5.37. Influence of the stiff column *L* in the maximum bending moment in the *x*-direction

		Max. Positive Bending Moment			
Column *L* (m)	*SD*	Left (kN-m)	Δ% Left (%)	Right (kN-m)	Δ% Right (%)
9	-2	181.27	0.63	161.54	-2.54
14	-1	162.57	-9.75	183.03	10.43
19	0	180.13	0	165.75	0
24	1	271.17	50.54	221.28	33.50
29	2	243.15	34.99	174.31	5.16
$\lvert\bar{x}\rvert = \Sigma \lvert\Delta\%\rvert / 4$		=	23.98		12.91
ρ	=	0.784		0.422	

Table 5.38. Influence of the stiff column *L* in the maximum positive and negative shear in the *x*-direction

		Max. Positive Shear				Max. Negative Shear			
Column *L* (m)	*SD*	Left (kN)	Δ% Left (%)	Right (kN)	Δ% Right (%)	Left (kN)	Δ% Left (%)	Right (kN)	Δ% Right (%)
9	-2	315.14	-0.35	234.76	-21.36	-275.18	25.86	-264.78	-45.66
14	-1	273.23	-13.61	311.31	4.28	-243.82	11.52	-312.18	-35.93
19	0	316.26	0	298.53	0	-218.64	0	-487.28	0
24	1	591.13	86.91	401.16	34.38	-526.32	140.72	-522.89	7.31
29	2	490.52	55.10	403.26	35.08	-528.03	141.51	-528.05	8.37
$\lvert\bar{x}\rvert = \Sigma \lvert\Delta\%\rvert / 4$		=	38.99		23.78		79.90		24.32
ρ	=	0.772		0.935		-0.802		-0.933	

The results show that, in general, there was a tendency for the maximum positive bending moment in the left column to increase with increasing stiff column length. A similar trend was also observed in the right column, albeit with a weaker linear correlation compared to the left column. In the case of the maximum positive and negative shear in both the left and right columns, the maximum positive shear became more positive with increasing stiff column length, while the maximum negative shear became more negative, resulting in negative linear correlations for the latter case.

5.7.2.8 Influence of the Stiff Column Spacing (Column *S*)

The following tables show the influence of the stiff column spacing in the loading conditions examined:

Table 5.39. Influence of the stiff column *S* in the maximum bending moment in the *x*-direction

		Max. Positive Bending Moment			
Column *S* (m)	*SD*	Left (kN-m)	Δ% Left (%)	Right (kN-m)	Δ% Right (%)
1.2	-2	274.90	52.61	144.68	-12.71
1.4	-1	192.36	6.79	117.65	-29.02
1.6	0	180.13	0	165.75	0
1.8	1	189.14	5.00	245.76	48.27
2.0	2	212.49	17.96	319.98	93.05
$\|\bar{x}\| = \Sigma \|\Delta\%\| / 4$		=	20.59		45.76
ρ	=	-0.529		0.913	

Table 5.40. Influence of the stiff column *S* in the maximum positive and negative shear in the *x*-direction

		Max. Positive Shear				Max. Negative Shear			
Column *S* (m)	*SD*	Left (kN)	Δ% Left (%)	Right (kN)	Δ% Right (%)	Left (kN)	Δ% Left (%)	Right (kN)	Δ% Right (%)
1.2	-2	498.35	57.58	187.03	-37.35	-290.04	32.66	187.03	-138.38
1.4	-1	241.38	-23.68	145.84	-51.15	-294.08	34.50	-246.60	-49.39
1.6	0	316.26	0	298.53	0	-218.64	0	-487.28	0
1.8	1	215.38	-31.90	521.51	74.69	-233.05	6.59	-607.32	24.63
2.0	2	323.30	2.23	799.29	167.74	-248.73	13.76	-1110.15	127.83
$\|\bar{x}\| = \Sigma \|\Delta\%\| / 4$		=	28.85		82.73		21.88		85.06
ρ	=	-0.537		0.933		0.671		-0.980	

The results include the calculation of negative linear correlations between the stiff column spacing and the maximum positive bending moment and maximum positive shear of the left column, and between the stiff column spacing and the maximum negative shear of the right column. The strongest negative linear correlation was observed in the negative shear of the right column. In the right column, the maximum bending moment and maximum positive shear tended to increase with stiff column spacing, and the maximum negative shear of the left column became less negative with increasing stiff column spacing, resulting in the calculation of positive linear correlations in all cases. The strongest positive linear correlations were observed in the bending moment and shear of the right column.

5.7.2.9 Summary of the Effect of the Variables in the Bending Moment and Shear in the *x*-direction

The following tables show the values of the overall average $|\bar{X}|$ of the $|\bar{x}|$ data calculated in previous tables for the bending moment and shear loading conditions examined:

Table 5.41. Overall influence of the variables in the bending moment of the stiff columns in the *x*-direction

	Max. Positive Bending Moment $\|\bar{x}\|$		
Variable	Δ% Left (%)	Δ% Right (%)	$\|\bar{X}\|$ (%)
LTP D_r	19.14	19.45	19.30
Clay I_L	62.35	37.07	49.71
Column q_u	14.54	9.30	11.92
LTP H	54.75	59.42	57.09
Column D	59.82	46.63	53.23
Column L	23.98	12.91	18.45
Column S	20.59	45.76	33.18

Table 5.42. Overall influence of the variables in the shear of the stiff columns in the *x*-direction

	Max. Positive Shear $\lvert\bar{x}\rvert$		Max. Negative Shear $\lvert\bar{x}\rvert$		
Variable	Δ% Left (%)	Δ% Right (%)	Δ% Left (%)	Δ% Right (%)	$\lvert\bar{X}\rvert$ (%)
LTP D_r	18.63	27.62	16.56	20.15	20.74
Clay I_L	112.77	65.65	75.97	43.43	74.46
Column q_u	26.75	12.89	30.38	9.66	19.92
LTP H	53.43	58.73	68.73	65.65	61.64
Column D	37.09	40.01	76.19	17.59	42.72
Column L	38.99	23.78	79.9	24.32	41.75
Column S	28.85	82.73	21.88	85.06	54.63

The results from the previous tables indicate that the undrained shear strength ratio of the soft clay, with the liquidity index as an indicator of its overconsolidation ratio, was the material-based variable that produced the most significant percent changes in the development of bending moment and shear of the stiff columns, in the *x*-direction. The material-based variable with the least influence in the bending moment and shear loading conditions examined was the unconfined compressive strength of the stiff columns. In terms of the geometry-based variables examined, the LTP thickness was the variable that most impacted the bending moment and shear loading induced in the stiff columns, while the geometry-based variable with the least influence was the stiff column length.

5.7.3 *Bending Moment and Shear in the y-direction*

This section presents the parametric results of the bending moment and shear that developed in the *y*-direction of the stiff columns after the footing was laterally loaded. The structure of this

section is similar to the previous one in terms of showing the load distributions of the base model, and then further examining particular loading conditions of interest using tables to provide insight on the changes observed.

5.7.3.1 Base Model Loading Conditions

The figures below show the distributions of bending moment and shear in the *y*-direction of the left and right columns of the base model:

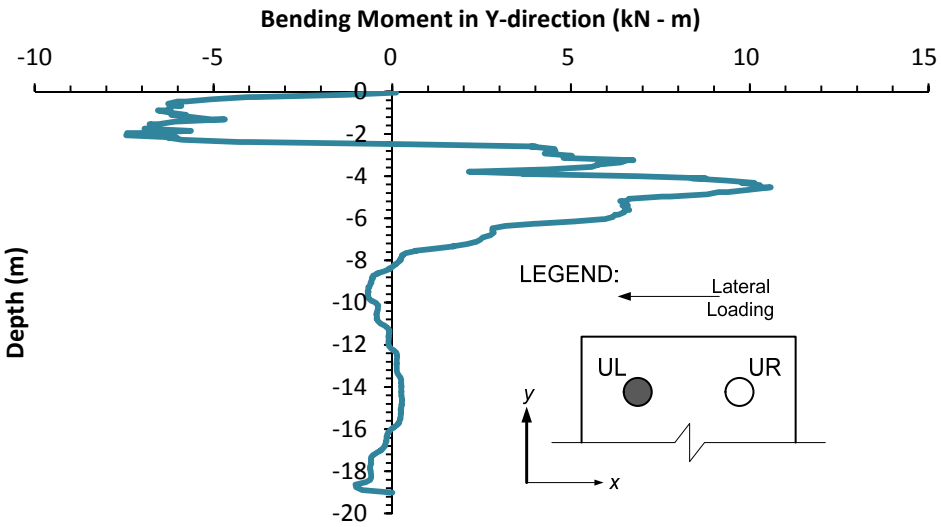

Fig. 5.27. Distribution of the bending moment in the *y*-direction of the left column – Base model.

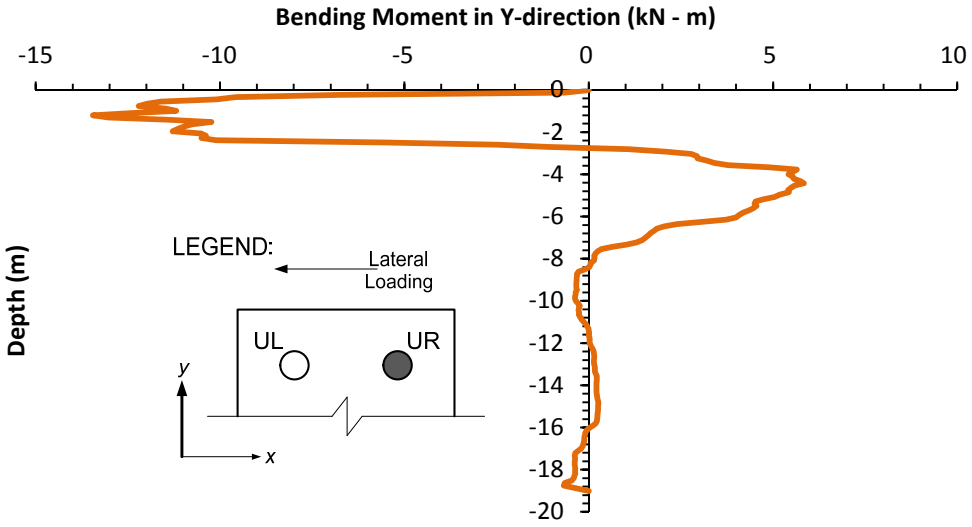

Fig. 5.28. Distribution of the bending moment in the *y*-direction of the right column – Base model.

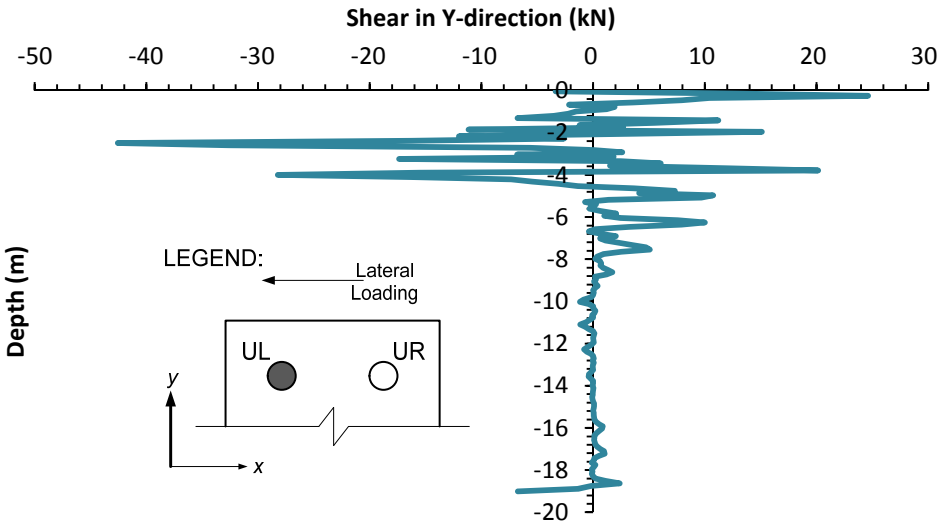

Fig. 5.29. Distribution of the shear in the *y*-direction of the left column – Base model.

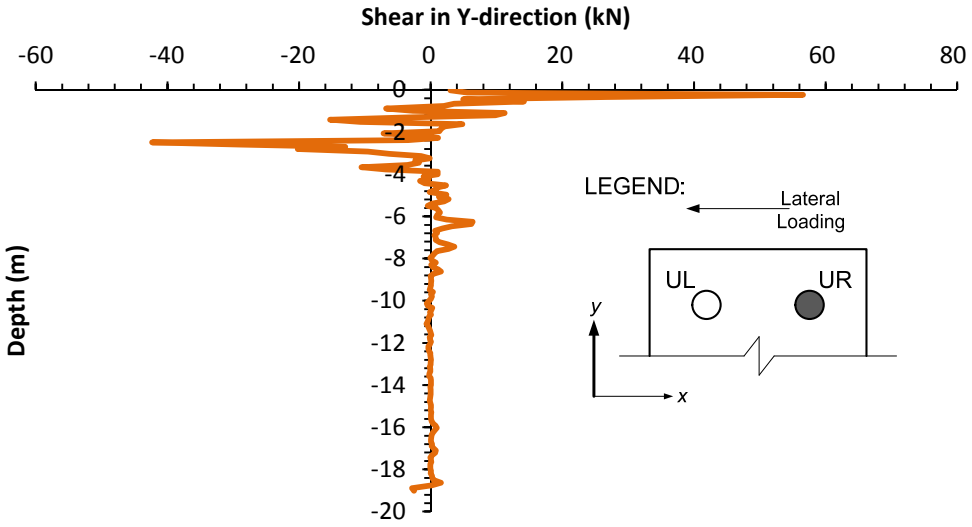

Fig. 5.30. Distribution of the shear in the *y*-direction of the right column – Base model.

The loading conditions examined were the maximum positive and maximum negative bending moment, and the maximum positive and negative shear experienced by the stiff columns in the *y*-direction.

5.7.3.2 Influence of the Load Transfer Platform Relative Density (LTP D_r)

The following tables show the influence of the relative density of the LTP in the loading conditions examined:

Table 5.43. Influence of the LTP D_r in the maximum positive and negative bending moment in the *y*-direction

		Max. Positive Bending Moment				Max. Negative Bending Moment			
LTP D_r (%)	*SD*	Left (kN-m)	Δ% Left (%)	Right (kN-m)	Δ% Right (%)	Left (kN-m)	Δ% Left (%)	Right (kN-m)	Δ% Right (%)
60.0	-2	10.42	-0.10	6.26	7.19	-7.70	3.49	-17.10	27.14
67.5	-1	10.32	-1.05	6.07	3.94	-7.26	-2.42	-15.29	13.68
75.0	0	10.43	0	5.84	0	-7.44	0	-13.45	0
82.5	1	10.42	-0.10	5.56	-4.79	-7.34	-1.34	-10.50	-21.93
90.0	2	11.30	8.34	6.41	9.76	-11.59	55.78	-20.05	49.07
$\|\bar{x}\| = \Sigma \|\Delta\%\| / 4$		=	2.40		6.42		15.76		27.96
ρ	=	0.724		-0.098		-0.666		-0.049	

Table 5.44. Influence of the LTP D_r in the maximum positive and negative shear in the *y*-direction

		Max. Positive Shear				Max. Negative Shear			
LTP D_r (%)	*SD*	Left (kN)	Δ% Left (%)	Right (kN)	Δ% Right (%)	Left (kN)	Δ% Left (%)	Right (kN)	Δ% Right (%)
60.0	-2	25.64	4.14	65.02	14.96	-31.39	-26.25	-45.69	7.99
67.5	-1	24.66	0.16	59.45	5.11	-34.86	-18.09	-42.64	0.78
75.0	0	24.62	0	56.56	0	-42.56	0	-42.31	0
82.5	1	27.13	10.19	48.76	-13.79	-51.43	20.84	-39.08	-7.63
90.0	2	31.41	27.58	88.90	57.18	-60.14	41.31	-71.49	68.97
$\|\bar{x}\| = \Sigma \|\Delta\%\| / 4$		=	10.52		22.76		26.62		21.34
ρ	=	0.784		0.385		-0.990		-0.575	

The results showed that the maximum positive and negative bending moments in the *y*-direction of the left column generally increased positively and negatively, respectively, with increasing relative density. On the other hand, there was very little correlation between the relative density, and the maximum positive and negative bending moments that developed in the right column. A similar trend was observed with the shear responses however stronger shear correlations were calculated in the right column compared to the bending moment correlations in this same column.

5.7.3.3 Influence of the Undrained Shear Strength Ratio of the Soft Clay (s_u/σ_v') as Reflected in Values of the Overconsolidation Ratio (*OCR*) with the Liquidity Index (I_L)

The following tables show the influence of the undrained shear strength ratio of the soft clay, reflected by its overconsolidation ratio using the liquidity index, in the loading conditions examined:

Table 5.45. Influence of the soft clay s_u/σ_v', reflected by *OCR* with I_L, in the maximum positive and negative bending moment in the *y*-direction

		Max. Positive Bending Moment				Max. Negative Bending Moment			
Clay I_L	*SD*	Left (kN-m)	Δ% Left (%)	Right (kN-m)	Δ% Right (%)	Left (kN-m)	Δ% Left (%)	Right (kN-m)	Δ% Right (%)
0.500	-2	21.48	105.94	7.34	25.68	-18.36	146.77	-23.3	73.23
0.625	-1	15.27	46.40	7.15	22.43	-9.44	26.88	-14.74	9.59
0.750	0	10.43	0	5.84	0	-7.44	0	-13.45	0
0.875	1	9.78	-6.23	5.02	-14.04	-8.55	14.92	-18.00	33.83
1.000	2	8.41	-19.37	4.43	-24.14	-4.70	-36.83	-13.83	2.83
$\|\bar{x}\| = \Sigma \|\Delta\%\| / 4$		=	44.49		21.57		56.35		29.87
ρ	=	-0.932		-0.982		0.864		0.602	

Table 5.46 Influence of the soft clay s_u/σ_v', reflected by *OCR* with I_L, in the maximum positive and negative shear in the *y*-direction

		Max. Positive Shear				Max. Negative Shear			
Clay I_L	*SD*	Left (kN)	Δ% Left (%)	Right (kN)	Δ% Right (%)	Left (kN)	Δ% Left (%)	Right (kN)	Δ% Right (%)
0.500	-2	75.75	207.68	117.83	108.33	-107.38	152.30	-94.8	124.06
0.625	-1	37.42	51.99	75.73	33.89	-78.20	83.74	-63.34	49.70
0.750	0	24.62	0	56.56	0	-42.56	0	-42.31	0
0.875	1	26.58	7.96	70.26	24.22	-34.90	-18.00	-48.64	14.96
1.000	2	18.24	-25.91	44.96	-20.51	-23.32	-45.21	-28.11	-33.56
$\|\bar{x}\| = \Sigma \|\Delta\%\| / 4$		=	73.39		46.74		74.81		55.57
ρ	=	-0.866		-0.861		0.963		0.922	

The results show that decreasing the liquidity index of the soft clay, which corresponded to the consideration of a less plastic, less compressible and stronger clayey material with a higher undrained shear strength ratio, produced a positive increase in the maximum positive shear and bending moment of both stiff columns, and it produced a negative increase in the maximum negative bending moment and shear of both stiff columns. This behavior resulted in the calculation of negative linear correlations between the liquidity index and the positive bending moment and positive shear of both stiff columns.

5.7.3.4 Influence of the Unconfined Compressive Strength of the Stiff Columns (q_u)

The following tables show the influence of the unconfined compressive strength of the stiff columns in the loading conditions examined:

Table 5.47. Influence of the stiff column q_u in the maximum positive and negative bending moment in the *y*-direction

		Max. Positive Bending Moment				Max. Negative Bending Moment			
Column q_u (MPa)	*SD*	Left (kN-m)	Δ% Left (%)	Right (kN-m)	Δ% Right (%)	Left (kN-m)	Δ% Left (%)	Right (kN-m)	Δ% Right (%)
8.8	-2	8.56	-17.93	5.40	-7.53	-7.68	3.23	-14.48	7.66
11.3	-1	8.94	-14.29	5.54	-5.14	-6.39	-14.11	-11.88	-11.67
13.8	0	10.43	0	5.84	0	-7.44	0	-13.45	0
16.3	1	11.40	9.30	5.91	1.20	-7.13	-4.17	-13.14	-2.30
18.8	2	12.67	21.48	6.16	5.48	-7.76	4.30	-14.59	8.48
$\|\bar{x}\| = \Sigma \|\Delta\%\| / 4$		=	15.75		4.84		6.45		7.53
ρ	=	0.989		0.987		-0.257		-0.211	

Table 5.48. Influence of the stiff column q_u in the maximum positive and negative shear in the *y*-direction

		Max. Positive Shear				Max. Negative Shear			
Column q_u (MPa)	*SD*	Left (kN)	Δ% Left (%)	Right (kN)	Δ% Right (%)	Left (kN)	Δ% Left (%)	Right (kN)	Δ% Right (%)
8.8	-2	26.83	8.98	58.16	2.83	-41.79	-1.81	-52.17	23.30
11.3	-1	22.72	-7.72	49.99	-11.62	-41.76	-1.88	-41.21	-2.60
13.8	0	24.62	0	56.56	0	-42.56	0	-42.31	0
16.3	1	25.10	1.95	54.05	-4.44	-42.55	-0.02	-35.90	-15.15
18.8	2	27.95	13.53	59.52	5.23	-47.80	12.31	-36.72	-13.21
$\|\bar{x}\| = \Sigma \|\Delta\%\| / 4$		=	8.05		6.03		4.00		13.57
ρ	=	0.361		0.285		-0.794		0.882	

The results show that maximum positive bending moment tended to increase positively with increasing stiff column strength, and this was true for both stiff columns. On the other hand, the maximum negative bending moment tended to increase negatively with increasing stiff column strength, and although negative, the correlations were significantly weaker than those calculated for the positive moment. With respect to the shear, the results indicate that the maximum negative shear in the left column increased negatively with increasing stiff column strength, resulting in a negative correlation. The maximum negative shear of the right column on the other hand, became less negative with increasing stiff column strength. In the case of the maximum positive shear of both stiff columns, the results show that this quantity increased positively with stiff column strength, albeit with weaker linear correlations compared to those calculated in the negative shear.

5.7.3.5 Influence of the Load Transfer Platform Thickness (LTP *H*)

The following tables show the influence of the thickness of the LTP in the loading conditions examined:

Table 5.49. Influence of the LTP *H* in the maximum positive and negative bending moment in the *y*-direction

		Max. Positive Bending Moment				Max. Negative Bending Moment			
LTP *H* (m)	*SD*	Left (kN-m)	Δ% Left (%)	Right (kN-m)	Δ% Right (%)	Left (kN-m)	Δ% Left (%)	Right (kN-m)	Δ% Right (%)
0.45	-2	6.00	-42.47	3.61	-38.18	-6.41	-13.84	-4.79	-64.39
0.60	-1	8.03	-23.01	5.84	0	-10.74	44.35	-8.18	-39.18
0.75	0	10.43	0	5.84	0	-7.44	0	-13.45	0
0.90	1	24.10	131.06	6.79	16.27	-15.72	111.29	-12.74	-5.28
1.05	2	19.52	87.15	15.13	159.08	-14.48	94.62	-0.81	-93.98
$\|\bar{x}\| = \Sigma \|\Delta\%\| / 4$		=	70.92		53.38		66.03		50.71
ρ	=	0.873		0.852		-0.809		0.101	

Table 5.50. Influence of the LTP *H* in the maximum positive and negative shear in the *y*-direction

		Max. Positive Shear				Max. Negative Shear			
LTP *H* (m)	*SD*	Left (kN)	Δ% Left (%)	Right (kN)	Δ% Right (%)	Left (kN)	Δ% Left (%)	Right (kN)	Δ% Right (%)
0.45	-2	18.37	-25.39	24.94	-55.91	-23.36	-45.11	-23.52	-44.41
0.60	-1	35.18	42.89	25.48	-54.95	-39.64	-6.86	-40.58	-4.09
0.75	0	24.62	0	56.56	0	-42.56	0	-42.31	0
0.90	1	137.74	459.46	99.28	75.53	-120.78	183.79	-80.16	89.46
1.05	2	50.44	104.87	32.22	-43.03	-75.11	76.48	-35.09	-17.06
$\|\bar{x}\| = \Sigma \|\Delta\%\| / 4$		=	158.15		57.36		78.06		38.76
ρ	=	0.541		0.442		-0.755		-0.465	

The results show that the maximum positive bending moment increased positively with increasing LTP thickness, and this was true for both stiff columns. The maximum negative bending moment of the left column increased negatively with increasing LTP thickness, however a weak positive correlation was observed on the right column. In the case of the shear of the stiff columns, both the maximum positive and negative shear increased positively and negatively, respectively, with increasing LTP thickness, with the strongest correlation calculated on the maximum negative shear of the left column.

5.7.3.6 Influence of the Stiff Column Diameter (Column *D*)

The following tables show the influence of the stiff column diameter in the loading conditions examined:

Table 5.51. Influence of the stiff column *D* in the maximum positive and negative bending moment in the *y*-direction

		Max. Positive Bending Moment				Max. Negative Bending Moment			
Column *D* (m)	*SD*	Left (kN-m)	Δ% Left (%)	Right (kN-m)	Δ% Right (%)	Left (kN-m)	Δ% Left (%)	Right (kN-m)	Δ% Right (%)
0.30	-2	7.32	-29.82	3.17	-45.72	-5.60	-24.73	-2.58	-80.82
0.33	-1	11.47	9.97	4.92	-15.75	-9.24	24.19	-13.86	3.05
0.36	0	10.43	0	5.84	0	-7.44	0	-13.45	0
0.39	1	13.58	30.20	7.43	27.23	-16.53	122.18	-14.58	8.40
0.42	2	19.74	89.26	10.19	74.49	-29.41	295.30	-15.07	12.04
$\lvert\bar{x}\rvert = \Sigma \lvert\Delta\%\rvert / 4$		=	39.81		40.80		116.6		26.08
ρ	=	0.920		0.983		-0.891		-0.774	

Table 5.52. Influence of the stiff column *D* in the maximum positive and negative shear in the *y*-direction

		Max. Positive Shear				Max. Negative Shear			
Column *D* (m)	*SD*	Left (kN)	Δ% Left (%)	Right (kN)	Δ% Right (%)	Left (kN)	Δ% Left (%)	Right (kN)	Δ% Right (%)
0.30	-2	39.70	61.25	29.33	-48.14	-32.16	-24.44	-22.98	-45.69
0.33	-1	43.97	78.59	48.39	-14.44	-75.06	76.36	-31.2	-26.26
0.36	0	24.62	0	56.56	0	-42.56	0	-42.31	0
0.39	1	41.61	69.01	47.37	-16.25	-77.74	82.66	-26.39	-37.63
0.42	2	81.14	229.57	81.73	44.50	-142.63	235.13	-71.35	68.64
$\lvert\bar{x}\rvert = \Sigma \lvert\Delta\%\rvert / 4$		=	109.61		30.83		104.65		44.56
ρ	=	0.608		0.862		-0.819		-0.742	

In general, the results show that the bending moment and shear increased, whether positively or negatively with increasing stiff column diameter, depending of the loading conditions examined, and this was true for both the left and right columns. Such trends resulted in the calculation of negative correlations for the negative moment and negative shear.

5.7.3.7 Influence of the Stiff Column Length (Column *L*)

The following tables show the influence of the stiff column length in the loading conditions examined:

Table 5.53. Influence of the stiff column *L* in the maximum positive and negative bending moment in the *y*-direction

		Max. Positive Bending Moment				Max. Negative Bending Moment			
Column *L* (m)	*SD*	Left (kN-m)	Δ% Left (%)	Right (kN-m)	Δ% Right (%)	Left (kN-m)	Δ% Left (%)	Right (kN-m)	Δ% Right (%)
9	-2	6.20	-40.56	8.37	43.32	-9.63	29.44	-1.74	-87.06
14	-1	16.16	54.94	6.47	10.79	-5.69	-23.52	-0.46	-96.58
19	0	10.43	0	5.84	0	-7.44	0	-13.45	0
24	1	10.98	5.27	11.60	98.63	-13.44	80.65	-23.47	74.50
29	2	11.93	14.38	8.05	37.84	-12.43	67.07	-6.39	-52.49
$\|\bar{x}\| = \Sigma \|\Delta\%\| / 4$		=	28.79		47.65		50.17		77.66
ρ	=	0.279		0.317		-0.647		-0.537	

Table 5.54. Influence of the stiff column *L* in the maximum positive and negative shear in the *y*-direction

		Max. Positive Shear				Max. Negative Shear			
Column *L* (m)	*SD*	Left (kN)	Δ% Left (%)	Right (kN)	Δ% Right (%)	Left (kN)	Δ% Left (%)	Right (kN)	Δ% Right (%)
9	-2	27.44	11.45	31.68	-43.99	-29.15	-31.51	-63.99	51.24
14	-1	89.05	261.7	15.99	-71.73	-61.24	43.89	-30.44	-28.05
19	0	24.62	0	56.56	0	-42.56	0	-42.31	0
24	1	40.97	66.41	109.49	93.58	-72.8	71.05	-113.84	169.06
29	2	82.93	236.84	19.67	-65.22	-53.89	26.62	-31.78	-24.89
$\|\bar{x}\| = \Sigma \|\Delta\%\| / 4$		=	144.1		68.63		43.27		68.31
ρ	=	0.323		0.285		-0.574		-0.086	

In general, the correlations were associated with the positive or negative increment, when applicable, of the loading conditions examined with increased stiff column length. The strongest correlations were estimated for the maximum negative bending moment of both stiff columns, and the maximum negative shear of the left column.

5.7.3.8 Influence of the Stiff Column Spacing (Column *S*)

The following tables show the influence of the stiff column spacing in the loading conditions examined:

Table 5.55. Influence of the stiff column *S* in the maximum positive and negative bending moment in the *y*-direction

		Max. Positive Bending Moment				Max. Negative Bending Moment			
Column *S* (m)	*SD*	Left (kN-m)	Δ% Left (%)	Right (kN-m)	Δ% Right (%)	Left (kN-m)	Δ% Left (%)	Right (kN-m)	Δ% Right (%)
1.2	-2	29.03	178.33	20.50	251.03	-4.50	-39.52	-0.56	-95.84
1.4	-1	23.16	122.05	13.93	138.53	-13.69	84.01	-2.79	-79.26
1.6	0	10.43	0	5.84	0	-7.44	0	-13.45	0
1.8	1	9.92	-4.89	4.55	-22.09	-18.36	146.77	-17.77	32.12
2.0	2	11.92	14.29	4.12	-29.45	-34.93	369.49	-32.81	143.94
$\lvert\bar{x}\rvert = \Sigma \lvert\Delta\%\rvert / 4$		=	79.89		110.28		159.95		87.79
ρ	=	-0.864		-0.926		-0.864		-0.969	

Table 5.56. Influence of the stiff column *S* in the maximum positive and negative shear in the *y*-direction

		Max. Positive Shear				Max. Negative Shear			
Column *S* (m)	*SD*	Left (kN)	Δ% Left (%)	Right (kN)	Δ% Right (%)	Left (kN)	Δ% Left (%)	Right (kN)	Δ% Right (%)
1.2	-2	170.61	592.97	43.32	-23.41	-163.80	284.87	43.32	-202.39
1.4	-1	65.75	167.06	28.09	-50.34	-154.53	263.09	-34.14	-19.31
1.6	0	24.62	0	56.56	0	-42.56	0	-42.31	0
1.8	1	57.31	132.78	43.85	-22.47	-83.14	95.35	-37.67	-10.97
2.0	2	62.32	153.13	119.78	111.78	-84.92	99.53	-63.8	50.79
$\lvert\bar{x}\rvert = \Sigma \lvert\Delta\%\rvert / 4$		=	261.49		52.00		185.71		70.87
ρ	=	-0.643		0.745		0.701		-0.841	

The results indicate that for both stiff columns, the maximum positive bending moment increased positively with decreasing stiff column spacing, while the maximum negative bending moment increased negatively with increasing stiff column spacing. In the case of the shear of the left column, the maximum positive shear and the maximum negative shear tended to increase positively and negatively, respectively, with decreasing stiff column spacing. In the case of the right column, the maximum positive shear increased positively with increasing stiff column spacing, and the maximum negative shear increased negatively with increasing stiff column spacing.

5.7.3.9 Summary of the Effect of the Variables in the Bending Moment and Shear in the *y*-direction

The following tables show the values of the overall average $|\bar{X}|$ of the $|\bar{x}|$ data calculated in previous tables for the bending moment and shear loading conditions examined:

Table 5.57. Overall influence of the variables in the bending moment of the stiff columns in the *y*-direction

	Max. Positive Bending Moment $\|\bar{x}\|$		Max. Negative Bending Moment $\|\bar{x}\|$		
Variable	Δ% Left (%)	Δ% Right (%)	Δ% Left (%)	Δ% Right (%)	$\|\bar{X}\|$ (%)
LTP D_r	2.40	6.42	15.76	27.96	13.14
Clay I_L	44.49	21.57	56.35	29.87	38.07
Column q_u	15.75	4.84	6.45	7.53	8.64
LTP H	70.92	53.38	66.03	50.71	60.26
Column D	39.81	40.80	116.6	26.08	55.82
Column L	28.79	47.65	50.17	77.66	51.07
Column S	79.89	110.28	159.95	87.79	109.48

Table 5.58. Overall influence of the variables in the shear of the stiff columns in the *y*-direction

	Max. Positive Shear $\|\bar{x}\|$		Max. Negative Shear $\|\bar{x}\|$		
Variable	Δ% Left (%)	Δ% Right (%)	Δ% Left (%)	Δ% Right (%)	$\|\bar{X}\|$ (%)
LTP D_r	10.52	22.76	26.62	21.34	20.31
Clay I_L	73.39	46.74	74.81	55.57	62.63
Column q_u	8.05	6.03	4.01	13.57	7.92
LTP H	158.15	57.36	78.06	38.76	83.08
Column D	109.61	30.83	104.65	44.56	72.41
Column L	144.10	68.63	43.27	68.31	81.08
Column S	261.49	52.00	185.71	70.87	142.52

The results shown in the previous tables indicate that the undrained shear strength ratio, as reflected by the overconsolidation ratio with the liquidity index of the soft clay, was the material-based variable that most significantly influenced the changes in the bending moment and shear experienced by the stiff columns in the *y*-direction. The material-based variable with the least influence in the loading conditions examined was the unconfined compressive strength of the stiff columns. The geometry-based variables that most significantly influenced the changes in bending moment in the *y*-direction were the stiff column spacing followed by the thickness of the LTP. The geometry-based variable with the least influence on the bending moment in the *y*-direction was the stiff column length. In terms of shear, the geometry-based variables that produced the most significant changes in this type of loading were the stiff column spacing followed by the thickness of the LTP, and the geometry-based variable with the least influence was the stiff column diameter.

5.7.4 *Axial Load*

This section presents the parametric results that examine the influence of the variables in the axial load induced in the stiff columns. The structure of this section is similar to the previous sections in which the base model distributions of both stiff columns are presented, and particular loading conditions are selected for further examination using tables.

5.7.4.1 Base Model Loading Conditions

The figures below show the distributions of the axial load of the left and right columns of the base model:

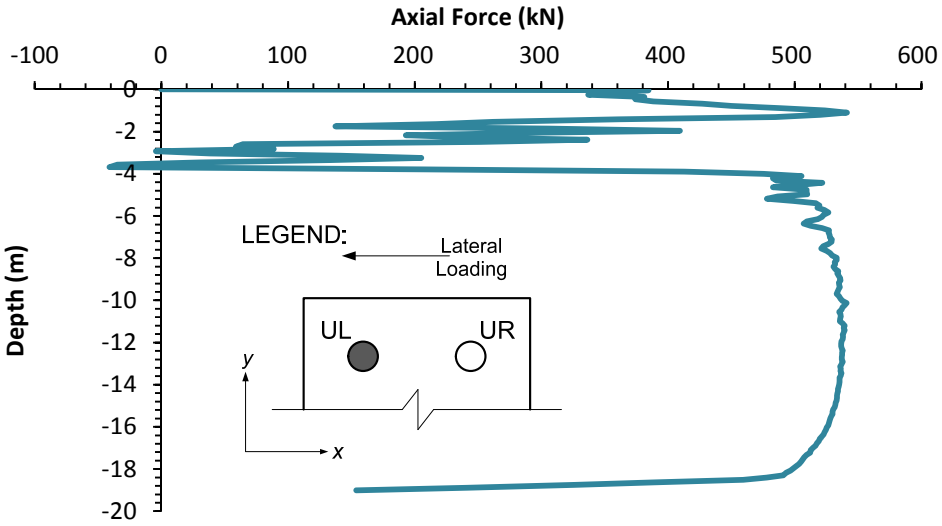

Fig. 5.31. Distribution of the axial load of the left column – Base model.

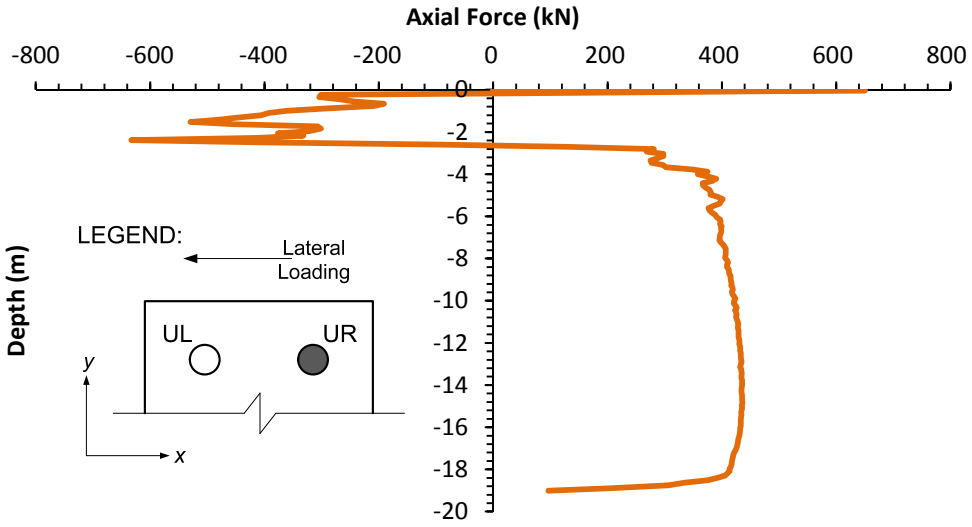

Fig. 5.32. Distribution of the axial load of the right column – Base model.

The loading conditions examined were the minimum axial load at the top of the stiff columns, and the maximum axial load at the bottom of the stiff columns.

5.7.4.2 Influence of the Load Transfer Platform Relative Density (LTP D_r)

The following table shows the influence of the relative density of the LTP in the loading conditions examined:

Table 5.59. Influence of the LTP D_r in the maximum and minimum axial load of the stiff columns

		Max. Bottom Axial Load				Min. Top Axial Load			
LTP D_r (%)	*SD*	Left (kN)	Δ% Left (%)	Right (kN)	Δ% Right (%)	Left (kN)	Δ% Left (%)	Right (kN)	Δ% Right (%)
60.0	-2	529.37	-2.14	440.92	1.15	23.62	-157.72	-443.83	-29.88
67.5	-1	535.46	-1.01	438.54	0.61	16.40	-140.08	-465.82	-26.41
75.0	0	540.92	0	435.89	0	-40.92	0	-632.98	0
82.5	1	544.34	0.63	434.98	-0.21	-98.18	139.93	-778.54	23.00
90.0	2	539.53	-0.26	432.67	-0.74	-269.28	558.06	-1294.03	104.43
$\|\bar{x}\| = \Sigma \|\Delta\%\| / 4$		=	1.01		0.68		248.95		45.93
ρ	=	0.803		-0.991		-0.924		-0.918	

The results show that the maximum bottom axial load in the left column tended to increase positively with increasing relative density. The results in the right column show that the maximum bottom axial load became less positive with increasing relative density of the LTP, resulting in the calculation of a negative linear correlation as opposed to the positive linear correlation estimated in the left column. In the case of the minimum top axial load, this load tended to become more negative with increasing relative density, producing more tension at the top of both stiff columns.

5.7.4.3 Influence of the Undrained Shear Strength Ratio of the Soft Clay (s_u/σ_v') as Reflected in Values of the Overconsolidation Ratio (OCR) with the Liquidity Index (I_L)

The following table shows the influence of the undrained shear strength ratio of the soft clay, reflected by its overconsolidation ratio using the liquidity index, in the loading conditions examined:

Table 5.60 Influence of the soft clay s_u/σ_v', reflected by *OCR* with I_L, in the maximum and minimum axial load of the stiff columns

		Max. Bottom Axial Load				Min. Top Axial Load			
Clay I_L	*SD*	Left (kN)	Δ% Left (%)	Right (kN)	Δ% Right (%)	Left (kN)	Δ% Left (%)	Right (kN)	Δ% Right (%)
0.500	-2	519.08	-4.04	390.39	-10.44	-1794.33	4284.97	-2376.17	275.39
0.625	-1	543.64	0.50	421.80	-3.23	-369.97	804.13	-1215.93	92.10
0.750	0	540.92	0	435.89	0	-40.92	0	-632.98	0
0.875	1	558.96	3.34	474.85	8.94	-43.97	7.45	-643.37	1.64
1.000	2	607.97	12.4	563.87	29.36	79.66	-294.67	-160.00	-74.72
$\lvert\bar{x}\rvert = \Sigma \lvert\Delta\%\rvert / 4$		=	5.07		12.99		1347.81		110.96
ρ	=	0.917		0.947		0.827		0.928	

The results show that the maximum bottom axial load in both stiff columns tended to increase positively with decreasing undrained shear strength ratio, shown in the table as an increase in the liquidity index thus producing a decrease in the overconsolidation ratio. In the case of the minimum top axial load, the tendency was for the load to become more positive, or less negative, with decreasing undrained shear strength ratio. This suggested the development of less tension at the top of both stiff columns.

5.7.4.4 Influence of the Unconfined Compressive Strength of the Stiff Columns (q_u)

The following table shows the influence of the unconfined compressive strength of the stiff columns in the loading conditions examined:

Table 5.61. Influence of the stiff column q_u in the maximum and minimum axial load of the stiff columns

		Max. Bottom Axial Load				Min. Top Axial Load			
Column q_u (MPa)	*SD*	Left (kN)	Δ% Left (%)	Right (kN)	Δ% Right (%)	Left (kN)	Δ% Left (%)	Right (kN)	Δ% Right (%)
8.8	-2	541.51	0.11	434.45	-0.33	891.4	-2278.4	-41.39	-93.46
11.3	-1	536.49	-0.82	436.48	0.14	286.08	-799.12	-291.81	-53.90
13.8	0	540.92	0	435.89	0	-40.92	0	-632.98	0
16.3	1	544.71	0.70	435.98	0.02	-295.19	621.38	-687.20	8.57
18.8	2	547.30	1.18	434.83	-0.24	-692.29	1591.81	-940.88	48.64
$\|\bar{x}\| = \Sigma \|\Delta\%\| / 4$		=	0.70		0.18		1322.68		51.14
ρ	=	0.764		0.049		-0.988		-0.982	

The results show that in the case of the left column, increasing the unconfined compressive strength increased positively the maximum bottom axial load experienced by this stiff column, and in the case of the right column, there were no significant changes experienced by the maximum axial load when varying the unconfined compressive strength. When examining the minimum axial load at the top of both stiff columns, the results show that this load became more negative with increasing unconfined compressive strength.

5.7.4.5 Influence of the Load Transfer Platform Thickness (LTP *H*)

The following table shows the influence of the thickness of the LTP in the loading conditions examined:

Table 5.62. Influence of the LTP *H* in the maximum and minimum axial load of the stiff columns

		Max. Bottom Axial Load				Min. Top Axial Load			
LTP *H* (m)	*SD*	Left (kN)	Δ% Left (%)	Right (kN)	Δ% Right (%)	Left (kN)	Δ% Left (%)	Right (kN)	Δ% Right (%)
0.45	-2	527.00	-2.57	468.38	7.45	250.04	-711.05	179.55	-128.37
0.60	-1	537.46	-0.64	446.36	2.40	307.39	-851.20	-83.39	-86.83
0.75	0	540.92	0	435.89	0	-40.92	0	-632.98	0
0.90	1	549.27	1.54	420.27	-3.58	-1023.81	2401.98	-1899.00	300.01
1.05	2	545.65	0.87	411.04	-5.70	-928.58	2169.26	-1971.72	211.50
$\|\bar{x}\| = \Sigma \|\Delta\%\| / 4$		=	1.41		4.78		1533.37		181.68
ρ	=	0.906		-0.989		-0.906		-0.962	

The results show that an increase in the thickness of the LTP produced a positive increase in the maximum axial load at the bottom of the left column and a decrease in this axial load at the bottom of the right column. An increase of the thickness of the LTP also produced a negative increase of the minimum axial load in both stiff columns, suggesting that a thicker LTP would be associated with the development of more tension at the top of the stiff columns.

5.7.4.6 Influence of the Stiff Column Diameter (Column *D*)

The following table shows the influence of the stiff column diameter in the loading conditions examined:

Table 5.63. Influence of the stiff column *D* in the maximum and minimum axial load of the stiff columns

		Max. Bottom Axial Load				Min. Top Axial Load			
Column *D* (m)	*SD*	Left (kN)	Δ% Left (%)	Right (kN)	Δ% Right (%)	Left (kN)	Δ% Left (%)	Right (kN)	Δ% Right (%)
0.30	-2	518.20	-4.20	393.61	-9.70	368.02	-999.36	-3.04	-99.52
0.33	-1	541.75	0.15	416.71	-4.40	112.63	-375.24	-480.79	-24.04
0.36	0	540.92	0	435.89	0	-40.92	0	-632.98	0
0.39	1	568.61	5.12	444.31	1.93	-402.66	884.02	-1058.01	67.15
0.42	2	563.55	4.18	404.34	-7.24	-1847.46	4414.81	-1567.74	147.68
$\|\bar{x}\| = \Sigma \|\Delta\%\| / 4$		=	3.41		5.82		1668.36		84.60
ρ	=	0.920		0.367		-0.893		-0.988	

The results show that an increase in the column diameter produced a positive increase in the maximum axial load at the bottom of both the left and right columns. However, the linear correlation calculated for the latter column is significantly weaker compared to the former. The results also show that an increase of the column diameter was accompanied by a negative increase in the minimum axial load observed at the top of the stiff columns, suggesting that more tension developed at the top of these rigid vertical elements as the column diameter became progressively greater.

5.7.4.7 Influence of the Stiff Column Length (Column *L*)

The following table shows the influence of the stiff column length in the loading conditions examined:

Table 5.64. Influence of the stiff column *L* in the maximum and minimum axial load of the stiff columns

		Max. Bottom Axial Load				Min. Top Axial Load			
Column *L* (m)	*SD*	Left (kN)	Δ% Left (%)	Right (kN)	Δ% Right (%)	Left (kN)	Δ% Left (%)	Right (kN)	Δ% Right (%)
9	-2	502.97	-7.02	435.43	-0.11	-352.40	761.19	-417.12	-34.10
14	-1	525.21	-2.9	424.90	-2.52	-196.50	380.21	-633.10	0.02
19	0	540.92	0	435.89	0	-40.92	0	-632.98	0
24	1	533.47	-1.38	446.48	2.43	-1044.97	2453.69	-1773.86	180.24
29	2	548.28	1.36	454.17	4.19	-857.19	1994.79	-733.45	15.87
$\|\bar{x}\| = \Sigma \|\Delta\%\| / 4$		=	3.17		2.31		1397.47		57.56
ρ	=	0.895		0.830		-0.679		-0.523	

The results show that the maximum axial load at the bottom of both stiff columns increased positively with increasing stiff column length. In the case of the minimum axial load at the top of the stiff columns, this load tended to increase negatively with increasing stiff column length, thus producing more tension at the top of the stiff columns as they became longer.

5.7.4.8 Influence of the Stiff Column Spacing (Column *S*)

The following table shows the influence of the stiff column spacing in the loading conditions examined:

Table 5.65. Influence of the stiff column *S* in the maximum and minimum axial load of the stiff columns

		Max. Bottom Axial Load				Min. Top Axial Load			
Column *S* (m)	*SD*	Left (kN)	Δ% Left (%)	Right (kN)	Δ% Right (%)	Left (kN)	Δ% Left (%)	Right (kN)	Δ% Right (%)
1.2	-2	538.87	-0.38	454.04	4.16	-691.14	1589.00	-474.83	-24.98
1.4	-1	552.49	2.14	439.95	0.93	-394.43	863.91	-354.50	-44.00
1.6	0	540.92	0	435.89	0	-40.92	0	-632.98	0
1.8	1	550.58	1.79	440.07	0.96	-434.78	962.51	-1132.38	78.90
2.0	2	553.46	2.32	416.93	-4.35	-992.10	2324.49	-1958.40	209.39
$\|\bar{x}\| = \Sigma \|\Delta\%\| / 4$		=	1.66		2.60		1434.98		89.32
ρ	=	0.630		-0.878		-0.286		-0.902	

The results indicate that increasing the stiff column spacing tended to positively increase the maximum axial load at the bottom of the left column and it decreased the maximum axial load at the bottom of the right column, thus resulting in the calculation of a negative linear correlation for the latter case. In the case of the minimum axial load at the top of both stiff columns, in general, there was a negative increase in this load with increasing stiff column spacing, yet the linear correlation calculated on the left column is significantly weaker than the one calculated on the right column.

5.7.4.9 Summary of the Effect of the Variables in the Axial Load

The following table shows the values of the overall average $|\bar{X}|$ of the $|\bar{x}|$ data calculated in previous tables for the axial loading conditions examined:

Table 5.66. Overall influence of the variables in the axial load of the stiff columns

	Max. Bottom Axial Load $\|\bar{x}\|$		Min. Top Axial Load $\|\bar{x}\|$		
Variable	Δ% Left (%)	Δ% Right (%)	Δ% Left (%)	Δ% Right (%)	$\|\bar{X}\|$ (%)
LTP D_r	1.01	0.68	248.95	45.93	74.14
Clay I_L	5.07	12.99	1347.81	110.96	369.21
Column q_u	0.70	0.18	1322.68	51.14	343.68
LTP H	1.41	4.78	1533.37	181.68	430.31
Column D	3.41	5.82	1668.36	84.6	440.55
Column L	3.17	2.31	1397.47	57.56	365.13
Column S	1.66	2.60	1434.98	89.32	382.14

Based on the results shown in the previous table, the undrained shear strength ratio in terms of the overconsolidation ratio with the liquidity index of the soft soil was, overall, the material-based variable that most significantly influenced the changes in terms of percent change of the axial load induced in the stiff columns. The material-based variable with the least influence in the axial load of the stiff columns was the relative density of the LTP. In terms of the geometry-based variables examined, the stiff column diameter was the variable that most significantly influenced the changes in axial load followed by strong contribution coming from the thickness of the LTP. The geometry-based variable with the least influence in the percent changes of the axial loading conditions examined was the stiff column length.

5.7.5 *Overall Summary of the Influence of the Geometry-Based and Material-Based Variables*

In order to better understand and visualize the influence of the various geometry-based and material-based variables examined in the parametric analysis, the following table puts together all of the overall averages that were previously calculated. The highlighted quantities represent the variables that had the highest influence in each output examined.

Table 5.67. Summary of parametric results using $|\bar{x}|$ or $|\bar{X}|$

Variable	*LL* at yield (%)	In *x*-direction Bending Moment (%)	In *x*-direction Shear (%)	In *y*-direction Bending Moment (%)	In *y*-direction Shear (%)	Axial Load (%)
LTP D_r	6.63	19.30	20.74	13.14	20.31	74.14
Clay I_L	19.54	49.71	74.46	38.07	62.63	369.21
Column q_u	3.92	11.92	19.92	8.64	7.92	343.68
LTP *H*	47.25	57.09	61.64	60.26	83.08	430.31
Column *D*	6.35	53.23	42.72	55.82	72.41	440.55
Column *L*	10.31	18.45	41.75	51.07	81.08	365.13
Column *S*	3.36	33.18	54.63	109.48	142.52	382.14

5.8 CONCLUSIONS

This chapter presented the results of a parametric study that was conducted to investigate the influence of different variables in the lateral response of stiff column-supported shallow foundations. The results from the parametric study indicated that the material-based variable that most significantly controlled the changes in the lateral response of the stiff column-supported shallow foundation in terms of the lateral load-displacement response, the bending moment, shear and axial load induced in the stiff columns, was the undrained shear strength ratio of the soft clay surrounding the stiff columns, as reflected by the overconsolidation ratio using the liquidity index of the soft clayey soil. The material-based variable with the least influence in the lateral load-displacement response of the stiff column-supported shallow foundation was the unconfined compressive strength of the stiff columns, and the same trend was observed in the

bending moment and shear induced in the *x*-direction and *y*-direction of the stiff columns. The relative density of the LTP was the material-based variable with the least influence in the axial load of the stiff columns.

Different trends were observed when examining the influence of the geometry-based variables in the lateral response of the stiff column-supported shallow foundation. The geometry-based variable that produced the most significant changes in the lateral load-displacement response, bending moment and shear of the stiff columns in the *x*-direction was the thickness of the LTP. The stiff column spacing was the geometry-based variable that most significantly impacted the bending moment and shear induced in the *y*-direction. The axial load was most significantly influenced by the diameter of the stiff columns. The stiff column length was the geometry-based variable with the least impact in the bending moment and shear of the stiff columns in the *x*-direction, and the stiff column length had the least impact in the axial load of the stiff columns. The stiff column length also had the least impact in the bending moment induced in the *y*-direction of the stiff columns, while the stiff column diameter had the least impact in the shear induced in the *y*-direction of the stiff columns. The geometry-based variable that had the least impact in the lateral load-displacement response was the stiff column spacing. Overall, the undrained shear strength ratio of the soft soil surrounding the stiff columns, the thickness of the LTP, the stiff column spacing and the stiff column diameter were the variables that most significantly impacted the lateral response of stiff column-supported shallow foundations.

CHAPTER 6: CONCLUSIONS

The following conclusions summarize the findings gathered in this research project:

- The thickness of the LTP, the coarse-granular mattress placed above the soil-column composite, significantly controlled the lateral response of stiff column-supported shallow foundations. The experimental and numerical results showed that the lateral capacity of these systems increased with increasing LTP thickness. The numerical results showed that the LTP thickness also controlled the load and lateral deformations induced in the stiff columns.
- From the results of the parametric study, the undrained shear strength ratio of the soft soil was the material-based variable that produced the most significant impact in the lateral response of stiff column-supported shallow foundations. In addition to the thickness of the LTP, the results of the parametric study also suggested that the stiff column diameter and stiff column spacing were the geometry-based variables with the greatest influence in the lateral response of such systems.

Based on the conclusions summarized previously, the following is a series of observations of future work that can improve the understanding of the lateral response of stiff column-supported shallow foundations:

- The influence of the areal extension of the LTP was not examined in this work and it would be of interest to assess its influence in the lateral response of these systems.
- The influence of reinforcement above the stiff columns and inside the LTP would also provide additional insight into their effect in the lateral response of stiff column-supported shallow foundations.
- Further studies are recommended to better characterize the type of failure experienced by the stiff columns. While some findings related to the location of the failure surface were detailed in this work, a more comprehensive assessment is recommended to better understand the failure modes experienced by these rigid vertical elements after the stiff column-supported shallow foundation is laterally loaded.
- The examination of different column layouts (3 stiff columns, 5 stiff columns, etc.) underneath the foundation would improve the understanding of the lateral response of such systems.

CHAPTER 7: REFERENCES

ACI (American Concrete Institute). (2011). *Building code requirements for structural concrete (ACI 318M-11) and commentary*, Farmington Hills, MI, USA.

Adams, T.E. (2011). *Stability of levees and floodwalls supported by deep-mixed shear walls: five case studies in the New Orleans area*. Ph.D. Dissertation, Virginia Tech, Blacksburg, VA, 241p.

Alamgir, M., Miura, N., Poorooshasb, H.B. and Madhav, M.R. (1996). "Deformation analysis of soft ground reinforced by columnar inclusions". *Computers and Geotechnics*, 18(4), pp. 267-290

Amano, H.T., Morita, T., Tsukada, H. and Takahashi, M. (1986). "Design of deep mixing method for high road embankment – Hayashima I.C. –" *Proceedings of the 21th Annual Conference of the Japanese Society of Soil Mechanics and Foundation Engineering, JSSMFE*, 2-2, pp. 1999-2002 (in Japanese).

Ang, A.H-S. and Tang, W.H. (2007). Probability Concepts in Engineering, Emphasis in Civil and Environmental Engineering. 2nd Edition, John Wiley & Sons, New Jersey, USA, 406p.

Ardiaca, D. H. (2009). "Mohr-Coulomb parameters for modelling of concrete structures." *Plaxis Bulletin*, Plaxis bv, Delft, Netherlands

ASIRI (Multiple Authors) (2012). *Recommendations for the design, construction and control of rigid inclusion ground improvements*. Presses des Ponts et Chaussée, France. 316p.

Bai, X., Kim, Y.U. and Wang, M.C. (2001). "Load transfer behavior of soil-cement in soft ground". *Foundations and Ground Improvement*, ASCE Geotechnical Special Publication No. 113, pp. 61-68.

Baguelin, F., Jézéquel, J.F. and Shields, D.H. (1978). *The pressuremeter and foundation engineering*. Trans Tech Publications, Clausthal, Germany.

Baker, S. (1999a). "Three dimensional consolidation settlement of stabilized soil using lime/cement columns", *Dry Mix Methods for Deep Soil Stabilization*, Bredenberg, Holms & Broms (eds), Balkema, Rotterdam, pp. 207-213

Baker, S. (1999b). "Numerical analysis of load distribution between lime/cement columns and surrounding soil using finite element method", *Dry Mix Methods for Deep Soil Stabilization*, Bredenberg, Holms & Broms (eds), Balkema, Rotterdam, pp. 215-220

Baker, S. (2000). *Deformation behaviour of lime/cement column stabilized clay*. Ph.D. Dissertation. Chalmers University of Technology, Sweden, 203p.

Bathe, K.J. (1982). *Finite element analysis in engineering analysis*. Prentice-Hall, New Jersey, USA.

Baudouin, G. (2010). *Sols renforcés par inclusions rigides: modélisation physique en centrifugeuse de remblais et de dallage*. Ph.D Dissertation, University of Nantes, 285p (in French).

Beer, F.P., Russell, E. and DeWolf, J.T. (2006). *Mechanics of Materials*. McGraw Hill.

Biot, M.A. (1956). “General solutions of the equations of elasticity and consolidation for a porous material”. *Journal of Applied Mechanics*, 78, pp. 91-96.

Brinkgreve, R. B. J. (1994). *Geomaterial models and numerical analysis of softening*, Ph.D. Dissertation, Delft University of Technology, The Netherlands, 156p.

Brinkgreve, R. B. J. (2005). "Selection of soil models and parameters for geotechnical engineering application." *Proc., Soil Constitutive Models - Evaluation, Selection, and Calibration, January 24, 2005 - January 26, 2005*, American Society of Civil Engineers, pp. 69-98.

Brinkgreve, R.B.J., Broere, W. and Waterman, D. (2006). *PLAXIS 2D – Version 8*. Plaxis bv, Delft, Netherlands.

Brinkgreve, R.B.J., Engin, E. and Swolfs, W.M. (2013). *PLAXIS 3D*. Plaxis bv, Delft, Netherlands.

Bruce, D.A. and Bruce, M.E.C (2003). “The practitioner’s guide to deep mixing” *Proceedings of the 3rd International Conference on Grouting and Ground Treatment*, ASCE Geotechnical Special Publication No. 120, pp. 474-488.

Bruce, M.E.C., Berg, R.R., Collin, J.G., Filz, G.M., Terashi, M. and Yang, D.S. (2013). FHWA Design Manual: Deep mixing for embankment and foundation support. Publication No. FHWA-HRT-13-046, Washington D.C., 244p.

Burke, G.K. (2004). “Jet grouting systems: advantages and disadvantages” Geotechnical Special Publication No. 124: GeoSupport 2004 - Drilled Shafts, Micropiling, Deep Mixing, Remedial Methods, and Specialty Foundation Systems, *Proceedings of Sessions of the Geosupport Conference: Innovation and Cooperation in the Geoindustry, January 29, 2004 - January 31, 2004*, American Society of Civil Engineering, pp 875-886.

Buschmeier, B. and Masse, F. (2012). “Discussion of differences in design methodology between granular and grouted inclusions”. *XXVI Reunión Nacional de Mecánica de Suelos e Ingeniería Geotécnica, November 14-16, 2012*, Cancun, Mexico, 11p.

Buschmeier, B., Masse, F., Swift, S., and Walker, M. (2012). “Full scale instrumented load test for support of oil tanks on deep soft clay deposits in Louisiana using Controlled Modulus Columns.” *ISSMGE - TC 211 International Symposium on Ground Improvement, May 31- June 1, 2012*, Brussels, Belgium, 14p.

Carter, J.P., Randolph, M.F. and Wroth, C.P. (1979). “Stress and pore pressure changes in clay during and after the expansion of a cylindrical cavity.” *International Journal for Numerical and Analytical Methods in Geomechanics*, 3(4), 305-322.

Chevalier B., Combe G., Fantino R., Grange S. and Villard P. (2010a). “Étude des mécanismes de report de charge dans les matelas granulaires des remblais sur sol compressible renforcé par inclusions rigides”, *Rapport* 4-10-4-02. (in French).

Chevalier, B., Briancon L., Villard, P. and Combe, G. (2010b). “Prediction of load transfers in granular layers used in rigid inclusions techniques – experimental and discrete element method analysis”. *GeoFlorida 2010: Advances in Analysis, Modeling and Design*, ASCE Geotechnical Special Publication No. 199, pp. 1718-1726.

Chevalier, B., Villard, P. and Combe, G. (2011). “Investigation of load-transfer mechanisms in geotechnical earth structures with thin fill platforms reinforced by rigid inclusions”. *International Journal of Geomechanics*, 11(3), pp. 239-250.

Cinicioglu, O. (2005). *In-situ shear strength by centrifuge modelling*. Ph.D. Dissertation, University of Colorado, Boulder, CO, 281p.

Coduto, D.P., Kitch, W.A. and Yeung, M-C. R. (2015). *Foundation Design: Principles and Practices*, Third Edition, Prentice Hall, 984p.

Dao, T.P.T. (2011). *Validation of PLAXIS Embedded Piles for Lateral Loading*. Master of Science Thesis, Faculty of Civil Engineering and Geosciences, Section of Geo Engineering, Delft University of Technology, The Netherlands.

Darcy, H. (1856). *Les fontaines publiques de la ville de Dijon: exposition et application des principes a suivre et des formules a employer dans les questions de distribution d'eau*. Dalmont, V., Paris, 647p. (in French)

Dinh, A.Q. (2009). *Étude sur modèle physique des mécanismes de transfert de charge dans les sols renforcés par inclusions rigides. Application au dimensionnement*. Ph.D Dissertation, ENPC, France, 245p. (in French)

Duncan, J.M. and Buchignani A.L. (1976). An engineering manual for settlement studies. Department of Civil Engineering, University of California, Berkeley, CA, 94 pp.

Duncan, J.M., Williams, G.W., Sehn, A.L. and Seed, R.B. (1991). "Estimation of earth pressures due to compaction". *Journal of Geotechnical Engineering*, 117(12), pp. 1833-1847.

Duncan, J.M., Williams, G.W., Sehn, A.L. and Seed, R.B. (1993). Closure to "Estimation of earth pressures due to compaction". *Journal of Geotechnical Engineering*, 119(7), pp. 1172-1177.

Duncan, J.M. and Sleep, M. (2014). Manual for geotechnical engineering reliability calculations. 2nd Edition, Report of a study performed by the Virginia Tech Center for Geotechnical Practice and Research, CGPR No. 76, Virginia Polytechnic Institute and State University, 75p.

Duncan, J.M., Wright, S.G. and Brandon, T.L. (2014). *Soil strength and Slope Stability*. 2nd Edition, John Wiley & Sons, New Jersey, USA, 307p.

Federal Highway Administration (1999). Demonstration project 116, Ground improvement technical summaries, Vols. I & II, Publication No. FHWA-SA-98-08, Washington D.C., 418p.

Fellenius, B.H. (1999). *Basics of Foundation Design*, 2nd Edition, BiTech, Richmond, BC, 164p.

Filz, G.M. (2009). "Design of deep mixing support for embankments and levees," *Proceedings of the International Symposium of Deep Mixing & Admixture Stabilization, Okinawa, Japan, May 19-21*, 23p.

Fiovarante, V., Ghionna, V. N., Pedroni, S. and Veggi, S. (1997). "Soil improvement through vertical jet-grouting columns – a centrifuge study" *Proceedings of the 14th International Conference on Soil Mechanics and Foundation Engineering*, Hamburg, 3(14), pp. 1681-1684.

Han, J. and Gabr, M. A. (2002) "Numerical analysis of geosynthetic-reinforced and pile-dupported earth platforms over soft soil". *Journal of Geotechnical and Geoenvironmental Engineering*, 128(1), pp. 44-53.

Han, J., and Wayne, M. H. (2000). “Pile-soil-geosynthetic interactions in geosynthetic reinforced platform/piled embankments over soft soil”. *Paper No. 000777, Presentation at 79th Annual Transportation Research Board Meeting*, Washington D.C., 23p.

Hansbo, S. and Massarsch, K. R. (2005). “Standardisation of deep mixing methods” *Deep Mixing '05: International conference on deep mixing best practice and recent advances, Stockholm, May 23 – 25*, pp. 3-10.

Hasegawa, M., Sasaki, H. and Usui, M. (1984). “Strain measurements of improved ground by deep mixing method”, *Proceedings of the 39th JSCE*, pp. 297-298 (in Japanese).

Hayashi, H. (1990). “Field measurement of deformation of DJM pile subjected to horizontal load”, *Proceedings of the 45th JSCE*, pp. 426-427 (in Japanese).

Hewlett, W.J. and Randolph, M.F. (1988). “Analysis of piled embankments”. *Ground Engineering*, 21(3), pp. 12-18.

Hill, R. (1950). *The mathematical theory of plasticity*, Clarendon Press, Oxford.

Holm, G. (2002). “Nordic dry deep mixing method execution procedure”. *Proceedings of Deep Mixing Workshop 2002 in Tokyo, Port and Airport Research Institute & Coastal Development Institute of Technology*, pp. 102-109.

Huat, B. B. K., Craig, W. H. and Ali, P. (1994). “The mechanics of piled embankment” *Proceedings of the International Conference on Design and Construction of Deep Foundations*, pp. 1069-82.

Hushmand, A. (2011). Personal Communication.

Hushmand, A. (2014). Personal Communication.

Hussin, J.D. (1994). Ground modification with Vibro Concrete Columns. ASCE South Florida Section Meeting, September 30 to October 1, Ft. Lauderdale, FL.

Hussin, J.D., Abernathy, Z.W. & Hall L.A. (2001). “Embankment construction in soft soils using Vibro Concrete Columns (VCC)” *Proceedings of conference of Foundations and Ground Improvement American Society of Civil Engineers June 9 to June 13*, Blacksburg, VA, pp. 433-444.

Jacky, J. (1944). “The coefficient of earth pressure at rest”. *Magyar Menok es Epitesz Egylet Kozloi*, J. Soc. Of Hungarian Arch. And Engrs., Hungary

Jacobson, J., Filz, G.M. and Mitchell, J.K. (2003). Factors affecting strength sain in Lime-Cement Columns and development of a laboratory testing procedure. Report prepared for the

Virginia Transportation Research Council, Virginia Polytechnic Institute and State University, 69p.

Jamiliokowski, M., Ladd, C. C., Germaine, J. T., and Lancellotta, R. (1985). "New developments in field and laboratory testing of soils" *Proceedings of the 11th International Conference on Soil Mechanics and Foundation Engineering*, San Francisco, 1, pp. 57-153.

Japanese Geotechnical Society (2000). Standard practice for making and curing stabilized soil specimens without compaction (JGS 0821-2000). Geotechnical Test Procedure and Commentary Rep. No. Chapter 7 (in Japanese).

Jenck, O. (2005). *Le renforcement des sols compressibles par inclusions rigides verticales. Modélisation physique et numérique*. Ph.D. Dissertation, INSA Lyon, France, 383p. (in French).

Karastanev, D., Kitazume, M., Miyajima, S. and Ikeda, T. (1997). "Bearing capacity of shallow foundation on column type DDM improved ground" *Proceedings of the 14th International Conference on Soil Mechanics and Foundation Engineering*, Hamburg, 3(14), pp. 1621-1624.

Kempton, G., Russell D., Pierpoint, N. D., and Jones, C. J. F. P. (1998). "Two- and three dimensional numerical analysis of the performance of piled embankments" *Proceedings of the 6th International Conference on Geosynthetics*, pp. 767-72.

Ketcham, S.A. (1989). *Development of an earthquake motion simulator for centrifuge testing and the dynamic response of a model sand embankment*. Ph,D. Dissertation, University of Colorado, Boulder, CO, 285p.

Kitazume, M. (1994). *Model and analytical studies on stability of improved ground by deep mixing method*, Ph.D. Dissertation, Tokyo Institute of Technology, 73p. (in Japanese).

Kitazume, M., Tabata, T., Ishiyama, S. and Karastanev, D. (1996). "Bearing capacity of improved ground with column type DMM", *Proceedings of the 2nd International Conference on Ground Improvement Geosystems, IS-Tokyo '96*, 1, pp. 503-508.

Kitazume, M., Okano, K. and Miyajima, S. (2000). "Centrifuge model tests on failure envelope of column type deep mixing method improved ground". *Soils and Foundations*, Japanese Geotechnical Society, 40(4), pp. 43-55.

Kitazume, M. and Maruyama, K. (2005). "Collapse failure of group column type deep mixing improved ground under embankment", *Proceedings of the International Conference on Deep Mixing – Best Practice and Recent Advances*, 1.2, pp. 245-254.

Kitazume, M. (2006). "Application of physical modelling for investigating ground failure pattern", *Proceedings of the Sixth International Conference on Physical Modelling in Geotechnics, 6th ICPMG '06, Hong Kong*, pp. 63-74.

Kitazume, M. and Maruyama, K. (2006). “External stability of group column type deep mixing improved ground under embankment”, *Soils and Foundations*, Japanese Geotechnical Society, 46(3), pp. 323-340.

Kitazume, M. and Maruyama, K. (2007). “Internal stability of group column type deep mixing improved ground under embankment”, *Soils and Foundations*, Japanese Geotechnical Society, 47(3), pp. 437-455.

Kitazume M. (2008). Stability of group column type DM improved ground under embankment loading. Report of the Port and Airport Research Institute, Vol. 47-1, Japan.

Kitazume M. and Terashi M. (2013). *The Deep Mixing Method*, Taylor and Francis Group, London, UK, 436p.

Kivelo, M. (1997). “Undrained shear strength of Lime/Cement Columns”, *Proceedings of the 14th International Conference of Soil Mechanics and Foundation Engineering*, Hamburg, 2, pp. pp. 1173-1180.

Kivelo, M. (1998). *Stabilization of embankments on soft soil with Lime/Cement Columns*, Ph.D. Dissertation, Royal Institute of Technology, Stockholm, Sweden, 170p.

Kivelo, M. and Broms, B.B. (1999). “Mechanical behavior and shear resistance of Lime/Cement Columns”, *Dry Mix Methods for Deep Soil Stabilization*, Bredenberg, Holms & Broms (eds), Balkema, Rotterdam, pp. 193-200.

Ko, H.-Y. (1988). “The Colorado centrifuge facility”. *Centrifuge 88: Proceedings of the International Conference on Geotechnical Centrifuge Modeling, Paris, April 25-27*, pp. 73-75.

Kosho, A. (2011). “Ground improvement using the vibro-stone column technique”. *Proceedings of the 21st European Young Geotechnical Engineers' Conference*, Rotterdam, The Netherlands, pp. 78-82.

Kulhawy, F. H., and Mayne, P. W. (1990). Manual on estimating soil properties for foundation design. Cornell University, Ithaca, NY.

Kutter, B. L., (1992). “Dynamic centrifuge modeling of geotechnical structures”. *Transportation Research Record 1336, TRB,* National Research Council, Washington, DC, pp. 24-30.

Laurent, Y. (2002). *Renforcement des massifs de fondation par inclusions rigides verticales. Étude bibliographique et numérique*. Mémoire de DEA, INSA Lyon, 142p. (in French)

Lawson, C. R. (1992). “Soil reinforcement with geosynthetics”. *Applied Ground Improvement Techniques*, Southeast Asian Geotechnical Society (SEAGS), pp. 55-74.

Low, B.K., Tang, S.K. and Choa, V. (1994). "Arching in piled embankments". *Journal of Geotechnical Engineering*, 120(11), pp. 1917-1938.

Macari, E.J., Znidarcic, D., Shiffman, R.L. and Ko, H.-Y. (1987). Speswhite Clay Triaxial Test Program. Report prepared for Exxon Production Research Company, University of Colorado, Boulder, CO, 63p.

Mankbadi, R., Mansfield J., Wilson-Fahmy, R., Hanna, S. and Krstic, V. (2004). "Ground improvement utilizing Vibro-Concrete Columns." *Proceedings of the GeoSupport Conference: Innovation and Cooperation in the Geo-Industry, January 29-31, 2003*, Orlando, FL, 12p.

Masse, F., Pearlman, S.L. and Taube, M.G. (2009). Controlled Modulus Columns™ (CMC) for support of above-ground storage tanks." *Ohio River Valley Soils Seminar XL (ORVSS)*, Lexington, KY, USA, 17p.

Masse, F., Parinella, C. and Wyman, R. (2011a). "Redevelopment of brownfield sites using Controlled Modulus Columns as an alternate to deep foundations." *2011 Pan-Am CGS Geotechnical Conference*, Toronto, Canada, 9p.

Masse, F., Carey, M. and Ingram, I. (2011b). "Controlled Modulus Columns (CMC): Application to the support of Mechanically Stabilized Earth Walls (MSE Walls)." *2011 Pan-Am CGS Geotechnical Conference*, Toronto, Canada, 10p.

Masse, F., Pearlman, S.L., Walker, M.P. and Swift, S.S. (2012). “Use of Controlled Modulus Columns in retail & industrial development projects.” *2012 DFI Annual Conference on Deep Foundations*, Houston, TX, USA, 12p.

Masse, F. (2013). Personal Communication.

McGuire, M. (2011). *Critical height and surface deformations of column-supported embankments*, Ph.D. Dissertation, Virginia Tech, Blacksburg, VA, 392p.

Mindlin, R.D. (1951). “Influence of rotatory inertia and shear in flexural motions of isotropic elastic plates”. *Journal of Applied Mechanics*, 18, pp. 31-38.

Miyake, M., Wanda, M. and Satoh, T. (1991). “Deformation characteristics of ground improved by a group of treated soil”, *Centrifuge 91*, Balkema, pp. 295-302.

Nakanishi, M. (2002). “Execution and equipment of cement deep mixing (CDM) method” *Proceedings of Deep Mixing Workshop 2002 in Tokyo, Port and Airport Research Institute & Coastal Development Institute of Technology*, pp. 80-90.

Niven, M.P. (2005). *Stability of embankments founded on soft soil improved with deep-mixing-methods columns*, Ph.D. Dissertation, Virginia Tech, Blacksburg, VA, 247p.

Omine, K., Ochiai, H. and Bolton, M.D. (1999). “Homogenization method for numerical analysis of improved ground with cement-treated soil columns.” *Dry Mix Methods for Deep Soil Stabilization*, Bredenberg, Holms & Broms (eds), Balkema, Rotterdam, pp. 161-168.

Ooi, T. A., Chan, S. F. and Wong, S. N. (1987) “Design, construction, and performance of pile supported embankments”. *Proceedings of the 9th Southeast Asian Geotechnical Conference*, pp. 2-1 to 2-12.

Plomteux C., Porbaha A. and Spaulding, C. (2004). “CMC foundation system for embankment support – A case history”, *Proceedings of the GeoSupport Conference: Innovation and Cooperation in the Geo-Industry, January 29-31, 2003*, Orlando, Florida, USA, 13p.

Popescu, R. and Prevost J.H. (1993). “Centrifuge validation of a numerical model for dynamic soil liquefaction” *Soil Dynamics and Earthquake Engineering*, 12(1993), 73-90.

Porbaha, A. (1998a). “State of the art in deep mixing technology; Part I. Basic concepts and overview.” *Ground Improvement*, 2, pp. 81-92.

Porbaha, A. (1998b). “State of the art in deep mixing technology; Part II. Applications.” *Ground Improvement*, 2, pp. 125-139.

Porbaha, A. (2001). “State of the art in construction aspects of deep mixing technology.” *Ground Improvement*, 5(3), pp. 123-138.

Randolph, M.F. and Wroth, C.P. (1979). “An analytical solution for the consolidation around a driven pile.” *International Journal for Numerical and Analytical Methods in Geomechanics*, 3(3), 217-229.

Randolph, M.F., Carter, J.P. and Wroth, C.P. (1979). “Driven piles in clay – the effects of installation and subsequent consolidation.” *Geotechnique*, 29(4), 361-393.

Reid, W.M. and Buchanan, N.W. (1984) “Bridge approach support piling.” *Piling and Ground Treatment*, Thomas Telford, London, pp. 267-74

Roscoe, K.H. and Burland, J.B. (1968). “On the generalized stress-strain behavior of ‘wet’ clay”, *Engineering plasticity*, Heyman, J. & Leckie, F.A. (eds), Cambridge University Press, Cambridge, pp. 535-609.

Russell, D. and Pierpoint, N. (1997). “An assessment of design methods for piled embankments.” *Ground Engineering*, 30(11), pp. 39-44.

Salgado, R. (2008). *The Engineering of Foundations*, McGraw Hill, 896p.

Schmertmann, J.H. (1975). “Measurement of in situ shear strength”, P*roceedings, specialty conference on in situ measurement of soil properties*, American Society of Civil Engineers, 2: pp. 69-98.

Shin, C.-J. (1987). *Dynamic soil-structure interaction*. Ph.D. Dissertation, University of Colorado, Boulder, CO, 251p.

Skjong, R., Bitner-Gregersen, E., Cramer, E., Croker, A., Hagen, Ø., Korneliussen, G., Lacasse, S., Lotsberg, I., Nadim, F. and Ronold, K.O. (1996). Guideline for offshore structural reliability analysis general. Technical report No. 95-2018. Det Norske Veritas Research As, Norway.

Smith, I. M., and Griffiths, D. V. (1988). *Programming the finite element method*, 2nd Edition, John Wiley & Sons, New York, USA, 482p.

Smith, M.E. (2005). *Design of bridge layers in geosynthetic-reinforced column-supported embankments*, Ph.D. Dissertation, Virginia Tech, Blacksburg, VA, 235p.

Stewart, D. and Randolph, M. F. (1994). "T-bar penetration testing in soft clay". *Journal of Geotechnical Engineering*, 120(12), pp. 2230–2235.

Stocker, M. and Seidel, A. (2005). "Twenty-seven years of soil mixing in Germany: The Bauer Mixed-in-Place-Technique." *Deep Mixing '05: International conference on deep mixing best practice and recent advances, Stockholm, May 23 – 25*, pp. 11-14.

Taylor, R.N. (1995). "Centrifuge in modeling: principles and scale effects." *Geotechnical Centrifuge Technology*, Taylor, R.N. (ed). Blackie Academic and Professional, pp. 19-33.

Terashi M., Kitazume M. and Minagawa S. (1991). “Bearing capacity of improved ground by sand compaction piles”. *ASTM Special Technical Publication*, 1089, pp. 7- 61.

Terashi, M. (2002). “Development of deep mixing machine in Japan.” *Proceedings of Deep Mixing Workshop 2002 in Tokyo, Port and Airport Research Institute & Coastal Development Institute of Technology*, pp. 317-325.

Terzaghi, K. (1925). *Erdbaumechanik auf bodenphysikalischer grundlage*. Deuticke, F., Leipzig, 399p. (in German)

Terzaghi, K. (1943). *Theoretical Soil Mechanics*. John Wiley & Sons, New York, USA, 510p.

Terzaghi, K., Peck, R.B. and Mesri, G. (1996). *Soil Mechanics in Engineering Practice*, 3rd Edition, John Wiley & Sons, New York, USA, 512p.

Tresca, H. (1864). Comptes Rendus de l’Academie des Sciences, Paris, 59, 754.

U.S. Department of Navy (1982). *NAVFAC DM7.2, Foundations and Earth Structures*. Naval Facilities Engineering Command, VA.

Vermeer, P. A., and de Borst, R. (1984). "Non-associated pasticity for soils, concrete and rock." *Heron*, 29(3).

Warner, J. (2004). *Practical Handbook of Grouting: Soil, Rock and Structures*. John Wiley & Sons, New Jersey, USA, 720p.

Welsh, J.P. (1997). Excellence in Geotechnical Engineering: Ground Modification Milestones. Central PA Section, ASCE and PennDOT Meeting, October 23-24, Harrisburg, PA, 16p.

Wilson-Fahmy, R., Ro, K.S. and Leiendecker, K. (2011). "Evaluation of four ground improvement techniques for embankment support over soft ground", *Case Studies and Recent Advances in Ground Improvement, A Specialty Seminar Presented by ASCE Metropolitan Section Geotechnical Group, May 12, 2011*. New York City, New York, USA, 22p.

Wood, D.M. (1983). "Index properties and critical state soil mechanics" *Proceedings of the symposium of recent developments in laboratory and field tests and analysis of geotechnical problems*, Bangkok, pp. 301.309.

Wood, D.M. (1990). *Soil behavior and critical state soil mechanics*. Cambridge University Press.

Yasui, S., Yokozawa, K., Yasuoka, N., and Kondo, H. (2005). "Recent technical trends in Dry Mixing (DJM) in Japan." *Deep Mixing '05: International conference on deep mixing best practice and recent advances, Stockholm, May 23 – 25*, pp. 15-22.

Yu, H.S. 2000. *Cavity expansion methods in Geomechanics*. Kluwer Academic Publishers, Dordrecht, The Netherlands.

Zamiskie, E.M., Lambrechts, J.R., Yang K-Y., Rodriguez J.M. and McDonnell, M. (2004). "Vibro Concrete Columns solve problems for victory bridge approach fill." *Proceedings of Geo-Trans 2004, July 27-31*, Los Angeles, CA, pp. 1884-1893.

CHAPTER 8: APPENDICES

8.1 APPENDIX A: Centrifuge Tests – Calibration of Equipment

This appendix includes the calibrations that were performed for the equipment that was used in the centrifuge tests, specifically the calibration of the Pore Pressure Transducers (PPTs) that were used to measure excess pore-water pressures, the Load Cells that were used to record the load during the tests and the Linearly Variable Deformation Transformer (LVDT) used to record the lateral displacements of the footing during in-flight lateral lesting. NOTE: All calibrations were performed with an excitation of 10 Volt.

CALIBRATION OF PPTS:

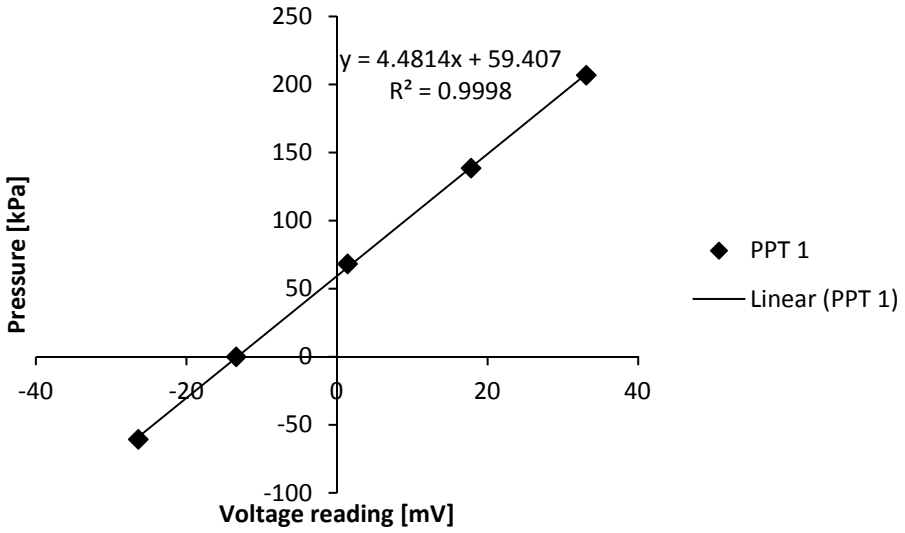

Fig. A81-01. Calibration of PPT1.

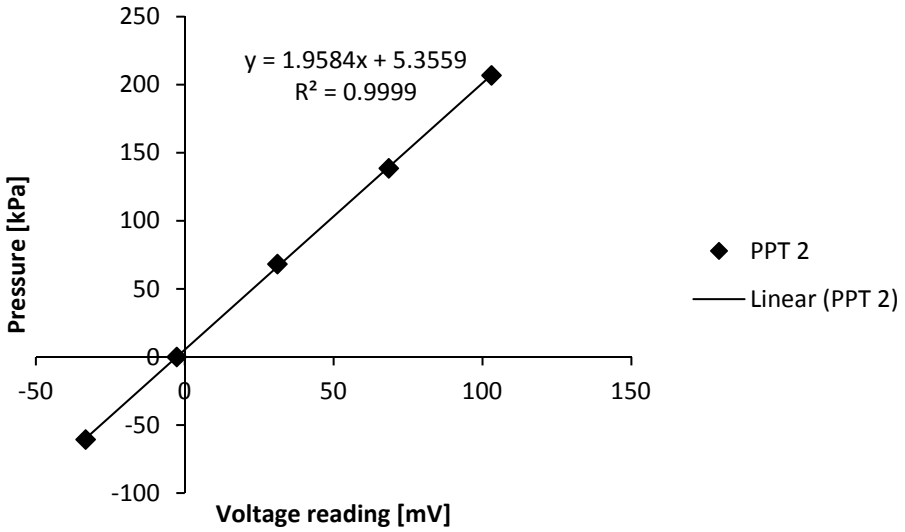

Fig. A81-02. Calibration of PPT2.

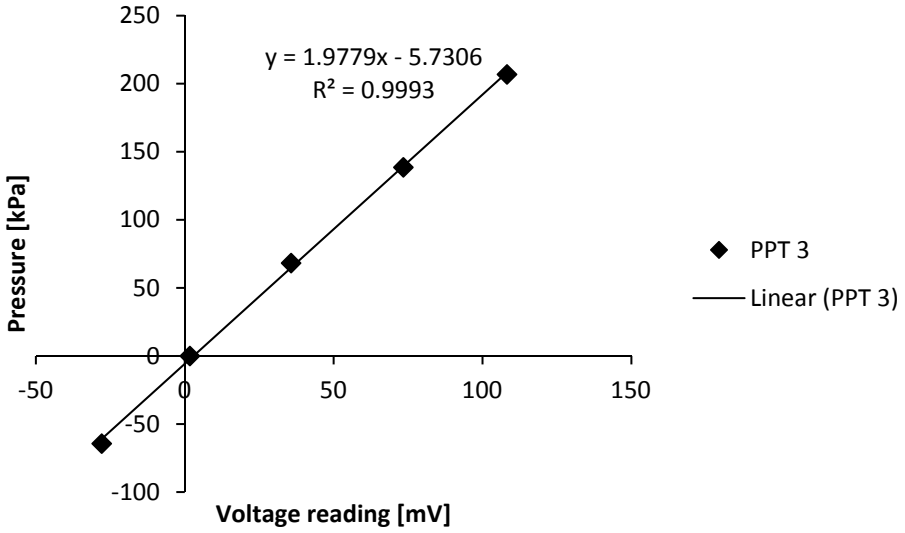

Fig. A81-03. Calibration of PPT3.

CALIBRATION OF LVDT FOR HORIZONTAL DISPLACEMENTS:

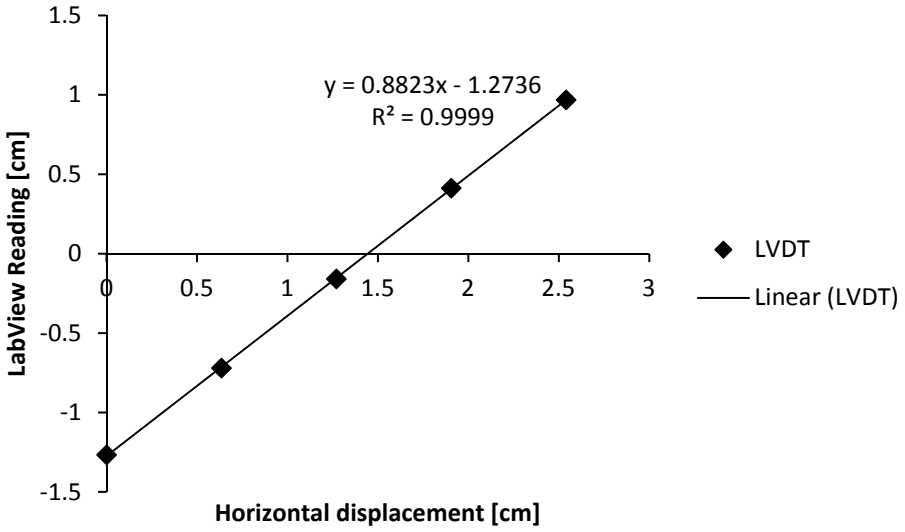

Fig. A81-04. Calibration of LVDT for horizontal displacement.

CALIBRATION OF LOAD CELLS:

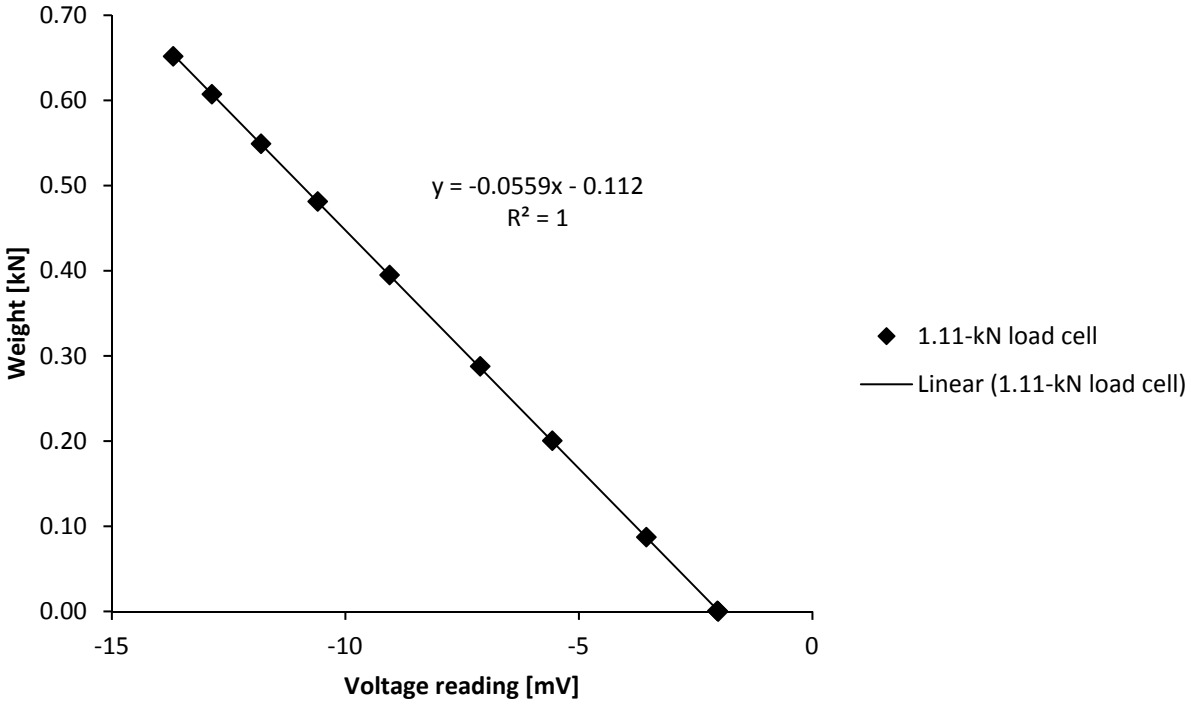

Fig. A81-05. Calibration of 1.11-kN load cell.

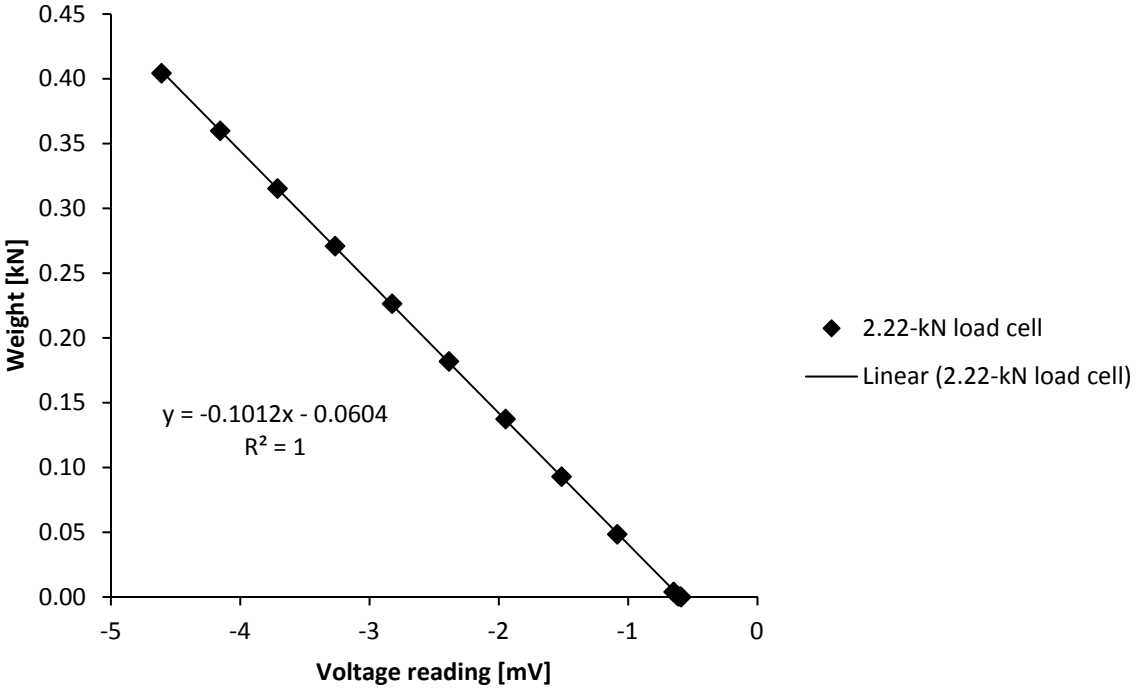

Fig. A81-06. Calibration of 2.22-kN load cell.

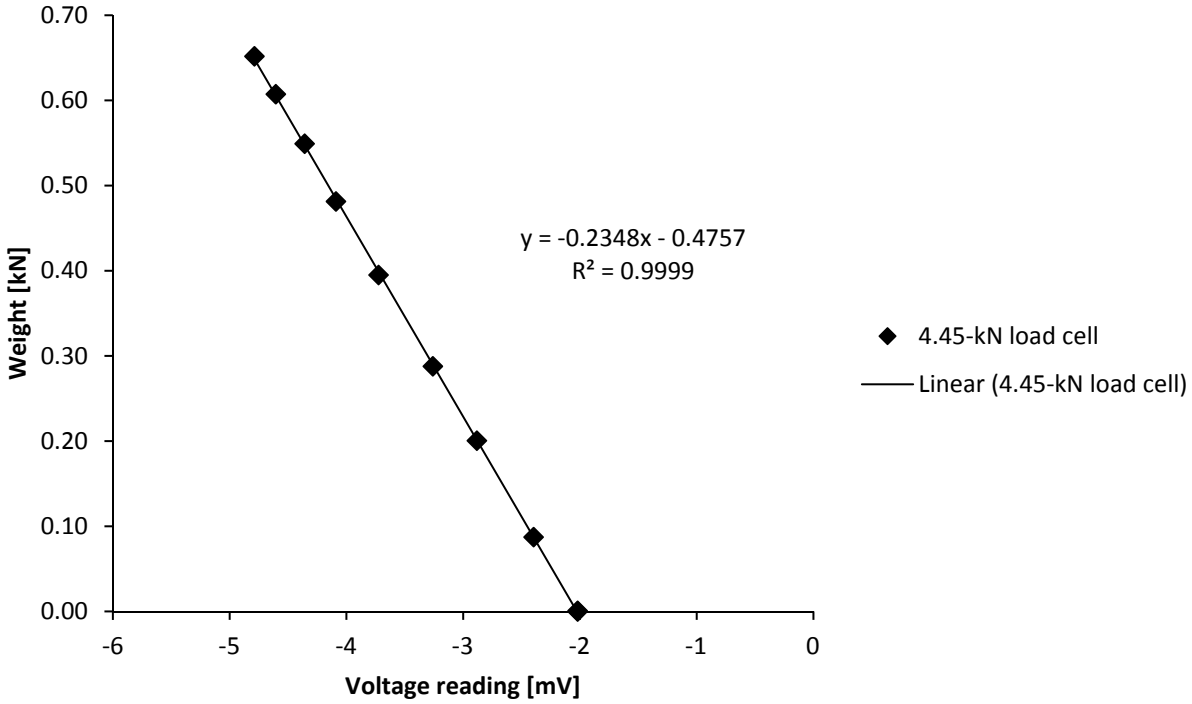

Fig. A81-07. Calibration of 4.45-kN load cell.

NOTE: The following information was provided for the 13.34-kN load cell:

Equation from calibration of 3000-lb load cell: $y = 0.700\frac{kN}{mV}x - 0.014kN$

8.2 APPENDIX B: Centrifuge Tests – Dissipation of Excess Pore-Water Pressures during Self-Weight Consolidation at 50G

This appendix includes the measurements of excess pore-water pressures that were recorded at PPT1 and that were monitored during the self-weight consolidation stages of the lateral load tests. These measurements were used as reference to finish consolidation and due to limitations with usage and availability of the centrifuge, self-weight consolidation was ran in successive stages as indicated in the plots.

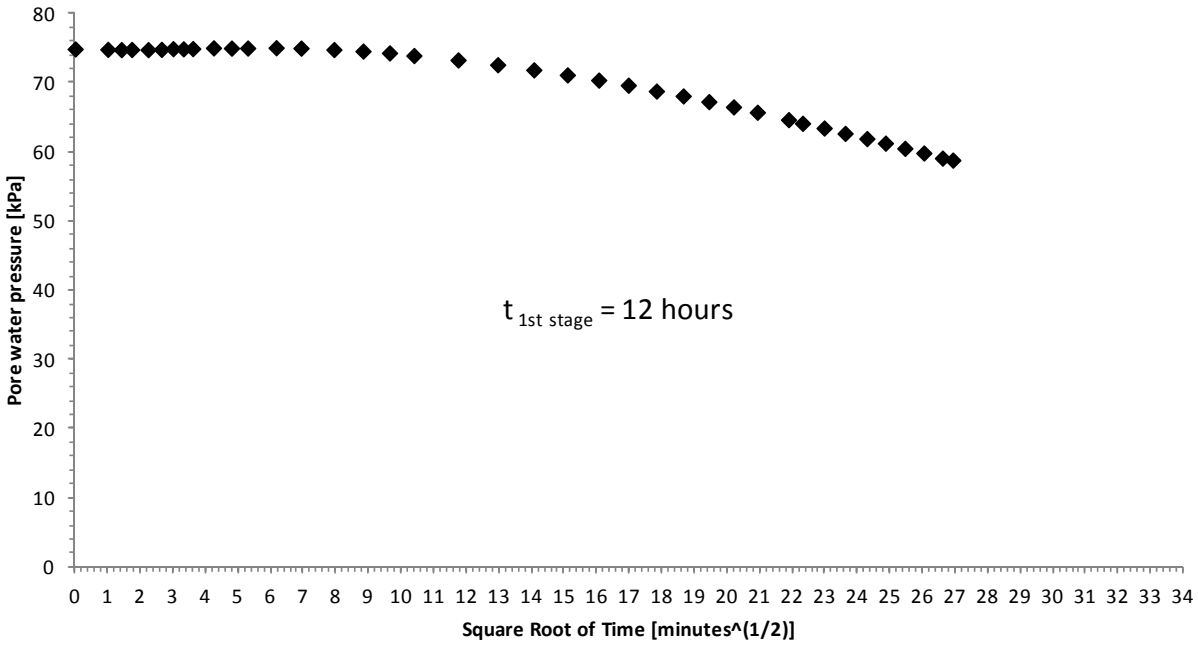

Fig. A82-01. Excess pore-water pressure dissipation during self-weight consolidation at PPT1 location – LTP = 0.45 m – Lateral test – 1st stage.

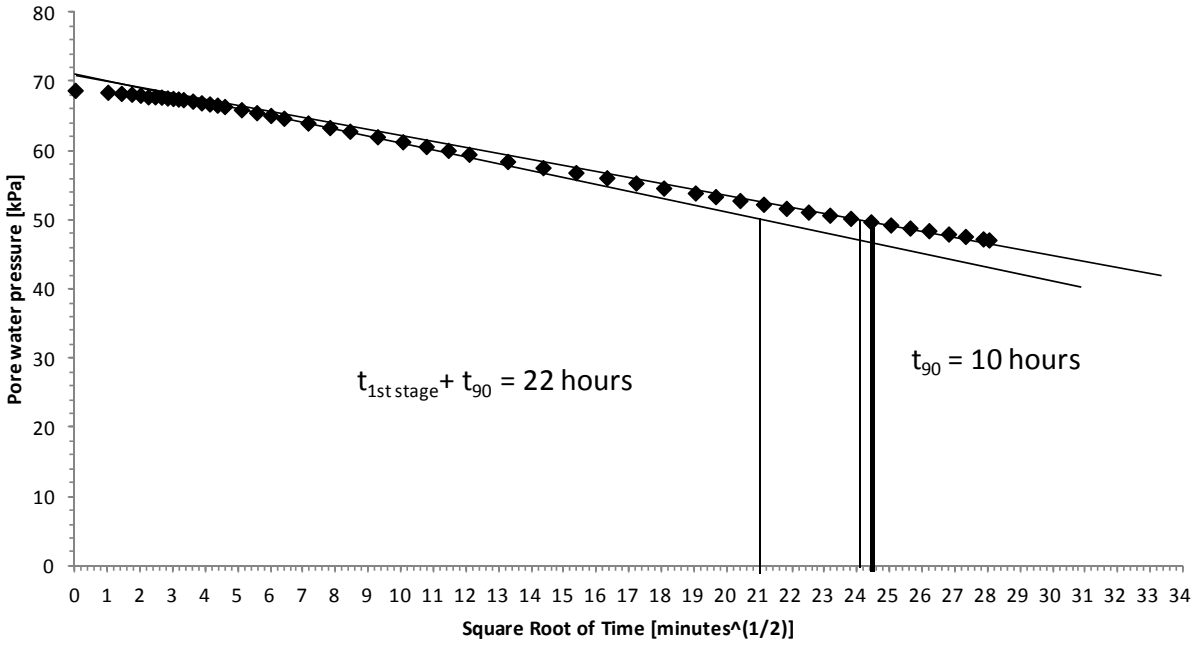

Fig. A82-02. Excess pore-water pressure dissipation during self-weight consolidation at PPT1 location – LTP = 0.45 m – Lateral test – Final stage.

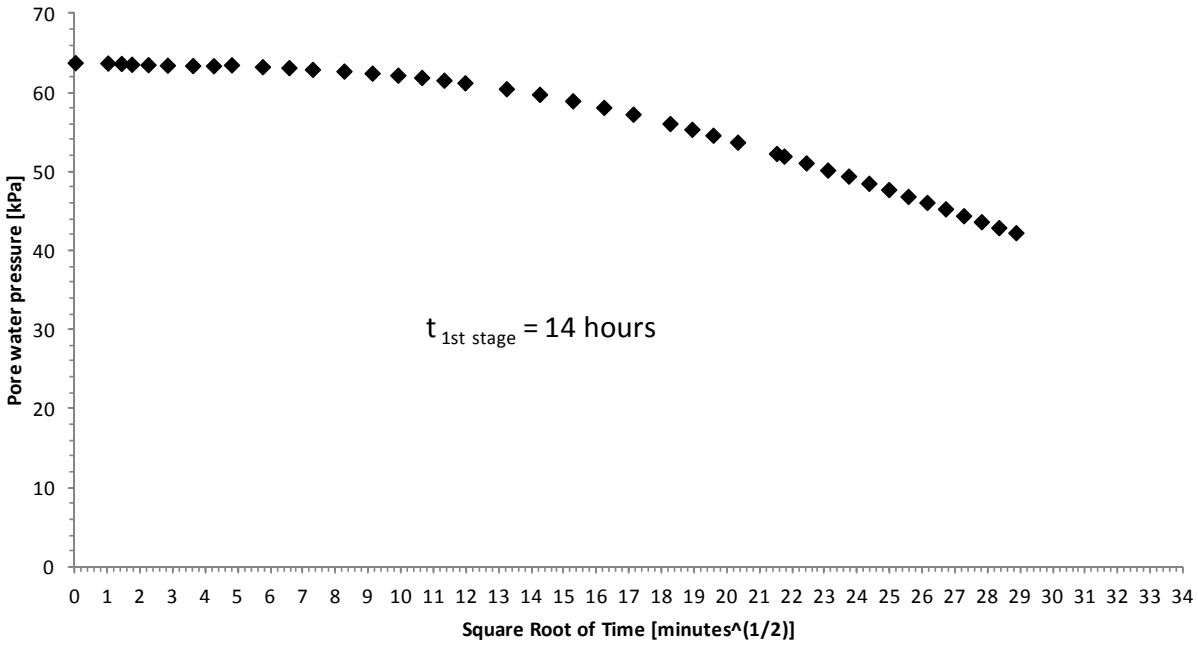

Fig. A82-03. Excess pore-water pressure dissipation during self-weight consolidation at PPT1 location – LTP = 0.60 m – Lateral test – 1st stage.

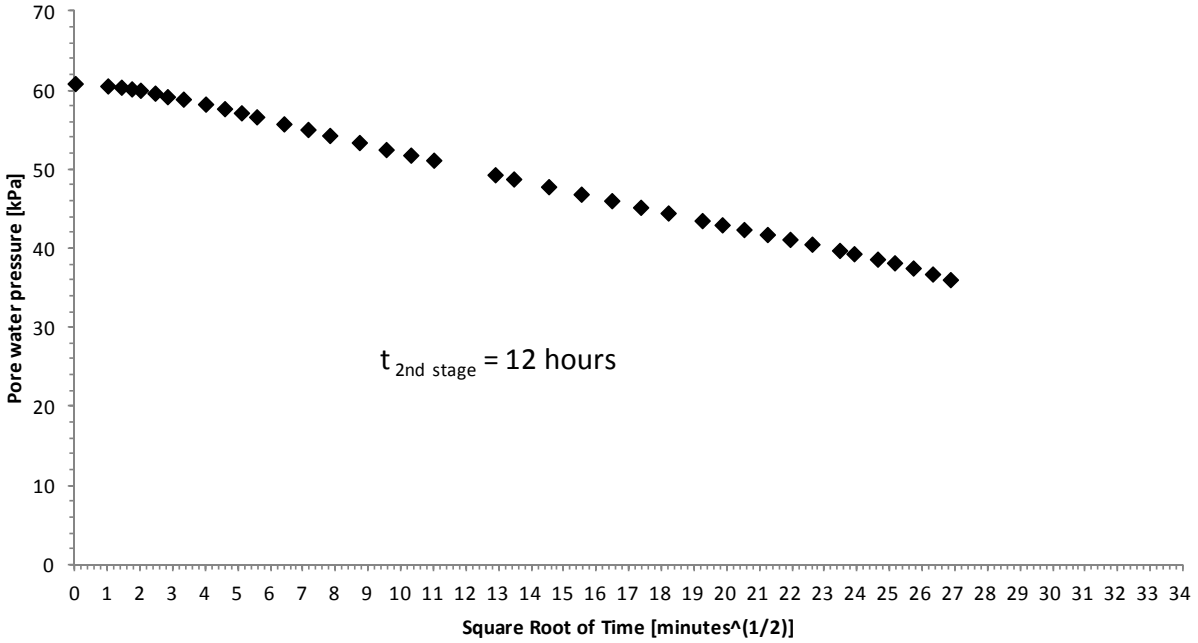

Fig. A82-04. Excess pore-water pressure dissipation during self-weight consolidation at PPT1 location – LTP = 0.60 m – Lateral test – 2nd stage.

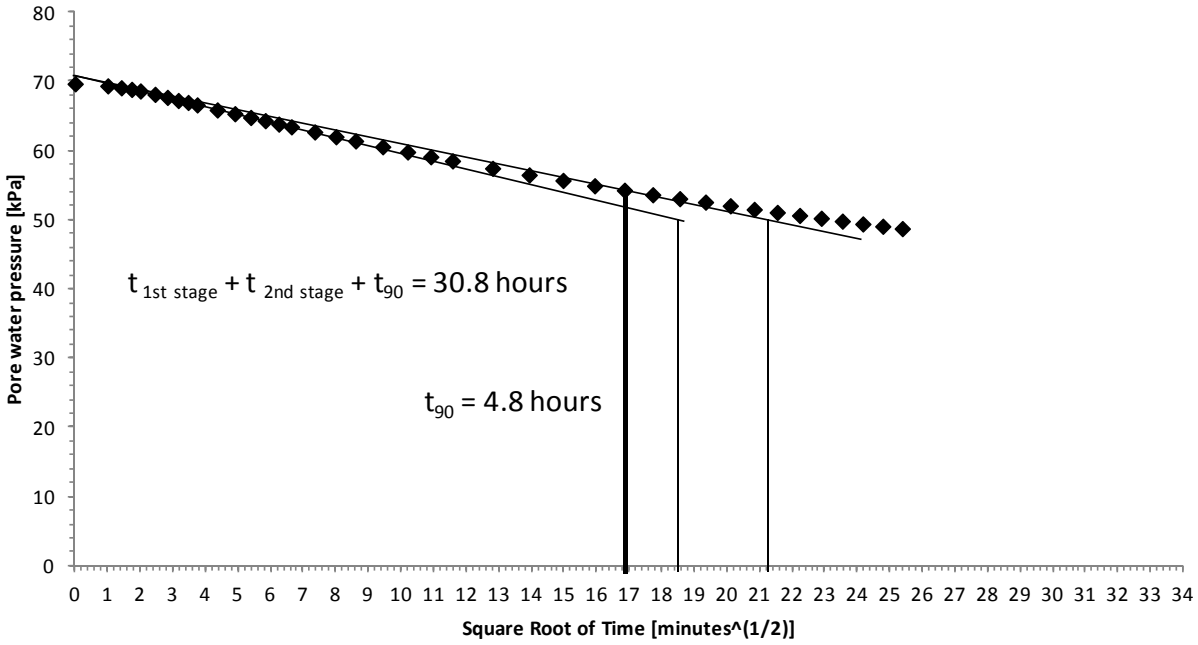

Fig. A82-05. Excess pore-water pressure dissipation during self-weight consolidation at PPT1 location – LTP = 0.60 m – Lateral test – Final stage.

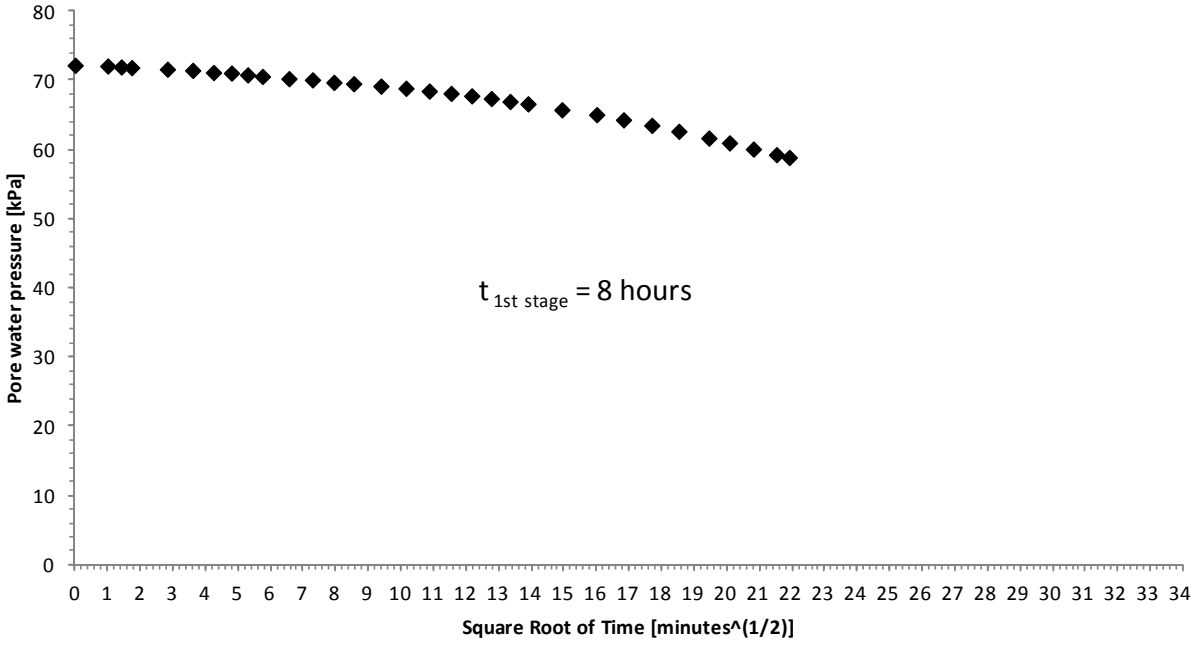

Fig. A82-06. Excess pore-water pressure dissipation during self-weight consolidation at PPT1 location – LTP = 0.70 m – Lateral test – 1st stage.

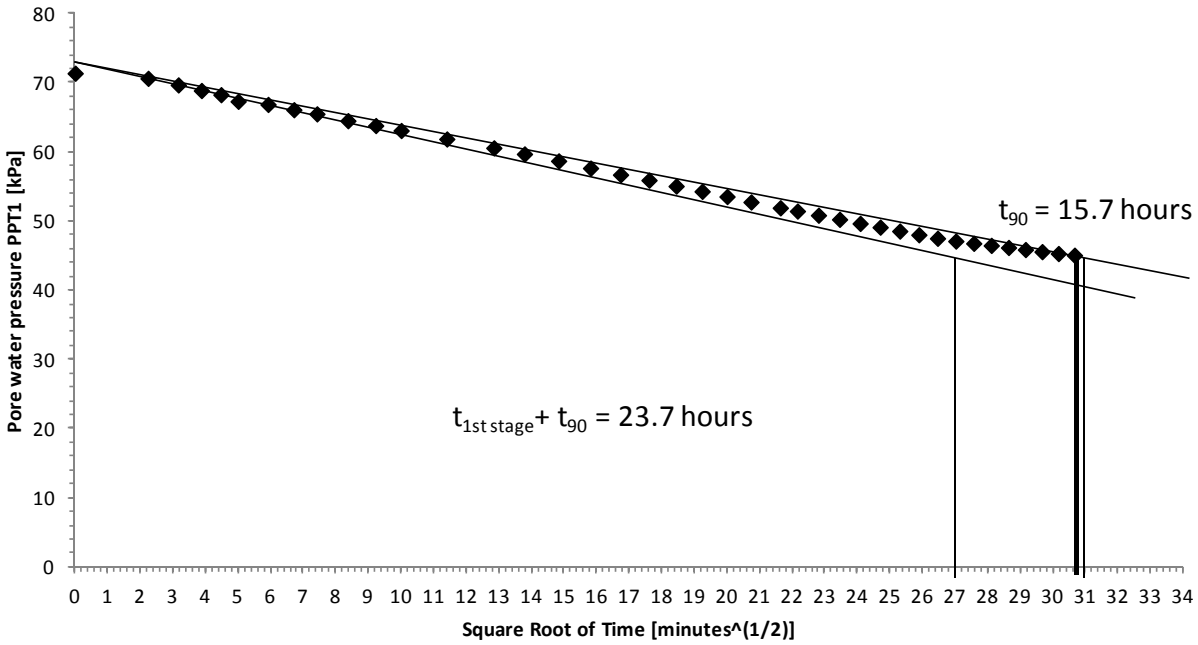

Fig. A82-07. Excess pore-water pressure dissipation during self-weight consolidation at PPT1 location – LTP = 0.70 m – Lateral test – Final stage.

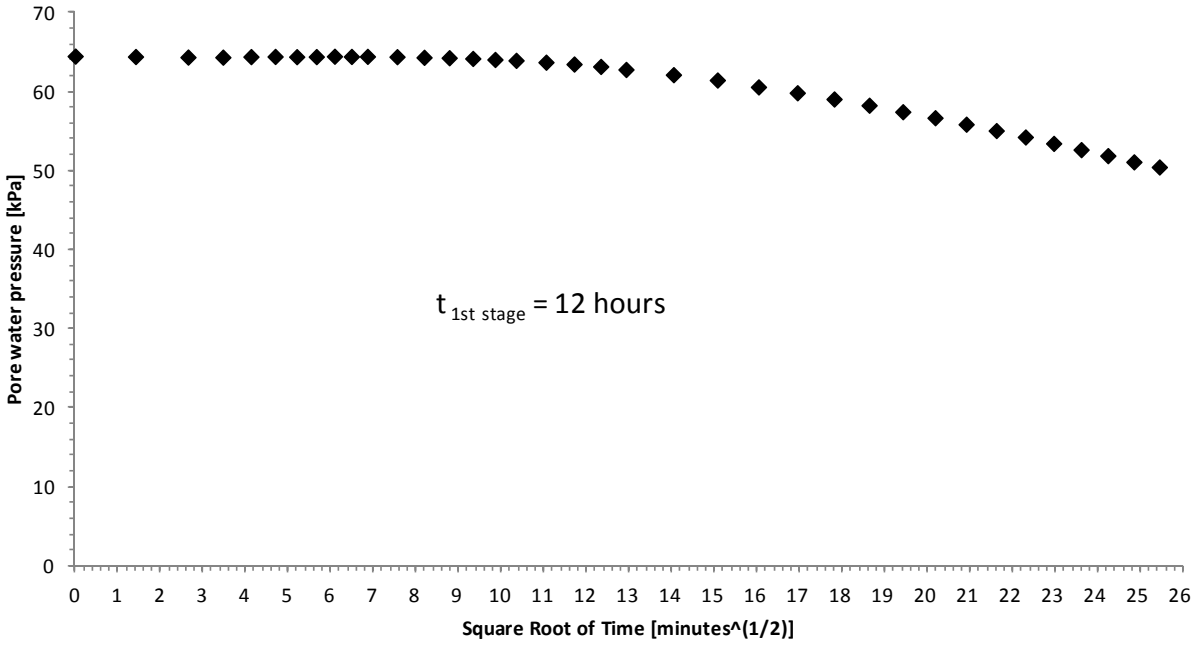

Fig. A82-08. Excess pore-water pressure dissipation during self-weight consolidation at PPT1 location – LTP = 1.20 m – Lateral test – 1st stage.

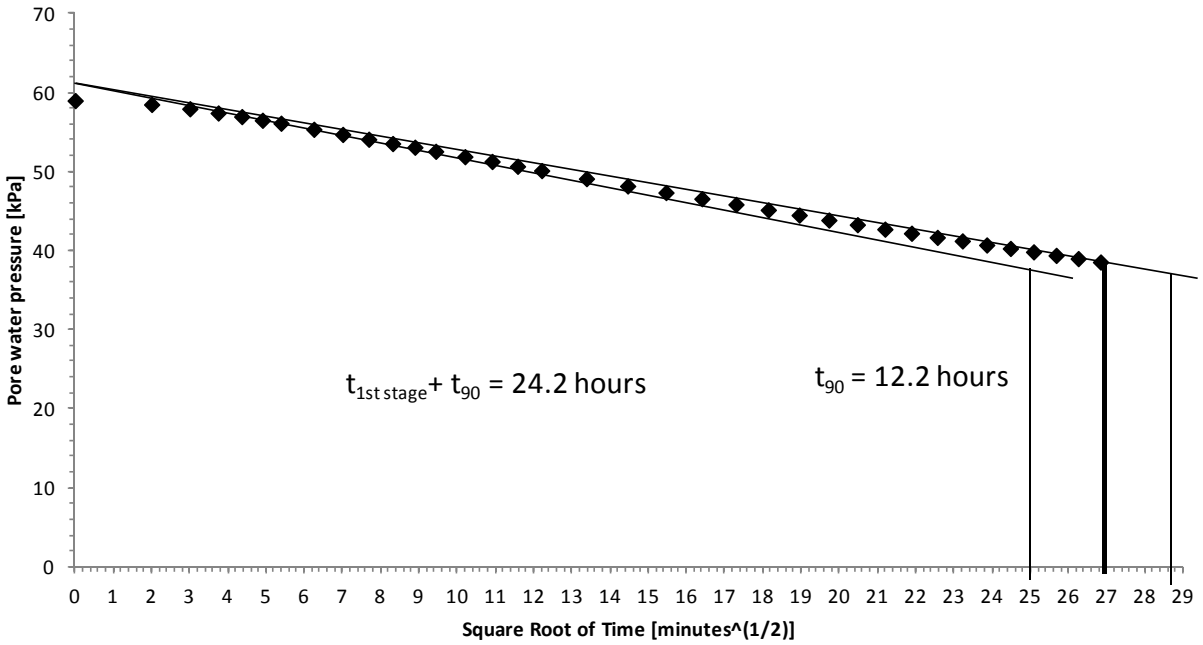

Fig. A82-09. Excess pore-water pressure dissipation during self-weight consolidation at PPT1 location – LTP = 1.20 m – Lateral test – Final stage.

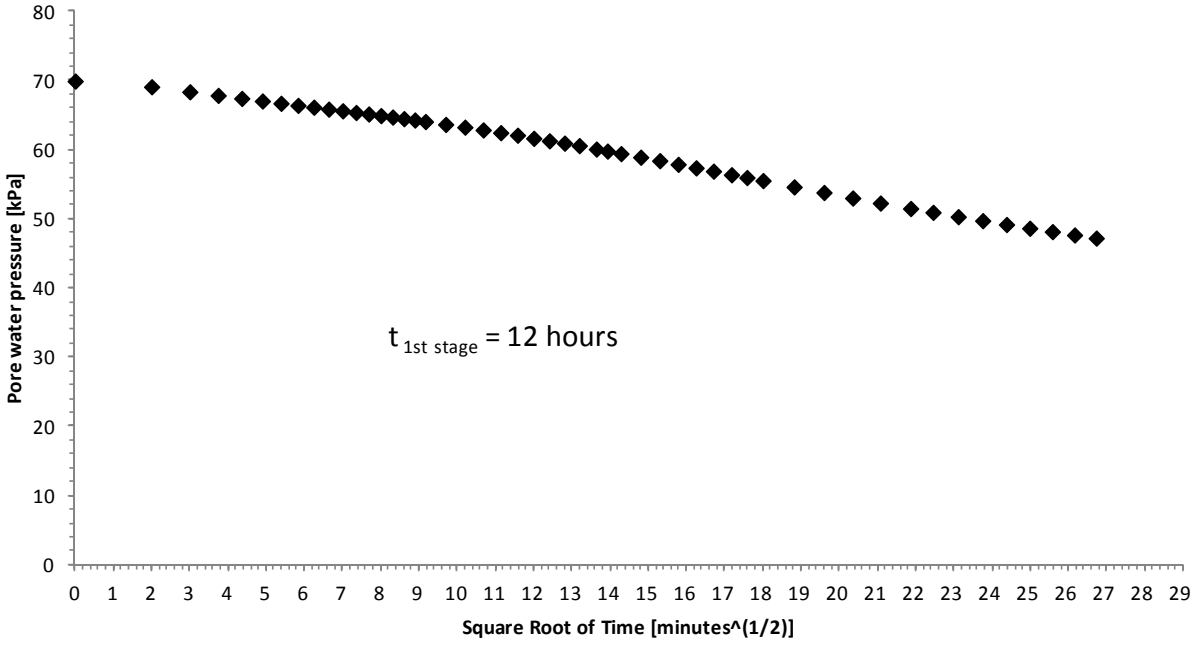

Fig. A82-10. Excess pore-water pressure dissipation during self-weight consolidation at PPT1 location – LTP = 1.20 m – Vertical test – 1st stage.

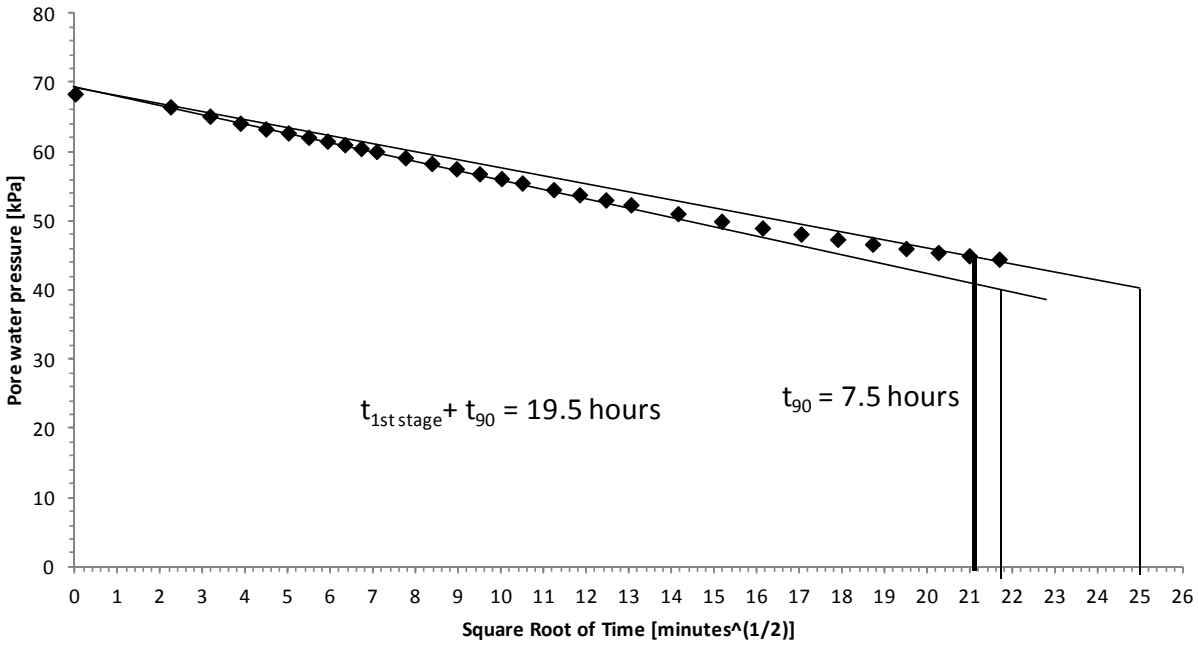

Fig. A82-11. Excess pore-water pressure dissipation during self-weight consolidation at PPT1 location – LTP = 1.20 m – Vertical test – Final stage.

8.3 APPENDIX C: Centrifuge Tests – Work vs. Lateral Load

This appendix includes the work vs. lateral load curves that were plotted with the purpose of estimating the lateral load at failure for each of the centrifuge models that were laterally tested.

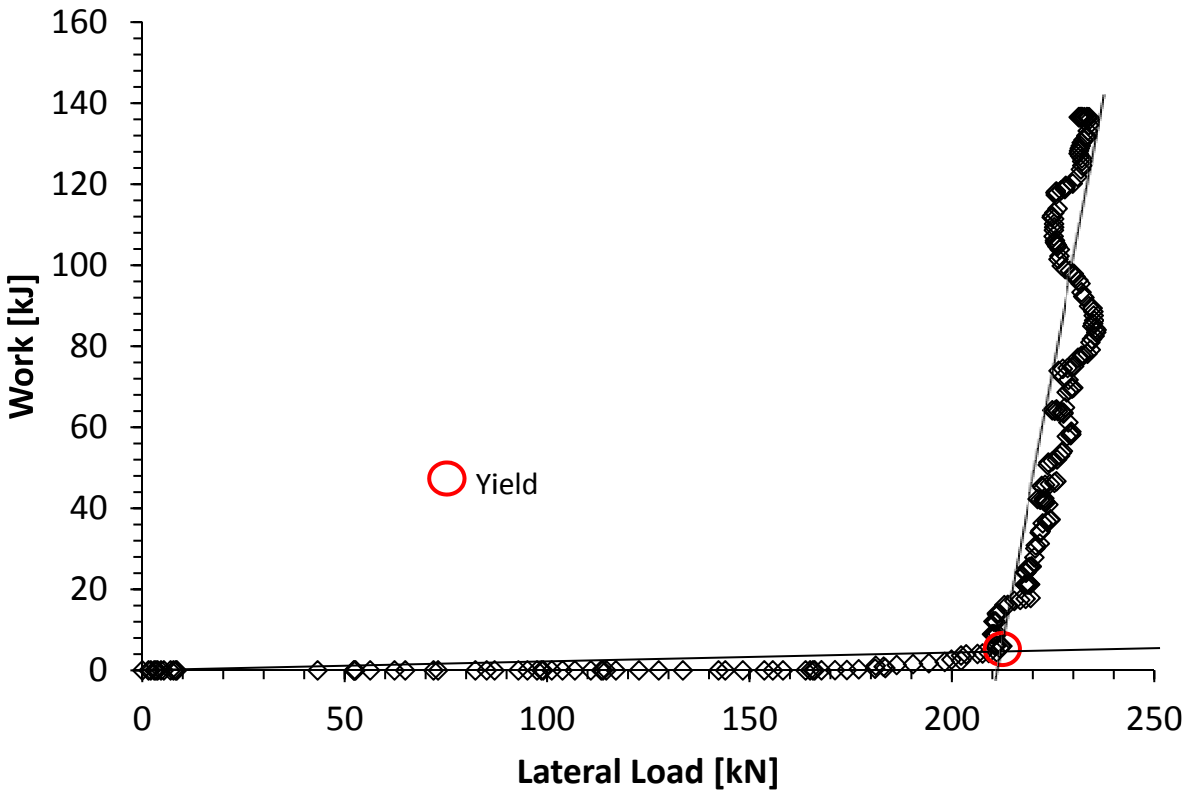

Fig. A83-01. Work vs. lateral load curve of the lateral load test with a LTP H = 1.20 m.

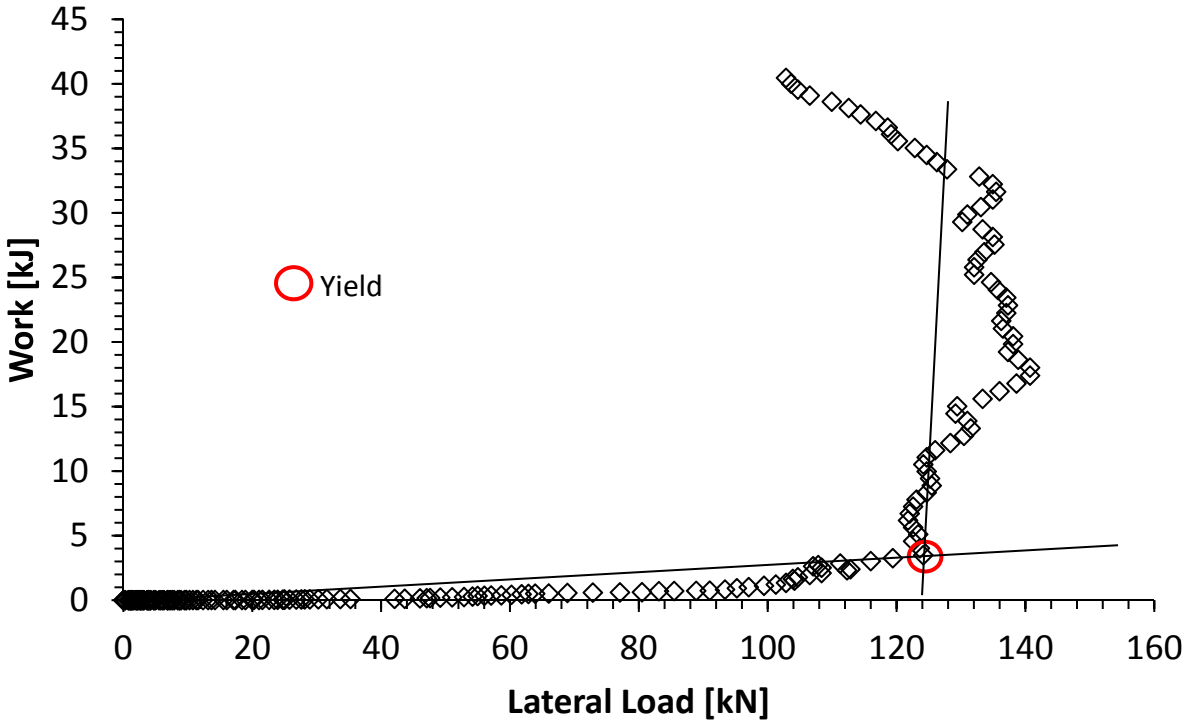

Fig. A83-02. Work vs. lateral load curve of the lateral load test with a LTP H = 0.70 m.

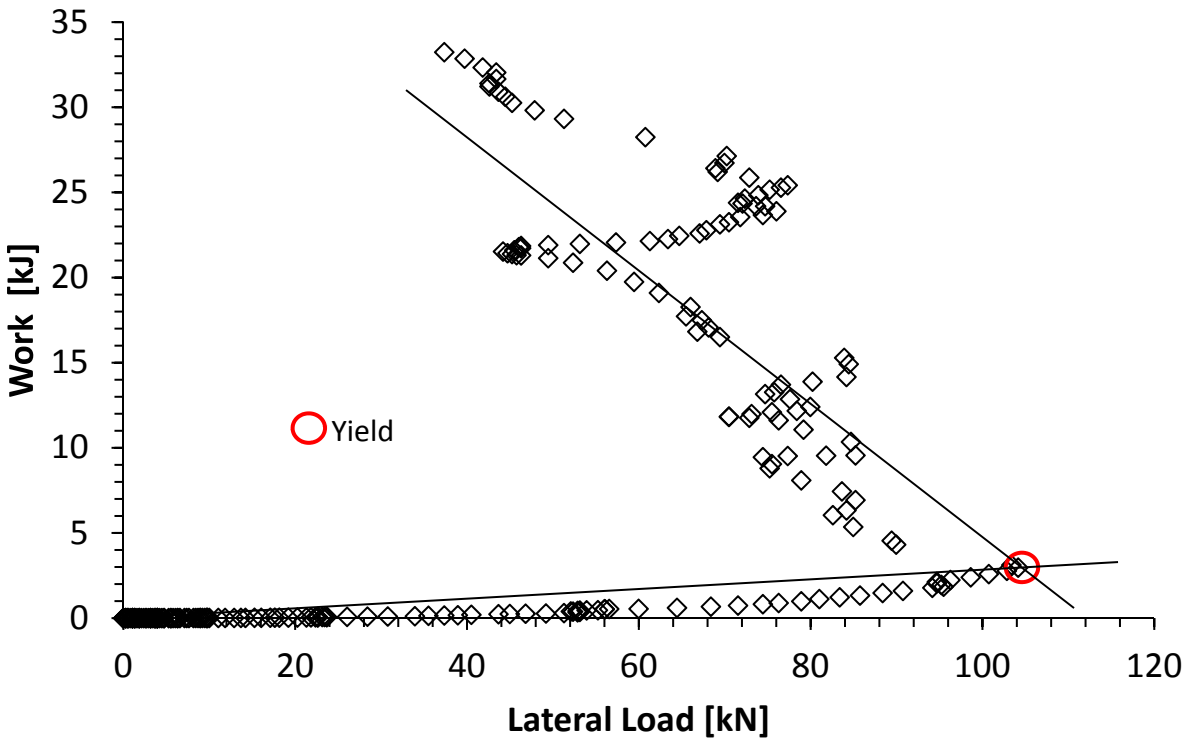

Fig. A83-03. Work vs. lateral load curve of the lateral load test with a LTP H = 0.60 m.

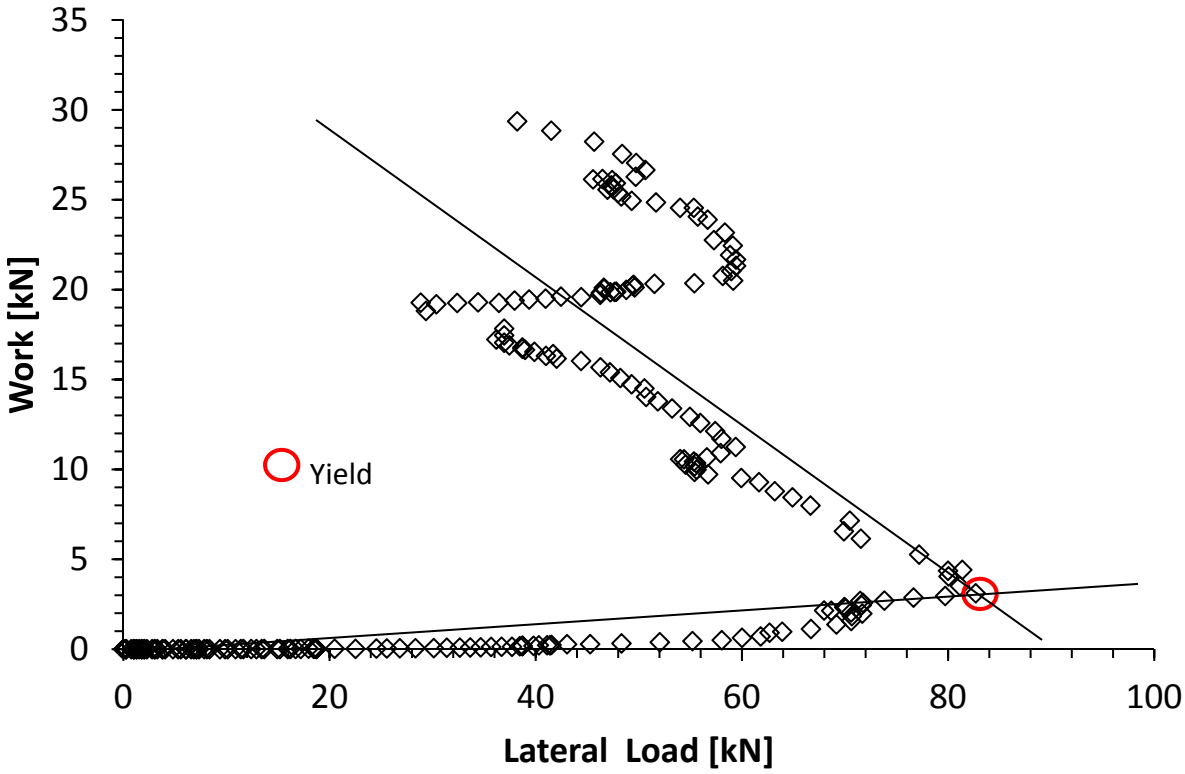

Fig. A83-04. Work vs. lateral load curve of the lateral load test with a LTP H = 0.45 m.

8.4 APPENDIX D: Numerical Modeling – Work vs. Lateral Load

This appendix includes the work vs. lateral load curves that were plotted with the purpose of estimating the lateral load at failure for each of the lateral load tests that were numerically examined in PLAXIS 3D.

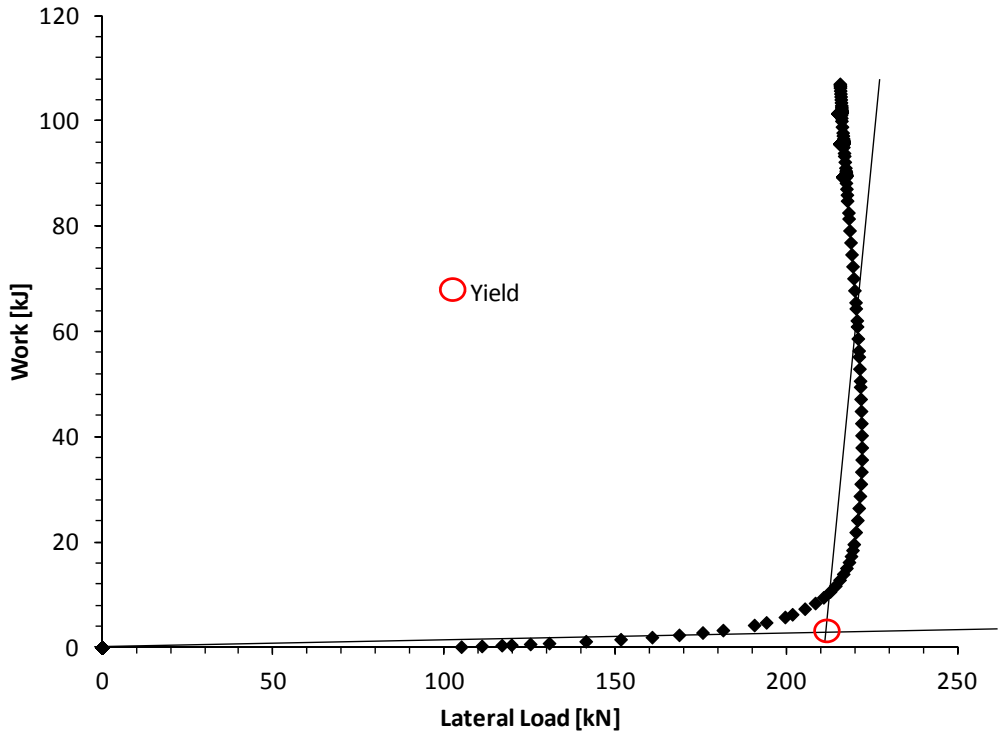

Fig. A84-01. Work vs. lateral load curve of the lateral load test with a LTP H = 1.20 m.

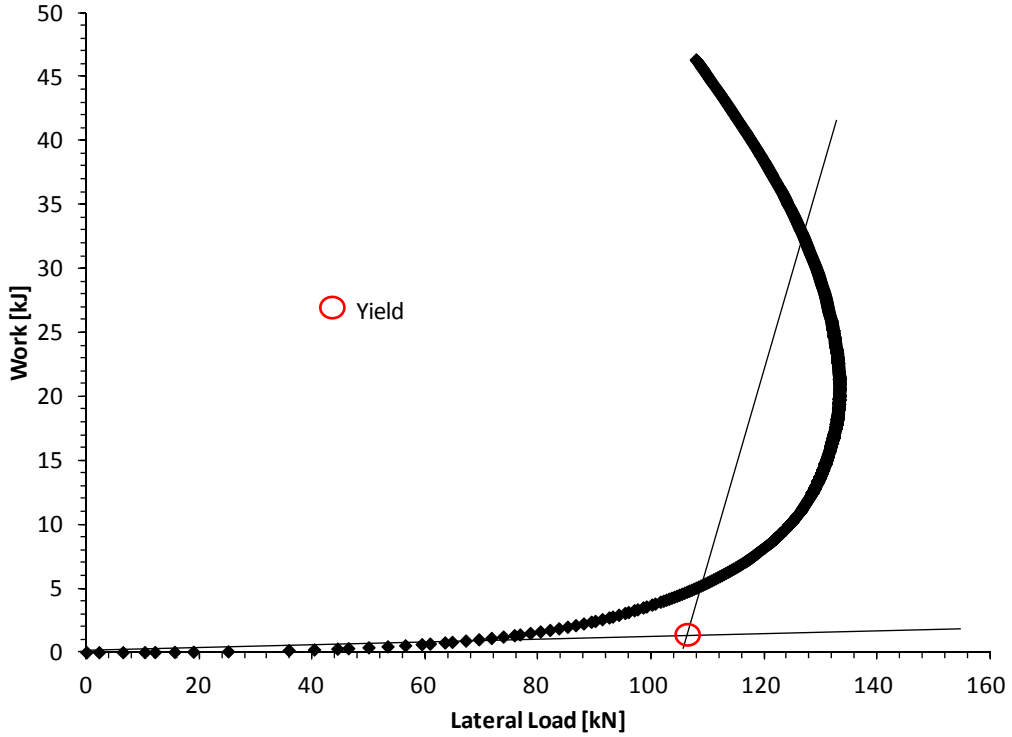

Fig. A84-02. Work vs. lateral load curve of the lateral load test with a LTP H = 0.70 m.

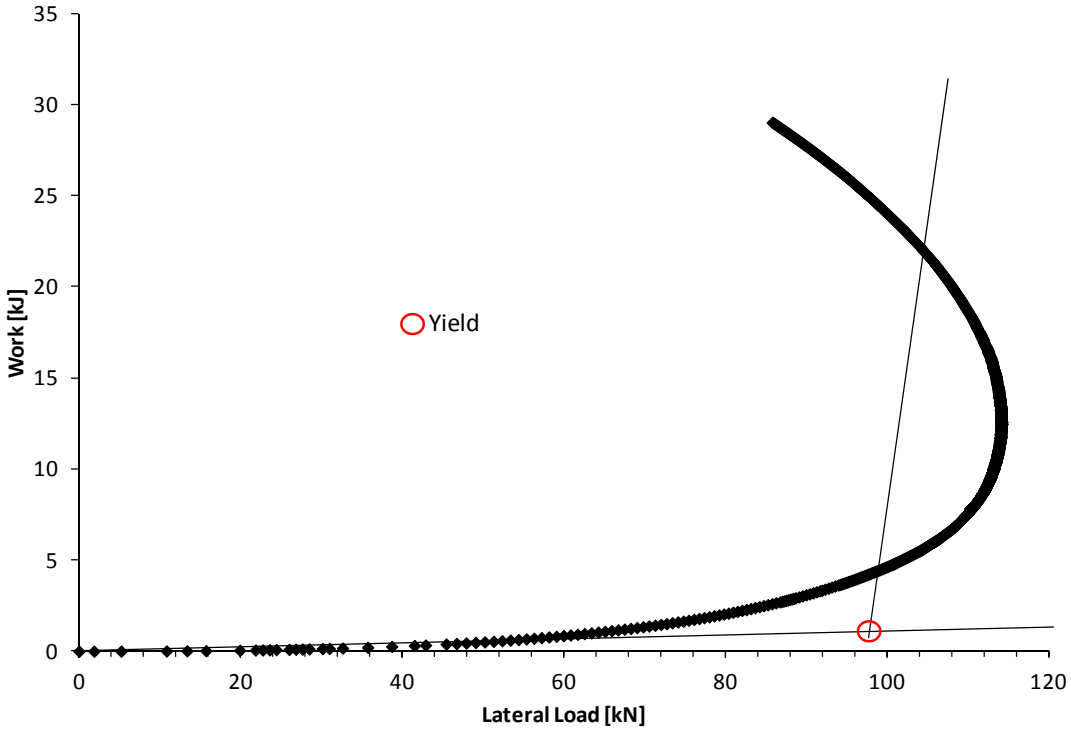

Fig. A84-03. Work vs. lateral load curve of the lateral load test with a LTP H = 0.60 m.

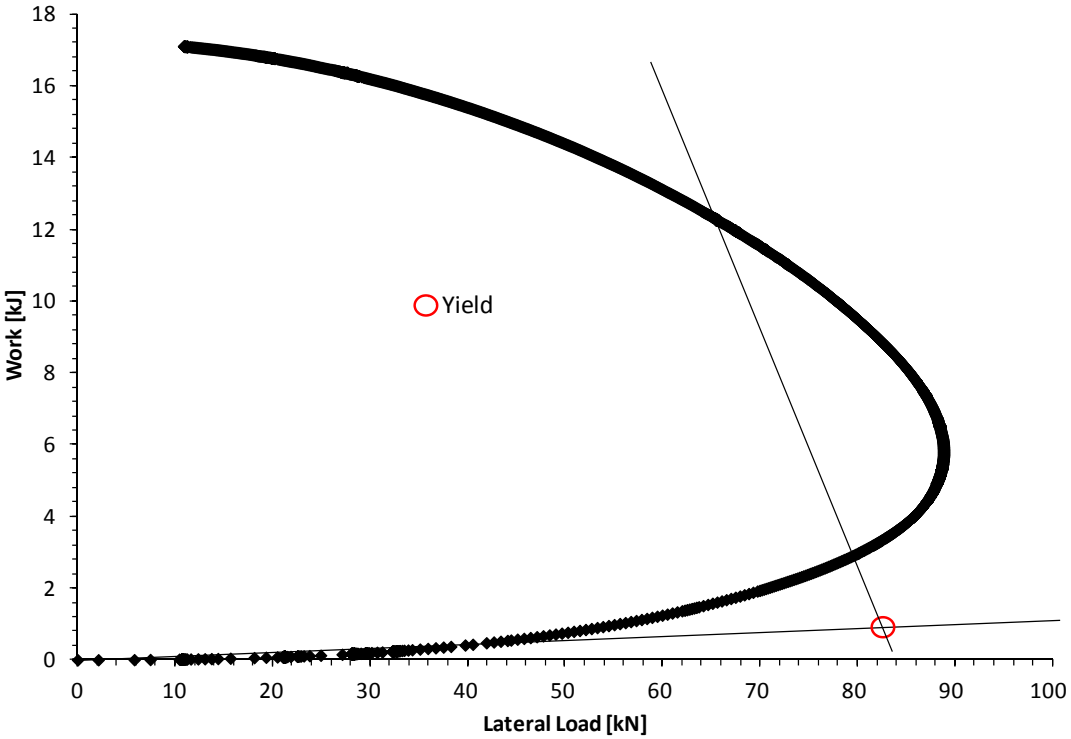

Fig. A84-04. Work vs. lateral load curve of the lateral load test with a LTP H = 0.45 m.